THE WEAR BEHAVIOUR OF ION IMPLANTED BIOMATERIALS

by

Derrick Kwadwo Boampong B.Eng (Hons)

A thesis submitted for the degree of Doctor of Philosophy at the University of Durham

Centre for Biomedical Engineering
School of Engineering
University of Durham
South Road
Durham
DH1 3LE

September, 2003

Abstract

The tribological performance of biomaterials used for artificial joints is of much importance, and require low coefficients of friction, resistance to wear and the ability to withstand many millions of cycles under a multitude of loading regimes. Currently used material combinations include Ti6Al4V, 316L stainless steel and Co-Cr-Mo articulating against UHMWPE. Although typical wear rates are low (60 $mm^3/10^6$ cycles), the UHMWPE wear debris produced during articulation has been linked to osteolysis, leading to loosening of prostheses and necessitating revision surgery. This study aimed to characterise the surfaces and quantitatively assess the tribological performance of such biomaterials when surface modified by N^+ ion implantation. Beyond this, investigation of the physical effects of the N^+ ion implantations were carried out with a view to determination of an optimum ion implantation protocol.

The tribological performance of the materials, were quantitatively assessed using multidirectional pin-on-plate wear testing. Surface characterisation of the materials, were studied using a combination of optical microscopy, AFM, non-contacting interferometry, SEM, and XPS. A significant increase in the surface microhardness of the modified materials was measured post ion implantation. This was attributed to the formation of ion implantation induced lattice disorder and hard phase nitride precipitates on the metallic surfaces, and cross-linking incorporating new formed chemical bonds on the polymeric surfaces. N^+ ion implantation with 5 x 10^{15} N^+ ions/cm^2 significantly enhanced the wear resistance of UHMWPE by $\approx$ 55 % when articulated against 2 x 10^{17} N^+ ions/cm^2 implanted Ti6Al4V; by $\approx$ 48 % when articulated against 2 x 10^{17} N^+ ions/cm^2 implanted stainless steel; and by $\approx$ 48 % when articulated against 2 x 10^{17} N^+ ions/cm^2 implanted Co-Cr-Mo.

The technique of ion implantation offers potential as a modification method, to improve wear resistance of these biomaterials for articulating applications such as in total joint replacement.

Acknowledgements

I would like to express my deepest gratitude to my supervisors Dr Sarah Green and Professor Anthony Unsworth for their expertise and advice during the period covered by this PhD work, Dr Sarah Green in particular for her continuous guidance and motivation throughout the project.

Additionally, many thanks to the expert technical staff in the mechanical and electrical workshops at the School of Engineering, University of Durham, in particular Kevan Moore, Colin Wintrope, and Ian Huthinson for their friendship, tolerance, and hours of work they invested into this project. I would also like to thank all other members of the academic staff at the School of Engineering, for their assistance during the course of this work.

I acknowledge the many organisations who have supported my work on this thesis: Depuy Johnson and Johnson for supplying the selected bulk biomaterials, Tech-Ni-Plant Ltd for carrying out the N^+ ion implantation, Nottingham University, Department of Materials (Martin Roe in particular) for carrying out the XPS surface analysis, and EPSRC for the financial support to make the project possible.

Finally I would like to thank my friends within the Engineering department. I would also like to thank my family and friends in London for their endless support, Mum and Dad in particular for their encouragement and believing in me. Last but not the least, I would like to thank my darling Noomi Bates for her tolerance, endless support and understanding especially during the last few months of hard work.

Declaration

The work contained in this thesis has not been submitted elsewhere for any other degree or qualification, and that, unless otherwise referenced, it is my own work.

Statement of copyright

Contents

CHAPTER THREE - TRIBOLOGY AND SURFACE MODIFICATION

EXPERIMENTAL WORK – CHAPTERS FOUR, FIVE, AND SIX

List of Tables

List of figures

Notation

at. %	Atomic Percent
AFM	Atomic Force Microscopy
ASTM	American Society for Testing and Materials
BCC	Body Centred Cubic
Contam	Contamination
CM	Contact Mode
Co-Cr-Mo	Cobalt Chrome Molybdenum
CRT	Cathode Ray Tube
E_B	Binding Energy
ERD	Energy Recoil Discharge
E_k	Kinetic Energy of Photoelectron
eV	Electron Volt
F	Force
GDS	Glow Discharge Spectroscopy
GIXD	Grazing Incidence X-ray Diffraction
HCP	Hexagonal Close-Packed
HDPE	High Density Polyethylene
hv	Energy of Exciting X-ray Photon
IBAD	Ion Beam Assisted Deposistion
IBT	Ion Beam Texturising
k_o	Wear Factor
LDPE	Low Density Polyethylene
m	Mass
Max	Maximum
NCM	Non Contact Mode
NCI	Non-contacting Interferometer
P	Load
PMMA	Polymethylmethacrylate
PTFE	Polytetrafluoroethylene
PVD	Physical Vapour Deposition
r	Radius
R_a	Arithmetic Mean Surface Roughness
R_p	Maximum Height of Profile

R_{pm}	Mean Height of Profile
R_t	Maximum Peak to Value Height
R_{tm}	Mean Peak to Value Height
S	Sliding Distance
SEM	Scanning Electron Microscope
SPM	Scanning Probe Microscope
STM	Scanning Tunnelling Microspe
TEM	Transmission Electron Microscope
Ti6Al4V	Titanium-6Aluminium-4Vanadium
TJR(s)	Total Joint Replacement(s)
UHMWPE	Ultra High Molecular Weight Polyethylene
V	Volume Loss
Wt	Weight
X	Sliding Distance
XPS	X-ray Photoelectron Spectroscope
ρ	Density
μ	Coefficient of Friction
ϕ	Work Function or Minimum Threshold Radiation Energy
θ	Knoop Diamond Indenter Angle
α	Half Knoop Diamond Indenter Angle
%	Percent
3-D	Three Dimensional

CHAPTER ONE – INTRODUCTION

2001-2010 has been designated the Bone and Joint Decade by the World Health Organisation (WHO) and the mission is to 'advance the understanding and treatment of musculoskeletal disorders through prevention, education and research' [1].

Natural synovial joints e.g., hip joints, are complex and delicate structures capable of functioning under critical conditions and are probably the most optimal tribosystems that exist [2, 3]. They are self-lubricating and the articulating surfaces are regenerative, ensuring that normally they function over long periods of time. The performance of natural synovial joints is due to the optimised combination of articular cartilage, a load bearing connective tissue covering the bones involved in the joint, and synovial fluid, which is a nutrient fluid secreted within the joint area. Figure 1.1 shows the structure of a typical natural synovial joint (adapted from [4]).

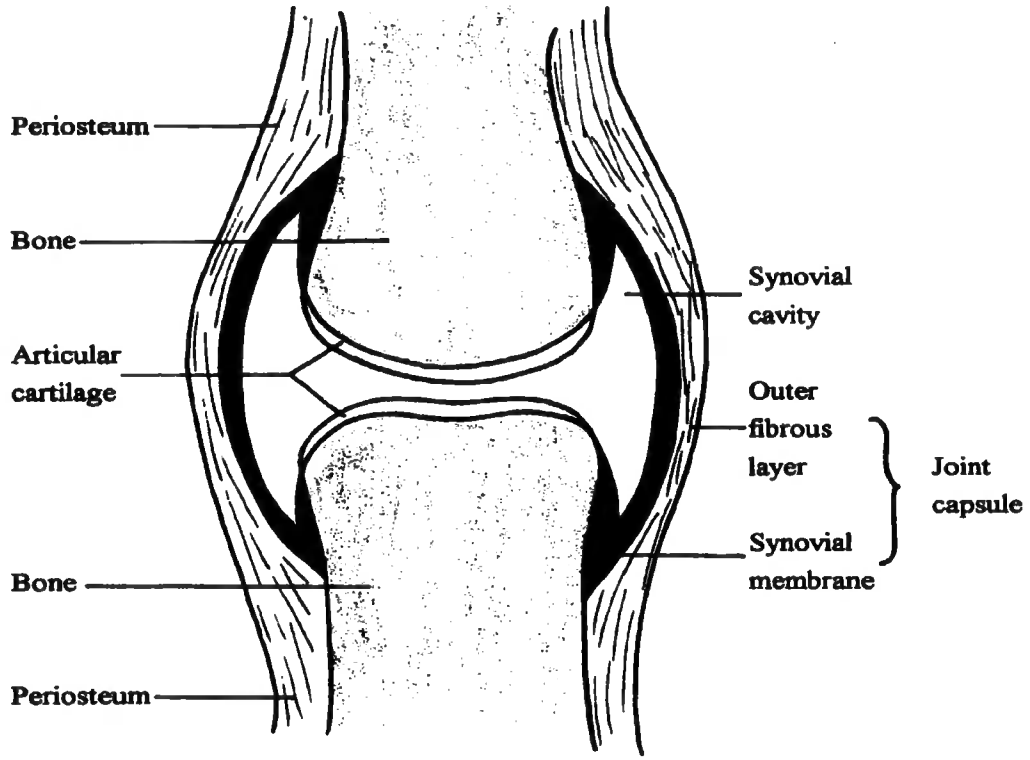

Figure 1.1. A simple natural synovial joint structure

Unfortunately, natural synovial joints are susceptible to degenerative and inflammatory diseases that result in pain and joint stiffness, as a result of a breakdown in the joint structure. Apart from normal ageing or accidental damage of the articular cartilage, the

most common degenerative processes affecting the joints are primary or secondary osteoarthritis (osteoarthrosis), and to a lesser extent rheumatoid arthritis (inflammation of the synovial membrane) and chondromalacia (softening of the cartilage) [2, 4]. In fact 90% of the population over the age of 40 suffers from some degree of degenerative joint disease.

Degeneration of the weight bearing joints often requires surgery to relieve pain and increase mobility. Ultimately when the natural joint can no longer perform adequately, replacement of the diseased joint surfaces by metal, plastic or ceramic artificial materials is accomplished through arthroplastic ('plastic repair of a joint') surgery. Total joint replacement (TJR) arthroplasty is the surgical technique that replaces all articulating degenerated natural surfaces with artificial materials by creation of a new prosthetic joint, and is recognised as a major achievement in orthopaedic surgery [2]. During the past half-century the design and clinical use of a wide variety of joint prostheses has matured and developed into a stage where most of the articulating joints can now be replaced. Much of this progress is due to the development of new biomaterials that are very much better able to withstand the mechanical and biological demands. In recently used TJRs, components that are typically anchored to the bone using polymethylmethacrylate (PMMA) bone cement are known as cemented total joints. PMMA acts as a grouting agent by filling the gap between the implant and the bone, and interdigitates with the bone to provide an interference fit. When the components are coated with porous surfaces for ingrowth of living bone, the replacements are known as non-cemented TJRs [5, 6]. Prosthetic joint replacement has dramatically improved the lives of millions of people worldwide [7].

Since 1962, the most widely accepted implant configuration includes a metal component articulating against a polymeric component, which is mainly ultra high molecular weight polyethylene (UHMWPE). Although other bearing couples have been investigated such as metal-on-metal, ceramic-on-ceramic or metal-on-ceramic, today metal-on-UHMWPE TJR are an international standard of care for degenerative joint disorders [2, 5, 8-10], and is an effective and popular treatment modality providing immediate pain relief and remarkable restoration of mobility for patients with joint disorders. The success of the UHMWPE polymer as the bearing surface is attributed to its excellent wear and abrasion resistance compared with other polymers such as polytetrafluoroethylene (PTFE) [11]. Initially, PTFE was tried as the polymeric bearing

surface material for total hip replacement, but was unsuccessful due to excessive and unacceptable wear rates. The most commonly used metallic components in TJR today include Ti6Al4V, 316L stainless steel and Co-Cr-Mo alloys [12], the structure, compositions and properties of which are discussed more in detail in chapter two. Producing the artificial joints is however, an extremely difficult and also a challenging biomedical and material science problem, since such devices must meet a number of diverse requirements, such as tissue compatibility to avoid adverse tissue reactions, mechanical strength, strong fixation, excellent corrosion and wear resistance, in order to function adequately during long-term use [2, 3, 5].

Despite major technical advances over the last several decades and significant material improvements, unresolved problems that can lead to failure of the prosthetic joint still remain. Some of the factors that may affect the long-term performance of total joint replacements includes [13-16]:

1. Friction, which produces a shear force to the UHMWPE component and motion relative to the bone
2. Wear of the UHMWPE surface and the production of wear debris, which can lead to adverse cell response and eventual loosening and revision of the implant
3. Metal ion release into the body from metal bearing surfaces from the repeated removal and reformation of passive oxides, and
4. Micro abrasion by third-body particulates such as bone cement debris, which can gradually increase the metal surface roughness and hence further increase the UHMWPE wear

Aseptic loosening and osteolysis remain the biggest problem with the cemented total joints, whereas failure of porous-ingrowth implants to provide consistent pain relief and the potential toxic effects of metal ion leaching on living tissues are the unanswered problems with non-cemented TJRs [5, 17, 18]. Osteolysis has been reported in association with both stable and loose uncemented and cemented femoral components [19], indicating that the problem is broad in scope. It occurs when periprosthetic bone loss appears localised around the implant, and can be distinguished from bone loss that is more evenly distributed around the implant. The definitive measure of clinical aseptic failure of a joint arthroplasty is the progressive loss of prosthetic bone that can necessitate a re-operation [7].

UHMWPE as an articulating surface has been the principal material of choice for TJR prostheses for many years, e.g., as acetabular cups and tibial components due to its favourable characteristics (section 2.4.1), and approximately one million components are implanted on a yearly basis. However, wear which is sometimes excessive due to articulation (especially in prostheses implanted into younger and more active patients) is a major obstacle limiting the longevity of implanted UHMWPE components, despite the recognised success and worldwide acceptance of TJR [8, 9, 11, 18-21]. The consequence of this wear can be mechanical failure as a result of the wear through of the UHMWPE acetabular component in total hip replacement (THR) or fracture of the tibial component in total knee replacement (TKR), or biological due to osteolytic reactions to particulate sub-micron UHMWPE wear debris in the bone tissue that surrounds the prostheses [11, 15, 22, 23]. Mechanical failure due to wear has been significantly reduced with modern surgical techniques and advanced designs, such that the biological failure due to wear debris has become increasingly important in determining the long-term survival of total joint prostheses. Although the bulk UHMWPE material can be well tolerated *in vivo*, the sub-micron wear particles can be detrimental, and the production and accumulation of wear debris is well known to be associated with adverse tissue response which can lead to loosening and eventual revision of the prosthetic joint [15, 22, 24, 25]. When the wear particles are present in sufficient numbers phagocytosis can result in the activation of macrophages and in the direct resorption of the bone by macrophages. Revell *et al* [21], proposed that the body may tolerate low debris levels if they are below some critical point, hence minimising the wear of UHMWPE (which is the main aim of this work) is essential for improving long-term performance of the implant.

Rarely do a material's properties perfectly match every requirement in a given application and biomaterials are no exception. The majority of materials failures arise from deficiencies of the surface material in dealing with friction, wear, corrosion, fatigue etc. Even after thorough consideration of all options and selection of the best available material, surface properties often still limit performance and function [26, 27]. The surface material is the only part of any component that has to coexist with the external environment. It follows therefore that designers should choose bulk material from the standpoint of structural and economic criteria, and surface material to deal with the external conditions. Surface modification technology deals with the methods for achieving these desired surface requirements and their behaviour in service [28]. The

basic concept of surface modification is the use of treatment process such that, bulk material that possesses some combination of desirable properties such as low cost, high strength or good toughness, but is lacking in some specific surface property such as low friction, low wear, low corrosion or adhesion, is possible [29]. The process modifies surface properties while preserving bulk attributes of the material, and a wide variety of surface properties including tribological, mechanical, chemical and others that directly influence biocompatibility and functionality can be modified [26, 27, 29].

Ion-beam modification is a surface modification technology that is becoming popular for improving medical device function and biocompatibility, without the expense and time required to develop new materials. Processes such as ion implantation and ion-beam assisted deposition have proven successful in this area because they can provide beneficial surface layers with desirable properties without detrimentally affecting the bulk properties. Ion implantation in particular has been successful in biomaterial modification such as in improving the wear resistance of artificial joint components, and improving wettability of biomedical polymers, without the application of hard coatings [26, 27, 30]. The process offers several unique advantages over other surface modification techniques such as surface coatings. It facilitates both chemical and structural modification of the near surface volume of a material without the creation of a defined interface between modified and unmodified volume. Modifications can be performed at low temperatures with no distortion or changes in surface finish of the material. In so doing a gradual transition in chemistry, structure and properties is produced avoiding the possibility of interfacial delamination [31].

The aims of this work were to characterise the surface and quantitatively assess the tribological performance of the commercially used biomaterials (Ti6Al4V, stainless steel, Co-Cr-Mo, and UHMWPE) when surface modified by N^+ ion implantation, and to investigate and understand the chemical, structural, and topographic modifications induced by the modification, with a view to optimising the tribological performance of the biomaterials.

CHAPTER TWO – BIOMATERIALS (LITERATURE REVIEW)

2.0 Introduction

Many definitions have been proposed for the term "*biomaterial*". It has been defined as a nonviable material used in a medical device, intended to interact with biological systems (Williams, 1987 from [32]), or as a synthetic material used to replace part of living system or to function in intimate contact with living tissues [28]. These materials are of great use in the treatment of disease or injury. Some of the uses of biomaterials are indicated in table 2.1 (adapted from reference [28]). Complex chemical functions such as those of the liver, and complex electrical or electrochemical functions such as those of the brain and sense organs cannot be carried out by biomaterials. The success of a biomaterial in the body depends on factors such as the material properties, design and biocompatibility of the material used, as well as other factors, including the surgeon's technique used, health and condition of the patient, and the activities of the patient. It is known that the activity level of the patient increases the rate of wear of joint components [14].

Table 2.1. Uses of Biomaterials

Problem Area	Examples
Replacement of disease or damaged part	Artificial hip joint, kidney dialysis machine
Assist in healing	Sutures, bone plates and screws
Improved function	Cardiac pacemaker, contact lens
Correct functional abnormality	Harrington spinal rod
Correct cosmetic problem	Augmentation mammoplasty, chin augmentation
Aid to diagnosis	Probes and catheters
Aid to treatment	Catheters, drains
Regenerate tissue	Tissue engineering, e.g., skin grafts

Materials used as biomaterials in the body include metals, polymers, ceramics and composites, and only the metallic and polymeric biomaterials used in TJR applications are discussed here in detail. The success of a joint replacement lies with the orthopaedic

surgeon, not only to perform the surgery, but also to select the replacement that is best suited for the patient. The selection process can be influenced by the age and weight, along with the activity level of the patient post surgery [28, 33]. It is therefore important to have a complete understanding of the joint replacement and the behaviour of materials utilised in total joint applications. Metallic joint replacement components share many common features including biocompatibility or low toxicity (i.e., the ability of a matrerial to perform with an appropriate host response in a specific application [Williams, 1987 from [32]]), high corrosion resistance *in vivo*, high static and fatigue strength, and mechanical shock resistance [34]. They can be forged and/or machined into complex shapes using standard manufacturing methods, and when polished, work very well as low-friction femoral components in both TKRs and THRs. The three most important group of alloys used for femoral components are titanium alloys, austenitic stainless steels, and cobalt chrome alloys. The compositions, microstructures and properties of each of the metallic biomaterial alloys are discussed separately in sections 2.1, 2.2, and 2.3. The polymeric biomaterials, mainly UHMWPE and XLPE are also discussed in section 2.4. All these biomaterials were used during the experimental work.

2.1 Titanium Alloys

2.1.0 Introduction

Attempts to use titanium for implant fabrication date back to the late 1930s when it was found that titanium was tolerated in cat femurs. Its low density (4.5 g/cm^3) compared to 316L stainless steel (7.9 g/cm^3) and Co-Cr-Mo alloy (8.3 g/cm^3), low modulus (110 GPa) compared to 316L stainless steel (190 GPa) and Co-Cr-Mo (210 GPa), and good mechanical and chemical properties, are salient features for implant application [2, 28, 32]. The Ti6Al4V alloy is the most commonly used titanium-based biomaterial and is widely used to manufacture implants.

As biomaterials Ti6Al4V alloys are among the most biocompatible and gained increased usage in TJRs for many years. The favourable characteristics of the alloy include remarkable corrosion resistance under static conditions due to a protective oxide surface layer (TiO_2), excellent fatigue strength in chlorine solutions, high tensile strength, excellent ductility, formability and machinability, low density, and low modulus of elasticity [18, 35, 36]. They have low rigidity (high compliance) compared

with the other metallic biomaterials used for TJRs and hence have the theoretical advantage of reducing the incidence of proximal bone resorption due to stress shielding. The reaction of tissue that is adjacent to Ti6Al4V alloy implant has been reported to be extremely benign [37], and direct bone ingrowth or osseointegration with its implants does occur [18, 38]. The main disadvantages of the alloy as biomaterials include relatively poor surface wear resistance, notch sensitivity, potential toxicity of Al and V ions (produced during articulation), and more expensive and not as easy to polish (compared to stainless steel and cobalt chrome alloys) [18]. When subjected to wear, the passive oxide layer can be removed allowing active corrosion to occur while the alloy re-passivates [39]. Although they are still widely used as stem materials for modular THRs, Ti6Al4V alloys are no longer recommended for use as bearing surfaces, due to a high incidence of aseptic loosening which has been associated with tissue blackening and metallosis [18, 37, 40], caused by the creation of the metallic particulate debris. The origin of the debris was linked with the formation of poorly adhering surface oxide layers, which periodically detached from the alloy's bearing surface due to articulation in the prosthetic joint. The incidence of such failures was higher than in joint replacement devices that used cobalt chrome or austenitic stainless steel alloys as the bearing surface.

2.1.1 Composition, Microstructure and Properties

The chemical composition specification for wrought Ti6Al4V alloy set by the British (BS 7252: Part 3: 1990) and American (ASTM F136) standards are shown in table 2.2 [28, 32, 34]. The main alloying elements are Al, 5.5-6.5 wt %, and V, 3.5-4.5 wt. %.

Table 2.2. Chemical Composition of Wrought Ti6AL4V Alloy

Element	Composition (wt. %)	
	BS 7252: Part 3: 1990[a]	ASTM F136[b]
Nitrogen	0.05 max	0.05 max
Carbon	0.08 max	0.08 max
Hydrogen	0.015 max	0.0125 max
Iron	0.30 max	0.25 max
Oxygen	0.20 max	0.13 max
Vanadium	3.5-4.5	3.5-4.5[c]
Aluminium	5.5-6.75	5.5-6.5[c]
Titanium	Balance	88.3-90.8[c]

[a]From [34], [b]from [28], and [c]from [32].

Titanium is a transition metal with an incomplete shell in its electronic structure, which enables it to form solid solutions with most substitutional elements. It is an allotropic material, exhibiting a hexagonal close-packed (hcp) crystal structure (α-Ti) up to 882.5 °C (the beta transus), transforming into a body centred cubic (bcc) structure (β-Ti) above this temperature [2]. In its elemental form it has a high melting point of 1678 °C. The alloys of titanium may be classified as either alpha (α), near-α, $\alpha + \beta$, meta-stable or stable beta (β), depending on their room temperature microstructure. The alloying elements fall into three categories [2]; α - stabilisers such as Al, O, N, and C; β - stabilisers such as V, Mo, and, Nb; and neutral such as Zr. The addition of alloying elements to Ti enables it to have a wide range of properties. The α, and near-α titanium alloys have single-phase microstructures which promotes good weldability, and excellent corrosion resistance, but their use as biomedical materials are principally limited by their low ambient temperature strength due to the presence of only the α phase. However, the stabilising effect of Al results in excellent strength characteristics and oxidation resistance at high temperatures (300-600 °C). In contrast, $\alpha + \beta$ alloys exhibit higher strength due to the presence of both α and β phases, and their properties depend on composition, the relative proportions of the α / β phases, and the alloy's prior thermal treatment and thermo-mechanical processing conditions. β alloys, meta-stable or stable, have high strength, good formability, and high hardenability.

The Ti6Al4V alloy used for implants is an $\alpha + \beta$ alloy and its microstructure depends on heat treating and mechanical working. Al tends to stabilise the α phase by increasing the transformation temperature from α to β phase, whereas V stabilises the β phase by lowering the transformation temperature from α to β [28, 32]. During heat treatments and mechanical working, three different microstructures of the alloy can be formed depending on the heat treatment conditions. If the alloy is heated into the β phase field (> 1000 °C) and then cooled slowly to room temperature, the α phase precipitates out as plates having a specific crystallographic orientation within grains of the β matrix. A two-phase structure known as the Widmanstatten structure is produced [32] (figure 2.1). If the cooling from the β phase field is very fast a "*basketweave*" microstructure will develop due to martensitic or bainitic (non-diffusional shear) solid-state transformations. Ti6Al4V alloy used for implants are commonly heated and worked at temperatures near but not exceeding the β transus, and then annealed to give a micro-structure of fine-grained α with β as isolated particles at grain boundaries [32] (mill annealed, figure 2.2). All of the three microstructures in Ti6Al4V alloy lead to about the same yield and ultimate tensile strengths, but the mill-annealed condition is superior in high-cycle fatigue, which is a significant consideration. The Ti6Al4V alloy used in this study had a microstructure of the mill-annealed type.

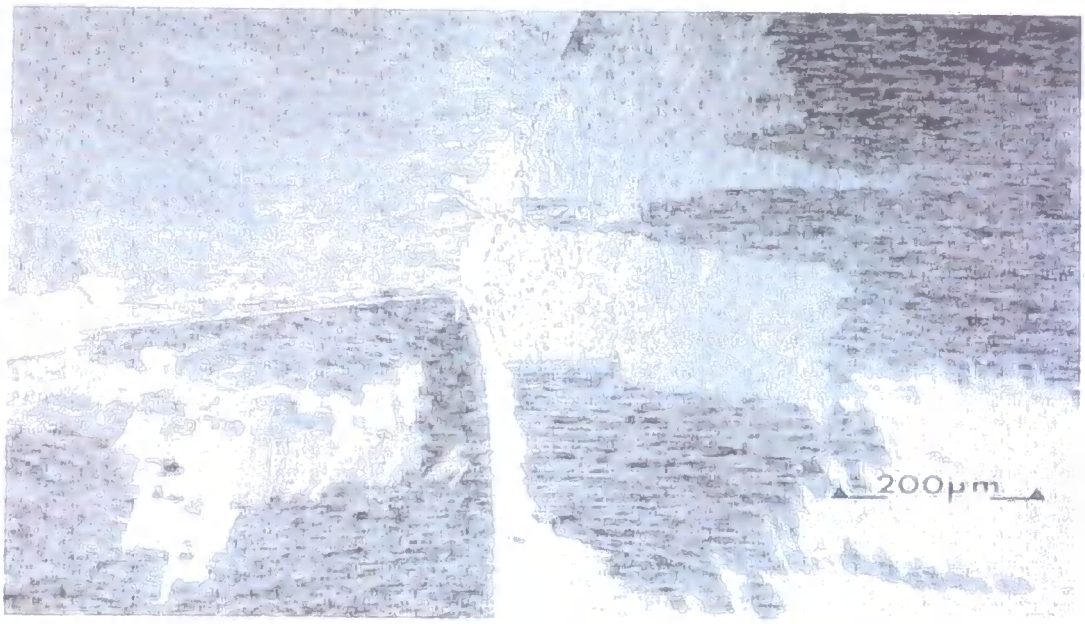

Figure 2.1. Widmanstatten structure in cast Ti6Al4V (ASTM F136) [32]

Figure 2.2. Micro-structure of wrought and mill annealed Ti6Al4V, showing small grains of α (light) and β (dark) [32]

Table 2.3 lists some of the typical mechanical properties of wrought Ti6AL4V implant metal [2, 28, 32, 41]. The alloy has modulus that is roughly half those of 316L stainless steel (table 2.5) and Co-Cr-Mo (table 2.8), combined with relatively high strength and

low ductility. When compared by the specific strength (strength/density), Ti6Al4V alloys excels over any other implant material [28].

Table 2.3. Typical Mechanical Properties of Wrought Ti6AL4V Alloy (ASTM F136)

Property	Value
Young's modulus (GPa)	116
Tensile strength (MPa)	965
Yield strength (MPa)	896
Minimum 0.2 % proof strength (MPa)[a]	780
Fatigue endurance limit (at 10^7 cycles, R = -1) (MPa)	620
Strain to failure (%)	10
Reduction of area (%)	25

[a]From BS 7252: Part 3: 199 [34].

Titanium is very reactive at high temperature and burns readily in the presence of oxygen. It therefore requires an inert atmosphere for high-temperature processing, and is normally processed by vacuum melting. Oxygen diffuses readily in the metal and the dissolved oxygen embrittles the material. As a result, hot working or forging operations are carried out below 925°C [28].

2.2 Stainless Steel Alloys

2.2.0 Introduction

The first stainless steel used for implant materials was the 18-8 (type 302), and then the 18-8sMo with improved corrosion resistance in salt water was introduced and became known as type 316 [28]. The carbon content of the alloy was reduced from 0.08 wt. % to 0.03 wt. % max for better corrosion resistance in chloride solution, and became known as the type 316L in the 1950s, where L denotes the low carbon content. They are austenitic stainless steels (both the type 316 and 316L) and are most widely used for implants. Although there are several types of stainless steels available the most common in practice is the type 316L stainless steel, which is recommended by the American Society for Testing and Materials (ASTM) for implant fabrication [28].

As biomaterials, 316L stainless steel has been applied for many years as permanent or temporary implants. The mechanical properties of stainless steel (table 2.5) are lower than those of Ti6AL4V alloy (table 2.3), but its friction and wear characteristics are far better. 316L stainless steel is cheap, easy to machine and to polish compared to Ti6Al4V alloys. 316L stainless steel implants have acceptable friction and wear properties in joint implants, and most explanted hip prostheses do not show significant *in vivo* wear. However, in some cases, crevice corrosion, which is often associated with wear, has been observed [42, 43], and synergistic effects of fatigue in chlorine solutions can not be avoided at present. During long-term contact with body fluids and tissues, 316L stainless steel implants have been reported [16, 43] to show metallic wear and corrosion. The *in vitro* immersion of stainless steel in physiological solutions has found toxic ions such as Cr, Ni, and Mo to be present both in solutions, and in the corrosion products [21, 44].

In the UK, stemmed austenitic stainless steel (or one piece femoral components) are probably the most popular found designs of THR, and the early Charnley THR (circa 1965-70) used a stemmed femoral component based on 18-10 austenitic stainless steel (known at the time as EN58J) [34]. Thackrays (now DePuy Johnson & Johnson) of Leeds introduced 316LVM a double-vacuum remelted 18Cr-10Ni stainless steel with superior corrosion resistance compared to the EN58J, and subsequently introduced a new stainless steel alloy based on Rex 734 in 1980 which remains in use to the present day and is known as Ortron 90 [34]. It is a high nitrogen 21Cr-10Ni-2.5Mo austenitic stainless steel with superior fatigue strength, corrosion and corrosion fatigue resistance, than the types EN58J or 316LVM.

2.2.1 Composition, Microstructure and Properties

The chemical composition of 316L stainless steel (ASTM) [28, 32] and Ortron 90 (BS 7252: Part 9: 1993) [34] are shown in the table 2.4. The alloy is predominantly iron (Fe) alloyed with major amounts of chromium (Cr), and nickel (Ni), and minor amounts of nitrogen (N), manganese (Mn), molybdenum (Mo) which enhances the alloy's resistance to pitting corrosion in salt water, phosphorous (P), silicon (Si), and sulphur (S). Both the Cr and Ni contents can influence the stability of the austenitic phase. Although Cr is a reactive element, it can be passivated with its alloys to give an excellent corrosion resistance. Its main function in stainless steel is to permit the

development of a corrosion resistant steel by forming a strongly adherent surface oxide layer, chromium oxide (Cr_2O_3). However, Cr tends to stabilise the ferritic body-centred cubic (bcc) phase, which is weak compared with the austenitic face-centred cubic (fcc) phase. Mo and Si are also ferrite stabilisers. The Ni present in the stainless steel serves to stabilise the austenitic phase at room temperature to counter the tendency to form ferrite, and to enhance the corrosion resistance of the alloy.

The most important reason for the low carbon content of the 316L stainless steel alloy relates to corrosion in that, if the C content exceeds 0.03 wt. % there is the increased danger of formation of carbides such as chromium carbides ($Cr_{23}C_6$) [28, 32]. These carbides have the tendency to precipitate at grain boundaries. Such precipitation depletes the adjacent grain boundary regions of Cr and hence reduces the ability to form Cr_2O_3. Stainless steels in which such carbides have formed are called '*sensitised*' and are prone to fail through corrosion-assisted fractures that originate at the weakened grain boundaries. Under the ASTM specifications, the desirable form of 316L stainless steel for implant fabrication is a single-phase austenite (fcc) with no free ferritic (bcc) or carbide phases in the microstructure [32]. It should also be free from inclusions such as sulphide stringers, which can arise from unclean steel-making practices and predispose the steel to pitting-type corrosion at the metal-inclusion interfaces.

Table 2.4. Composition of 316L Stainless Steel and Wrought Ortron 90

Element	Composition (wt %)	
	316L Stainless Steel[a]	Ortron 90[b]
Carbon	0.03 max	0.08 max
Manganese	2.00 max	2.00-4.25
Phosphorous	0.03 max	0.025 max
Sulphur	0.03 max	0.01 max
Silicon	0.75 max	0.75 max
Nitrogen	0.1 max[c]	0.25-0.50
Copper	0.50 max[c]	0.25 max
Chromium	17.00-20.00	19.5-22.0
Nickel	12.00-14.00	9.0-11.0
Molybdenum	2.00-4.00	2.0-3.0
Iron	60-65[c]	Balance

[a]From Annual Book of ASTM Standards, Part 46, 1980, p 578 (from [28]), [b]from [34], and [c]from [32].

Table 2.5 lists the mechanical properties of 316L stainless steel [2, 28, 32, 41], and table 2.6 lists the mechanical properties of the alloy's surgical implants under different conditions [28]. From table 2.6, a wide range of properties can be obtained depending on the heat treatment to obtain softer materials, or cold-working for greater strength and hardness. In comparison with Ti6Al4V alloy (table 2.3) and Co-Cr-Mo alloy (table 2.8), 316L stainless steel has moderate yield and ultimate strength combined with high ductility.

Table 2.5. Typical Mechanical Properties of 316L Stainless Steel

Property	Value
Young's modulus (GPa)	190
Tensile strength (MPa)	586
Yield strength (MPa)	331
Fatigue endurance limit (at 10^7 cycles, R = -1) (MPa)	241 - 276
Strain to failure (%)	40

Table 2.6. Mechanical Properties of 316L Stainless Steel Surgical Implants under Different Conditions

	Annealed	Cold-finish	Cold-worked
Ultimate tensile strength, min (MPa)	505	605	860
Yield strength (0.2% offset), min (MPa)	195	295	690
Elongation (50.8 mm), min (MPa)	40	35	12

316L stainless steel is known to work-harden very rapidly [28] and hence cannot be cold-worked without intermediate heat treatments. Heat treatments can however, cause the formation of chromium carbide (CrC_4) in the grain boundaries, and surface oxide scales. Care should therefore be taken during the heat treatments to prevent the formation of such carbides and oxide scales. Surface oxide scales can be removed either chemically with acid or mechanically by sandblasting when formed, before use. After the scales are removed the surface of the components are polished to a mirror finish, cleaned, degreased, and passivated in nitric acid [28]. The components are washed and cleaned again before packaging and sterilising.

2.3 Cobalt-Chrome Alloys

2.3.0 Introduction

Cobalt-chrome alloys were first developed for dental prostheses and were easy to obtain in complex shapes using casting techniques. As biomaterials, the alloys based on the Co-Cr-Mo system have been widely used for many years as femoral components and other medical implants. Its orthopaedic prostheses are durable and wear resistant, however, the mating component of UHMWPE easily wears down over time owing to articulation against the hard Co-Cr-Mo alloy. The wear particles of the UHMWPE activate a biological response that leads to bone resorption [27], and ultimately to implant loosening and failure. Of the metal alloys currently used in total hip replacements, Co-Cr-Mo alloy is significantly more resistant to roughening processes [21].

2.3.1 Composition, Microstructure and properties

Table 2.7 lists the chemical composition of Co-Cr-Mo alloy (ASTM F75) used for implant fabrication [32]. The two basic elements of the alloy are cobalt (Co), and chromium (Cr). Molybdenum (Mo) is added to produce finer grains, which results in higher strengths after casting. The main attribute of the alloy is that they have excellent corrosion resistance in chloride environments due to their bulk composition and the presence of the surface oxide layer chromium oxide (Cr_2O_3). They have good abrasive wear properties, about 0.14 mm/year in joint simulation test [28] and good frictional properties with themselves or other materials. The constituent elements particularly Co are very expensive, hence Co-Cr-Mo alloys costs are significantly higher than for example 316L stainless steel.

Table 2.7. Chemical Composition of Co-Co-Mo alloy (ASTM F75)

Element	Composition (wt. %)
Cobalt	58.9 – 69.5
Chromium	27.0 – 30.0
Molybdenum	5.0 – 7.0
Manganese	1.0 max
Silicon	1.0 max
Nickel	1.0 max
Iron	0.75 max
Carbon	0.35 max
Nitrogen	0.25 max

Table 2.8 lists the mechanical properties of Co-Cr-Mo alloy [2, 28, 32, 41]. Compared with Ti6AL4V alloy (table 2.2) and stainless steel alloy (table 2.4), Co-Cr-Mo alloy has slightly higher modulus and much higher strength, but lower ductility. As with the other alloys, the increased strength is accompanied by decreased ductility. Although these properties may be regulated to a great degree by heat treatment, Co-Cr-Mo is quite difficult to machine because of its high intrinsic hardness. The high modulus of elasticity does not change with the changes in ultimate tensile strength and this may have some implications of different load transfer modes to the bone, although it is not established clearly what the effect of the increased modulus is [28].

Table 2.8. Typical Mechanical Properties of Co-Cr-Mo

Property	Value
Young's modulus (Gpa)	210
Yield strength (MPa)	448 - 517
Tensile strength (MPa)	655 - 889
Fatigue endurance limit (at 10^7 cycles, R = -1) (MPa)	207 - 310
Strain to failure (%)	8
Reduction of area (%)	8

At least three methods of manufacture, investment (lost wax) casting, powder metallurgy processing, and hot forging can be used to make Co-Cr-Mo femoral heads. However, because the alloys are particularly susceptible to work-hardening, the normal fabrication process used for the other metals cannot be used. The alloy is cast by a lost wax or investment casting method [28].

2.4 Polyethylene

2.4.0 Introduction

Polyethylene is the largest tonnage plastic material and has the simplest basic structure of any polymer. As a simple semicrystalline thermoplastic polymer it can be processed to have a wide range of microstructures and material properties that are useful in numerous structural applications. Its attractive features include excellent chemical and corrosion resistance, excellent stiffness to weight ratio, good processability, toughness, flexibility, and cheapness.

It is made from the monomer ('mer') unit ethylene ($CH_2 = CH_2$). These 'mer' units combine with one another to form chains through a primary covalent bond, where the carbon (C) atoms share electrons with two other hydrogen (H) and carbon atoms:

$$- CH_2 - (CH_2 - CH_2)_n - CH_2 -$$

Where, n indicates the number of repeating units [28]. There are three major classes of polyethylene commercially available. These are based on characteristics such as

molecular weight and density, dictated by chain length and structure, either linear or branched. These three major grades are known as low density, high density, and ultrahigh molecular weight polyethylene. Low density polyethylene (LDPE) is typically branched but can be linear, and is polymerised by reacting ethylene gas at high pressure (100-300 MPa) in the presence of a peroxide catalyst to initiate polymerisation. The high pressure polymerisation causes branching of the linear chains. High density polyethylene (HDPE) is linear and ultrahigh molecular weight polyethylene (UHMWPE) consists of long linear chains as well. To prevent any chain branching and to obtain a better packing of the chains to increase density and crystallinity, UHMWPE and some HDPE chains are polymerised using Ziegler-Natta catalyst (made of titanium chloride and organo-aluminum components such as triethylaluminum or diethylaluminum) at low pressure (10 MPa). Some properties of the above three classes of polyethylene are shown in table 2.9 [28, 32, 33].

After the fabrication of a polyethylene part its surface properties can be changed by cross-linking, especially where increased wear resistance is required as in TJRs. This can be done by exposing the polyethylene to ionising radiation in the presence of a cross-linking agent such as acetylene. The radiation disrupts covalent bonds and forms free radicals in the cross-linking agent, resulting in the production of an increased density of covalent intermolecular bonds in the polyethylene. The radiation acts throughout the body of the polyethylene part, whereas the cross-linking agent acts on its surface to produce significant cross-linking of the polyethylene. Other cross-linking processes include chemical cross-linking with silane or peroxide chemistry.

Table 2.9. Properties of Polyethylene

Property	Low density	High density	UHMWPE
Molecular weight (g/mol)[a, b]	$3 \sim 4 \times 10^3$	5×10^5	2×10^6[c]
Density (g/cm^3) [a, b]	0.90 – 0.92	0.92 – 0.96	0.93 – 0.94
Tensile strength (MPa)[a, b]	7.6	23 – 40	27 min
Elongation (%)[a, b]	150	400 – 500	200 – 250
Modulus of elasticity (MPa)	96 – 260[a, b]	410 – 1240[a, b]	800 – 1500[d]
Crystallinity (%)[d]	40 – 50	60 – 80	45 – 55[e]
Microstructure[d]	Typically branched	Spherulitic	Lamellar

[a, b]From [28, 32], [c]data from ASTM F648 [d]from [33], and [e]from [45].

2.4.1 UHMWPE

UHMWPE is defined by ASTM D 4020 as a linear polyethylene with a weight average molecular weight (Mw) of greater than 3.1 million g/mol (> 1 million g/mol defined by ISO 11542) [8]. It is the most widely used polymeric prosthetic material and has been used extensively for orthopaedic implant fabrications, especially in TJRs for nearly four decades. The mechanical and tribological properties of the material favour its use as a bearing material in many joint replacement devices such as tibial bearings in knee arthroplasties, acetabular bearings in hip arthroplasties, as buttons to resurface the patella in total knee arthroplasty, in sleeves to permit semi-constrained rotation in elbow and wrist arthroplasty designs, and in counterfaces inserted into the glenoid in shoulder arthroplasty. It is particularly stable for this purpose because of its durability, high melting point (> 127 °C), hardness and low density. Because of its high molecular weight, UHMWPE implants can be processed with ram extrusion, a process which is difficult to use with low molecular weight polymers [46].

As a biomaterial, UHMWPE is biocompatible and its unique structure gives it desirable properties such as the low coefficient of friction when sliding against a metallic surface, excellent wear resistance, abrasion resistance and toughness, compared with other polymers such as PTFE [33, 47], and has been used as the material of choice for the bearing surfaces in TJR for nearly four decades. Although most of its replacements have proved successful in the last two-and-a-half decades, occasional problems have arisen particularly in cases where the implantation was performed on heavier and/or younger and/or more active patients. The generation of UHMWPE wear debris is detrimental to tissue and has been linked to complications including tissue inflammation, bone loss (osteolysis), and implant loosening [17, 19, 23, 48], necessitating revision surgery. The sub-micron sized UHMWPE wear debris produced during articulation limits the life of its prosthetic components. At this size UHMWPE is no longer biocompatible and macrophages identify the debris as foreign bodies and attempt to consume them. However, the immune cells are not able to digest the particles and this triggers an immune response of swelling of the joint area, and leads to osteolysis and bone resorption. The loss of bone density leads to eventual loosening of the prostheses and ultimately failure of the joint replacement as the bone tissue can no longer support the replacement [33].

Recent advances in improving the wear behaviour of UHMWPE polymer have focused around the creation of a highly cross-linked structure. It has been shown that cross-linking of the molecular chains dramatically reduces the abrasive and adhesive wear of UHMWPE in several *in vitro* joint simulator studies [10, 33, 49], and improves the material's mechanical properties [50]. Materials that are stiffer with increased tensile strength, creep resistance, and decreased ductility are produced. The process has the additional advantage of permitting a lower molecular weight base material to be used, so that components can be injection-moulded rather than machined. The moulding offers the opportunity of mass-production of complex three-dimensional shapes. The speculation is that cross-linking of the polymer enhances the resistance to plastic flow and lamellae alignment at the articulating surface resulting in better resistance to wear.

There are many variables that can affect the performance of UHMWPE including, resin type and processing conditions, post processing conditions such as cross-linking, sterilisation methods, and post-sterilisation aging prior to implantation, as well as design parameters such as conformity and thickness.

2.4.1.1 Microstructure and Properties

At the nanometer length scale UHMWPE has a semi-crystalline microstructure consisting of a crystalline phase embedded within an amorphous matrix. The crystalline phase consists of folded rows of carbon atoms packed into lamellae, typically 10-50 nm in thickness and on the order of 10-50 μm in length, whereas the surrounding amouphous phase consists of randomly oriented and entangled polymer chains traversed by tie molecules which interconnect lamellae and provide resistance to mechanical deformation. At this scale the material is a complex composite material which can evolve over time in response to its mechanical, chemical, and thermal history [8]. The carbon positions on the chains in the crystalline region can be defined by an orthorhombic unit cell with dimensions of, a = 0.74 nm, b = 0.49 nm, and c = 0.25 nm [33].

The large number of tie molecules and long linear chains gives UHMWPE outstanding mechanical properties, some of which are shown in table 2.10 (adapted from [51]). Its mechanical properties are inextricably linked to its chemical structure, molecular weight, crystalline organisation, and thermal history, as with any polycrystalline

polymer. All of these factors affect the morphological, chemical, and mechanical processes, which may influence the wear and performance of the material across a wide range of characteristic dimensions, after implantation.

Table 2.10. Mechanical Properties of UHMWPE (density 0.93 g/cm^3)

Property	Value
Compressive yield strength (MPa)	12.4
Flexural strength (MPa)	14.5
Ultimate tensile strength (MPa)	38
Young modulus (MPa)	1037
Fatigue endurance limit (10^7 cycles) (MPa)	15.6
Coefficient of friction: serum lubricant (*in vitro*)	0.04 – 0.16
Wear rate	(1.6 μm/year)

2.4.2 XLPE

The process of cross-linking of polyethylene has been known for decades to improve abrasion resistance of the polymer for industrial applications. The linking of linear polymer chains by covalent bonds produces a cross-link network between which the molecular segments remain flexible. Thus at the appropriate temperature, the polymer may be rubbery, rigid, or even crystallised if the segments can pack together sufficiently closely. Segmental motion is progressively restricted as the degree of cross-linking increases. The process of cross-linking of polyethylene is typically accomplished by peroxide chemistry, ionising radiation, or silane chemistry, and the degree of the cross-linking is affected by the amount of peroxide, level of ionising energy, and whether the polymer is re-melted or annealed to remove free radicals, and if so, the environment in which it is performed.

The use of peroxides has received the most attention in chemical cross-linking. Peroxides can be obtained in either a powder or liquid state and is usually mixed with the medical grade resin prior to processing. The elevated temperatures present during processing decompose the peroxide to create free radicals, which form cross-links with neighbouring chains. Typically a peroxide concentration of ranging from 0.1 to 0.2 %

by weight is necessary to produce a highly cross-linked polyethylene network structure [8].

All ionising radiation processes lead to the formation of free radicals in polymeric materials through homolytic chain cleavage. The effects of radiation cross-linking on the structure of the polymer can however, be detrimental or beneficial to wear behaviour depending on the processing environments and degree of cross-linking. Chain scission and free radical formation is caused by irradiation, and depending on the environment these free radicals react with each other to form cross-links. Gamma radiation in air and subsequent ageing is known to have detrimental impact on the structure and mechanical properties of polyethylene, whereas gamma radiation in an inert environment induces cross-linking and is beneficial to the wear behaviour [33].

The third type of cross-linking using silane chemistry has been used in acetabular liners [8]. This procedure of cross-linking was developed by Dow Corning Limited (Barry, Glamorgan), and modified under licence by the British Steel Corporation (BSC Tubes Division, Corby, Northamptonshire) [52]. A silane compound containing a vinyl group is grafted onto the polyethylene chain. Vinyl trimethoxysilane is usually used and the grafting is achieved with a peroxide such as dicumyl peroxide in an extruder at a temperature of about 220 °C. Antioxidants, stabilisers and colouring pigments are added before extrusion. The cross-linking stage involves steam autoclaving the product at 120 °C for hours when the methoxy groups are hydrolysed to hydroxyl groups, and the hydroxyl groups on neighbouring chains condense together to form cross-links. Polyethylene cross-linked in this way has a less tightly bound network than that cross-linked by a single covalent bond. Such cross-linked materials are expected to deform further, having similar wear resistance as that of non cross-linked polyethylenes, but should be superior with regard to cold flow (creep) an advantage for prosthetic applications. Atkinson *et al* showed that, silane cross-linked high density polyethylene are superior over UHMWPE (RCH 1000) with regard to creep resistance, and wear properties [52]. The material can be injection moulded prior to cross-linking, a considerable advantage from a manufacturing point of view.

CHAPTER THREE – TRIBOLOGY AND SURFACE MODIFICATION (LITERATURE REVIEW)

3.1 TRIBOLOGY

3.1.0 Introduction

Tribology is defined as "the science and technology of interacting surfaces in relative motion", and embraces the study of friction, wear, and lubrication [2, 53, 54]. Friction, wear, and lubrication are all phenomena familiar from everyday experience, but wear is particularly well known because it leads to catastrophic failure and represents one of the most costly problems facing industry today [55]. In many kinds of mechanisms artificial or natural, the movement of one solid surface over another is of great importance. Low friction is desirable in many instances e.g., the operation of joints such as the human joints demands a low friction force, whereas in other instances high friction is desirable e.g., a vehicle tyre and the road surface. Damage to surfaces generally involving the loss of material (wear) will occur whenever surfaces move over each other and in most cases this is detrimental. For example, the loss by wear of relatively small amounts of material can be enough to cause complete failure of large and complex materials. High wear rates can be desirable sometimes as in the case of friction e.g., grinding and polishing. The reduction of friction and often wear can be achieved by the method of lubricating the surfaces in some way, hence the study of lubrication is very closely related to that of friction and wear.

The tribology of TJR is extremely complex. Unlike many tribological systems total joint articulation exhibits extremely low levels of wear and can function effectively for well over ten years. While healthy natural joints exhibit remarkable tribological characteristics due to the intrinsic properties of articular cartilage (high compliance) and synovial fluid, and subsequent optimised lubrication modes, TJRs based on current available materials experience mixed/boundary lubrication [2]. This lower lubrication performance is generally attributed to high rigidity (low compliance) of the artificial materials. As some surface contact takes place during articulation, the friction between artificial materials is much higher than in natural joints (μ = 0.005 in natural joints, and 0.02 in artificial joints) and non-recoverable wear of the artificial joint materials takes place [2].

3.1.1 Wear

Wear is defined as the progressive removal of material with the generation of wear particles, that occur as a result of relative motion between two opposing surfaces under load [7, 53, 56]. It is perhaps the most important yet least understood aspect of tribology and for this reason is attracting considerable attention at the present time. A common feature of the wear life of most engineering components is the relatively small percentage of the weight of the device that needs to be removed before correct functioning is impaired. However, it is not always disadvantageous and many processes such as metal cutting (e.g., polishing) rely on the phenomenon [54].

There are numerous mechanisms of wear [57, 58] including adhesion, abrasion, fatigue, corrosion, and erosion known as the five main types of wear, and delamination, penetration, pitting, fretting, and cavitation, which are descriptive of the appearance of the worn surfaces [53]. Adhesion involves the formation of surface bonds when surfaces are pressed together under load and sufficient relative motion pulls material away from one or more of the surfaces, usually from the weaker material surface. During abrasion, asperities or protuberances on the harder surface or as a separate component between the sliding surfaces cut and plow through the softer surface, resulting in removal of material from the softer surface. There are two types two-body and three-body abrasive wear. Two-body wear is caused by the hard protuberances on the harder surface, whereas in three-body wear the hard particles are free to roll and slide between the two contacting surfaces. When local stresses exceed the fatigue strength of a material it fails after a certain number of loading cycles, releasing material from the surface. Such a wear mechanism is known as fatigue wear. A wear process in which chemical or electrochemical reactions with the environment predominates e.g., oxidative wear is known as corrosive wear, and erosive wear is the loss of material from a solid surface due to a relative motion in contact with a fluid which contains solid particles.

The various wear mechanisms are not mutually exclusive and in many situations two or more wear processes may take place simultaneously. Adhesive wear for instance might liberate wear particles which subsequently give rise to an abrasive action, and in the case of polymers, abrasion, adhesion and possibly fatigue might contribute to the overall wear process [53]. Abrasive wear can be controlled by making the harder surface in a hard-on-soft bearing combination very smooth and by effective sealing to

exclude abrasive particles. Fatigue wear can be controlled by awareness at the design stage of the material of the stress levels in local contacts and the frequency of stress reversals. Corrosive wear can be minimised by careful choice of the tribological materials or the environment to ensure that harmful chemical reactions do not take place. Adhesive wear is the most common and least preventable form of wear mechanism in joint tribology, since adhesion takes place so readily between interacting surfaces in relative motion [58]. It can often be controlled but rarely eliminated and most recorded studies of wear (in joint tribology) have been concerned with the adhesive wear mechanism.

3.1.1.1. Wear in TJR

Wear determines the useful life of artificial joints, and in TJRs wear of the joint surfaces is known to be one of the most common causes of failure and lack of durability of the prosthetic implants. Although the mechanical consequences of wear can limit the functional life of a joint replacement, the clinical problems from wear more frequently are due to the release of an excessive amount of wear particles into the biological environment, and when particles within a certain size-range are phagocytosed in sufficient amount, the macrophages enter into an activated state of metabolism, releasing substances that can result in periprosthetic bone resorption which leads to the eventual loosening of the implant [7].

3.1.1.1.1 Wear of Polymers in TJR

Wear of polymeric components in TJRs is mainly brought about by the association of two mechanisms: creep (material flow or plastic deformation) due to loading, and mass reduction due to wear debris formation [7, 58, 59]. Creep contributes to the deformation of a polymer bearing but does not produce wear particles, and is known to be dominant initially perhaps for the first million loading cycles or so (in THR). Its rate decreases rapidly over time, becoming negligible by the first twelve to eighteen months after implantation. Wear continues insidiously and is generally the major factor determining the long-term penetration of the metallic femoral head into the polymer cup, and accounts for most of the change in the surface of the polymer bearing over the longer term. Most joint replacements have one primary polymeric bearing surface (acetabular cup or tibial tray) made of UHMWPE. There are many variables that affect the wear of

a UHMWPE bearing *in vivo*. The wear resistance of polyethylene is a function of the base resin, manufacturing, and the method of sterilisation of the component [60]. The clinical manifestations of UHMWPE wear in THRs include the removal of material, which results in progressive penetration of the femoral head into the polyethylene acetabular component and a reduction in the thickness of the polyethylene bearing.

Although numerous mechanisms for the wear of UHMWPE have been suggested abrasive wear, adhesive wear, and fatigue wear have been identified as the basic wear mechanisms in TJRs [7, 57, 58, 61]. These wear mechanisms are associated with the scales of irregularities on the hard metallic counterfaces, the surface feature of the polymer, and the overall geometrical conformity of the mating components respectively.

Abrasive wear as discussed earlier is caused by hard asperities on the counterface metal (two body wear) or hard particles (third bodies) between the articulating surfaces. These particles penetrate the softer polymer and remove material by a micro-cutting or shearing process. Multidirectional scratches are observed as the main features of abraded polymeric materials. This wear mechanism is normally associated with relatively rough counterfaces, hence the surface roughness of the counterface is the determining factor for the abrasive wear of a given polymer. It has been found that an important parameter governing abrasive wear of polymers is the work required to rupture material during sliding, being approximately equal to the product of the breaking strength and the elongation to break [57]. Therefore any measure enhancing the strength without appreciably diminishing the toughness would be expected to improve abrasive wear resistance of polymeric materials.

Adhesive wear is associated with intermolecular forces mainly including attractive van der waals and repulsive electrostatic or double layer forces, which bond solids together. It is also highly dependent on the presence of intermediate material such as liquids. Dry clean solids readily adhere, but in liquids the long-range forces can be reduced by an order of magnitude or so [58]. When most polymers slide over clean hard smooth counterfaces, the interfacial shear strength of the adhesive junction is observed to be greater than that of the polymer [57] and the contact ruptures within the polymer as sliding continues, owing to its soft or low strength nature. The polymer is then transferred to the harder counterface and subsequently removed as wear debris. However, if there is a layer of fluid present between the contacting surfaces, the

attractive forces are almost attenuated, adhesive junctions can hardly be formed and wear would be decreased significantly. Adhesive wear is therefore obviously likely to be significant during sliding of polymers against metals under unlubricated or starved lubrication conditions. It is generally thought that TJRs are wetted by the liquid present within the joint capsule, but the possibility of dry patches being encountered at some stage is constantly being raised and not yet answered satisfactorily [58]. Molecular topography has been noted to control the extent and form of the transferred layers. For example, smooth molecules such as those in high-density polyethylene will form very thin and highly oriented layers, thus giving rise to low adhesive wear rate [54], and highly cross-linked materials have also been found not to transfer polymer to the counterface [57]. Therefore cross-linked polymers possess high resistance to adhesive wear and hence any measure that can effectively reduce polymer transfer such as enhancing lubrication or cross-linking reaction, would be expected to improve the adhesive wear resistance of polymers.

Fatigue wear is only observed after a substantial period of rubbing and hence may not be detected in short-term tests. Its rate is usually known to be lower than that of either adhesive or abrasive wear [58]. It probably results from the formation of cracks associated with elastic deformation over a number of contact cycles in the form of pitting, cracking, spalling and delamination. Particles of wear debris become removed by the growth and intersection of small cracks on the polymer surface whose orientation is roughly perpendicular to the direction of sliding. It occurs only when the counterface is smooth and adhesive action is almost eliminated, because on rough counterfaces abrasive and adhesive actions are so high. Typical surface features of micro-fatigue such as in UHMWPE acetabular cups (in THR) are regular and irregular arrays of surface ripples and bumps. Fatigue wear can also occur well below the surface (macro-fatigue wear) in the form of delamination, in the case of high stress and lower conformity such as in knee joints (TKR) [57, 58].

In many prosthetic devices where polymeric materials slide on metals, abrasive wear may be encountered initially, but in due course a transfer film of polymer builds up on the metal counterface and adhesion between the bulk polymer and transfer film will occur [53]. Practical wear mechanisms frequently operate sequentially and although it is difficult to separate the individual contributions of the wear mechanisms quantitatively, it is clear that wear resistance of polymers would be significantly improved if the

abrasion and adhesion actions could be reduced. This is largely because the rate of fatigue wear is very low. Ion beam modifications especially ion implantation may improve the tribological behaviour of polymers by shifting the dominant wear mechanism from abrasive or adhesive to fatigue wear.

3.1.1.1.2 Metal Wear Processes in TJR

The metal components in TJR are damaged by articulation (friction) even when rubbing against the soft polymeric materials. 316L stainless steel is less sensitive to wear damaging (but crevice corrosion may occur in some cases where groves or scratches are present), than Co-Cr-Mo (moderate), and Ti6Al4V (severe) alloys [21].

Passive oxide-type films are present on implant metal surfaces that protect them from corrosion *in vivo*, however, minute concentrations of metal ions can be detected in the body fluids and organs whenever metallic implants are placed in the body [21]. Tissue culture studies have shown that cell replication is slowed in the presence of ions found in two commonly implanted alloys Co-Cr-Mo and Ti6Al4V, while other studies demonstrate that bone and fibrous tissue will grow into intimate apposition with implants fabricated from these same materials [5]. For 316L stainless steel, the passive film is provided by the chromium contained in the metal. It produces a chromium oxide film (Cr_2O_3) by reacting with available oxygen in the air or with oxygen contained in the body environment. This passive film although very thin, about 2-5 nm thick, protects the underlying metal from further oxidation (corrosion). The chromium in Co-Cr-Mo provides protection in a similar way to that of 316L stainless steel. In Ti6Al4V alloys, it is the titanium that provides the protective passive film by forming titanium oxide (TiO_2) [21].

Although passive surface films form extremely quickly (within nanoseconds), they can be damaged or sheared off from rubbing against another surface, exposing the metal temporarily to the environment. This exposure causes soluble metal ions to be released locally. If the rubbing occurs continuously as with hip motion, the passive film is constantly damaged and reformed, creating a constant source of metal ions. If these removed oxide films are hard (e.g., titanium oxide on Ti6AL4V alloy), they can act as three-body abrasives and metal wear as well as polymer wear can occur [21]. The presence of a third material between two rubbing materials is known as three-body wear

and this can accelerate the wear of the two initial surfaces if the third material is harder. Metal burnishing or micro-scratching can occur in hip replacements with body particles such as bone chips, bone cement debris, and metal particles to accelerate the passive film damage and production of metal ions. Significant levels of the major components of metal prostheses have been measured near the implant in synovial fluids and soft tissues, as well as throughout the body in the blood, urine and other tissues [62]. Haynes *et al* [62] found that, Co-Cr and 316L stainless steel particles become less toxic but may induce more bone resorbing mediators as they age *in vivo*. The long-term effects of ion leaching in TJR remain a concern, and await further elucidation. It has been shown by analysing metal release rates from metal-polyethylene wear tests that Co-Cr-Mo is gradually removed at a rate of about 0.1 μm per year (10^6 cycles), 316L stainless steel is removed on the order of 0.2 μm per year, and Ti6Al4V on the order of 1 μm per year (surface removal from femoral heads) [21].

A new passive film forms instantly from the reaction of the exposed metal surface with oxygen in the environment when damaged. Implant metal surfaces gradually give up metal from this oxidative wear process and this can lead to an increased surface roughness, which in turn can increase the mating polymer wear rate [16, 21]. In TJR the wear of the polymer is greatly influenced by the roughness of the metallic counterface. Laboratory studies using screening device wear testers have shown that the wear volume of UHMWPE is approximately proportional to the mean surface roughness of the counterface raised to a power greater than 1 [16, 21, 58, 63, 64]. Other authors have also found different relationships between the k_o and R_a, and the discrepancies in the results may be due to the different lubricants used and testing conditions [65].

The micro-topography of a surface determines its roughness and in TJR typical R_a values are initially in the range of 0.02–0.05 μm [21], and could increase with time due to surface abrasion particularly for Ti6Al4V alloy, and thus increase the mating polymer wear. This implies that minimising the surface roughness of the metal would reduce the long-term wear of the mating UHMWPE component.

3.1.1.2 Wear Testing and Measurements

One of the greatest limitations in the life of engineering components in general and TJRs in particular is the rate of wear of the bearing materials, hence it is a matter of

some importance that an attempt should be made to predict the likely 'wear rate' of proposed designs of joint replacements and to strive to ensure that this will be satisfactory [42, 53]. Another reason for carrying out wear tests is to study the basic mechanisms of wear under given conditions. The procedures which can be used in wear studies include monitoring the performance, wear rate and life of the complete machine assembly; testing components in bearing or joint simulators in the laboratory; and laboratory testing of specimens of materials under well controlled conditions.

Direct measurements of wear of prostheses *in vivo* can be made clinically either by radiographic measurements, e.g., of the penetration of the femoral head (metallic component) into the acetabulum (polymeric component), or measurement of dimensional changes in explanted prostheses [58]. These measurements however, do not of course, differentiate between wear and deformation due to creep.

A large number of joint simulators have been designed and become available worldwide in recent years to enable hip and knee joints to be evaluated prior to clinical trials. It is however far more difficult and expensive to design, build and operate a simulator than it is to produce a prosthesis. The value and great merit of using such simulators however, lies in the fact that they can give an improved understanding of the wear processes encountered in prostheses [58].

The possibility of utilising information obtained from simple laboratory equipment is the most attractive, since testing of bearing components in service is a long and sometimes disastrous procedure and the evaluation of TJRs in simulators are difficult and expensive [53]. The main purpose of laboratory wear testing equipment is to press together under a known load, specimens of materials which are sliding together at known speeds under controlled environments and to record the amount of material removed by wear. The laboratory equipment are known as screening devices, and a wide variety of screening test arrangements are used to examine the behaviour of materials for prostheses to develop an understanding of the nature of the wear processes as well as the levels of wear for the design of future prosthetic joint development. The most widely used screening devices include pin-on-ring, pin-on-disc, annulus-on-flat, and reciprocating pin-on-plate testing machines. Pin-on-disc is particularly useful in studying basic wear mechanisms because the operating conditions are steady and well controlled. However, due to the high speed and unidirectional motion employed, most

of the pin-on-disc machines fail to replicate the reciprocating motion that characterises joint motion (flexion-extension). The reciprocating pin-on-plate action more closely resembles the conditions encountered in the load bearing joints of the lower limb [50, 58] and therefore, if an attempt is to be made to produce realistic quantitative data to predict the tribological performance of total joints *in vivo*, the reciprocating pin-on-plate machine has many advantages.

Wear pairs of implant materials or complete prostheses are usually recorded in the laboratory by measurement of weight loss, measurement of dimensional changes, examination of particles of wear, the collection of wear debris, and optical measurements of changes in surface features. In general, extensive experimental studies with such recording techniques have shown that wear increases as the normal load (P) increases, wear increases as the sliding distance (X) increases, and wear increases as the hardness (H) of the softer sliding component increases [53]. For practical purposes, wear of the much harder metallic materials are neglected and only the wear of the softer polymeric materials are measured. The wear of a polymer against a hard metallic counterface, if the mean contact stresses are not so high, is given with fair accuracy by a relationship of the form [66, 67]:

$$k_o = V/PX \qquad \text{equation 3.1.}$$

Where, k_o is the wear factor in (mm^3/Nm), P is the applied load in (N), X is the total sliding distance in (meters, m), and V is the volume of material removed by wear or lost in (mm^3).

$$V = m/\rho \qquad \text{equation 3.2.}$$

Which implies:

$$k_o = m/\rho PX \qquad \text{equation 3.3.}$$

Where m is the mass and ρ the density of the polymer. The wear factor is a measure of the rate at which a given combination of materials wears in the environment of the test and is widely used for comparative purposes when the tribological performance of combinations of potential prosthetic materials are assessed [58].

It is well known that simple wear machines have low-wear phenomenon and it has been proposed that conventional wear testers may be overly simplistic in terms of motion/loading configurations, and that low UHMWPE wear may be closely associated with the linear motion of the conventional wear testers [10, 11, 68]. Wang *et al* [11] proposed that UHMWPE undergoes a molecular reorganisation process at the wear surface driven by plastic strain accumulation at the wear surface by repeated cyclic asperity contact during sliding. The molecules are stretched along the direction of sliding in a simple linear sliding contact, leading to a significant degree of strain hardening due to preferred orientation of the surface molecules. Linear motion wear testers not only underestimate wear factors by orders of magnitude compared with joint simulators and clinical results but also produce incorrect wear rate rankings for polymers. Bragdon *et al* [68] and Wang *et al* [11], have shown that higher clinical wear rates in UHMWPE components (acetabular cups) may be associated with the multidirectional motion of the human joint, and emphasised that in order to produce a wear rate that is comparable to average clinical wear rates with undamaged metallic counterface, the motion of the wear tester or joint simulator must be multi-dirctional.

3.1.2 Friction

Friction is a force that can be defined as the resistance to movement between two surfaces in contact [7]. Two classes of relative motion; sliding and rolling may be involved. Although there is a distinction between rolling and sliding friction, they are not mutually exclusive and even rolling nearly always involves some sliding. In both ideal rolling and sliding a tangential force (F) is needed to move the upper body over the stationary counterface, and the ratio between this force and the normal load (P) is known as the coefficient of friction (μ) [54]:

$$\mu = F/P \qquad \text{equation 3.4.}$$

The phenomenon of friction has been studied extensively since Leonardo da Vinci raised the importance of the subject, but the well known three laws of dry friction stated below are attributed to Amontons (1699) and Coulomb (1785) [53, 54]:

1. The friction force is directly proportional to the applied normal load
2. The friction force is independent of the apparent area of contact

3. The friction force is independent of the sliding velocity.

The First Law amounts to the statement that μ is independent of the normal load, and is true for most metals and other materials under conditions of lubricated or unlubricated sliding. However, polymers often do not obey this law. The Second Law is well attested for most materials with the exception of polymers again, and the Third Law is less well founded. It is commonly observed that the frictional force needed to initiate sliding is usually greater than that to maintain it, and hence the coefficient of static friction (μ_s) is greater than that of dynamic friction (μ_d). However, once sliding is established μ_d is found for many systems to be nearly independent of sliding velocity over quite a wide range, although at very high speeds μ_d falls with increasing velocity. In natural hip joints the coefficient of friction is typically 0.005 [69].

3.1.3 Lubrication

For most practical uses lubricants are used to reduce the friction and wear between surfaces, and to provide components with smooth running conditions and adequate life [53, 54]. Lubrication is normally achieved by introducing a liquid, or gas, between the sliding surfaces, and they function by introducing between the surfaces a layer of material with lower shear strength than the surfaces themselves. In some systems the lubricant does not completely prevent asperity contact although it reduces it and may also reduce the strengths of the junctions formed. In other cases they completely separate the surfaces and no asperity junctions are formed at all. Hence to a greater or lesser extent, the use of a lubricant will always reduce the rate of sliding wear. There are three main lubrication regimes known as fluid-film, boundary lubrication, and an intermediate condition called mixed lubrication. Subcategories of fluid film lubrication such as hydrodynamic, elastohydrodynamic and squeeze-film lubrication also exist.

The situation is described as 'fluid-film lubrication' if the lubricant is thick enough to prevent the opposing solids from coming into direct contact. This condition provides low friction and a high resistance to wear, and is often referred to as the ideal form of lubrication. Coefficients of friction in the range 10^{-3} – 10^{-2} have been recorded in bearings [53]. The behaviour of the conjunction is governed by the physical properties of the bulk lubricant (such as viscosity), and frictional resistance arises purely from the shearing of the viscous fluid.

Elastohydrodynamic lubrication is a form of lubrication where elastic deformation of the bearing solids promotes the formation of adequate fluid films, whereas hydrodynamic lubrication is when substantial load-carrying pressures are generated by the motion of the bearing surfaces. Both types of lubrication are related to fluid-film lubrication.

The condition is called 'boundary lubrication' if the solid surfaces are not separated by the lubricant and contact takes place over an area comparable to that which develops in dry contact. The frictional characteristics are determined by the properties of the solids and the lubricant at their common interfaces. The contact characteristics in this case are governed by physical and chemical properties of thin surface films of molecular proportions. The coefficient of friction is essentially independent of viscosity. The surface action determining the behaviour of boundary lubricants can be described in order of 'film strength' in the following terms [53]:

1. Physically adsorbed layers of gaseous, liquid, or solid lubricants;
2. Chemically adsorbed layers;
3. Films formed by chemical reaction.

In the mixed lubrication regime the contact characteristics are determined by varying combination of fluid-film and boundary lubrication effects, and it is an important lubrication condition since many machine elements move intermittently and hence operate in the boundary, mixed and fluid-film regimes (e.g., synovial joints).

The lubrication regime of natural synovial joints is not clear. All natural joints operate in a lubricant known as synovial fuid, which is an aqueous solution containing hyaluronic acid and protein. Hyaluronic acid molecules lead to non-newtonian behaviour of the fluid and greatly increases its viscosity, thus facilitating hydrodynamic lubrication. The protein content is thought to provide effective boundary lubrication when the hydrodynamic films become too thin, to prevent solid-solid contact. The relatively soft and porous cartilage which normally coats the bone surfaces in joints, enables an element of squeeze-film lubrication to be provided [70]. Natural joints are complex in their lubrication, thus elastohydrodynamic, boundary, and mixed lubrication all operate at different parts of the swing/stance phase, during a gait cycle.

3.2 SURFACE MODIFICATION

3.2.0 Introduction

Over the past decades surface engineering has been gaining momentum due to concerns over the environment, cost of manufacture, conservation of strategic materials, and bulk material performance [29]. The common objectives in the use of surface engineering for tribological applications are to increase the wear resistance of the surface material and to modify its frictional behaviour, both of which are achieved together in some cases [54]. Surface modification and surface coatings are the two main methods used in surface engineering. The surface modification process is generally considered when good is not good enough, devices can not function without it, and product differentiation is desired [27], and there are numerous applications for surface modification techniques to improve the long-term performance of materials. The microstructure of the surface material may be modified selectively without changing its composition as in transformation hardening or melting followed by rapid solidification. Alternatively, both composition and microstructure may be changed together, and this can often be achieved by thermally-enhanced diffusion of a different chemical species into the surface. The changes in composition and microstructure that can be brought about by these methods are however limited, and surface coatings of completely different materials can be applied for many purposes.

The range of services currently offered by surface treatment industries is varied and continually expanding. Examples include surface modification approaches such as ion beam processing, diffusion (nitriding and carburising), laser and plasma processes, chemical plating and grafting or bonding, and conventional coating processes such as dipping and spraying, and vacuum deposition techniques such as sputtering. Of the available techniques, ion beam processing techniques have been particularly successful in biomaterial surface modification primarily because they combine versatility and low temperature processing with excellent process control, reliability, and reproducibility. There are several ion beam processing techniques used for surface modification of materials, each having their own relative advantages and disadvantages. The techniques include ion implantation, ion-beam-assisted deposition (IBAD), ion beam texurising (IBT), and ion beam polishing and sharpening technologies [26, 27], each of which will be discussed under the following sections (3.2.1 – 3.2.2). Ion implantation in particular

has proven successful in this area because it offers numerous beneficial surface property modifications without affecting the bulk properties of the materials.

3.2.1 Ion Implantation

Ion implantation is a simple technique for modifying the physical and or chemical properties of the near surface of a material significantly, when appropriate ions are embedded into the surface of the material from a beam of ionised particles [71, 72]. Unlike surface coatings, ion implantation uses a highly sophisticated process that actually penetrates surfaces, altering the composition to form a tougher barrier that resists wear, and it will not delaminate like conventional coatings. It can now be used for selectively improving the surface quality of engineering products and components by the controlled introduction of the 'foreign' atoms. The process upgrades the surface properties and improves the service life of the material, which may be crystalline, polycrystalline or amorphous and need not be homogeneous. By using high energy ions of the species to be introduced, ion implantation allows the controlled introduction of one or more species into the surface of the substrate and because the process is non-equilibrium, solubility limits may be exceeded with or without subsequent precipitation. This makes it possible to incorporate any kind of ion without developing a set of diffusion conditions or considering the control of chemical constraints. Surfaces may be treated by the process and produce an effective alloyed surface layer where composition varies as a function of depth, and unique alloys not possible through normal alloying can be produced through this technique. Two or more metals completely insoluble in each other can be alloyed in this manner theoretically.

Ion implantation can impact durability, wear resistance or surface hardness; improve resistance to rolling fatigue; reduce sliding friction; prevent adhesion; impart resistance to surface corrosion and chemical attack; and conserve valuable materials by keeping surface requirements separate from those of the bulk material. Table 3.1 shows a compilation of material properties influenced by ion implantation [73] (Dearnaley [74]). Nitrogen (N) has been the most investigated element in ion implantation studies due to its ability to harden steels and other engineering materials and the high ion current obtained with most commercially available ion sources [75]. This means ease of operation and economy of treatment.

Table 3.1. Material Properties Influenced by Ion Implantation

Friction	Corrosion resistance	Bonding
Wear	Electrochemistry	Lubrication
Hardening	Catalysis	Adhesion
Fatigue	Decorative finish	Reflectance

3.2.1.1 Process Overview

During the ion implantation process, ions are accelerated to a certain energy and directed towards the surface of the target material. The energy of the ions when they come into contact with the surface is typically between 20 and 200 keV, and these high energies cause the ions to penetrate the surface and so create significant changes. The ions typically penetrate the substrate of the material and lodge within its crystal structure, usually to a depth of several hundred nanometers in metals. The modifications created are therefore confined to the very near-surface region and only surface properties are affected. Physical dimensions and bulk properties of the treated material are left intact. Within a substrate of a material, the distribution of the implanted ions assumes a roughly Gaussian profile, with an average projected ion range. Figure 3.1 shows the classical Gaussian curve of the distribution of implanted species with depth within a target material. Due to the low depth of penetration into the target material, conventional ion implantation is thus most suitable for tribological applications where the depth of penetration of wear is low [76].

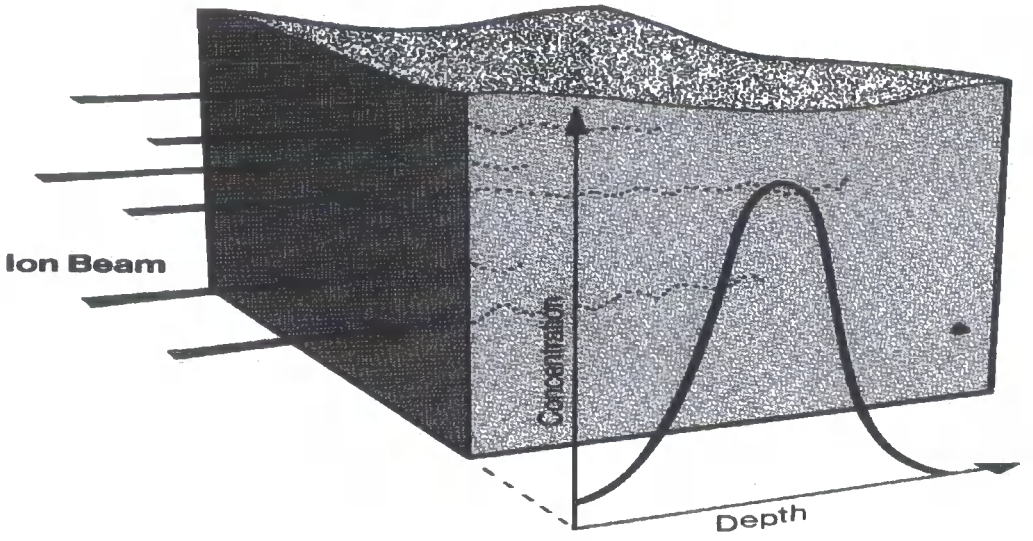

Figure 3.1. Distribution of ion implanted species with depth

Up to date, ion implantation has been successfully applied to metal, ceramic and polymer biomaterials, and because these materials differ structurally, the effects of implantation are quite distinct for each class of material [26, 27, 74, 77, 78]. In metal and ceramic biomaterials, physical changes induced by the process are due to atomic and nuclear collisions, which often leads to the formation of highly disordered and sometimes amorphous structures in the near-surface region. Chemical changes arise from the formation of hard-phase precipitates as a result of the formation of chemical bonds between the substrate atoms and implanted active ion species, or surface alloys resulting from the introduction of alloying elements. These physical and chemical changes typically combine to create surfaces that are harder and more resistant to wear and chemical attack, without changing any of the material's bulk properties [26, 27].

Numerous effects including improvements to surface related properties such as hardness, wear and chemical resistance, are observed as a result of ion implantation in polymers [9, 57, 79-81]. Surface properties are known to be more effectively modified by the process for polymers than any other materials because of the low bond strength of the material compared with that of metals or ceramics, such that the energy transferred to electrons by incoming ions can stimulate chemical reactions. These modification methods are based on the bombardment of the polymer surfaces by ions with energies higher than the energy of their chemical bonding. Two major competing

mechanisms are realised in polymers via ion bombardment. An ion penetrating the polymer surface interacts with substrate atoms primarily through electronic (ionisation) and nuclear (recoil) interactions. Ionisation is however, the dominant phenomenon at the beginning of the ion range and causes excitation and ionisation of polymer units, which generally leads to cross-linking in the adjacent polymer chains. Recoil interactions generally lead to chain scission. Ion-substrate interactions are complex as equilibrium exists between the two major competing processes of chain scission and cross-linking [82].

Typically the energy associated with ionisation is much larger than the bond energies found in simple organic molecules, such as H-CH (4.3 eV) and H_3C-CH_3 (3.7 keV). Therefore the energy available largely exceeds the amount required to cleave any bond, however, all bonds are not irreversibly broken at random and experimental results have shown that selectivity rules apply which do not follow bond energy considerations [83]. The cross-linking process creates a three-dimensionally cross-linked surface layer with much higher hardness and much improved wear resistance, while the scission process generally leads to the breaking of the long molecular chains, which can eventually result in polymer degradation. Ion implantation sometimes also results in selective enhancement or reduction of functional chemical groups, which can by modifying chemical interactions on the polymer surface, effect changes in surface wettability or critical surface tension [27]. In general the change in the properties brought about by ion implantation is due to the energy transfer from the penetrating ions to the polymer, resulting in excitations of electron and atomic energy levels, breakages of chemical bonds, formation of free radicals reactions, formation of cross-links, unsaturated structures, carbonisation structures etc., depending on the implantation parameters and conditions [84].

In many ways, the effects observed as a result of ion implantation in polymers, are similar to those produced by treatment with common ionising radiation [27], where some stability problems such as oxidation and degradation due to chain breakage and, perhaps, free radicals interactions with O have been reported to occur [45]. However, the larger ion size and much shallower depth of penetration during ion implantation result in significantly more pronounced effects confined to a very thin layer beneath the surface. Studies have shown that, it is necessary to perform a stabilisation treatment post irradiation, in order to enhance cross-linking and to reduce the possibility of polymer

degradation by oxidation and extraction of radicals [85-87]. Such a stabilisation treatment is also known to increase the likelihood of eliminating free radicals, thus preventing their reaction with diffused O during storage (in the absence of vacuum packaging) and improving cross-linking during *in vivo* service [88].

3.2.1.2 Advantages, Limitations and Features

Ion implantation has numerous unique advantages over other surface engineering treatments such as surface coatings, for treating material surfaces. The process broadens the designers' choice of engineering materials by making surface quality less dependent on bulk properties. Some of the advantages and limitations of the technique are listed below ([73, 89, 90]).

Advantages:

1. Selective surface modification without detrimentally affecting bulk properties
2. Low temperature process
3. No significant dimensional changes
4. No degradation of surface finish
5. No adhesion problems since there is no sharp interface between the implanted surface layer and the bulk
6. Clean vacuum process
7. A variety of ion species can be implanted with the same basic apparatus, and almost all elements of the periodic table has been implanted
8. Controllable depth concentrations
9. Highly controllable and reproducible
10. Solid solubility limit of implanted species can be exceeded
11. A fine dispersion of precipitates can be created providing optimum wear behaviour
12. Ion implantation creates no problems of disposal waste products

Limitations:

1. Line-of-sight or beam-line process
2. Shallow penetration of ions (typically less than a micron)
3. Relatively expensive equipment and processing costs

4. Vacuum compatibility
5. Heat effects may be significant
6. Study and development of ion sources needed to produce a high beam concentration that is relatively clean

An intrinsic basic limitation is the technique being a line-of sight process, making it impossible to be applied to samples having complicated re-entrant surfaces. Therefore sophisticated tooling may be required to ensure uniform treatment of multiple parts with complicated geometries. Also the relatively shallow depth of treatment prohibits the process from being effective in minimising wear in certain wear modes such as abrasive wear.

The entire process of ion implantation is conducted in a high vacuum environment and at room temperature. Being a vacuum clean technique eliminates the use of aggressive and dangerous chemicals for the pre-treatment. Ions are produced through a multi-step process where electrons are first stripped from atoms to form the ions, which are then extracted by attracting them to an oppositely charged region. The ions produced are accelerated by creating a graded potential difference in a tube. The accelerated ions then pass through a magnet, which selects only those ions of a desired species and charge state. A series of electrostatic and magnetic lens elements shapes the resulting ion beam and scans it over the target. Ion species, the ion beam energy, the dose (fluence), and the beam current density (flux) are the four major ion implantation parameters, and by accommodation of these parameters several effects can be obtained on the substrate.

3.2.1.3 Application to biomaterials

Failures of orthopaedic biomaterials have such important repercussions that many studies [5, 7, 35, 91-93] have been conducted on retrieved implants to better understand the basic mechanisms which can lead to failure. Ion implantation has been used as a technique for improving the surface properties of orthopaedic materials without detriment to bulk properties to improve joint function and prostheses longevity [94].

The primary success of ion implantation has come in the surface modification of metallic orthopaedic prostheses [26, 27, 77, 95]. A primary limitation to the clinical use of these materials is their tendency to release metal ions by corrosion into the

surrounding tissue. The ions released are regarded as a likely source of long-term problems due to their known toxic effects on human cells [31]. Ion implantation has been successfully used on the metallic components of artificial joints to improve surface properties such as wear resistance, hardness, corrosion resistance and fatigue life time of the components [75]. Some of these studies are discussed in sections 3.2.1.3.1 to 3.2.1.3.3.

Polymers have also gained extensive application in biomedical materials due to their conformity however, at present they have many deficiencies including low mechanical strength and poor wear resistance. Ion implantation may offer a solution to reduce these deficiencies. Implantation of polymers affects their mechanical, electrical and chemical properties, and has been shown that the structure of polymers is readily changed by ion-induced dehydrogenation, oxidation, carbonisation, and other mechanisms connected to the creation of multiple carbon bonds [79]. Many studies have suggested that implantation can lead to improved hardness, wettability, anticuagulability, anticalcific behaviour (of polyurethanes in particular), and critical tension of silicon rubber in particular (which is thought to be a primary cause for biofouling) [27, 57, 81, 96]. Some of these studies are discussed in section 3.2.1.3.4. The major interest of the ion implantation treatment is that it is localised in a very thin layer of the material.

3.2.1.3.1 Applications in Ti6Al4V alloy

Ti6Al4V alloys are used for bone and joint replacements due to their superior biocompatibility and many favourable characteristics. Its high corrosion resistance is due to the formation of the protective oxide film TiO_2 of about 1-4 nm thick, however, body fluids contain chloride ions that can induce the breakdown of such passive films on prostheses. Despite the numerous advantages of Ti6Al4V alloy as an implant biomaterial, the wear resistance of the alloy is relatively poor and has long been the concern among manufactures and surgeons who have observed a black sludge material in the vicinity of explanted artificial joints, and excessive wear of the mating UHMWPE [6, 35, 96-98]. Agins *et al* [37] have shown that Ti6Al4V alloy can be particularly susceptible to wear, thus generating metallic wear debris that can lead to aseptic loosening of the implant in joint replacements, and a series of other clinical retrieval and experimental wear studies [18, 35, 37, 40] have shown that Ti6Al4V alloy by itself without a surface treatment is not suitable for *in vivo* bearing applications due to the

poor surface wear characteristics. N^+ ion implantation in particular has proved to be a potential method for improving the wear, corrosion and fatigue properties of the metal. Surface hardness of the alloy is increased substantially by the N^+ ion modification, which in turn improves the resistance to wear.

Ion implantation of titanium alloys can induce changes in the chemical structure of the surface by creating hard phase carbide, nitride, or oxide precipitates depending on the implanted species (carbon, nitrogen, or oxygen). The increased surface activity produces more adherent oxide layers and reduces the coefficient of friction, ultimately improving the wear resistance [99]. The hardening (a factor of 3 or more [27, 100]) is attributed to the formation of the hard-phases, whereas the low friction coefficient comes from the physical changes such as modifications in the crystalline lattice structure that occur in the near-surface region of the material. Numerous studies have evaluated the changes induced in titanium by N^+ ion implantation in particular and most have demonstrated order-of magnitude improvements in the wear resistance of the implanted alloy.

Schmidt *et al* [89, 101] have shown using a pin-on-disc device that surface modification of titanium alloy by N^+ ion implantation can improve the tribological behaviour of Ti6Al4V/polymer sliding couples. They showed using a transmission electron microscopy (TEM) that implantation of nitrogen ions with doses above 2×10^{17} N^+ ions cm^{-2} formed finely dispersed TiN precipitates in the near-surface region, hardening the metal and reducing the number of particles removed from it as a result of articulation. They observed an increase in microhardness with implantation dose due to compound formation (TiN), and found wear reduction in both the implanted Ti6Al4V samples and mating unmodified UHMWPE attributed to an increase in microhardness and a decrease in oxide film thickness on the Ti6Al4V.

Garcia *et al* [77] studied the effects induced by N^+ ion implantation on titanium and observed improvements in the wear resistance and a decrease in the friction coefficient of the metal. N 1s XPS spectra showed a binding energy (397.3 eV) corresponding to the nitride formation, which is thought as the main cause of the mechanical and tribological improvement.

Rieu *et al* [91, 99] performed friction measurements of UHMWPE versus untreated and N^+ ion implanted Ti6Al4V alloy on a pin-on-disc and a cup-on-ball (TRIBOCUP) device, both in Ringer's solution. They observed abrasive wear to have occurred on the untreated titanium and the N^+ ion implanted Ti6Al4V to have demonstrated spectacular reduction of wear, in the pin-on-disc test. The improvement was constant for a wide range of implantation doses from 10^{17} to 10^{18} N^+ ions cm^{-2}, temperature from room temperature to 300 °C, and partial oxygen content within the implanter corresponding to a vacuum of 10^{-3} to 10^{-5} Pa. In the cup-on-ball test they observed the untreated Ti6Al4V ball to be covered with a black dull layer, black scales at the top of the polymer cup, and a decreased wear rate and no black layers with the implanted Ti6Al4V alloy test.

The structural modifications induced by N^+ ion implantation in Ti6Al4V alloy have also been studied using GIXD by Rieu *et al* [102]. Measurement of the nitrogen concentration profile using GDS showed a classical Gaussian curve, which generally peaked near 200 nm after the implantation. They observed new phases containing oxygen and or carbon to a depth of 50 nm. For ion doses of about 1×10^{17} N^+ ions/cm^2, they detected the α titanium (a shift of the α titanium diffraction lines to lower diffraction angles, corresponding to an increase of interstitial nitrogen atoms in the titanium solid solution), and TiO_x compounds were observed to be formed to a depth of 20 nm. They concluded from their findings that, the modification of the diffraction peak amplitudes demonstrated the existence of residual compressive stresses in the implanted layer. When they increased the ion dose to 5×10^{17} N^+ ions/cm^2, new lines which corresponded to the formation of nitrides (TiN_x) were observed and the oxides were observed to be progressively transformed into oxynitrides and a mixture of TiN-TiO. Nitrogen promotes α stabilisation hence the implanted layer was mostly transformed into α phase, with a progressive transition to the initial α-β structure underneath.

Yoshinari *et al* [103, 104] evaluated the effect of surface modifications to titanium on antibacterial activity, and their findings indicated that N^+ ion implantation is useful in providing antibacterial activity of oral bacterial to titanium implants exposed to the oral environment. They showed that titanium implants exposed to the oral cavity require N^+ ion implantation to inhibit the adherence of the oral bacteria, and that N^+ ion implantation is useful in controlling the adhesion of oral bacteria as well as ensuring resistance against wear (dental implants).

3.2.1.3.2 Applications in stainless steel

316L stainless steel has been utilised for many years for joint implants because of acceptable friction and wear characteristics, and most stainless steel explanted hip prostheses do not show significant *in vivo* wear. They have much better friction and wear characteristics compared to Ti6Al4V implants. However, during long-term contact with body fluids and tissues, they have been reported to show metallic wear and corrosion [44, 62, 99, 102, 105, 106]. Among the most common metallic biomaterials, 316L stainless steel has lowest corrosion resistance, and *in vitro* corrosion of the material in physiological solutions have shown that toxic ions such as Cr, Ni and Mo are present both in the solutions and in the corrosion products. Crevice corrosion, which is often associated with wear, and synergistic effects of fatigue in chlorine solutions have also been observed. Ion implantation has been shown to significantly improve the corrosion resistance and decrease the wear rate of the metal [43].

Richter *et al* [107] showed that plasma immersion N^+ ion implantation successfully hardened austenitic stainless steels and improved the hardness and wear resistance of the material significantly, compared with the untreated materials. They performed corrosion tests and showed that, corrosion resistance of the modified material was also significantly improved. Leitao *et al* [44] also showed that N^+ ion implantation with 1×10^{16} N^+ ions/cm^2 slightly improved the corrosion resistance of 316L stainless steel due to the formation of more stable films, whereas fluences of less than 1×10^{16} N^+ ions/cm^2 showed no improvements.

Rieu *et al* [91, 99, 102] observed in a pin-on-disc test, a very low wear on untreated 316L stainless steel characterised by few scratches on the steel disc and a non-measurable weight loss of the UHMWPE wear pins. However, in a ball-on-cup tribological test where mechanical and chemical conditions are much more severe than in the human body, they observed the 316L stainless steel ball to have become dark and the UHMWPE cup showing high wear with the production of chips of polyethylene. They observed a reduction in wear of the UHMWPE cup (reducing from 50-200 mg to less than 10 mg) when the 316L stainless steel ball was implanted with N^+ ions.

Ion implanted microstructures in 316L stainless steel are known to be complex due to the large number of nitrogen compounds that Fe, Cr and Ni can form. Rieu *et al* [102]

showed using GIXD that for low ion doses of about 1×10^{17} N^+ ions/cm^2, the diffraction lines corresponds to ε martensite with preferential orientations or texture. When they increased the N^+ ion dose to 5×10^{17} N^+ ions/cm^2, new lines which corresponded to the nitrides $(Cr,Fe)_2N_{1-x}$, Cr_2N, Fe_3N-Fe_2N and α' martensite formed, and CrN was preferentially formed because of the high activity of N with Cr. They found that at a N^+ ion dose of 2.5×10^{17} N^+ ions/cm^2, the spinel type compound Cr_2N-Fe_3O_4 appeared on the surface of the material and the ε–α' martensite underneath was progressively replaced by iron and chromium nitrides.

Besetti *et al* [31] evaluated the *in vivo* bone tissue response to ion implanted stainless steel implants inserted in the tibia diaphysis (cortical bone) and proximal tibia epiphysis (trabecular bone) of New Zealand White rabbits. They demonstrated that ion implanted SS had similar or slightly enhanced biological compatibility in contact with bone compared to untreated materials, and concluded that ion implanted 316L stainless steel may be a useful material in biomedical applications where reduced ion release or enhanced mechanical properties are required, such as in TJR.

3.2.1.3.3 Applications in Co-Cr-Mo alloys

Co-Cr-Mo alloys are easy to obtain in complex shapes using casting techniques. Their orthopaedic prostheses are durable and wear resistant however, the mating component of UHMWPE easily wears down over time owing to articulation against the hard alloy. Ion implantation modification of the mating Co-Cr-Mo bearing surface is a highly successful treatment solution to enhance the mechanical properties of the alloy and to the UHMWPE wear problem. Studies have shown that the process alters the dynamics of the fluid film lubrication in the metal/polymer couple and results in the decrease of the coefficient of friction, and in turn reduces the wear [27]. Implantation increases the surface energy and hardness of the alloy Co-Cr-Mo, and the increase in surface energy allows better retention of a lubricating fluid film, resulting in less wear on the UHMWPE component, because the articulating surfaces experience less direct contact. Physical changes induced in the alloy surface due to the ion bombardment causes the increase in surface energy.

Sioshansi *et al* (1991) compared the wear of UHMWPE disc sliding against treated and untreated Co-Cr-Mo pins, with results obtained using UHMWPE disc sliding against

zirconia pins in pin-on-disc experiments. They found wear and friction of UHMWPE against the treated Co-Cr-Mo pins to be much lower than those of the untreated pins, and slightly lower than they were for zirconia pins due to the surface improvements caused by N^+ ion implantation.

In joint simulator studies conducted to 2×10^6 cycles, ion implantation treated and untreated Co-Cr-Mo femur heads were tested against UHMWPE, and wear was evaluated through weight loss measurements by Taylor *et al* [98]. Results showed a 25% reduction in wear against treated components in comparison to untreated components. The wear of the UHMWPE against the treated Co-Cr-Mo alloy was close to that against zirconia (which they tested for comparison).

Onate *et al* [17] evaluated the wear performance of unmodified and N^+ ion implanted Co-Cr-Mo/UHMWPE wear couples using a knee wear simulator with a combined rolling-sliding movement (corresponding to the most unfavourable situation in the knee), and found that the weight loss of UHMWPE (0.13 mg) tested against modified Co-Cr-Mo and modified UHMWPE (0.24 mg) tested against unmodified Co-Cr-Mo, was significantly lower than that of unmodified UHMWPE (0.69 mg) tested against unmodified Co-Cr-Mo. They concluded that N^+ ion implantation (on Co-Cr-Mo or UHMWPE) improve the wear behaviour of UHMWPE, by reducing the formation of polyethylene wear debris and lessening the occurrence of any micro-delamination (up to 5 million wear cycles).

In general N^+ ion implantation has shown several beneficial effects in metallic biomaterials. The accelerated ion induce structural modifications in a layer less than a micron in the surface by producing new supersaturated phases leading to compressive residual stresses, are generally favourable for friction and wear resistance. There is always a residual atmosphere in the implantation machine chamber and oxygen from this atmosphere can be implanted into the material by complex surface reactions, even if the implanted ions in the accelerated beam is nitrogen or different.

3.2.1.3.4 Applications in UHMWPE

Generally the metallic component of a prosthesis bears and rubs against an UHMWPE part and surgeons have attributed the wear of the polymer part to two main mechanisms

[58]; abrasion (wear) with formation of debris, and creep with plastic flow. A surface treatment of the polymer can improve its abrasion resistance but not creep, which is a bulk property. Ion implantation was performed on UHMWPE and other polymers and surface properties such as wettability, wear resistance, hardness and chemical resistance were all significantly improved [79, 80, 84]. The optimal fluence used for polymers is lower than for metals because of the low hardness of the polymer compared with the metal. Ion implantation on UHMWPE has been actively investigated and preliminary studies have shown that N^+ ion implanted UHMWPE in particular exhibits a significantly reduced wear rate compared with the untreated material. However, the depth of implant is a limiting factor since wear on articulating surfaces is so great (> 1 mm in 10 years) [27].

Rieu *et al* [99, 102] studied N^+ ion implanted UHMWPE cups when rubbing against untreated 316L SS balls and observed a markedly reduced weight loss to less than 5-10 mg when the cup was implanted with 2×10^{14} N^+ ions/cm^2, compared to 50-200 mg when the cup was not implanted. They found wettability of the polymer to be increased with polar liquids such as water, synovial fluid or Ringer's solution. The contact angle of a flat surface with a drop of Ringer's solution decreased from 110° to 70° after their implantation. However, they observed that the polarisation of the surface was limited to the first atomic layers and the wettability increase disappeared after some cycles of friction due to the shallow depth of penetration of the N^+ ions.

Allen *et al* [96] showed that, when N^+ ion implanted UHMWPE (with an implantation dosage between 5×10^{15} and 1.4×10^{17} N^+ ions/cm^2) was worn against an ion implanted titanium alloy under water lubrication, no mass loss was detected up to a sliding distance of 100 000 m on a pin-on-disc wear machine. They observed that water improved the wear resistance not only through the provision of boundary lubrication and low shear strength films, but also acted to maintain a lower temperature and higher mechanical properties of the UHMWPE. They concluded that the higher strength of the N^+ ion implanted UHMWPE, presence of water film and a smooth metallic counterface, were all contributory factors in lowering the wear rate. Under dry conditions they found that the N^+ ion implanted layers deteriorated quickly with consequential increases in wear. Liao *et al* showed hardness increase of up to 15 times and modulus of elasticity increase of seven times with much enhanced wear behaviour in UHMWPE against a similarly implanted Ti6AL4V alloy [96].

Structural modifications induced by N^+ ion implantation in UHMWPE are very hard to study in the thin layer of implantation (< 1 μm) at the surface of the bulk high molecular weight polymer. Chen *et al* [108] investigated the structural and mechanical properties of N^+ ion implanted UHMWPE with fluences ranging from 1 x 10^{14} to 5 x 10^{15} N^+ ions/cm^2, using ERD, Raman spectroscopy and XPS. They showed by ERD that a hydrogen deficient surface layer was formed after ion implantation, and Raman spectroscopy observed damage to the chain structure of the polymer with the formation of a layer of hydrogenated amorphous carbon when the fluence exceeded 1 x 10^{15} ions/cm^2. XPS showed that nitrogen atoms formed chemical bonds with the UHMWPE, and hardness increase of up to four times was measured in their study.

3.2.2 Other Ion Beam Modification Processes

Ion beam assisted deposition (IBAD) is a vacuum deposition process that combines physical vapour deposition (PVD) with ion beam bombardment. During the process a vapour of coating atoms are generated with an electron beam evaporator and deposited on a substrate. Ions, typically gaseous species, are simultaneously extracted from plasma and accelerated into a growing PVD coating at energies of several hundred to thousand electron Volts (eV). The key factor controlling the coating properties in the process is the ion bombardment and the major processing parameters are coating materials, evaporation rate, ion species, ion energy and ion beam current density. As in ion implantation (section 3.2.1) the ions impart substantial energy to the coating and coating/substrate interface to achieve the benefits of substrate heating (which generally provides a denser, more uniform film), without significantly heating the substrate material and degrading bulk properties [27]. In addition the ions interact with coating atoms driving them into the substrate and producing a graded material interface, which enhances adhesion. These factors combine to allow deposition of uniform adherent and low stress films of any coating material on most substrates including extremely adherent metal coatings on polymers. Other advantages of the technique include superior control over coating microstructure and chemical composition, and high reliability and reproducibility. The primary limitation to its use for commercial application at present is the cost involved. One important application in biomaterials is the deposition of infection-resistant coatings on catheters and other implantable medical devices.

Ion beam texturising (IBT) is based on sputtering, which is the process of removing atoms from a solid surface by ion bombardment at a certain energy. The process results from atomic collisions between incident high energy particles and substrate atoms. The ion dose is typically an order of magnitude higher than the dose used in ion implantation (section 3.2.1), and the ion energy used is about several hundreds to thousand eV so as to encourage removal of substrate atoms rather than to implant ions into the surface. The process has the ability to create desirable micro-features and macro-features on biomaterial surfaces to meet the requirements of biocompatibility *in vivo* [26]. Their applications are primarily in the treatment of surfaces for enhanced tissue in-growth, and electrical charge transfer. Pace maker electrode tips with IBT surface features are known to show an improved threshold for pulsing and better sensing capabilities, and these changes are reported to improve the battery life of pacemakers.

Ion beam sharpening and polishing technologies are used for sharpening and polishing surgical instruments such as surgical blades, and also the process allows bevelled surfaces to be created on surgical tools.

3.2.3 Ion Implantation Effects on Friction and Wear

Under certain conditions ion implantation can exert a significant influence in the tribological response of a system depending on the type of wear and friction mechanisms present. Wear is a complex interplay between mechanical and chemical processes at solid interfaces involving adhesion, deformation and friction between the surfaces that results in the progressive removal of material [71]. Adhesion and friction are sensitive to surface composition and therefore ion implantation can be expected to have an influence on them. This is because ion implantation can significantly modify the composition of the near surface layer and thus reduce chemical affinity of surfaces in contact, change oxide growth rates and or strengthen the metal oxide interface. The deformation mode of wear can also be affected directly by ion implantation modifying the composition and microstructure of the near-surface layer. This can be achieved when the ion implantation increases the surface hardness of the material through mechanisms such as solid solution strengthening, and precipitate formation.

Large residual compressive stresses can be introduced into the surface of materials by ion implantation. This can protect against wear since the formation and propagation of micro-cracks and the subsequent formation of plate-like wear particles can be delayed by opposing these compressive stresses to sliding induced tensile stresses. Furthermore ion implantation can indirectly reduce the deformation type of wear by reducing the coefficient of friction between mating surfaces. Decreasing the coefficient friction reduces the intensity of stresses transmitted to the surface and relocates the maximum shear stress from the uppermost layer to a depth well below the surface. This is known to be achieved when the friction coefficient is reduced from more than 0.4 to less than 0.2 [109].

CHAPTER FOUR – EXPERIMENTAL METHODS

4.0 Introduction

The experimental methods and procedures used during the research work are described in detail, in this chapter. These include the pin-on-plate tribological wear test apparatus and test parameters, experimental materials, tribological wear test procedure, and material characterisation techniques used.

The objectives of the study were mainly to:

1. Surface modify the commercially used biomaterials Ti6Al4V, Co-Cr-Mo, stainless steel (REX 734), and UHMWPE by N^+ ion implantation, and quantify the tribological performance of modified and unmodified biomaterial couples using a multidirectional pin-on-plate wear test apparatus
2. Quantify the microstructural and chemical changes upon N^+ ion implantation and during tribological assessment using optical microscopy and XPS, and topographic and hardness changes using a combination of AFM, SEM, non-contacting interferometry and Knoop microhardness indentation
3. Correlate the tribological performance of the N^+ ion implanted biomaterials with the structural, chemical, topographic and hardness investigations and derive an optimum N^+ ion implantation surface modification protocol

4.1 Pin-On-Plate Wear Test Apparatus

Pin-on-plate wear tests were chosen rather than using pin-on-disc or any other screening device, or joint simulator apparatus, to simply compare the wear characteristics of the various biomaterial couples studied in this research work. They are widely used as screening devices in wear studies to screen different material combinations for use in artificial joints, due to their more realistic motion compared with *in vivo* conditions. The other screening devices (section 3.1.1.2), especially the pin-on-disc device is particularly useful in studying basic wear mechanisms, however, most fail to replicate the reciprocating motion that characterises joint motion. The reciprocating pin-on-plate action more closely resembles the conditions encountered in the load bearing joints of the lower limb. Unlike the joint simulator the machine does not attempt to recreate the

in vivo conditions but simply assesses the wear, which will occur when two materials come into contact under similar sliding speeds and stresses to those encountered in the body. However, reciprocating pin-on-plate machines have generally produced mean wear factors for UHMWPE articulating against metallic counterfaces of the order of 10^{-7} or 10^{-8} mm^3/Nm [24, 110, 111], values that are one or two orders of magnitude less than those found *in vivo*, and therefore lead to the suggestion of the use of multidirectional motion machines.

The Durham 4 station multidirectional pin-on-plate wear apparatus which employed both rotation and reciprocation motion was used in the experiments. A photo and schematic representation of the apparatus used are shown in figure 4.1 (a) and (b). The wear machine complied with the ASTM standards F 732-82 and F 732-00 [112, 113] however, it employed both rotation and reciprocation motion in order to address the *in vivo* kinematic situation more realistically (at least in the hip joint). The ASTM standard describes reciprocation only motion, and also changes to some parameter constraints set out in the standard were made, the details of which are listed in section 4.1.1. It has been shown that the addition of a rotational element to a relative motion between a pin and plate sample can produce *in vitro* results more in accordance with average clinical wear factors (*in vivo*) [10, 11, 49, 68, 114], and the UHMWPE wear particles generated known to be clinically relevant [115]. Work at Durham University on the wear of UHMWPE and XLPE has also indicated that the wear rig used in this study can produce realistic quantitative data to predict the tribological performance of total joints *in vivo*, more than the reciprocation alone geometry pin-on-plate wear rig can [50, 116-118].

The pin-on-plate wear test rig consisted of an aluminium sledge reciprocating along two fixed parallel bars. A heated bed and a stainless steel lubricant bath were positioned on top of the sledge. The bed was heated by electrical resistors positioned within, which subsequently heated the lubricant used in the lubricant bath. The electrical resistors together with a K-type thermocouple feedback system placed in the lubricant bath were connected to a controller which maintained the lubricant at a constant pre-set temperature of 37 ± 1 °C. The sledge together with the heated bed and stainless steel bath was driven by a crank alignment powered by a 125 W d.c. shunt motor. This produced the reciprocation motion between the plates and the stationary pins when positioned in their respective plate and pin holders. The motor speed was controlled

using a variable voltage supply and the required stroke length was achieved by adjusting the crank radius of the drive shaft.

Four test plates were located in the stainless steel bath, by means of a plastic frame into which corresponding apertures had been milled. Four test pins were held within stainless steel pin holders, which were in turn fitted vertically in machined arms attached to the main rig. Each pin holder was attached to a motor that rotated the pins around their central vertical axis, and each pin was notched at its upper end to provide good location and hence prevent pin rotation within the holder. The pin holders were free to move vertically in the arms and this allowed them to move downwards when pin wear took place during a test. Cantilevered loading arms to which weights were added at positions along the arms to exert an applied force on the pins rested on top of each pin holder. A screw mechanism on the lever arms allowed their adjustment so that they were horizontal and the point of contact was in the centre of the pin holder all the time.

An electronic lubricant level sensor made of three metal pins (one short and two of the same height) to sense the maximum and minimum levels of the lubricant in the bath was fitted to one side of the lubricant bath. This allowed distilled water to be fed into the bath from an elevated reservoir when required, to account for water evaporation from the lubricant bath. An electrical cut-out system which stopped the motors, turned off the heating bed, and prevented lubricant from being fed into the bath, was fitted on the rig to prevent the bath from running dry, and operated if the distilled water in the reservoir dropped below a minimum level.

A Hall effect probe attached to the reciprocating body and connected to an electronic counter was used to count the number of cycles covered during a tribological wear test, and the wear machine was covered with a perspex case cover to prevent contamination of the lubricant and specimens from the environment.

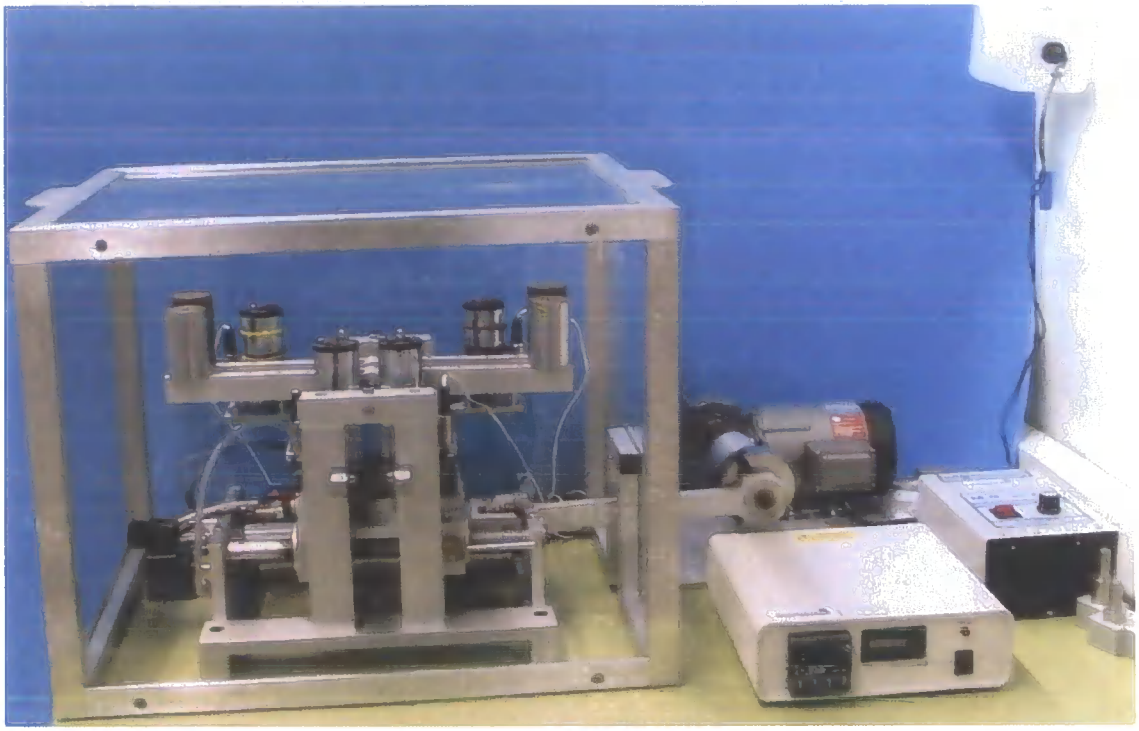

(a) Side View Photograph

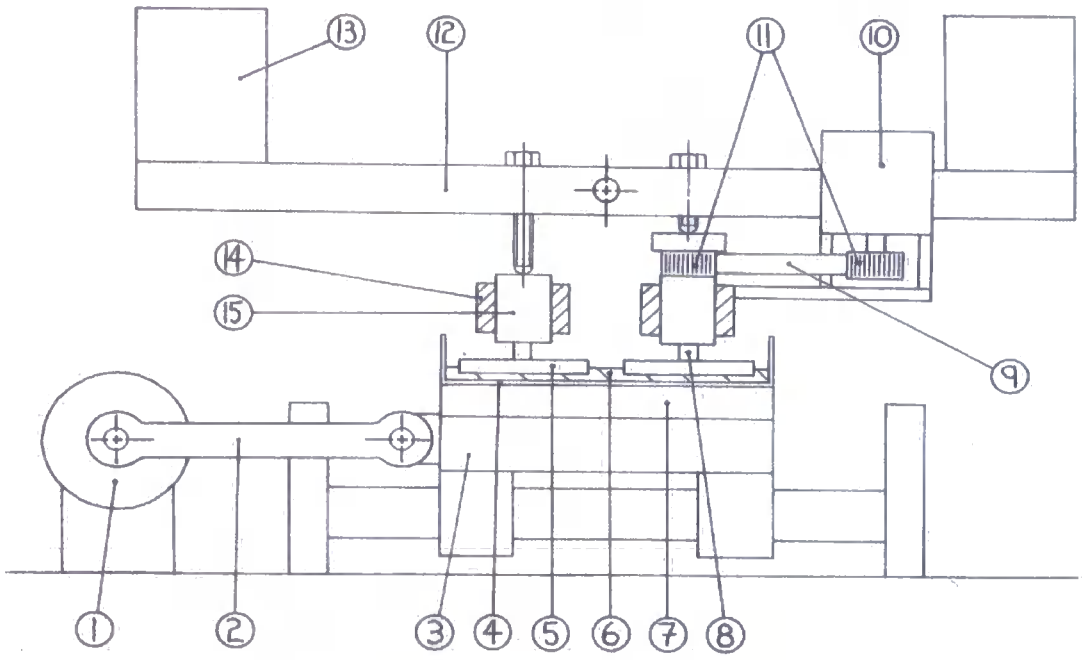

(b) Schematic Representation

Figure 4.1. Reciprocation and Rotation Pin-On-Plate Wear Apparatus. (a) Side view photograph and (b) Schematic representation, where 1 is 125 V DC Shunt motor; 2 is Crank arm; 3 is Reciprocating sledge; 4 is Bath; 5 is Plate; 6 is Plate holder; 7 is Heated base; 8 is Pin; 9 is Belt; 10 is Motor; 11 are Cogs; 12 is Moment arm; 13 is Mass; 14 is Pin holder locator; and 15 is Pin holder.

4.1.1 Test Parameters

The ASTM Standard Practice F 732-82 / F 732-00 is a standard laboratory test method (reciprocating pin-on-plate geometry only) for evaluating friction and wear properties of combinations of materials that are being considered for use as the bearing surfaces of total joint replacement prostheses [112, 113]. The standardised test parameters include lubricant, sliding speed, motion, load, geometry, frequency, contact area, counterface roughness, temperature, and contact stress.

The recommended parameters set out in the standard were followed during the tribological wear tests with regard to the motion, lubricant, temperature, and cleaning protocol. Various other parameters within the test were modified and kept constant to produce the desired conditions for the experiment. Several investigators have also modified or adapted versions of the standard and used them to assess the wear resistance of bearing surfaces for orthopaedic applications. Some of the parameters are discussed in detail under the following sections (4.1.1.1-4.1.1.5) below, with the changes to some parameters also detailed.

4.1.1.1 Lubricant

The ASTM standard recommends the use of filter-sterilised bovine blood serum lubricant, with a mass fraction of 0.2-0.3 % sodium azide to minimise bacterial degradation. The serum must be kept frozen and stored at all times until needed for testing to retard bacterial degradation. During testing, the volume, concentration, and temperature of the lubricant should be maintained constant throughout the test by continuously replacing evaporated water with distilled water. Newborn calf serum supplied by Harlan Sera-Lab (batch number 8030901) was used as the lubricant during this study. The undiluted serum was diluted to 30 % concentration by volume with distilled water, and 0.2 % sodium azide was added as a preservative to reduce bacterial degradation.

Human synovial fluid should be used as the lubricant during *in vitro* tests to simulate *in vivo* conditions, but this is not practical due to the difficulties in obtaining the fluid. As a result, the most common lubricants used in various wear tests include distilled water, saline solution, and bovine serum [4], and the wear mechanisms and wear rates have

been reported to vary during tests with different lubricants, significantly between distilled water or saline solution and bovine serum [119]. The criteria that a candidate lubricant should satisfy for the testing of polyethylene-on-metal or ceramic are that, there should be no polyethylene transfer film to the metal or ceramic counterface, the wear factor should be of the order of 1×10^{-6} mm^3/Nm, most of the wear debris should consist of particles smaller than a micrometer, and the worn polyethylene surface should look polished [120]. Bovine serum contains physiological concentrations of proteins and is accepted to satisfy the above criteria.

It has been reported that bovine serum as a lubricant in wear studies seems to reproduce the wear mechanisms found in the body more closely than non-biological lubricants such as distilled water and saline solution [119]. It has been found to produce wear phenomena qualitatively similar to that observed on *ex-vivo* prostheses probably via suppressing polyethylene transfer and associated damage to the counterfaces. Heavy transfer films of polyethylene have been reported on the surface of metallic counterfaces during tests in distilled water or saline solution, whereas no films have been obseerved when the tests were carried out in bovine serum [111, 119, 120]. It has been hypothesised that the proteins in serum may contribute to boundary lubrication of the bearing surfaces [121], changing the wear mechanisms involved and preventing adhesion of the polyethylene to the metallic counterface [119]. This is significant as the formation of transfer films is not typical of retrieved polyethylene components after extended use *in vivo*.

A laboratory study has suggested that the wear rates of UHMWPE under serum lubrication tend to be more reproducible and less scattered than those under water lubrication [122], and was attributed to the formation of a boundary lubricant film between the articulating surfaces which eliminated the formation of transfer films. Water and saline do not have satisfactory boundary lubrication properties. Low wear and friction properties have also been observed in tests with bovine serum when compared with water and saline solution lubricants. Despite the tribological advantages of bovine serum as a lubricant, its major disadvantage is the degradation of the long chain protein molecules under the mechanical action of the wear couple, ultimately reducing the practical 'life span' of the lubricant to only three or four days continuous use.

4.1.1.2 Motion and Speed

To simulate *in vivo* conditions the ASTM standard recommends that the relative motion between the pin and plate be oscillatory and the samples be run through a 25 mm stroke length at a rate of 1 cycle/s, to produce an average sliding speed of 50 mm/s (0.05 m/s). However, this could not be complied with during the experimental work (because of the 25 mm diameter rod form that the metallic biomaterials were manufactured to). The stroke length was reduced to reflect this.

Plate specimens of 4 mm thickness and 25 mm diameter were cut from the bulk, and polished (as described under section 4.2.1). A stroke of 18 mm at a rate of 1 cycle/s producing an average sliding speed of 36 mm/s (0.036 m/s) was set and kept constant throughout the experiments to run the different material couple combinations. To simulate *in vivo* conditions (of a hip joint) it has been estimated that an average speed between 20 and 50 mm/s (0.02-0.05 m/s) should be used [4] and the speed used in this study was within the estimated average range. The diameters of surgically used femoral components ranges between 22-32 mm (or greater than 32 mm) depending on design, producing an articulating distance in the range 27-39 mm / walking cycle (flexion/extension of 70° swing at 1 Hz during walking, Appendix A2).

4.1.1.3 Load

The test load used during this study was 40 N to produce an average contact stress of ≈ 2.04 MPa, and was kept constant throughout the various tests (Appendix A1). This was mainly due to the size of the flat-ended polymer wear pins used. The pins were machined to sizes of 18 mm long and 5 mm in diameter to provide wear face cross-sectional area of 19.6 mm^2. This is a standard polymer wear specimen used in previous pin-on-plate studies under a load of 40N or less at Durham University [50, 116]. The load in a typical THR ranges from 0-4000 N (up to five times body weight at impact), to produce a contact stress in the range of 0 – 12.4 MPa [112].

The standard recommends a test load of 225 N constant to within ± 3 % to be applied along the longitudinal axis of the polymer wear pin for the duration of the test to give an average contact stress of 3.54 MPa. This recommendation has been calculated for a flat

ended 13 mm long and 9 mm in diameter standard polymer wear specimen, with a cross-sectional area of 63.6 mm^2.

4.1.1.4 Surface Roughness

A surface roughness of 0.025–0.05 μm has been recommended by the ASTM standard for metallic counterfaces when articulating against polyethylene. Typical surface roughness values in previous wear tests were between 0.01–0.055 μm for metals, and between 0.15–1.5 μm for UHMWPE and XLPE [4, 65]. The surface finish of the metallic counterfaces used in the study was between 0.005–0.01 μm, better than that of the standard, and that of the polymeric wear pin surfaces was between 0.8-1.5 μm, which lies within the standard recommendation. R_a values greater than the recommended values are known to cause excessive wear of the mating polymer (section 3.1.1.1.2).

4.1.1.5 Temperature

The ASTM recommends the bulk temperature of the lubricant to be held at 37 ± 3 °C (F732-82) or 37 ± 1 °C (F732-00) body temperature, and this was followed for all tribological wear tests in this study.

4.1.2 Pin-On-Plate Test Procedure

The tribological wear test procedure described in detail below was employed for each individual test carried out in this study. Table 4.1 lists the biomaterial wear couple combinations tested during the study. In each test, the pin/plate combinations in the test stations were identical, and four sets of specimens for each material (both in the form of modified or unmodified) was used in the tests. Prior to the commencement of a test the polymer wear pins and metallic plates were carefully cleaned ultrasonically and dried with lint-free tissue to remove any contaminants from machining and microtoming, and grinding and polishing respectively. The pin and plate holders were carefully cleaned.

After the cleaning procedures, each pin and plate was carefully weighed four times and recorded, and the mean initial weight for each material was calculated from the weight results. Weighing was done on a Mettler Toledo AE200 balance, sensitive to 2 μg. After

weighing the pins and plates were placed in their respective holders and positioned in the wear rig. Each pin position on a plate was determined by guide markings on their holders to ensure correct positioning every time. Weights were applied to the lever arms of the rig to apply a force of 40 N to the pins, providing a contact stress of 2.04 MPa. The lever arms were positioned so as to act through the centre of the pin holders and were horizontal.

30 % bovine serum and 70 % distilled water to which was added 0.2 % sodium azide to retard bacterial growth, was used as the lubricant to cover the plates and left to equilibrate at 37 ± 1 °C before the test was started. In each test an unloaded soak control polymer pin was kept with its unnotched end in the same lubricant as the test pins. This enabled compensation for fluid absorbtion by the polymer wear pins due to their hydrophilic nature. A stroke length of 18 mm was set to enable the polymer wear pins to reciprocate and rotate within the diameter of the plates, to produce an average sliding distance of 36 mm per cycle. The reciprocation and rotation motion timed over various periods and the frequency was set at 1 Hz. The stroke length, and frequency of rotation and reciprocation gave a physiologically representative simulation of a replacement hip prosthesis during the walking cycle.

All tribological tests were typically run for a duration of at least 5 million wear cycles. The tests parameters that were used for the experiments are summarised and shown in table 4.2.

Table 4.1. Biomaterial Wear Couple Combinations Tested

Biomaterial Wear Couple Combination
Unmodified UHMWPE/Unmodified Ti6Al4V
1 x 10^{15} and 5 x 10^{15} N^+ ions/cm^2 implanted UHMWPE/Unmodified Ti6Al4V
5 x 10^{15} N^+ ions/cm^2 implanted UHMWPE/Unmodified Ti6Al4V
Unmodified UHMWPE/2 x 10^{17} N^+ ions/cm^2 implanted Ti6Al4V
Unmodified UHMWPE/1 x 10^{18} N^+ ions/cm^2 and 1 x 10^{21} N^+ ions/cm^2 implanted Ti6Al4V
5 x 10^{15} N^+ ions/cm^2 implanted UHMWPE/2 x 10^{17} N^+ ions/cm^2 implanted Ti6Al4V
Unmodified XLPE/Unmodified Ti6Al4V
5 x 10^{15} N^+ ions/cm^2 implanted and unmodified XLPE/2 x 10^{17} N^+ ions/cm^2 implanted Ti6Al4V
Unmodified UHMWPE/Unmodified Stainless Steel
Unmodified UHMWPE/2 x 10^{17} N^+ ions/cm^2 implanted Stainless Steel
5 x 10^{15} N^+ ions/cm^2 implanted UHMWPE/2 x 10^{17} N^+ ions/cm^2 implanted Stainless Steel
Unmodified UHMWPE/Unmodified Co-Cr-Mo
Unmodified UHMWPE/2 x 10^{17} N^+ ions/cm^2 implanted Co-Cr-Mo
5 x 10^{15} N^+ ions/cm^2 implanted UHMWPE/2 x 10^{17} N^+ ions/cm^2 implanted Co-Cr-Mo

Table 4.2. Tribological Wear Test Parameters

Wear pin diameter	5 mm
Counterface plate diameter	25 mm
Stroke length	18 mm
Sliding distance	36 mm/cycle
Motion	Multidirectional
Frequency of rotation and reciprocation	1 Hz
Nominal load	40 N
Contact stress	2.04 MPa
Lubricant	30 % bovine serum in 70 % distilled water at 37 ± 1 °C

4.1.2.1 Experimental Measurements and Errors

A gravimetric technique was used to measure the wear of the polymer wear pins. Preliminary pin-on-plate testing revealed no mass loss of the metallic plates respective to polymer pins, and the wear of the plates were neglected for the purpose of the experiments in line with previous pin-on-plate tests. The plates (both modified and unmodified forms) were weighed pre and post wear test to compare the weight loss under the different material combinations tested. The wear of the softer polymer was analysed in terms of the corresponding wear factors and wear mechanisms present.

At regular intervals of about 300,000 wear cycles of test the pins and plates were removed from their respective holders. The pins and plates were cleaned following the ASTM cleaning protocol (Appendix A3) and dried in a fume cupboard. Each wear pin as well as the control pin was weighed four times on the balance to calculate the mean weight, visually inspected, and further investigations carried out using an optical microscope and AFM. The surfaces of the wear tracks on the plates were characterised with AFM and non-contacting interferometer. After cleaning, weighing, and characterisations, the apparatus was then reassembled and started.

The wear of the polymeric test pins was defined as the weight loss with respect to the initial weight to which was subtracted any weight gain of the control pin, assuming weight gain of the control and test pins to be equal. The weight loss was converted into volume loss by dividing by the density of the polymer, and the corresponding polymer wear factors calculated using equation 3.3 (section 3.1.1.2). The densities (ρ) used to calculate the wear volumes were 0.927 g/cm^3 for the UHMWPE (Appendix B4) and 0.949 g/cm^3 for the XLPE material. Graphs of polymer wear volume loss (mm^3) versus sliding distance (km) were plotted, and the wear factors calculated using the slopes (mm^3/Nm) of the graphs divided by the constant 40 N nominal load. The slopes of the graphs were determined using linear regression by fitting trend lines on the wear curves, and the wear mechanism acting on the polymers were determined from surface analysis. Owing to the high sensitivity of the weighing balance used in the gravimetric determination of wear, the calculated errors in the volume loss measurement were minimised such that the error bars on the graphs fell within the data points. Descriptive statistics were used to calculate the mean polymer wear factors and standard deviation from the mean value (Appendix A5 – A7).

The wear factors reported were calculated taking into account only the reciprocating sliding distance and not the effects of rotational sliding distance on the UHMWPE pins, during the multidirectional wear tests. This is the simplified method of calculation recommended by the ASTM Standard Practice F 732-00. However, work at Durham University [118] using a developed computer programme has shown that rotation motion has an effect on the overall sliding distance of the UHMWPE pins, by increasing the average sliding distance by a factor of about 2.1 %. Therefore the sliding distance values used are slightly underestimated, and the wear factors reported without the consideration of the rotational effects during testing can be said to be slightly higher than the true wear factors and hence a worse case scenario, although a good approximation to the overall sliding distance.

Where calculable, a measure of how widely values are dispersed from the mean values (standard deviation) were made (Appendix A4), and the results shown on the reported experimental measurements.

4.2 Test Materials

4.2.0 Introduction

The commercially used biomaterials used during the research work are described under the following sections (4.2.1 and 4.2.2). The materials have been grouped into metallic and polymeric biomaterials, the former being Ti6Al4V, stainless steel (Rex) and Co-Cr-Mo alloys, and the latter UHMWPE and XLPE. All the materials were supplied by DePuy Johnson and Johnson, Leeds, UK, and are currently used in tribological applications.

4.2.1 Metallic Materials

The metallic materials used in this study were commercially used Ti6Al4V alloy, stainless steel (Rex), and Co-Cr-Mo alloy supplied from Depuy Johnson & Johnson, Leeds, UK, in the form of rods or bar stocks of length 2600 mm and 25 mm diameter. These materials were prepared into plates and used as the counterface materials during the pin-on-plate tribological wear tests.

The Ti6Al4V alloys displayed a 2-phase (duplex) $\alpha + \beta$ microstructure the microstructure and properties of which are described in section 2.1.1. The microstructures and properties of the stainless steel (Rex) and Co-Cr-Mo alloys are described in sections 2.2.1 and 2.3.1 respectively. Metallic biomaterial data as supplied from Depuy Johnson & Johnson are shown in Appendix B1-B3.

Each alloy rod material was cut into several flat disc shapes of thickness 4 mm and 25 mm diameter, using a Buehler Isomet 2000 Precision Saw Cutting Machine with Buehler Abrasive Cut-Off Wheel Blades. These flat discs were then metallographically polished and used as the counterface (plate) materials.

The cut metallic plates from each alloy were each metallographically prepared by wet grinding with intermediate water washes on grades 220, 500, 800 and 1200 grit SiC paper using a Buehler Metaserv Rotary Grinder. Polishing on a Buehler Universal Polisher using 6 μm and then 1 μm diamond pastes followed the grinding stages. Water rinse followed each of the wet grinding stages, and water rinse followed by isopropanol rinse and ultrasonic bath cleaning followed each of the two polishing stages to obtain the final surface finish of the materials.

Atomic force microscopy (AFM) and non-contacting optical microscopy (sections 4.3.2 and 4.3.3 respectively) were used to characterise the surface topography and roughness of the plate surfaces, and to obtain initial arithmetic mean surface roughness values (R_a) prior to N^+ ion implantation modifications and tribological wear tests. The initial mean R_a values for all materials were calculated from 10 measurements from 10 different areas on the surface.

The Knoop microhardness of each metallic plate was measured 10 times and the mean values recorded, using a *Mitutoyo MVK-H2* Microhardness device (section 4.3.4) prior to the materials being sent for N^+ ion implantation. Knoop indentations were made to obtain surface sensitive hardness measurements, in preference to Vickers indentations, which for the same load penetrate deeper into the sample.

4.2.2 Polymeric Materials

The polymeric materials used were ultra high molecular weight polyethylene (ENDURON), and cross-linked polyethylene (for comparison) supplied from Depuy Johnson & Johnson, Leeds, UK. The UHMWPE were supplied in the form of ram extruded long bar stocks of diameter 40 mm. The XLPE materials were injection moulded prior to cross-linking (using silane method) to 118 °C for 120 hours, with a gel content of 78 %, and were supplied in the form of plates of sizes 80 mm x 80 mm with a 50 mm x 8 mm pin attached to the centre of the plates. The structure and properties of polyethylene are described in section 2.4. UHMWPE data as supplied, are shown in (Appendix B4).

All polymeric wear pins used were machined from their bulk materials into flat-ended circular cylindrical wear pins of sizes 5 mm diameter wear face and 18 mm long, to produce a wear face surface area of 19.63 mm^2. To prevent any directional effects all the wear pins were machined with the same orientation within the supplied stock. The machined wear pins were notched at their upper ends to allow adequate fixation within the wear rig pin holders and to ensure correct orientation when replacing them after cleaning and weighing procedures during a tribological test.

Prior to surface characterisations, N^+ ion implantation modification, and tribological wear tests, the machined surfaces of the pins were microtomed to remove any machining marks and minimise any residual stresses introduced by machining. AFM and non-contacting optical interferometry were used to characterise the surface topography and roughness of the wear surfaces to obtain the mean R_a values. Initial mean R_a values calculated from 10 measurements on each polymeric wear pin material were recorded to be between 0.8-1.4 μm, which were within the range recommended by the ASTM Standard Practice F 732-00.

4.2.3 N^+ Ion Implantation

Nitrogen ion implantation work was performed at Tech-Ni-Plant Ltd, Aston Science Park, Birmingham, UK, using the Zymet Z-100^{TM} system. Some of the system specifications are shown in table 4.3.

The Zymet Z-100 is a 100 KeV, 10 mA ion implantation system. Based on ion implantation, the system utilises a vacuum process in which high velocity ions of a selected element are directed at a target material and come to rest in the near surface region of the material. Elemental materials existing either as a gas or vapour at 900 °C can be ionised and implanted into metals, ceramics, and polymers to change surface sensitive properties. N^+ ions were used to modify the biomaterials used in this study. The major components of the system include treatment chamber and work holder, beam generation and control system, vacuum system, and an electronic microprocessor control unit.

The standard Z-100 chamber accommodates parts up to 30 cm in height with available options to treat larger objects. It has a unique handling system (cool-Grip fixture) that is specifically designed to hold and cool the product during treatment (Appendix D, fig. D1.4). During the treatment process the material is first embedded in a low melting point (145 ° C) metal contained in a 20 cm diameter product tray, which is then attached to a water cooled manipulator. The process chamber door is closed and an automatic vacuum pump down cycle is initiated. The holder is then positioned at a chosen implant angle with respect to the beam direction (Appendix D, fig. D1.5). The disc may be continuously rotated during the implantation (for treating cylindrical objects) or kept stationary (for flat objects).

The beam generation system consists of the ion source, which is of the arc discharge type providing maximum beam currents greater than 10 mA, source power supplies, extraction electrode system, and the extraction power supply (Appendix D, fig. D1.2).

The extraction electrode lens transports the beam from the ion source aperture, which is 5 cm long, and causes it to diverge to become 20 cm long and 2 cm wide at the implant position which is 90 cm downstream. The ion beam curtain is then scanned from side to side by slowly oscillating the ion source and extraction electrode assembly (Appendix D, fig. D1.3). A standard mask projecting 250 cm^2 is used for product implantation.

During the implant, the swept ion beam is sampled in two collection cups at the centre of the oscillating beam scan (Appendix D, fig. D1.6). Beam current pulses are accrued in a current integrator until the desired dose has been reached, at which time an audible alarm sounds and the process automatically stops. During the implant, the estimated

time to completion is continuously displayed for the benefit of the operator. Before and after an implant the beam is directed off the product holder into additional beam collection cups situated to one side of the normal implant scan pattern.

The vacuum system is pumped by two 15.2 cm oil diffusion pumps, backed by two 14.7 cfm direct drive rotary mechanical pumps, one mounted on the beam-line chamber, the other on the process chamber. The microprocessor-controlled system is operated in the automatic mode normally and has protective circuits to prevent damage in the event of power failure, improper operation, or system malfunction. No liquid N is required to operate the system. The status of the machine both during set-up and operation is displayed on a 7.6 cm CRT screen.

Table 4.3. Specifications of the Zymet Z-100 ion implantation system

System Specifications	
Beam Energy:	50-100 keV
Ion Species:	N^+ (~ 40 %) + N_2^+ (~ 60 %)
Ion Current (maximum):	5 mA (electrical), 7.5 mA (particle)
Implantation Angle:	variable between + 0 ° and – 135 °

The metallic plates Ti6Al4V, stainless steel and Co-Cr-Mo alloys, were all N^+ ion implanted with ion doses of 2×10^{17} ions/cm^2 at an accelerating voltage of 90 keV, after the laboratory metallographic preparations described in section 4.2.1. Additional N^+ ion implantation to a dose of 1×10^{18} and 1×10^{21} ions/cm^2 were performed on Ti6Al4V samples, at the same accelerating voltage.

The polymeric wear samples (UHMWPE and XLPE) were N^+ ion implanted with doses of 1×10^{15} and 5×10^{15} ions/cm^2 at an accelerating voltage of 80 keV.

During the implantations, target temperature were kept below 100 °C, and the residual gas pressures in the implantation chamber to below 2×10^{-5} Pa to minimise the inclusion of oxygen. Low ion doses and ion energies were selected for the polymer materials due to their lower densities and thermal stability compared with the metals. Operating at low temperatures further ensured that any thermal degradation of the near substrate was avoided. Ion implantation time for the polymeric samples was about 4

minutes, and 70 minutes for the metallic samples. The ion implantation conditions used for each biomaterial implanted are listed in table 4.4.

Table 4.4. Biomaterial N^+ ion implantation conditions

Material	Ion dose (ions/cm^2)	Ion Energy (keV)	Beam Current (μA)
Ti6Al4V	2×10^{17}	90	2.8
	2×10^{18}	90	2.8
	2×10^{21}	90	2.8
Stainless steel (REX)	2×10^{17}	90	2.8
Co-Cr-Mo	2×10^{17}	90	2.8
UHMWPE	1×10^{15}	80	2.8
	5×10^{15}	80	2.8
XLPE	5×10^{15}	80	2.8

4.2.3.1 Implanted N^+ Ion Distribution

The profile of the depth and distribution of N^+ ion implantation within the various materials at their respective ion doses and energies were calculated using the TRIM Monte Carlo simulation computer program (SRIM 2000), developed by James F. Ziegler and J.P. Biersack [123].

4.3 Analytical Techniques

4.3.0 Introduction

The analytical techniques used to characterise the surfaces of the modified and unmodified materials during the experimental work are described briefly under the following sections (4.3.2 – 4.3.7).

4.3.1 Metallography

Metallography was carried out to investigate the microstructures of the materials used in the study prior to any N^+ ion implantation modification and tribological wear tests, with the exception of Co-Cr-Mo alloys, UHMWPE and XLPE materials. All the metallographic samples were prepared by grinding and subsequent polishing on a 6 μm and then 1 μm diamond cloth paste as described in detail in section 4.2.1.

Metallographic Ti6Al4V alloy samples were etched with 10 % HF (40 % aqueous solution), 30 % HNO_3 and 60 % distilled H_2O for 10 s, washed in a stream of distilled water and dried.

Stainless steel metallographic samples were etched with 15 cm^3 HNO_3, 15 cm^3 HCL and 70 cm^3 distilled H_2O for 10 s and washed in a stream of distilled water, followed by drying.

All etched metallographic samples were examined using AFM, SEM, and optical microscopy, the techniques of which are described under sections 4.3.2, 4.3.6, and 4.3.7 respectively.

4.3.2 Atomic Force Microscopy

Scanning Probe Microscopy (SPM) is a recent innovative technology that relies on a mechanical probe for the generation of magnified images. The instrument is operable in ambient air, liquid, or vacuum, and can resolve features in three dimensions down to sub-nanometre level, with no damage to the sample surface.

TopoMetrix TMX 1010 Explorer (Veeco Instruments, Cambridge) Atomic Force Microscopy (AFM) was used to characterise modified and unmodified material surfaces, to understand the topographical modification induced by N^+ ion implantation on the sub-micron scale, during the experimental work. In common with all SPMs, the AFM comprise of a force sensing probe, piezoelectric ceramics for positioning the probe, an electronic control unit, and a computer for controlling the scan parameters and generating and presenting images [124]. The force sensing system has a very high spatial resolution, on the sub-nanometre level. Unlike STM (conductive samples only), AFM allows scanning of both conductive and non-conductive samples. It can be divided into two primary scanning modes, contact mode (CM) and non-contact mode (NCM) atomic force microscopy, referring to whether or not the scanning probe actually comes into physical contact with the sample surface.

A silicon nitride (Si_3N_4) pyramidal probe integrated onto the end of a cantilever with a weak spring constant (K) is generally used in the contact AFM. Most of the cantilevers used are typically 100 or 200 μm long, with K of about 0.03-0.6 N/m. For the experimental work in this study, a cantilever of length 100 μm with a force constant of 0.21 N/m and a nominal resonance frequency of 66 kHz was used. During a scan, the cantilever is mounted onto the piezoelectric ceramic element, which is capable of producing x, y and z motions such that an area of surface could be scanned by the probe in the x and y directions whilst maintaining a constant height between sample and probe in the z direction. The probe tip mounted to the end of the cantilever (fig. 4.2) scans across the sample surface, coming into direct physical contact with the sample. The cantilever and probe exerts a positive loading force ranging from about 5-50 nN on the sample during a scan and places the probe tip in a constant state of repulsion with the sample. Varying topographic features cause deflections of the tip and cantilever as the probe tip scans. A light beam from a small laser is bounced off of the cantilever and reflected from a mirror on to a four-section photodetector. The amount of deflection of the cantilever or the force it applies to the sample is calculated from the difference in light intensity on the sectors of the photodetector, and the resulting change in detector current signal can be used in forming the AFM image. It is the simplest method involving the least instrument variables for gathering of topographic information even to the atomic level resolution.

There are several modes of contact scanning including topography, internal sensor, and fast track imaging, which can be acquired simultaneously. The most common and accurate method of producing a contact mode AFM image is to plot Z-piezo extension as the vertical scale. In this mode a feed back loop actively drives the Z-piezo scanner to minimise cantilever deflection. As the cantilever deflects during a scan, the change in sensor current immediately feeds back a correction voltage to the Z-piezo, restoring the cantilever to its original deflection (force), which can be adjusted using the set point current (fig. 4.3).

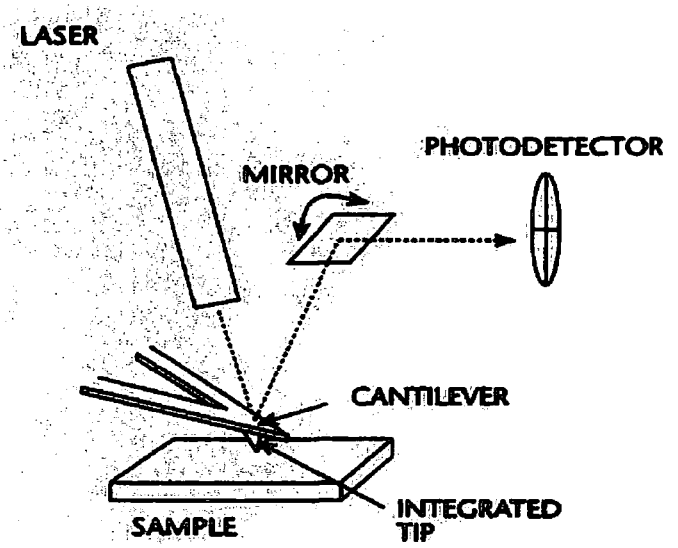

Figure 4.2. AFM imaging components (force sensor)

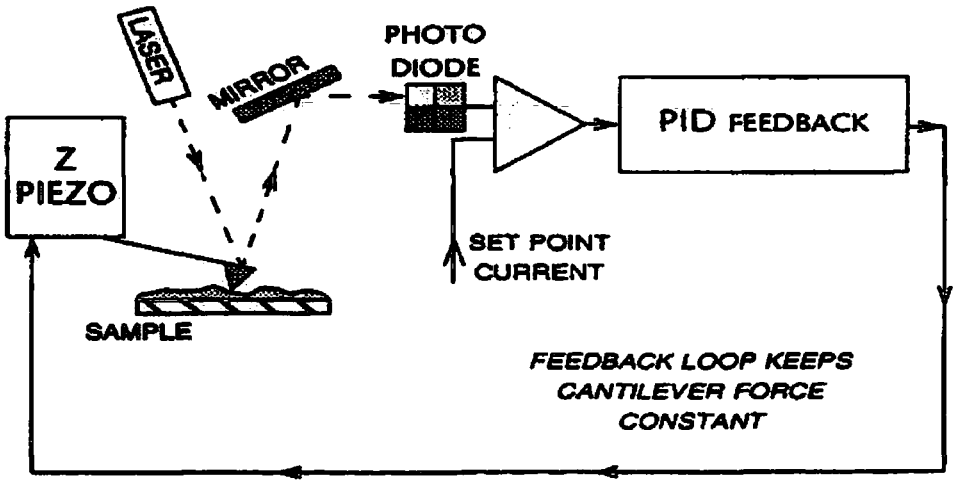

Figure 4.3. AFM Contact mode feedback loop

In non-contact mode AFM operation in common with CM, a silicon triangular pyramidal probe integrated onto the end of the cantilever is generally used. Unlike CM, the cantilever is oscillated at its resonant frequency above the sample. As the probe gets closer to the sample surface, the attractive force between the tip and the sample will change the oscillation amplitude and phase of the probe tip. Either change in phase or amplitude can be detected and used to control the tracking of the probe over the surface (feed back control loop) to obtain topographic data (figure 4.4). Amplitude detection is the non-contact method usually used for high-amplitude oscillation, whereas phase detection is usually used when the oscillation amplitude is relatively small. Non-contact scanning is sometimes preferable because as the cantilever moves across the sample surface in contact scanning, the lateral motion of the cantilever may cause damage to soft or fragile samples such as biological specimens or polymers. For this reason, NCM was mainly used on the polymeric samples investigated during the work.

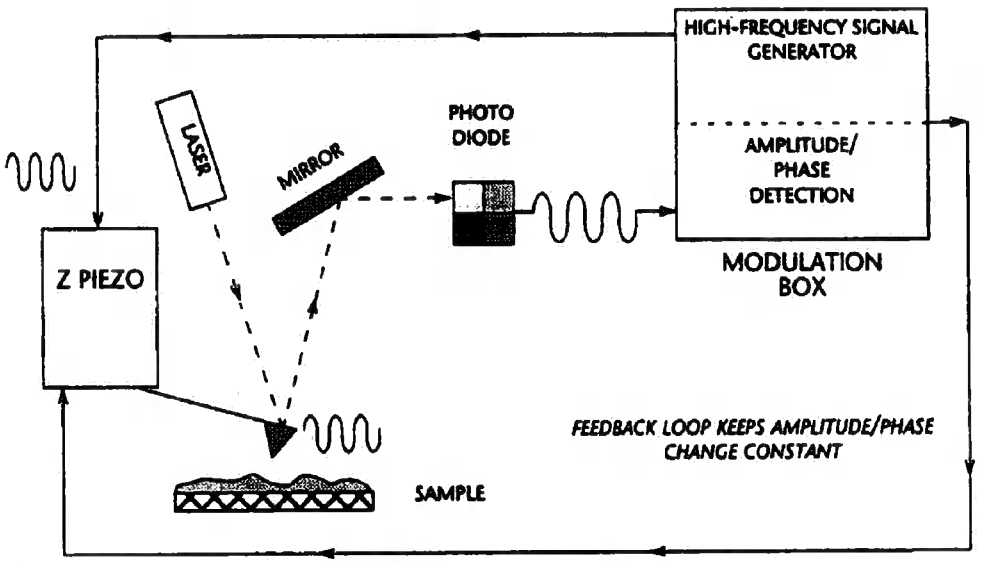

Figure 4.4. AFM Non-contact feedback loop

4.3.3 Non-contacting Interferometry

An optical non-contacting interferometer (*Zygo New View 100, Zygo Corporation, USA*) was used to investigate the surface topography and roughness parameters in particular, of the metallic and polymeric samples in both modified and unmodified forms, pre and post N^+ ion implantation and tribological wear tests. The non-contacting interferometer (NCI) analysis a surface area of 24488 mm^2, and mean arithmetic mean

surface roughness (R_a) values of materials reported are an average of 10 measurements from different areas on the material surface.

The NCI used is a general purpose imaging surface structure analyser that can provide imaged surface details of materials and accurate measurements to characterise them. It uses a scanning white light interferometry to image the microstructure and topography of surfaces in three dimensions without contacting the surface [125]. Light from the microscope divides into two, one portion reflecting from the test surface and the other from an internal high quality reference surface (fig. 4.5). Both portions are directed and recombined onto a solid-state camera where interference between the two light wave fronts shows as fringes. Measurements made on the fringes, is used to generate height information on the surface under examination.

The system can image depths of up to 100 um with 0.1 nm z-resolution.

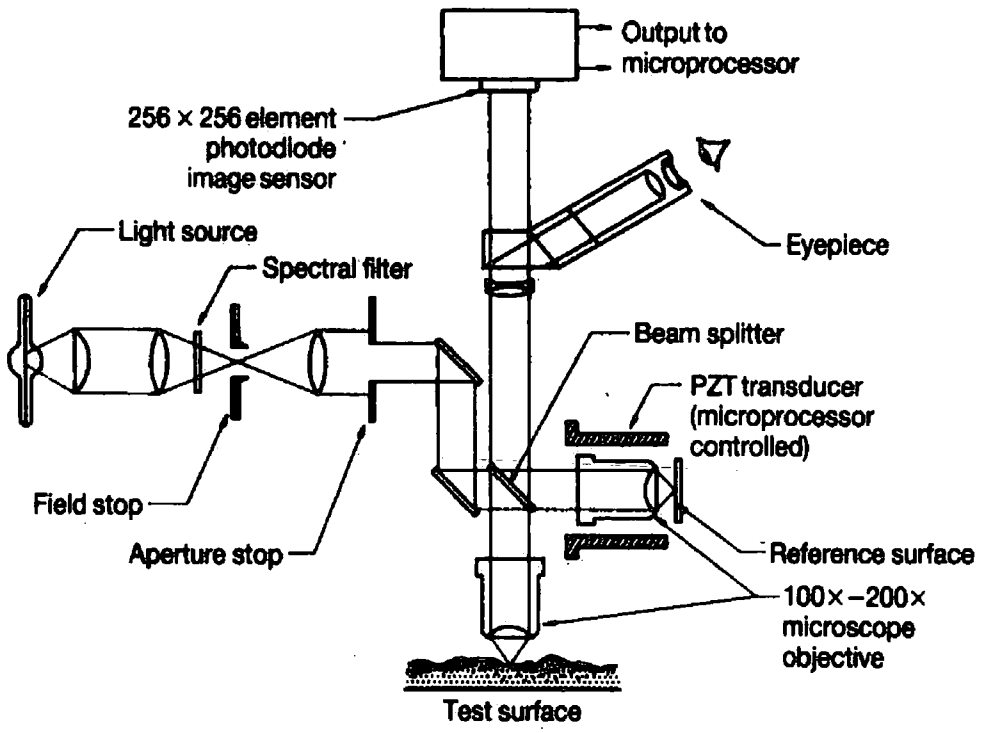

Figure 4.5. Schematic diagram of a non-contacting interferometer [54]

4.3.4 Microhardness Indentation

Hardness of a material is it's resistance to localised plastic deformation [126, 127]. For the mechanics of material testing, hardness is the resistance to indentation [71], and for metals it is a measure of their resistance to plastic deformation. There are three types of hardness measurements known as indentation, dynamic and scratch, depending on the way in which the test is conducted. Indentation hardness measurements were chosen during the research work. There are several indentation hardness tests including Brinell (1900), Meyer, Vickers, Rockwell and Microhardness.

Since the nitrogen ion implanted layers on the biomaterials used in this study were very thin, it was difficult to measure the hardness of the materials using high load indentation. Low load surface sensitive microhardness measurements were used to quantify N^+ ion implantation induced surface hardening and hardness of the unmodified metallic and polymeric materials, using a *Mitutoyo MVK-H2* Microhardness Testing Machine fitted with a Knoop diamond indenter. Knoop indenter was chosen rather than the Vickers pyramidal indenter, because the specific geometry of the Knoop indenter allows lower penetration depths than those obtained by the Vickers indenter with the same normal load [128], and thus provides a more surface specific measurement suitable for the thin surface layers produced during the work. The long and short diagonals of the Knoop pyramidal indenter have a 7:1 ratio, which produces indentations typically 15 % of the depth of an equivalent Vickers indent [129].

Microhardness testing was carried out normal to the surface of the material in all cases, at room temperature with loads ranging between 1 and 25 gf. For each test the small diamond indenter was forced into the surface of the material using the applied loads, and the resulting impression observed under a microscope and measured. The measurement is converted into a hardness number, which is designated by KHN on the machine. The Knoop microhardness values reported were an average of ten indentations on different areas on the surface of the materials, at the respective loads for a loading duration of 10 s (Appendix C2.1 – C2.3). The standard deviations from the mean hardness values were calculated at each indentation load during the measurements, and are shown on the reported values. Deviations from the mean values for all measurements were calculated to be less than 15 %.

4.3.5 X-ray Photoelectron Spectroscopy

X-ray photoelectron spectroscopy was used to determine the surface chemical species and chemical environment of the metallic and polymeric biomaterials both in the form of N^+ ion implanted and unimplanted samples, during the experimental work. It provides information of the surface composition and bonding states in thin layers near material surfaces.

Monochromatic or unmonochromatic X-rays are often used to excite photoelectrons from within a target and the energy of which carries information of the binding energy from the source atom, and thus the nature of the atoms in the material. The characteristic kinetic energy of the photoelectron (E_k) is given by the energy of the exciting X-ray photon ($h\nu$), which is totally absorbed in the process minus the characteristic binding energy (E_B) of the electron, which is emitted from the material surface (equation 5.1).

$$E_k = h\nu - E_B - \phi \qquad \text{equation 5.1.}$$

Where ϕ is the work function or minimum threshold radiation energy whose value depends on the material being analysed. XPS is a surface sensitive technique, as although incident radiation may excite electrons deep in the material because of energy loses due to inelastic collisions within the target atoms, only the electrons arising from the top few atomic layers may escape the surface and contribute to the spectra. The photoelectrons are also sensitive to the state of bonding of the atom from which they come, manifested as an energy shift of one or two eV, so for instance metallic Ti can be distinguished from Ti in an oxide (i.e. Ti6Al4V used in this study). Despite the advantages of XPS as a sensitive surface chemical analysis technique, it does not offer good spatial resolution because the exciting beam of X-rays covers a wide area and cannot be readily focused.

The surface chemical analysis of the metallic and polymeric samples were undertaken on a VG Scientific ESCALAB 5 X-ray photoelectron spectrometer using unmonochromated Mg Kα X-rays, operated at an anode potential of 10 kV and a filament emission current of 20 mA at the University of Nottingham. Mg source rather than an Al Kα radiation was used, in order to prevent Kβ satellite of the main oxygen

peak O 1s (530 eV) interfering with the Ti $2p^{3/2}$ peak (458.7 eV in TiO_2, and 455.6 eV in Ti-N). Al Kβ x-ray satellite occurs at 70 eV below the O 1s peak (i.e. 460 eV), whereas the Mg Kβ x-ray satellite occurs at 48 eV below O 1s (i.e. 482 eV) and therefore well away from the Ti $2p^{3/2}$ peak. The use of the Mg anode also had the advantage of marginally better peak resolution with respect to the Al anode.

The specimen take-off angle used was 90° and the area analysed was approximately 1 cm^2. The electron spectrometer comprised of a hemispherical sector analyser and was operated in the constant energy mode at electron pass energies of 20 eV for the high-resolution element peaks. The survey scan spectra for each sample was collected in the 0-1100 eV binding energy range using a pass energy of 50 eV. Interpretation of the spectra, background removal, peak fitting, and peak area determination were performed using a VGX 9000 computer software package. The instrument was standardised against the C 1s spectra peak at 285 eV to correct binding energy shifts due to charging. This correction was applied to all element peaks following background substraction or peak deconvolution to give 'true' binding energy values. Quantitative data (i.e., atomic % composition) were derived using elemental sensitivity factors (dividing peak areas by sensitivity factor for each element and normalising data to 100 %).

4.3.6 Scanning Electron Microscopy

A *JEOL JSM – IC 848* SEM (*JEOL Instruments, Japan*) equipped with a *PGT Avalon* Energy Dispersive X-ray analyser (EDX) was used to examine and determine the surface composition of the metallic biomaterials, microstructures of chemically etched Ti6Al4V and stainless steel samples, and modified and unmodified polymeric and metallic surfaces pre and post wear tests, during the experimental work. The surfaces of the polymer wear pins were sputtered with a thin gold coating to prevent charging by rendering them electrically conducting prior to examination. The attached EDX was mainly used for analysing the composition of the metallic biomaterials prior to modification and tribological wear tests.

The scanning electron microscope employs a beam of electrons directed at the surface of the test material, and is primarily used to study the surface or near surface structure of bulk materials [130]. Figure 4.6 shows the schematic representation of the main components and mode of operation of a simple SEM. Electrons are accelerated to an

energy usually between 1 and 30 keV from the electron source, usually of the tungsten filament thermionic emission type or field emission gun (a tungsten hairpin source used in this work). The beam of electrons are then demagnified by the condenser lenses before hitting the specimen surface, and then scanned across the specimen surface by the scan coils. A detector then counts the number of low energy secondary electrons or other radiation given off from each point on the surface, and at the same time, the spot of a cathode ray tube (CRT) is scanned across the screen. The brightness of the spot is modulated by amplified current from the detector.

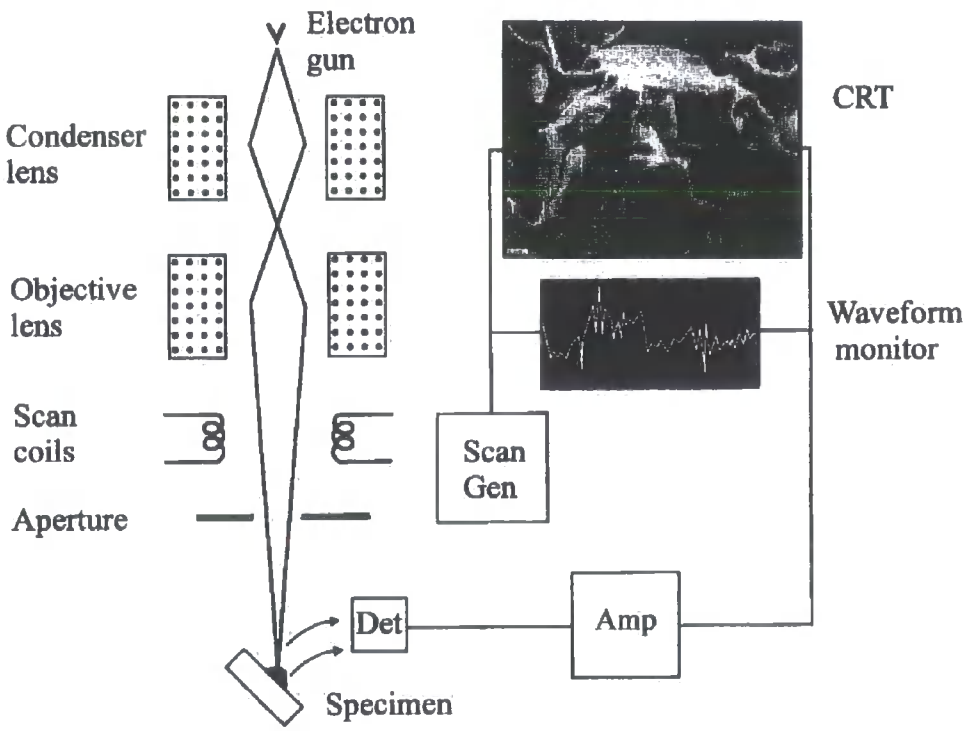

Figure 4.6. Schematic diagram showing the main components of an SEM [130]

4.3.7 Optical Microscopy

Examination of metallographic samples for microstructural determination, as well as investigation of tribological wear features on worn sample surfaces were carried out using optical microscopy with both conventional and Nomarski contrast techniques with an *Axiotech Reflected Light Microscope* (Zeiss Instruments Ltd) [131, 132].

CHAPTER FIVE – RESULTS

5.0 Introduction

The results of the experimental procedures outlined in Chapter 4 (same for all the biomaterials used in the research work) are reported in this chapter under the sections 5.1-5.3 respectively for Ti6Al4V alloy and UHMWPE; Stainless steel and UHMWPE; and Co-Cr-Mo and UHMWPE. These include metallography, N^+ ion implantation, microhardness, tribological wear test, topography, and chemical composition results of the selected biomaterials.

5.1 Ti6Al4V alloy, UHMWPE and XLPE

5.1.0 Introduction

The metallographic results of the microstructure of the Ti6Al4V alloy used in this study, N^+ ion implantation distribution in both Ti6Al4V and UHMWPE substrates, microhardness of the materials in both modified and unmodified forms, tribological wear test results of UHMWPE (modified and unmodified) articulating against Ti6Al4V, topography and standard roughness of the as polished and modified samples, and chemical composition of the modified and unmodified materials are all presented under the following sections (5.1.1 to 5.1.6).

5.1.1 Metallography

An optical photomicrograph, SEM micrograph, and AFM image of the etched metallographic Ti6Al4V samples are shown in figures 5.1, 5.2 and 5.3 (a) respectively. The optical micrograph (fig. 5.1) resolved the classic two phase α and β microstructures of the alloy (section 2.1.1). The sample was then examined under the SEM where high magnification was obtained to resolve the microsructures clearly (fig. 5.2).

In the top view 100 x 100 μm AFM image (fig. 5.3 *(a)*), microstructure phases of $\approx$ 10 μm diameter are visible on the etched sample surface, α being the bright and β dark areas. Bright areas represents high topography (hard spots) and dark areas imply low topography. Figure 5.3 *(b)* shows a top view 100 x 100 μm AFM image of the same

Ti6Al4V material implanted with 2 x 10^{17} N^+ ions/cm^2 and then etched. As can be seen, the classic two phase microstructure was difficult to resolve, as a result of the surface modification. Optical and SEM photomicrographs of the modified sample equally showed poor resolution of the duplex microstructure.

Figure 5.1. Optical photomicrograph of HF etched Ti6Al4V

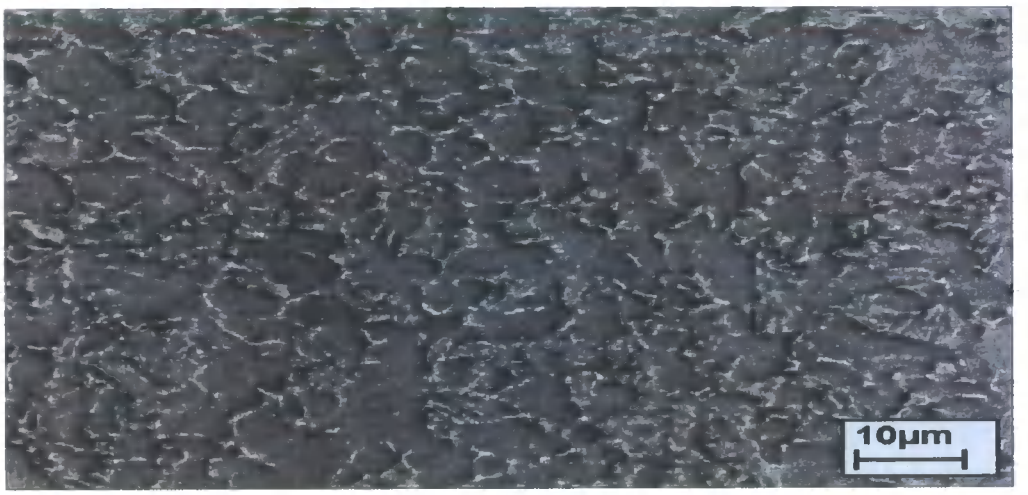

Figure 5.2. SEM micrograph of HF etched Ti6Al4V

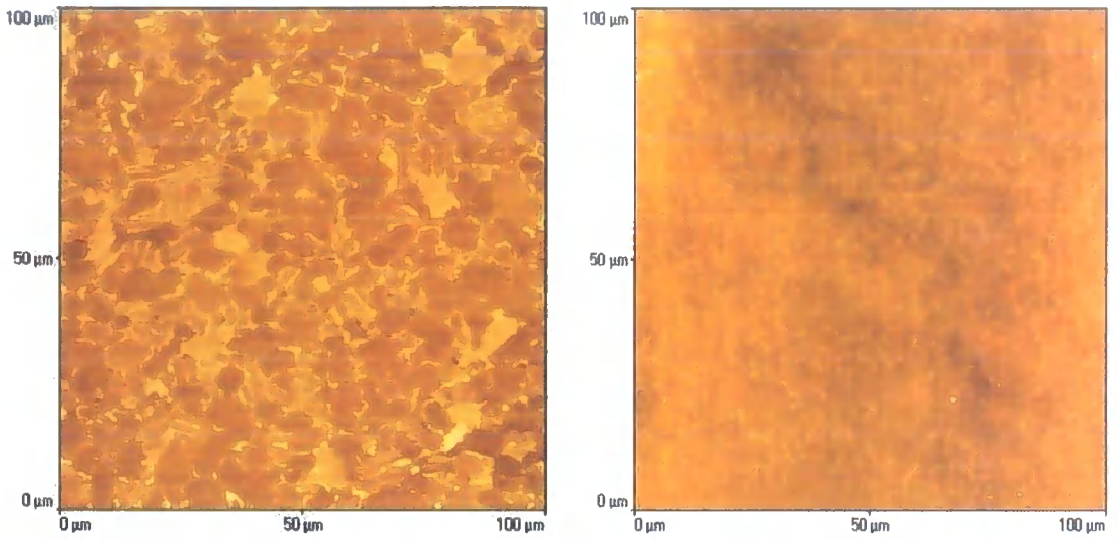

(a) Unmodified *(b)* 2 x 10^{17} N^+ ions/cm^2 implanted

Figure 5.3. Top view AFM images of HF etched *(a)* unmodified Ti6Al4V and *(b)* 2 x 10^{17} N^+ ions/cm^2 implanted Ti6Al4V

5.1.2 Projected N^+ Ion Distribution

The results of the TRIM stopping range calculations for N^+ ions into Ti6Al4V and UHMWPE are shown in figures 5.4 to 5.11. The calculations were made using N^+ as the bombarding ions, with an accelerating energy of 90 and 80 keV respectively for the Ti6Al4V and UHMWPE targets. Target densities of 4.4 g/cm^3 and 0.93 g/cm^3 were used respectively for Ti6Al4V and UHMWPE.

Simulation of the range of N^+ ions into Ti6Al4V target is shown in figure 5.4. The estimated mean longitudinal range of N^+ ions in the target was calculated to be at a depth of 0.15 µm with straggling of 0.05 µm. The overall distribution of the ions assumed approximately a classical Gaussian profile, as shown on the figure. The maximum N^+ ion penetration depth was approximately 0.25 µm into the Ti6Al4V surface. Figure 5.5 shows the calculations of the vacancy distribution produced by both N^+ ions and target atom recoil collisions, where a total of 358 target vacancies were produced by each incoming N^+ ion.

Figure 5.6 shows the energy transmitted to the target atom recoils from the incoming N^+ ion, where the energy dissipation can clearly be seen to be maximum at the mean

projected N^+ ion range for the transferral to recoils. Figure 5.7 shows the TRIM simulation of the ionisation energy loss of both ions and target atoms. The ionisation energy loss was observed to be highest closest to the sample surface, ionisation being an electronic effect.

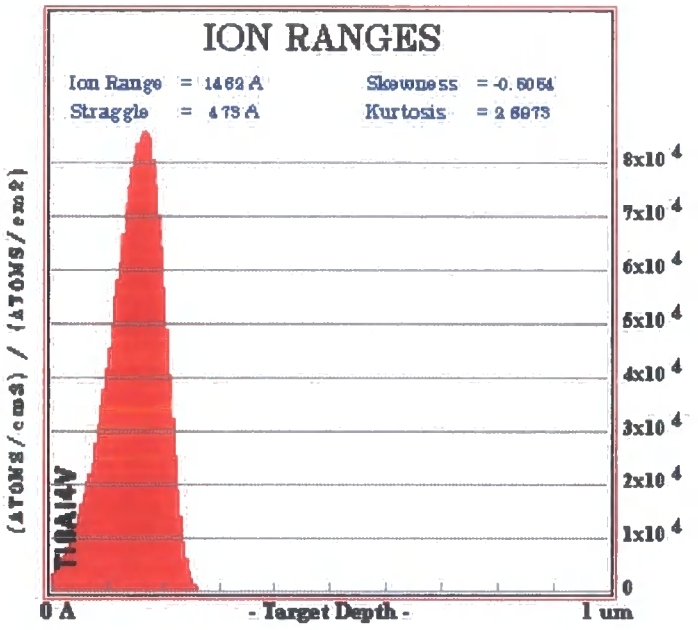

Figure 5.4. TRIM simulation of N^+ ion ranges in Ti6Al4V

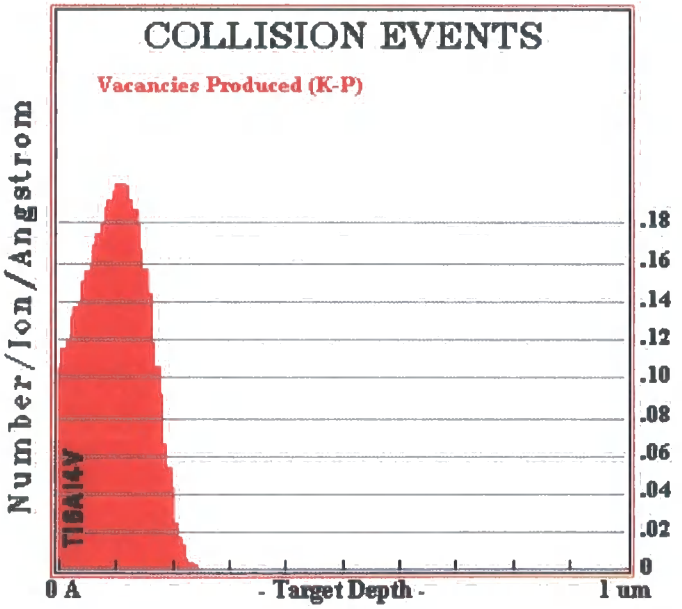

Figure 5.5. TRIM simulation of vacancy production within Ti6Al4V target

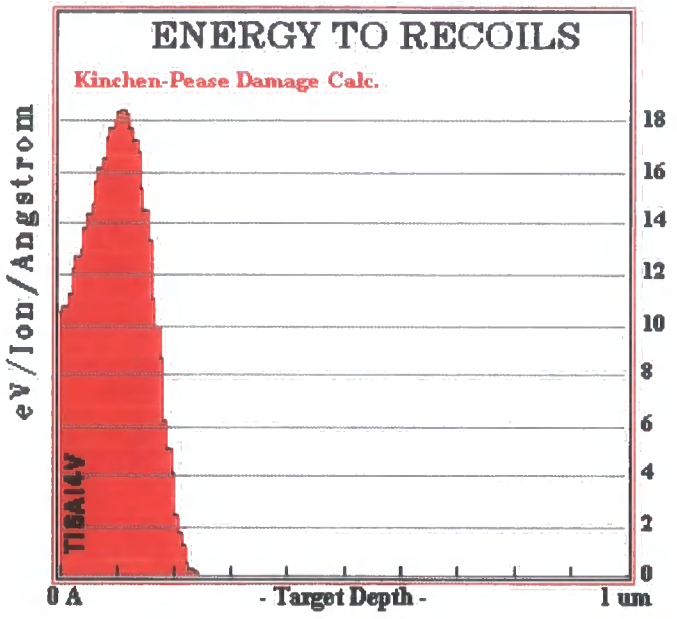

Figure 5.6. TRIM simulation of energy transferral to recoils for N^+ ion implantation into Ti6Al4V

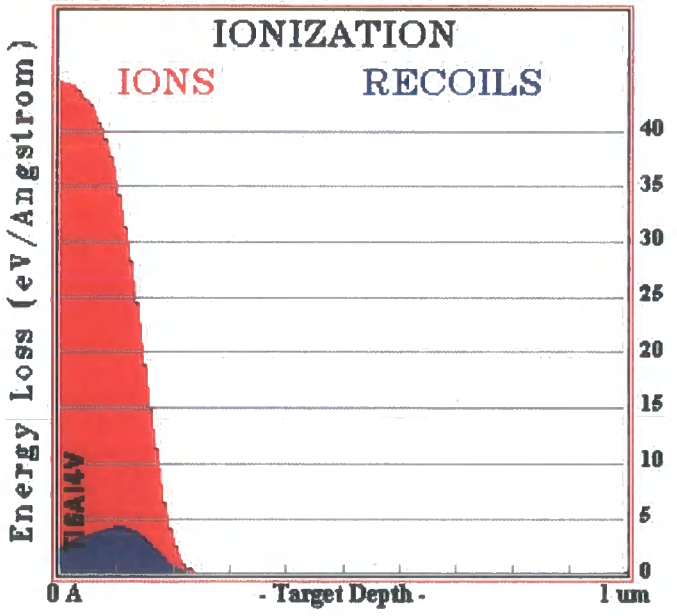

Figure 5.7. TRIM simulation of ionisation energy loss of N^+ ions into Ti6Al4V

Figure 5.8 shows the calculation for the range of N^+ ions into the UHMWPE target, where the mean longitudinal range of the ions was estimated at a depth of 0.26 μm with straggling of 0.04 μm. The distribution of the ions was observed to assume an

approximately Gaussian profile, and a 0.35 μm maximum depth of N^+ ions into UHMWPE surface was calculated. Calculation of the vacancy distribution produced by both N^+ ion collisions and UHMWPE atom recoil collisions are shown in figure 5.9, where a total of 368 target vacancies were produced by each incoming N^+ ion.

The energy transmitted to the target atom recoils from the incoming N^+ ions was calculated and the results shown in figure 5.10. The energy dissipation was maximum at the mean projected N^+ ion range for the transferral to recoils. Figure 5.11 shows the simulation of the ionisation energy loss of both ions and target atoms, where the ionisation energy loss was observed to be highest closest to the sample surface, ionisation being an electronic effect.

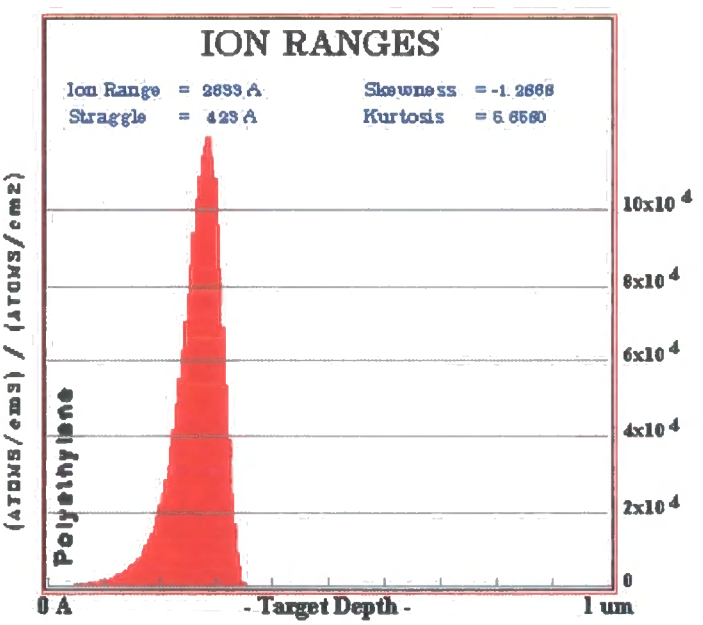

Figure 5.8. TRIM simulation of the range of N^+ ions in UHMWPE

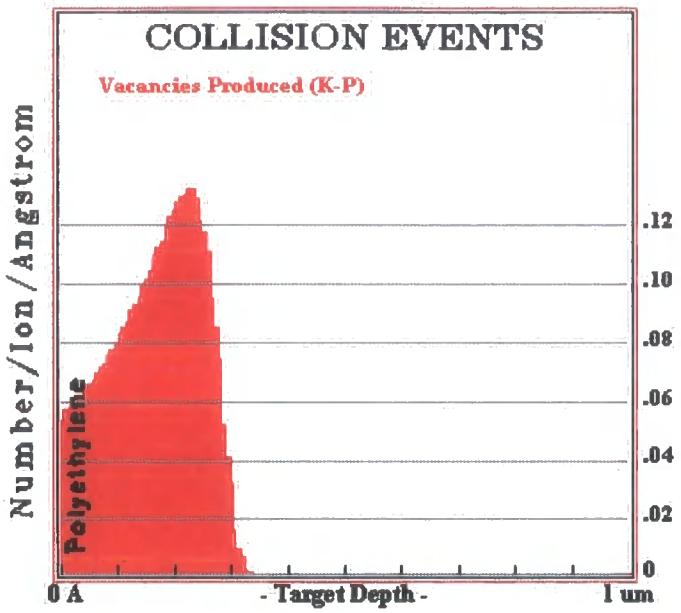

Figure 5.9. TRIM simulation of vacancy production within UHMWPE target upon N^+ ion implantation

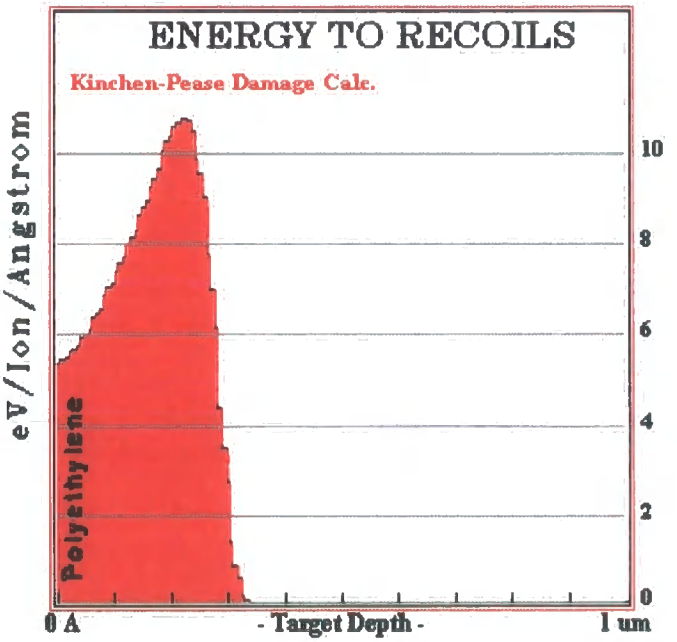

Figure 5.10. TRIM simulation of energy transferral to recoils for N^+ ion implantation into UHMWPE

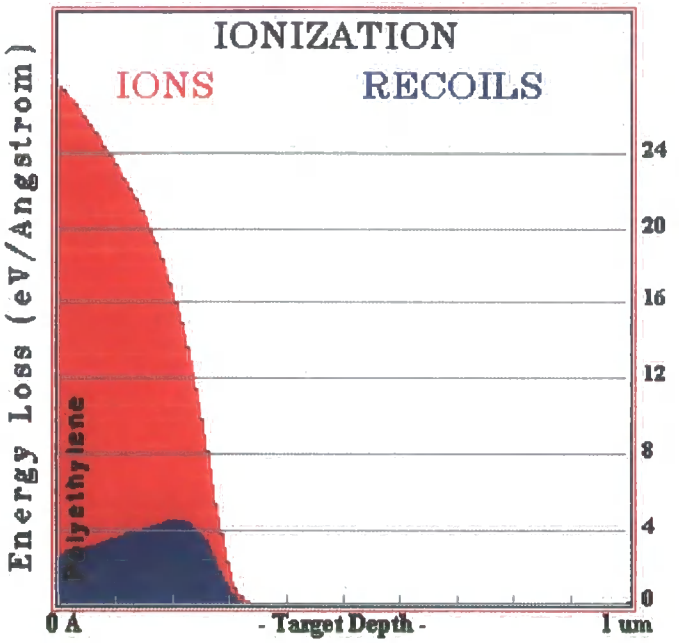

Figure 5.11. TRIM simulation of ionisation energy loss of N^+ ions into UHMWPE

5.1.3 Knoop Microhardness Determination

The Knoop microhardness results of the unmodified and N^+ ion implanted Ti6Al4V samples are reproduced in figure 5.12. The microhardnesses of the modified samples were observed to increase with decreasing indentation load, and the highest values were measured at an indentation load of 1 gf. Hardness of the N^+ ion implanted samples increased with increasing implantation dose, and the results indicated an increase in mean hardness from 347 ± 20 KHN_{1gf} for unmodified material, to 730 ± 32 KHN_{1gf} for material implanted with 2 x 10^{17} N^+ ions/cm^2, 1064 ± 119 KHN_{1gf} for material implanted with 1 x 10^{18} N^+ ions/cm^2, and 1413 ± 183 KHN_{1gf} for material implanted with 1 x 10^{21} N^+ ions/cm^2 (Appendix C2).

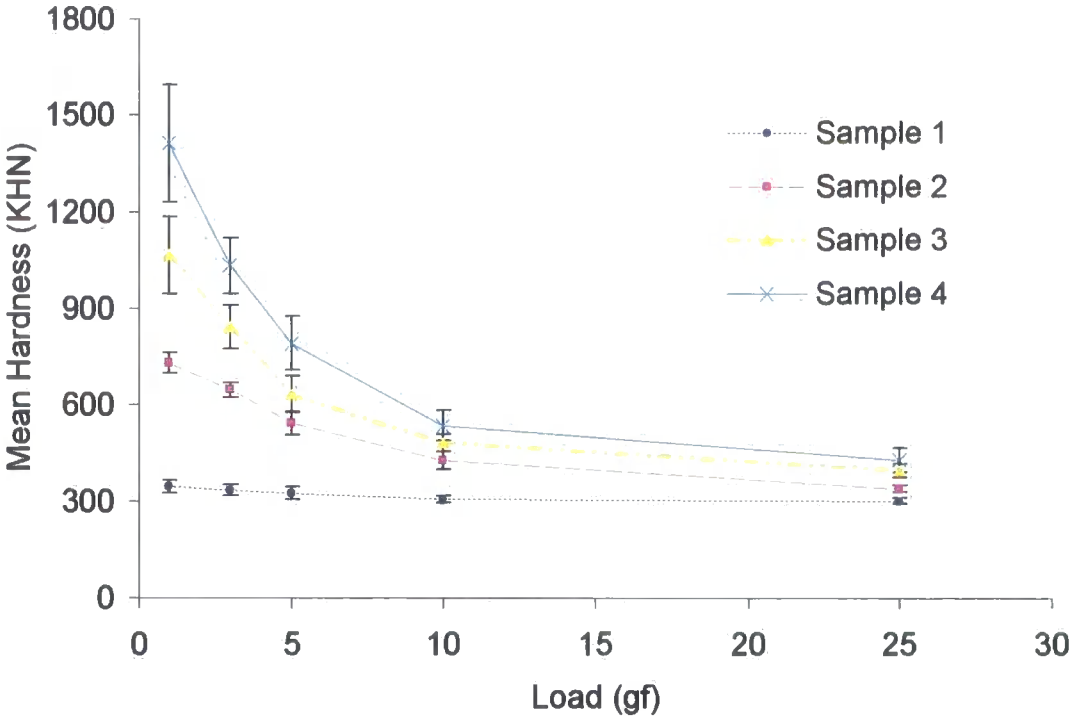

Figure 5.12. Knoop microhardness of unmodified and N^+ ion implanted Ti6Al4V. Where sample 1 is unmodified Ti6Al4V, sample 2 is 2 x 10^{17} N^+ ions/cm^2 implanted Ti6Al4V, sample 3 is 1 x 10^{18} N^+ ions/cm^2 implanted Ti6Al4V, and sample 4 is 1 x 10^{21} N^+ ions/cm^2 implanted Ti6Al4V.

Inspection of figures 5.13 to 5.15 demonstrates the surface dependence and depth graded property modification induced upon ion implantation respectively for samples modified with 2 x 10^{17}, 1 x 10^{18} and 1 x 10^{21} N^+ ions/cm^2, where the mean hardness values at different loads have been plotted against the mean knoop indent penetration depth into the samples. The indentation depths were calculated from the indent width using the Knoop indenter geometry (Appendix C1) for loads of 1, 3, 5, 10 and 25 gf respectively. The reported values are an average of 10 measurements under each load.

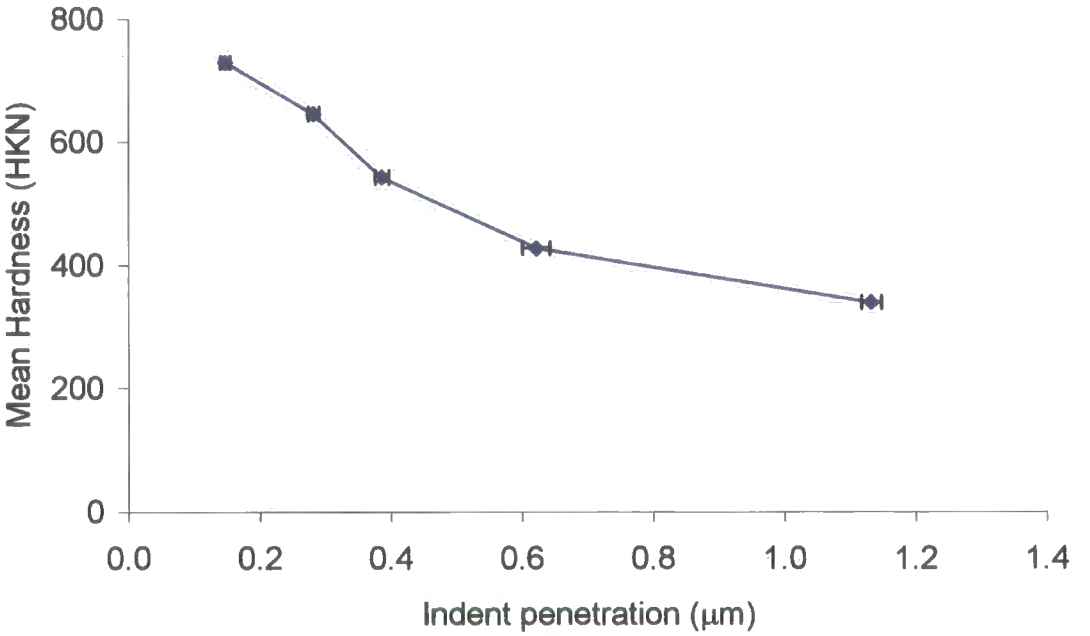

Figure 5.13. Depth dependence of Knoop microhardness for 2 x 10^{17} N^+ ion/cm^2 implanted Ti6Al4V

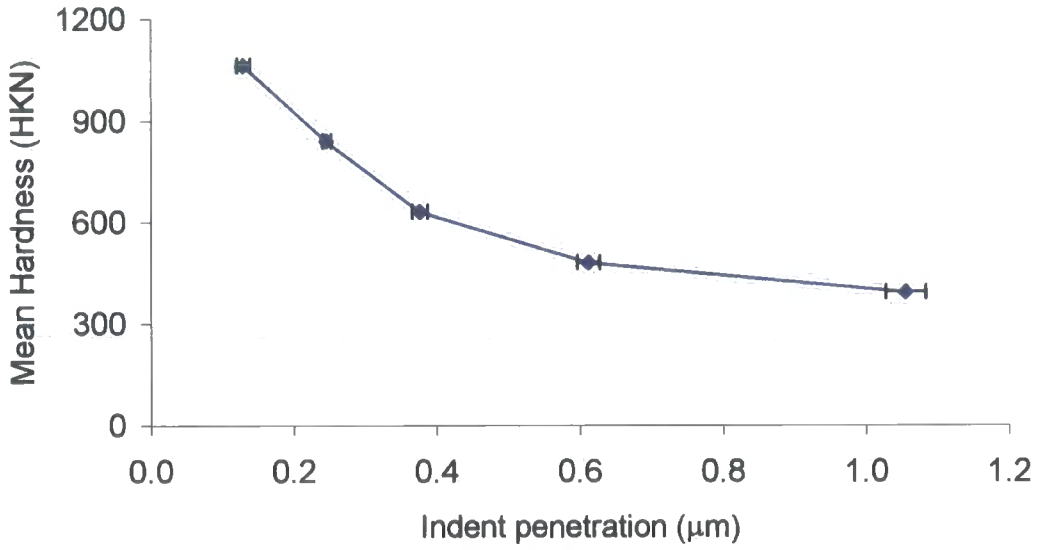

Figure 5.14. Depth dependence of Knoop microhardness for 1 x 10^{18} N^+ ion/cm^2 implanted Ti6Al4V

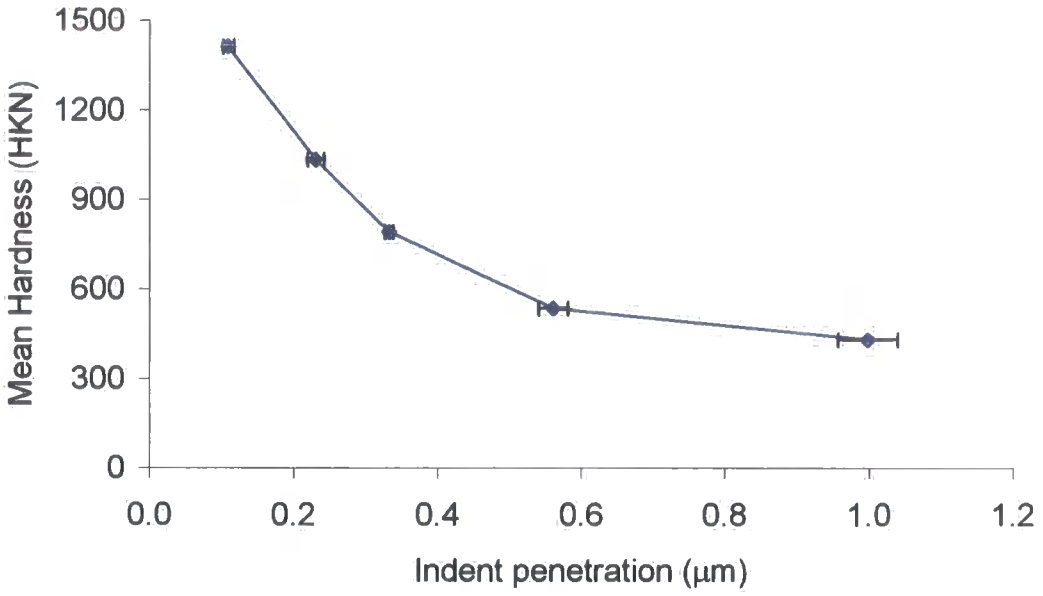

Figure 5.15. Depth dependence of Knoop microhardness for 1 x 10^{21} N^+ ion/cm^2 implanted Ti6Al4V

Because of the low yield strength of the UHMWPE and XLPE, Knoop indentations at loads higher than 1 gf were difficult to measure, producing excessive surface deformation of the material at the higher loads. Knoop microhardness were measured at a load of 1 gf and the results indicated an increase in mean hardness from 3.4 ± 0.5 KHN_{1gf} for unmodified UHMWPE, to 8.6 ± 0.7 KHN_{1gf} for UHMWPE implanted with 1 x 10^{15} N^+ ions/cm^2, and 12.8 ± 1.6 HKN_{1gf} for UHMWPE implanted with 5 x 10^{15} N^+ ions/cm^2. An increase in mean hardness from 6.1 ± 0.8 KHN_{1gf} for unmodified XLPE, to 14.5 ± 1.1 KHN_{1gf} for XLPE implanted with 5 x 10^{15} N^+ ions/cm^2 was also observed.

5.1.4 Tribological Wear Test

5.1.4.0 Introduction

The tribological wear test results of UHMWPE and XLPE wear pins (both in modified and unmodified forms) articulating against Ti6Al4V plates (modified and unmodified) are reported under the sections 5.1.4.1 to 5.1.4.6 (Appendix A6).

5.1.4.1 Unmodified UHMWPE against unmodified Ti6Al4V

Tribological wear test results of unmodified UHMWPE against unmodified Ti6Al4V sliding couple, expressed in volume loss of the unmodified UHMWPE wear pins against sliding distance are shown in figure 5.16. There were no significant differences between the wear factors of the UHMWPE wear pins. The overall mean wear factor (k_o) of unmodified UHMWPE rotating and sliding against unmodified Ti6Al4V was calculated to be $2.77 \pm 0.16 \times 10^{-6}$ mm^3/Nm over a sliding distance of 207 km (> 5.5 million sliding wear cycles). An initial slightly higher mean k_o of $3.04 \pm 0.17 \times 10^{-6}$ mm^3/Nm was measured up to a sliding distance of 67 km, due to a wearing in type process. The steady-state mean wear factor of $2.41 \pm 0.11 \times 10^{-6}$ mm^3/Nm was measured between 67-207 km sliding distance. Plate weight pre and post wear test (weight loss) are shown in table 5.1.

Extensive damage was observed via AFM, NCI, and optical microscopy, in the wear tracks of the Ti6Al4V counterface plates after only a few wear cycles and the damage was observed to increase with test duration. The bovine serum test lubricant discoloured to black with test duration and was found to contain dark particulate debris. Machining and microtoming marks on the surface of the UHMWPE wear pins wore away with test duration, and the surfaces became smooth, showing low R_a values (table 5.2) post wear. No polymer transfer films were seen on the surfaces of the unmodified Ti6Al4V plates, and the wear curves for all UHMWPE wear pins were linear.

AFM and NCI examinations of the unmodified Ti6Al4V plates post wear test, revealed distinctive wear tracks, characterised by random deep scratches and grooves in the wear tracks of the plates, with high R_a values. AFM revealed the granular structure of the worn unmodified UHMWPE pin surfaces, a surface morphology that resembled those of *ex-vivo* unmodified UHMWPE components, indicative of similar wear mechanisms of unmodified UHMWPE *in vitro* and *in vivo*.

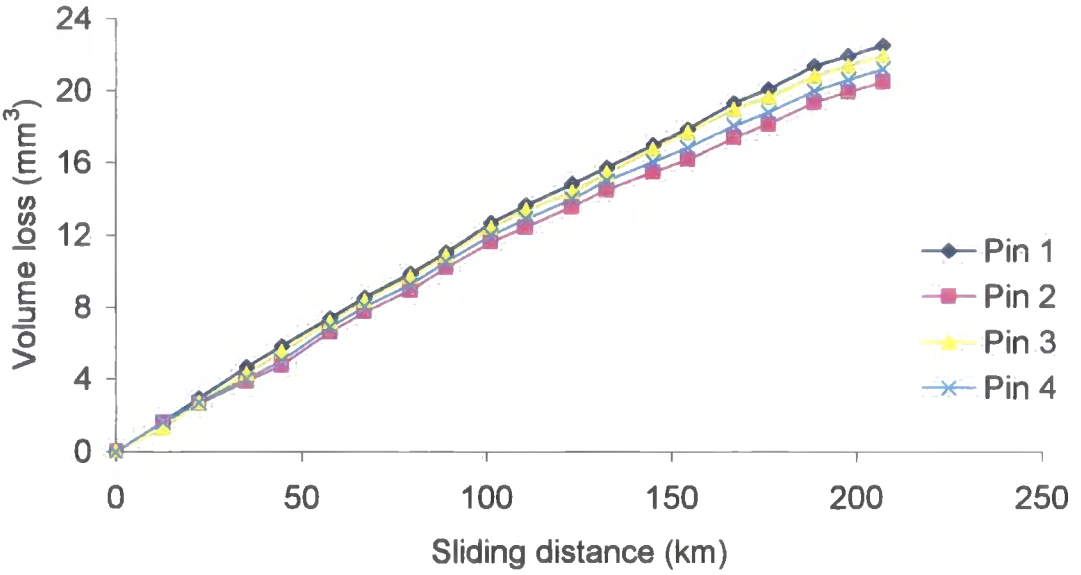

Figure 5.16. Wear of unmodified UHMWPE pins against unmodified Ti6Al4V plates

5.1.4.2 N^+ ion implanted UHMWPE against unmodified Ti6Al4V

A graph of 1 x 10^{15} and 5 x 10^{15} N^+ ion/cm^2 implanted UHMWPE pin volume loss against sliding distance when tested against unmodified Ti6Al4V is shown in figure 5.17. Modified UHMWPE mean wear factors of 2.44 ± 0.02 and 2.55 ± 0.04 x 10^{-6} mm^3/Nm were calculated respectively for 5 x 10^{15} and 1 x 10^{15} N^+ ion/cm^2 implanted UHMWPE samples over a sliding distance of 204 km (> 5.5 million sliding wear cycles). Initial mean wear factors of 2.56 ± 0.01 and 2.82 ± 0.05 x 10^{-6} mm^3/Nm were calculated for 5 x 10^{15} and 1 x 10^{15} N^+ ion/cm^2 implanted UHMWPE samples respectively up to a sliding distance of 95 km.

During the wear test, the implanted layer on the polymer pin surface was observed to wear away after only a few sliding wear cycles (≈ 10 km of sliding). As a result, the wear rates of the pins would be expected to continue steadily at the same rate as those with no surface modification. This was seen when steady-state mean wear factors of 2.26 ± 0.01 and 2.23 ± 0.03 x 10^{-6} mm^3/Nm were calculated respectively for 5 x 10^{15} and 1 x 10^{15} N^+ ion/cm^2 implanted UHMWPE between a sliding distance of 95-204 km. These values correspond closely with the steady-state mean k_o of unmodified

UHMWPE articulated against unmodified Ti6Al4V (section 5.1.4.1), which provides an indication of test repeatability and reproducibility.

Figure 5.18 shows the results of 5 x 10^{15} N^+ ion/cm^2 implanted UHMWPE articulated against unmodified Ti6Al4V. A mean k_o of 2.42 ± 0.07 x 10^{-6} mm^3/Nm was calculated for the modified UHMWPE over a sliding distance of 205 km (> 5.5 million wear cycles).

Surface damage was observed in the wear tracks of the unmodified Ti6Al4V counterface plates after a low number of wear cycles and increased with test duration. The damage was characterised by random deep scratches and grooves in the wear tracks of the plates and high R_a values, indicative of abrasive wear. Machining and microtoming marks as well as brown colouration due to N^+ ion implantation on the surfaces of the UHMWPE pins wore away, and the surfaces became smooth. The bovine serum lubricant discoloured to black with test duration and was found to contain dark particulate debris. The wear curves on the graph were linear, and no transfer films were observed on the plates during and post wear test.

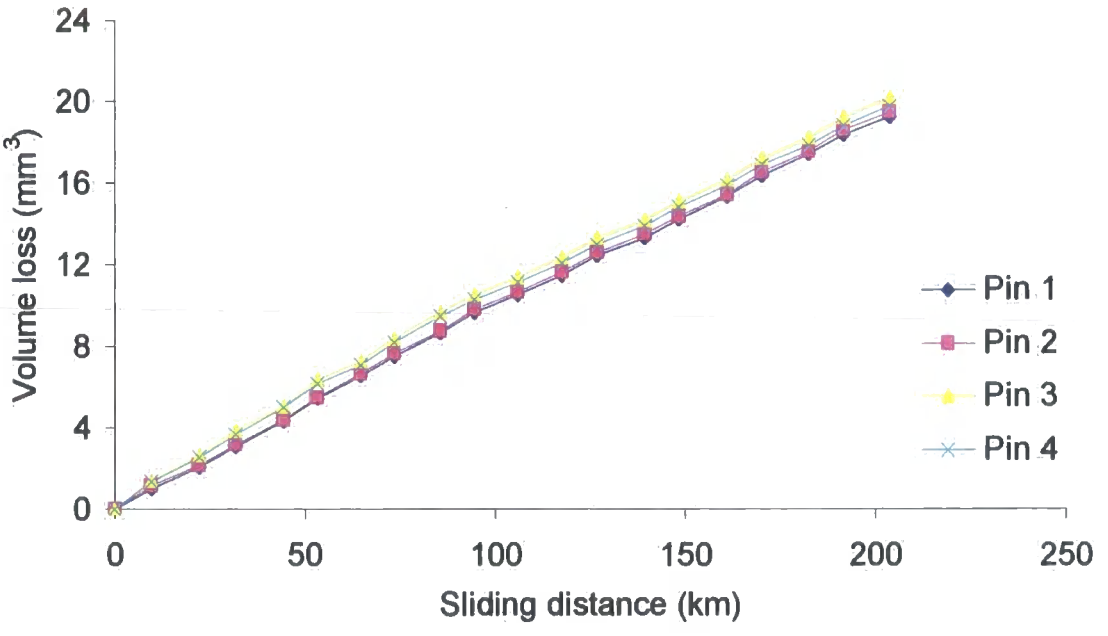

Figure 5.17. Wear of 1 x 10^{15} and 5 x 10^{15} N^+ ion/cm^2 implanted UHMWPE pins against unmodified Ti6Al4V plates. Where pins 1 and 2 are 5 x 10^{15} N^+ ion/cm^2 implanted UHMWPE samples, and pins 3 and 4 are 1 x 10^{15} N^+ ion/cm^2 implanted UHMWPE samples.

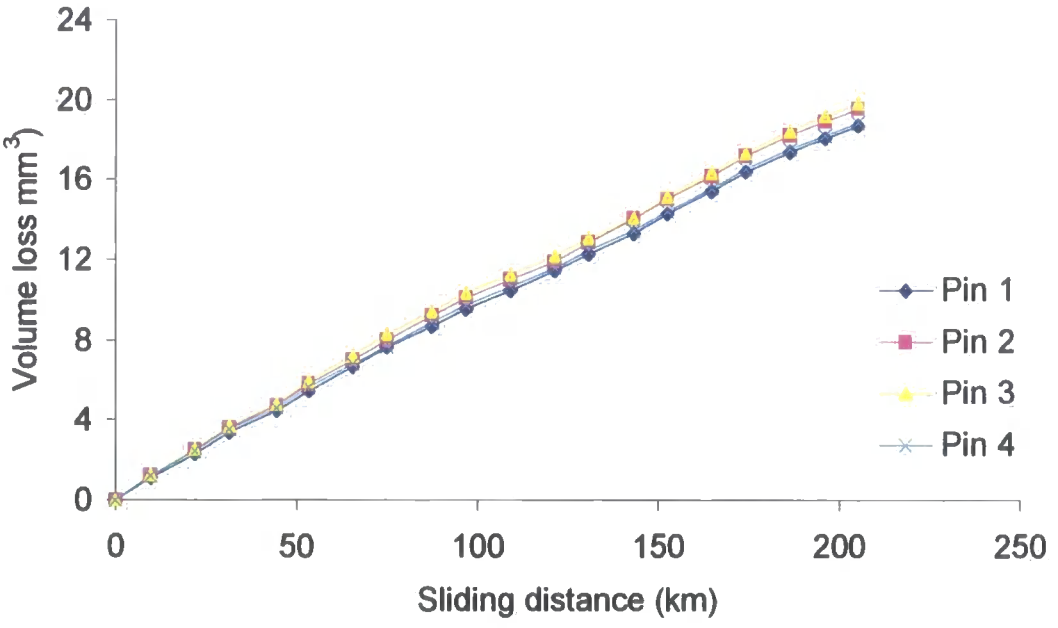

Figure 5.18. Wear of 5 x 10^{15} N^+ ion/cm^2 implanted UHMWPE pins against unmodified Ti6Al4V plates

5.1.4.3 Unmodified UHMWPE against N^+ ion implanted Ti6Al4V

The wear results of unmodified UHMWPE against N^+ ion implanted Ti6Al4V plates with 3 different implantation doses are reported in this section. Figures 5.19 and 5.20 show the wear graphs of unmodified UHMWPE pins sliding and rotating respectively against 2 x 10^{17} N^+ ions/cm^2 implanted Ti6Al4V; and 1 x 10^{18} and 1 x 10^{21} N^+ ions/cm^2 implanted Ti6Al4V plates.

For unmodified UHMWPE against 2 x 10^{17} N^+ ions/cm^2 implanted Ti6Al4V (fig. 19), an UHMWPE mean wear factor of 1.65 ± 0.05 x 10^{-6} mm^3/Nm was calculated over a test duration of 197 km (> 5 million sliding wear cycles). An initial slightly higher mean k_o of 1.86 ± 0.08 x 10^{-6} mm^3/Nm was measured up to a sliding distance of 63 km, due to a wearing in type process, and a steady-state mean wear factor of 1.50 ± 0.02 x 10^{-6} mm^3/Nm was measured between 63-197 km sliding distance. Compared with the unmodified Ti6Al4V plates articulated against unmodified UHMWPE pins (section 5.1.4.1), little damage was observed in the wear tracks of the 2 x 10^{17} N^+ ions/cm^2 Ti6Al4V plates during the test. Examinations of the wear tracks under AFM and NCI post wear revealed less distinctive wear tracks on the plates, and measured R_a values

(table 5.2) were about that of the pre wear plates. No dark colourations and black particulate debris were observed in the bovine serum lubricant for the duration of the test. The wear curves were linear and no transfer films were observed on the plates. As in the test with unmodified UHMWPE against unmodified Ti6Al4V plates, the unmodified UHMWPE worn pin surface morphology in this test resembled those of *ex-vivo* components.

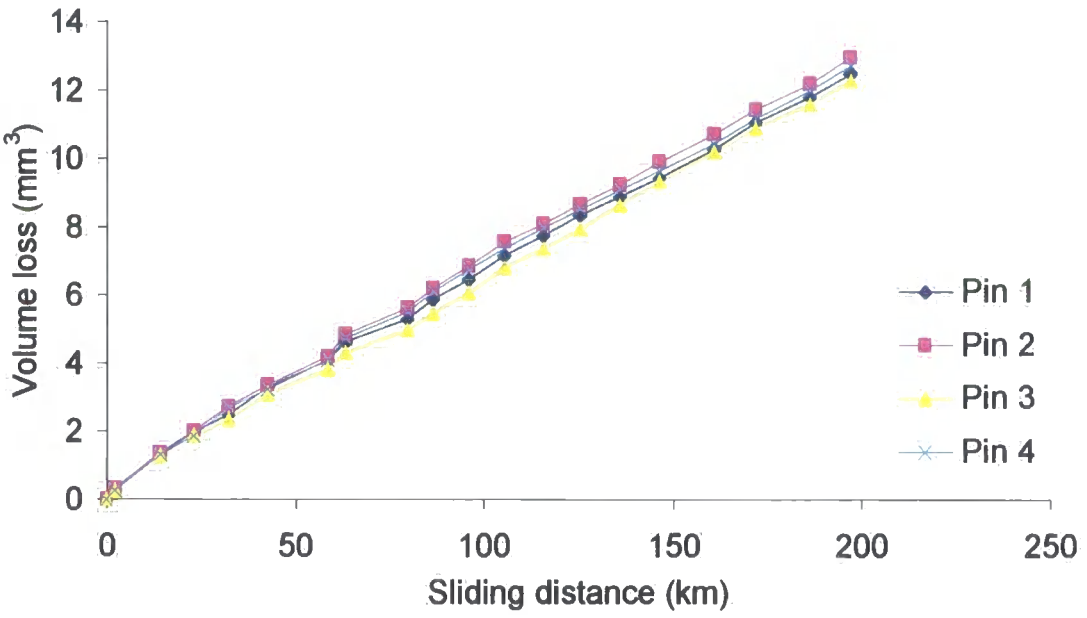

Figure 5.19. Wear of unmodified UHMWPE pins against 2 x 10^{17} N^+ ions/cm^2 implanted Ti6Al4V plates

Figure 5.20 shows the graph of unmodified UHMWPE wear volume loss against sliding distance, articulated against N^+ ion implanted Ti6Al4V plates implanted with two different implantation doses. Plates 1 and 2 were implanted with 1 x 10^{21} N^+ ions/cm^2, and plates 3 and 4 with 1 x 10^{18} N^+ ions/cm^2. Over the duration of the test, up to a sliding distance of 181 km (> 5 million sliding wear cycles), mean unmodified UHMWPE wear factors of 1.79 ± 0.03 and 2.08 ± 0.05 x 10^{-6} mm^3/Nm were calculated respectively when articulated against 1 x 10^{18} and 1 x 10^{21} N^+ ions/cm^2. The mean k_o of unmodified UHMWPE increased with N^+ ion implantation dose of the counterface Ti6Al4V plate, significantly so against 1 x 10^{21} N^+ ions/cm^2 implanted Ti6Al4V plates compared with unmodified UHMWPE against 2 x 10^{17} N^+ ions/cm^2 and 1 x 10^{18} N^+ ions/cm^2 implanted Ti6Al4V plates. Two distinct wear phases could clearly be seen on the graph for the polymer pins (fig.5.20). During the initial wear phase up to a sliding

distance of 58 km, similar mean UHMWPE wear factors of 2.47 ± 0.04 and 2.46 ± 0.06 x 10^{-6} mm^3/Nm were calculated respectively against 1 x 10^{18} and 1 x 10^{21} N^+ ions/cm^2, an indication of similar polymer wear mechanisms occurring. These values were higher than the mean values calculated over the duration of the test due to a wearing in type phenomenon. After this period, the polymer pin wear mechanisms changed to give the steady-state wear phases. Mean k_o of 1.35 ± 0.01 and 1.90 ± 0.01 x 10^{-6} mm^3/Nm were calculated respectively against the two different implantation doses for this wear phase (between 58-181 km sliding distance).

AFM examination of the worn samples revealed the wear tracks of the modified plates post testing, and compared with the surfaces of unmodified plates articulated against unmodified UHMWPE (section 5.1.4.1), the surface damage was minimal. However, the standard roughness values on the surface of the modified materials post wear increased with increasing implantation dose.

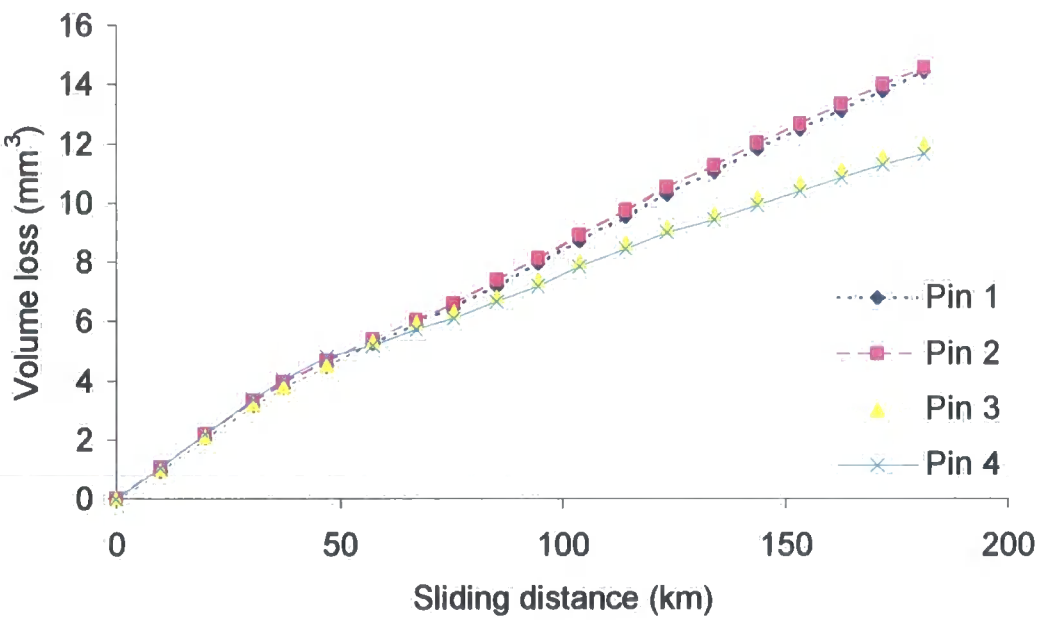

Figure 5.20. Wear of unmodified UHMWPE pins against 1 x 10^{21} and 1 x 10^{18} N^+ ions/cm^2 implanted Ti6Al4V plates. Where pins 1 and 2 are articulated against 1 x 10^{21} N^+ ion/cm^2 implanted Ti6Al4V plates, and pins 3 and 4 articulated against 1 x 10^{18} N^+ ion/cm^2 implanted Ti6Al4V plates.

5.1.4.4 N^+ ion implanted UHMWPE against N^+ ion implanted Ti6Al4V

5 x 10^{15} N^+ ions/cm^2 implanted UHMWPE wear pins were tested against 2 x 10^{17} N^+ ions/cm^2 implanted Ti6Al4V plates, and the graph of the wear volume loss of the modified UHMWPE against sliding distance is shown in figure 5.21.

A mean modified UHMWPE k_o of 1.27 ± 0.05 x 10^{-6} mm^3/Nm was calculated over the whole duration of the test, up to 193 km (> 5 million sliding wear cycles). There was a significant reduction in the wear of the modified UHMWPE compared to that of the unmodified UHMWPE articulated against unmodified Ti6Al4V (section 5.1.4.1). There was an initial mean k_o of 1.46 ± 0.01 x 10^{-6} mm^3/Nm up to a sliding distance of 66 km, and a mean steady-state k_o of 1.13 ± 0.09 x 10^{-6} mm^3/Nm was calculated between 66-193 km sliding distance.

Compared with modified and unmodified Ti6Al4V plates articulated against unmodified UHMWPE, few scratches were observed post wear on the 2 x 10^{17} N^+ ions/cm^2 Ti6Al4V plates (in the region of pin contact on the plate). Examination of the wear tracks under AFM and NCI revealed no distinctive wear tracks and the implanted UHMWPE worn pin surface morphology was observed again to resemble those of *ex-vivo* components. Measured mean surface R_a values on the plates (table 5.2) post wear, were found to be about the same as those pre wear test, and no dark colourations and black debris were observed in the bovine serum test lubricant for the duration of the test.

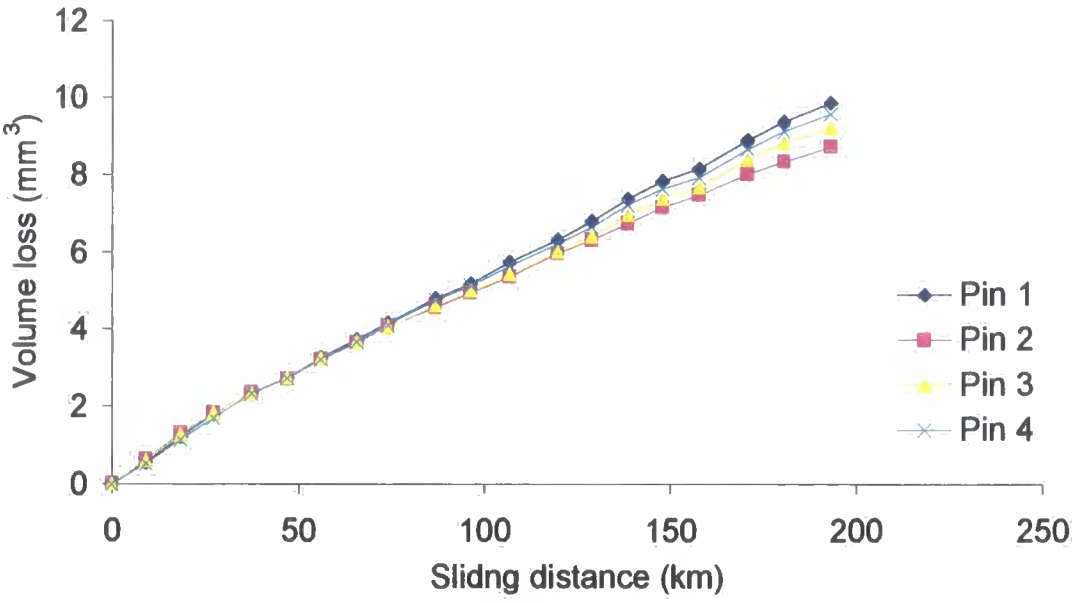

Figure 5.21. Wear of 5 x 10^{15} N^+ ions/cm^2 implanted UHMWPE pins against 2 x 10^{17} N^+ ions/cm^2 implanted Ti6Al4V plates

5.1.4.5 XLPE against Ti6Al4V

The wear of XLPE wear pins against unmodified Ti6Al4V plates was very high, and an initial mean k_o of 4.79 $\pm$ 0.01 x 10^{-6} mm^3/Nm was calculated after only a sliding distance of 58 km (1.6 million sliding wear cycles). As a result of the high initial wear rate of the XLPE samples, the test was stopped.

A wear test of unmodified and 5 x 10^{15} N^+ ions/cm^2 implanted XLPE (two wear pins of each material) against 2 x 10^{17} N^+ ions/cm^2 implanted Ti6Al4V was performed, and the results of the graph of the wear volume loss against sliding distance is shown in figure 5.22. The graph shows a difference in wear rates between the unmodified and modified XLPE wear pins. Mean k_o of 1.05 $\pm$ 0.02 x 10^{-6} mm^3/Nm was calculated for the implanted XLPE compared with 1.24 $\pm$ 0.02 x 10^{-6} mm^3/Nm for the unmodified XLPE wear pins over the whole duration of the test, up to 187 km (> 5 million sliding wear cycles). No surface damages and polymer transfer films were observed on the plates post wear by surface analysis and the bovine serum test lubricant showed no dark colouration with test duration. The mean wear factors calculated were of similar magnitude to that calculated for modified UHMWPE against modified Ti6Al4V.

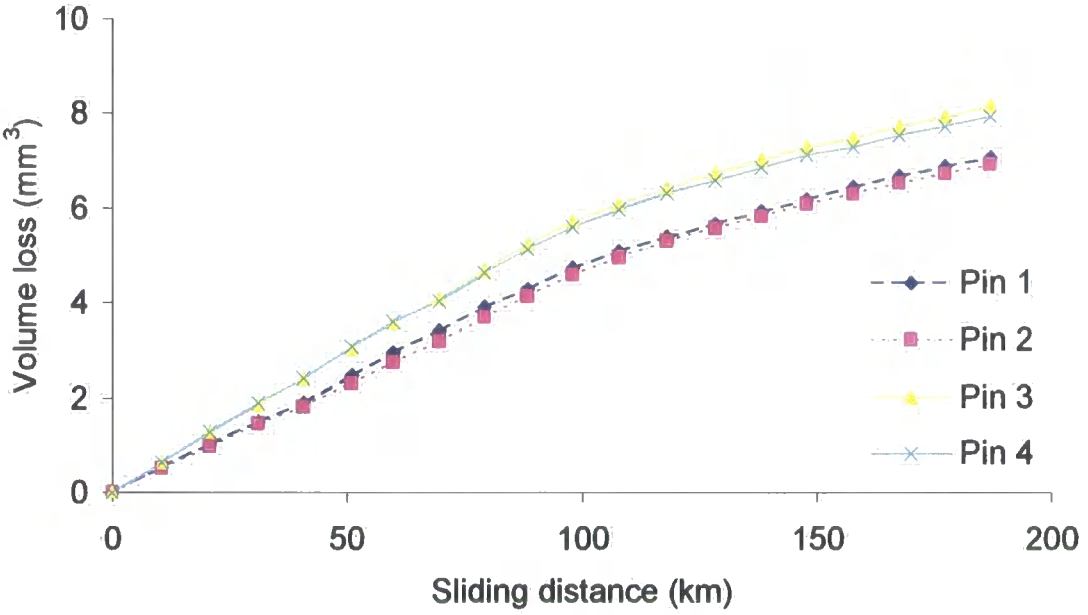

Figure 5.22. Wear of 5 x 10^{15} N^+ ions/cm^2 implanted and unmodified XLPE pins against 2 x 10^{17} N^+ ions/cm^2 implanted Ti6Al4V plates. Where pins 1 and 2 are 5 x 10^{15} N^+ ions/cm^2 implanted XLPE samples, and pins 3 and 4 are unmodified XLPE samples

5.1.4.7 Summary of Results

The tribological wear test results, and the mean R_a values of all the materials tested pre and post wear are summarised and presented respectively in tables 5.1 and 5.2. Table 5.3 summarises the measured changes in hardness for the Ti6Al4V, UHMWPE and XLPE substrates.

Figure 5.23 summarises the results of the mean wear curves of UHMWPE pins (modified and unmodified) articulated against Ti6Al4V plates (modified and unmodified).

Table 5.1. Summary of *in vitro* tribological performance of unmodified and N^+ ion implantation modified polymer/Ti6Al4V biomaterial wear couples after 5.5 million cycles wear testing

Wear Couple[a]	Mean Polymer Pin k_o (x 10^{-6} mm^3/Nm)	Mean Ti6Al4V Plate Wt Loss (μg)[b]
Unmodified UHMWPE/unmodified Ti6Al4V	2.77 ± 0.16	214 ± 0.08
(a) 5 x 10^{15} N^+ ions/cm^2 implanted UHMWPE/Unmodified Ti6Al4V	2.44 ± 0.02	200 ± 0.06
(b) 1 x 10^{15} N^+ ions/cm^2 implanted UHMWPE/Unmodified Ti6Al4V	2.55 ± 0.04	206 ± 0.04
5 x 10^{15} N^+ ions/cm^2 implanted UHMWPE/Unmodified Ti6Al4V	2.42 ± 0.07	198 ± 0.08
Unmodified UHMWPE/2 x 10^{17} ions/cm^2 implanted Ti6Al4V	1.65 ± 0.05	81 ± 0.06
(a) Unmodified UHMWPE/1 x 10^{18} N^+ ions cm^{-2} implanted Ti6Al4V	1.79 ± 0.03	99 ± 0.02
(b) Unmodified UHMWPE/1 x 10^{21} N^+ ions/cm^2 implanted Ti6Al4V	2.08 ± 0.05	126 ± 0.04
5 x 10^{15} N^+ ions/cm^2 implanted UHMWPE/2 x 10^{17} N^+ ions/cm^2 implanted Ti6Al4V	1.27 ± 0.05	79 ± 0.04
Unmodified XLPE/unmodified Ti6Al4V[c]	4.79 ± 0.01	210 ± 0.06
(a) 5 x 10^{15} N^+ ions/cm^2 implanted XLPE/2 x 10^{17} N^+ ions/cm^2 implanted Ti6Al4V	1.05 ± 0.02	104 ± 0.03
(b) Unmodified XLPE/2 x 10^{17} N^+ ions/cm^2 implanted Ti6Al4V	1.24 ± 0.02	128 ± 0.10

[a]Samples implanted with N^+ ions at 90 keV (Ti6Al4V), and 80 keV (polymer)

[b]Plate measured before and at the end of test

[c]Test stopped after 1.6 million cycles

Table 5.2. Mean arithmetic mean surface roughness (R_a) of Ti6Al4V, UHMWPE and XLPE samples measured by non-contacting optical interferometry

Sample Surface	Mean R_a (μm)	
	Pre Wear	Post Wear
Unmodified Ti6Al4V (articulated against modified and unmodified UHMWPE)	0.011 ± 0.002	0.082 ± 0.006
2 x 10^{17} N^+ ions/cm^2 implanted Ti6Al4V (articulated against modified and unmodified UHMWPE)	0.012 ± 0.002	0.016 ± 0.006
1 x 10^{18} N^+ ions/cm^2 implanted Ti6Al4V (articulated against unmodified UHMWPE)	0.032 ± 0.004	0.040 ± 0.002
1 x 10^{21} N^+ ions/cm^2 implanted Ti6Al4V (articulated against unmodified UHMWPE)	0.049 ± 0.006	0.058 ± 0.004
Unmodified UHMWPE (articulated against unmodified and modified Ti6Al4V)	1.2 ± 0.12	0.05 ± 0.02
1 x 10^{15} N^+ ions/cm^2 implanted UHMWPE (articulated against unmodified Ti6Al4V)	1.2 ± 0.13	0.06 ± 0.02
5 x 10^{15} N^+ ions/cm^2 implanted UHMWPE (articulated against unmodified and modified Ti6Al4V)	1.3 ± 0.15	0.05 ± 0.04
XLPE (articulated against unmodified and modified Ti6Al4V)	1.4 ± 0.14	0.06 ± 0.02
5 x 10^{15} N^+ ions/cm^2 implanted XLPE (articulated against modified Ti6Al4V)	1.4 ± 0.12	0.07 ± 0.03

Table 5.3. Summary of Knoop microhardness of unmodified and N^+ ion implantation modified Ti6Al4V, UHMWPE and XLPE substrates

Substrate[a]	Knoop Microhardness (KHN_{1gf})
Unmodified Ti6Al4V	347 ± 20
2 x 10^{17} N^+ ions/cm^2 implanted Ti6Al4V	730 ± 32
1 x 10^{18} N^+ ions/cm^2 implanted Ti6Al4V	1064 ± 119
1 x 10^{21} N^+ ions/cm^2 implanted Ti6Al4V	1413 ± 183
Unmodified UHMWPE	3.4 ± 0.5
1 x 10^{15} N^+ ions/cm^2 implanted UHMWPE	8.6 ± 0.7
5 x 10^{15} N^+ ions/cm^2 implanted UHMWPE	12.8 ± 1.6
Unmodified XLPE	6.1 ± 0.8
5 x 10^{15} N^+ ions/cm^2 implanted XLPE	14.5 ± 1.1

[a]Substrates implanted with N^+ ions at 90 keV (Ti6Al4V), and 80 keV (polymer)

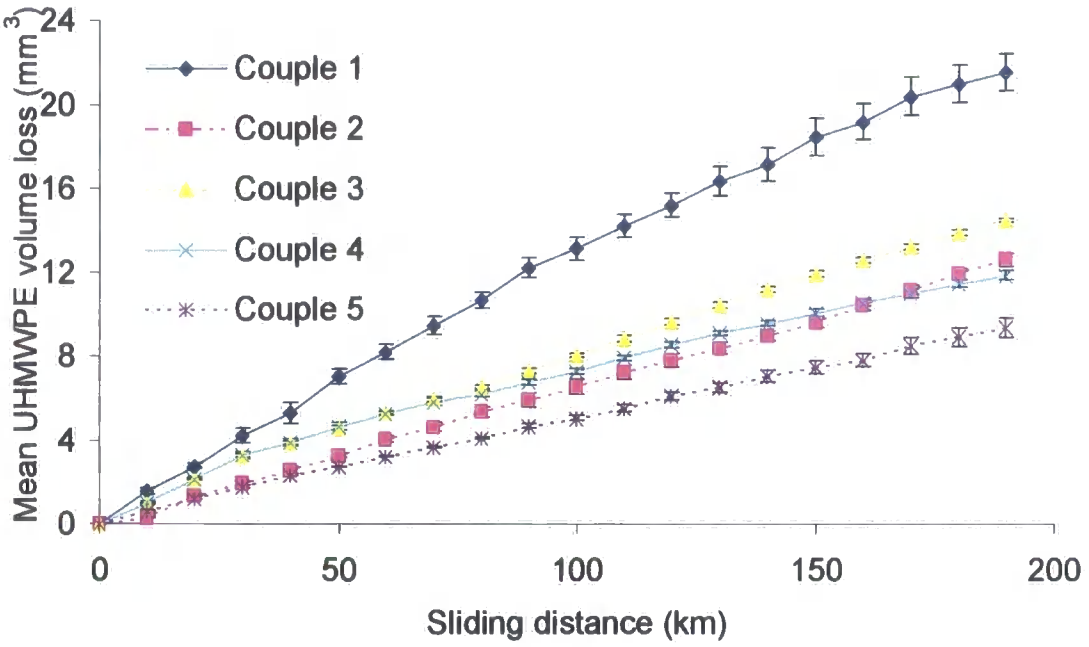

Figure 5.23. Mean wear behaviour of UHMWPE pins (modified and unmodified) against Ti6Al4V plates (modified and unmodified). Where couple 1 is unmodified UHMWPE/unmodified Ti6Al4V; couple 2 is Unmodified UHMWPE/2 x 10^{17} N^+ ions/cm^2 implanted Ti6Al4V; couple 3 is Unmodified UHMWPE/1 x 10^{21} N^+ ions/cm^2 implanted Ti6Al4V; couple 4 is Unmodified UHMWPE/1 x 10^{18} N^+ ions/cm^2 implanted Ti6Al4V; and couple 5 is 5 x 10^{15} N^+ ions/cm^2 implanted UHMWPE/2 x 10^{17} N^+ ions/cm^2 implanted Ti6Al4V wear couple (table 5.1).

5.1.5 Surface Topography

AFM images of non-implanted and N^+ ion implanted Ti6Al4V and UHMWPE surfaces, pre and post wear test are shown in figures 5.24 to 5.38.

A 100 x 100 μm top view AFM image of the surface topography, and surface analysis results of a line profile across the sample surface showing typical standard surface roughness data and section profile of the unmodified polished Ti6Al4V is shown in figure 5.24. The roughness data was produced from a single AFM traverse across the sample surface, where R_a is the roughness average, R_p is the maximum height of the profile above the mean line, R_t is maximum peak to valley height, and R_{pm} and R_{tm} are

mean values representative of the entire profile. The surfaces were characterised by scratch marks from polishing.

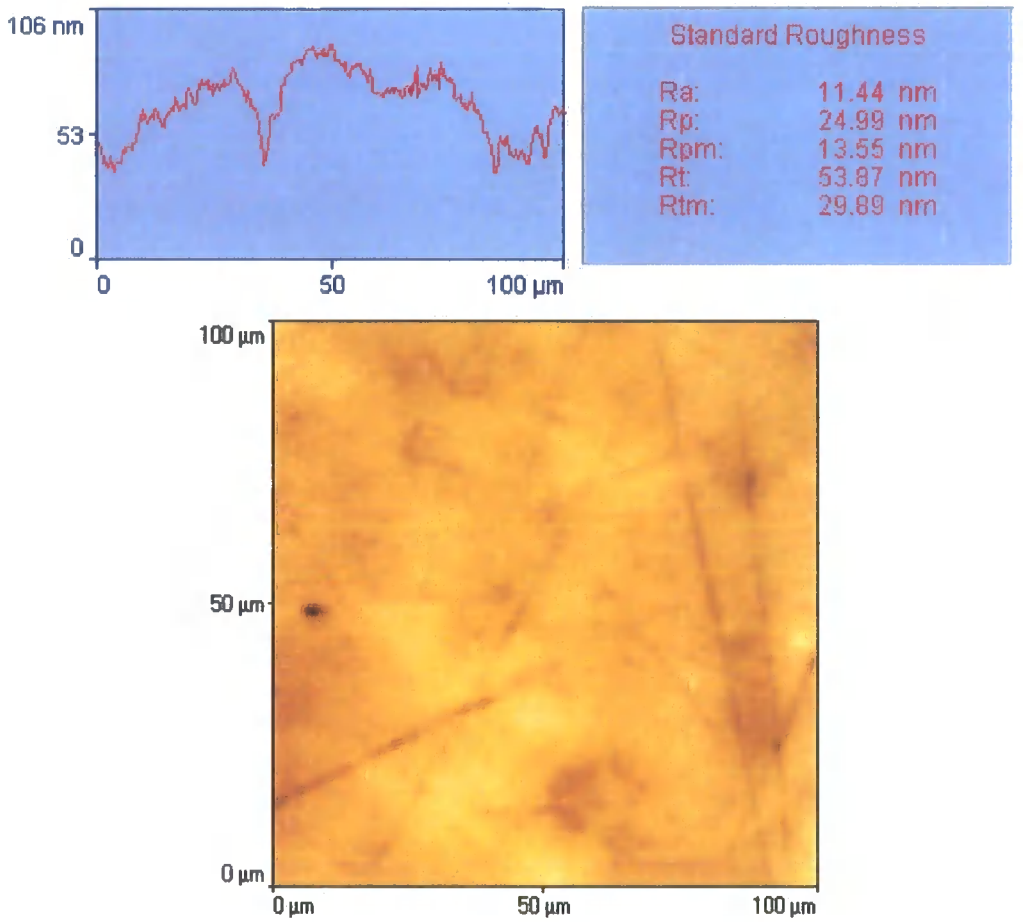

Figure 5.24. Top view AFM image and topographic data of polished Ti6Al4V

Upon N^+ ion implantation, changes in the surface topography were observed with the AFM only under high magnification. Figure 5.25 shows a series of 10 μm^2 top view AFM images of (a) unmodified (b) 2 x 10^{17} N^+ ions/cm^2 (c) 1 x 10^{18} N^+ ions/cm^2 (d) 1 x 10^{21} N^+ ions/cm^2 implanted Ti6Al4V samples. Line analysis of the surfaces on these images, produced topographic data showing an increase in surface roughness with ion implantation dose (fig. 5.26). Figure 5.27 to 5.29 shows higher magnification 3-D projection 2.2 μm^2 images of the modified surfaces, suggesting some form of surface degradation (sputtering and blister formation) on the surfaces, increasing with the implantation dose.

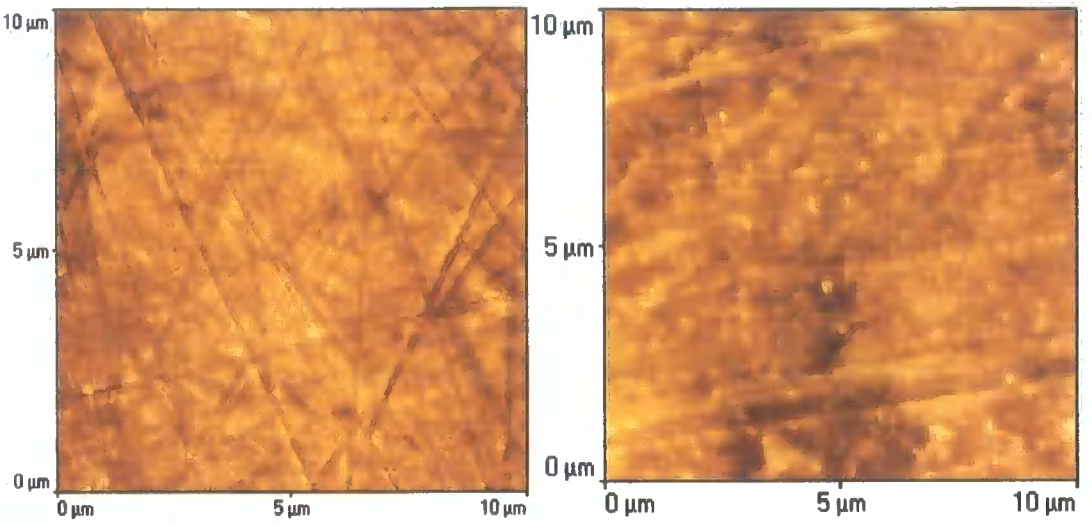

(a) Unmodified *(b)* 2x10^{17} N^+ ions/cm^2 implanted

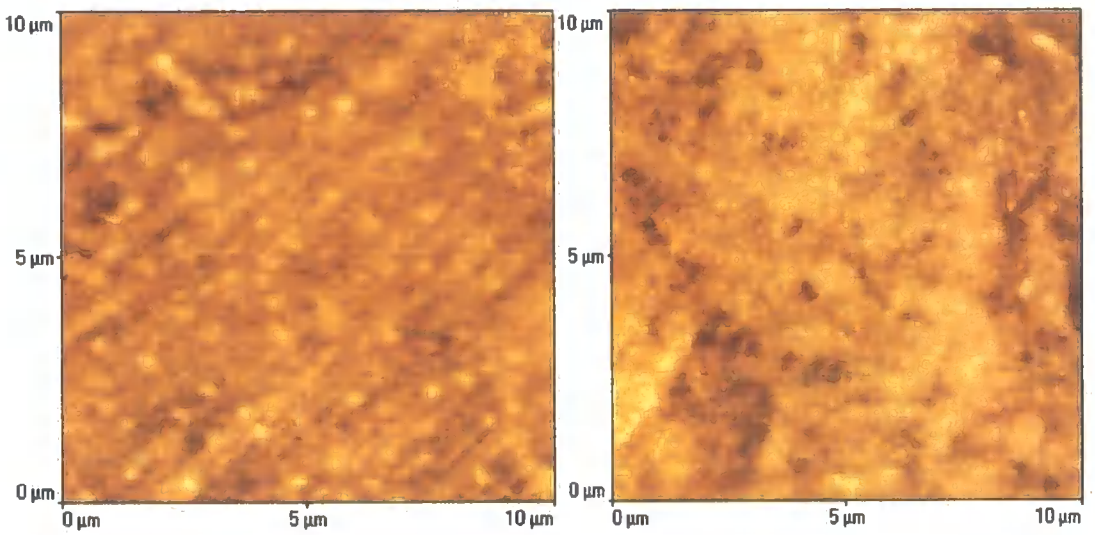

(c) 1x10^{18} N^+ ions/cm^2 implanted *(d)* 1 x 10^{21} N^+ ions/cm^2 implanted

Figure 5.25. Top view AFM images of unmodified and modified *(a)* unmodified, *(b)* 2 x 10^{17} N^+ ions/cm^2 implanted, *(c)* 1 x 10^{18} N^+ ions/cm^2 implanted, and *(d)* 1 x10^{21} N^+ ions/cm^2 implanted Ti6Al4V

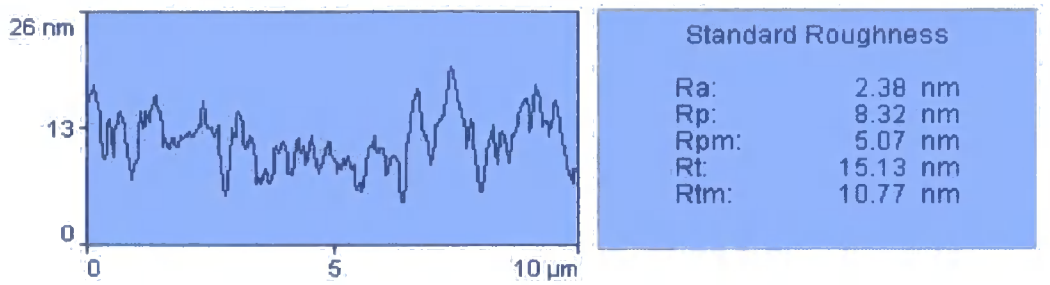

(a) Unmodified

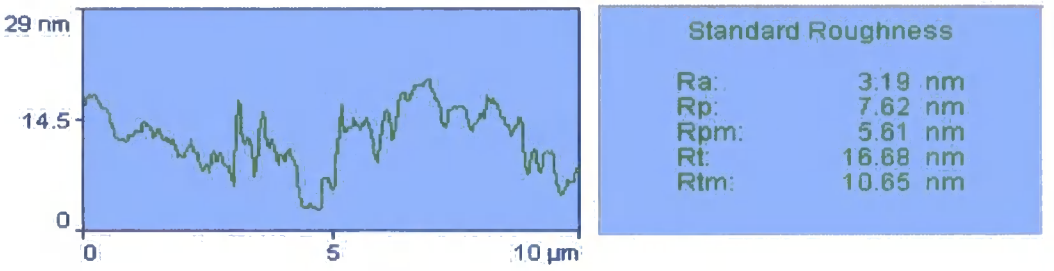

(b) 2 x 10^{17} N^+ ions/cm^2 implanted

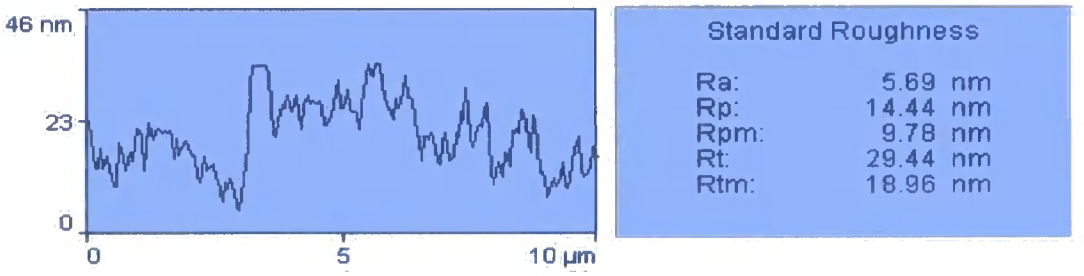

(c) 1 x 10^{18} N^+ ions/cm^2 implanted

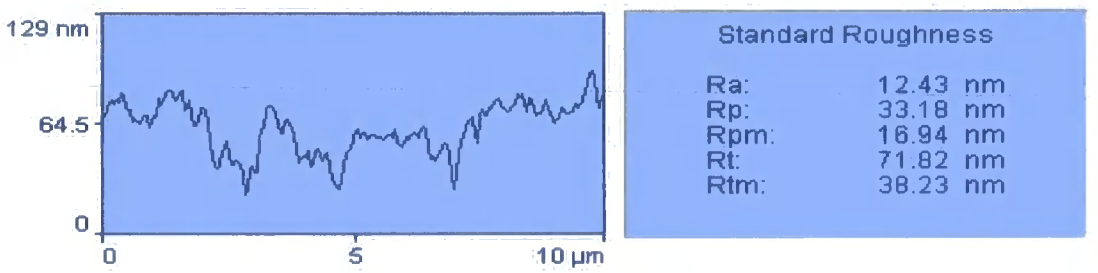

(d) 1 x10^{21} N^+ ions/cm^2 implanted

Figure 5.26. AFM line analysis profiles and topographic data of the 10 μm^2 top view AFM images of unmodified and modified Ti6Al4V

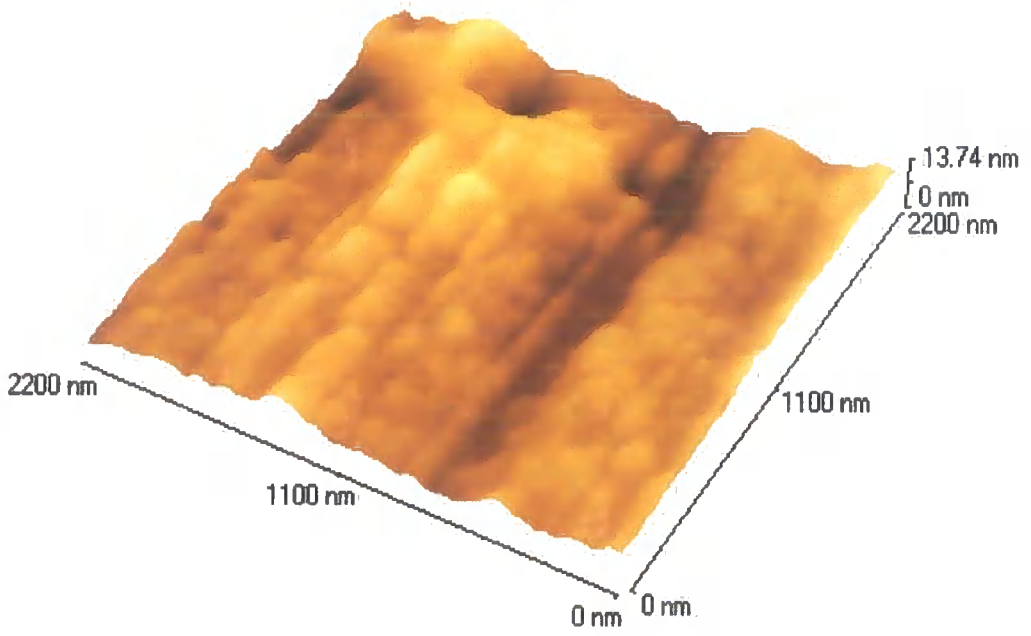

Figure 5.27. High magnification 3-D AFM projection image of 2 x 10^{17} N^+ ions/cm^2 implanted Ti6Al4V

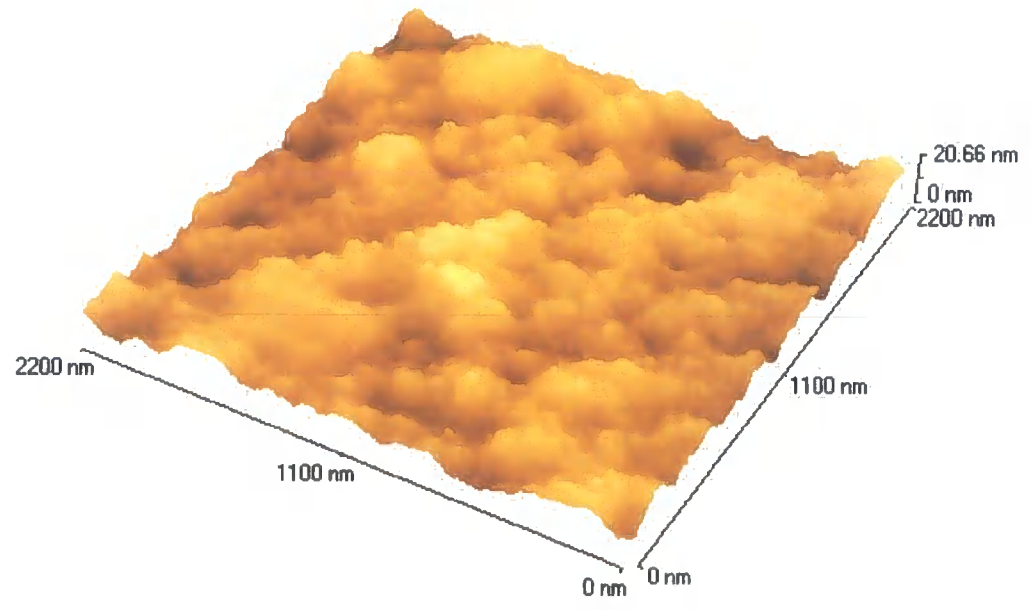

Figure 5.28. High magnification 3-D AFM projection image of 1 x 10^{18} N^+ ions/cm^2 implanted Ti6Al4V

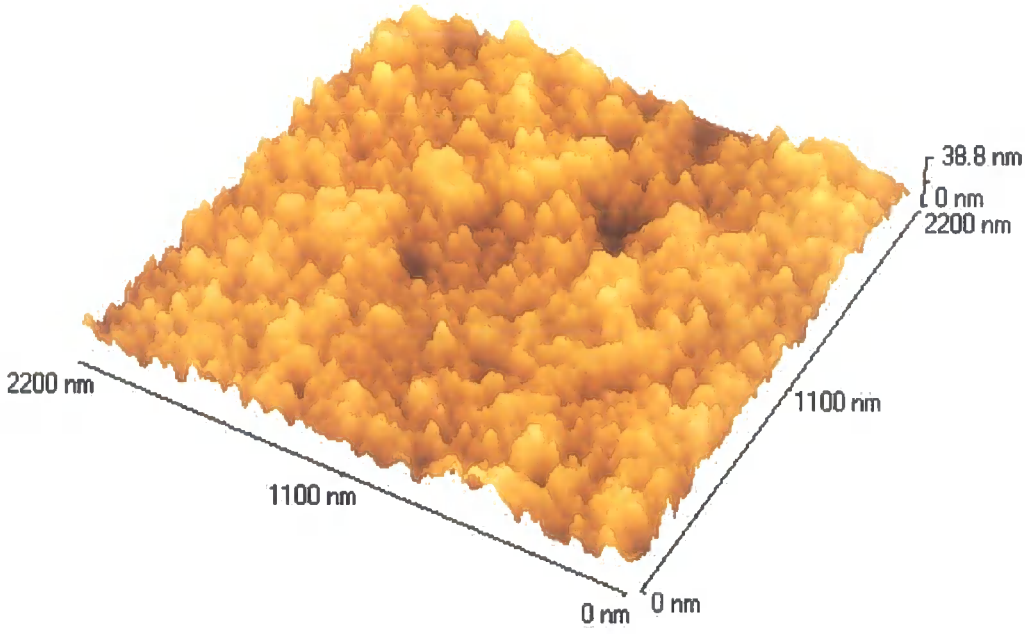

Figure 5.29. High magnification 3-D AFM projection image of 1 x 10^{21} N^+ ions/cm^2 implanted Ti6Al4V

AFM examination of the worn surface of unmodified Ti6Al4V plates post wear test against unmodified UHMWPE, revealed distinctive wear tracks characterised by severe scratches and higher standard roughness values. Figure 5.30 is typical of the surface topography of worn unmodified Ti6Al4V post wear. In contrast, the topography of the implanted plates showed less extensive damage in the region of pin contact on the plates and lower standard roughness values post wear, compared with the unmodified plates (figures 5.31-5.33). Further, AFM surface analysis of the worn modified plates showed that the standard roughness values of the plates increased with implantation dose (fig. 5.34).

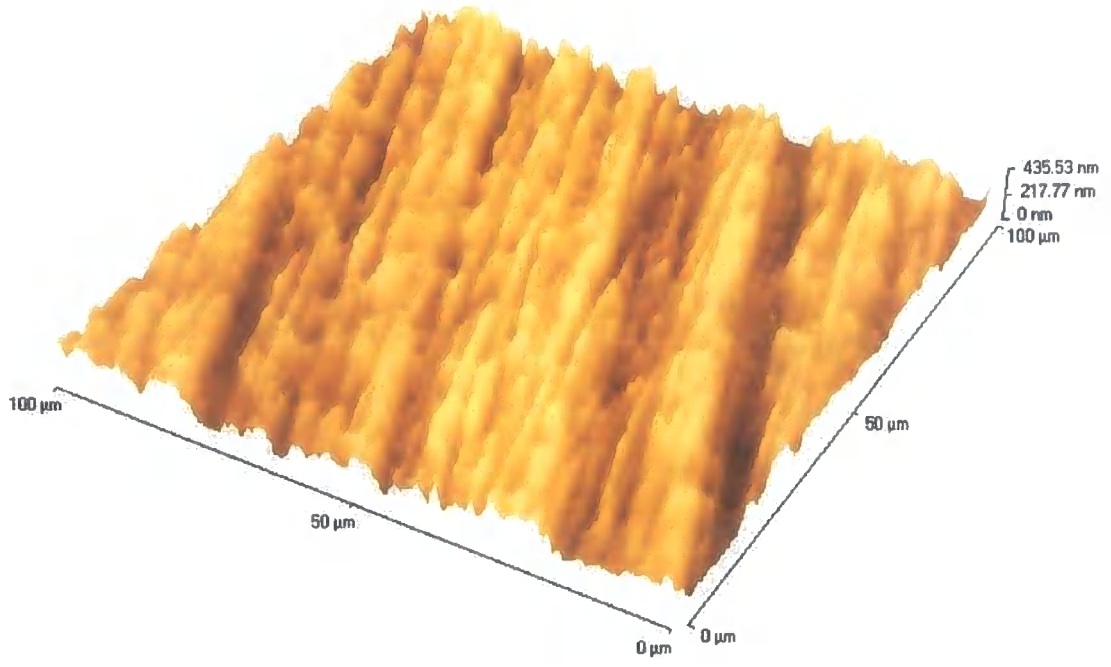

Figure 5.30. Unmodified Ti6Al4V alloy topography post *in vitro* wear testing (AFM) showing extensive surface damage in the wear track zone

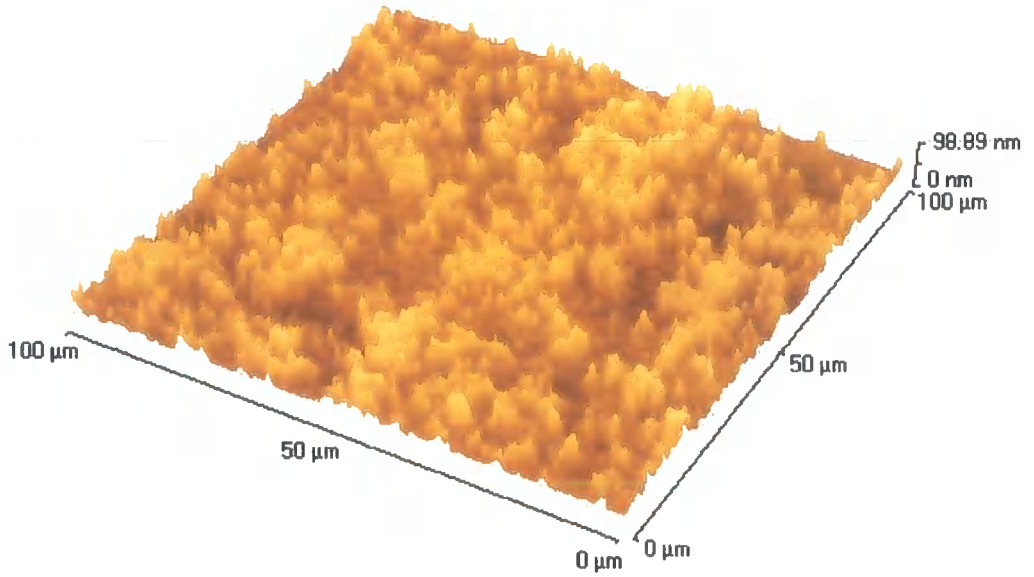

Figure 5.31. 2 x 10^{17} N^+ ions/cm^2 implanted Ti6Al4V topography (AFM) post *in vitro* wear testing (region of pin contact on plate)

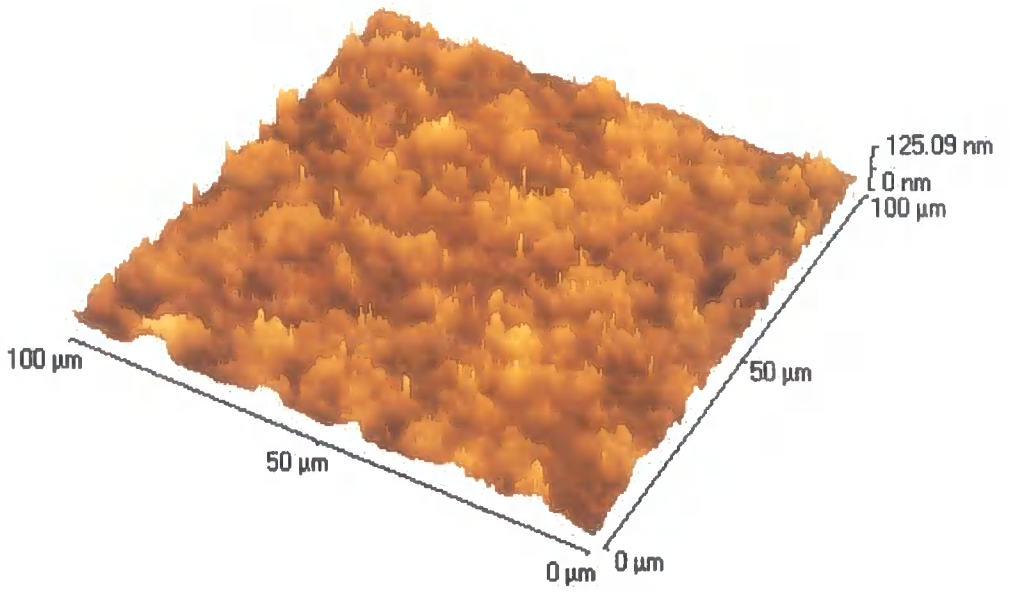

Figure 5.32. 1 x 10^{18} N^+ ions/cm^2 implanted Ti6Al4V topography (AFM) post *in vitro* wear testing (region of pin contact on plate)

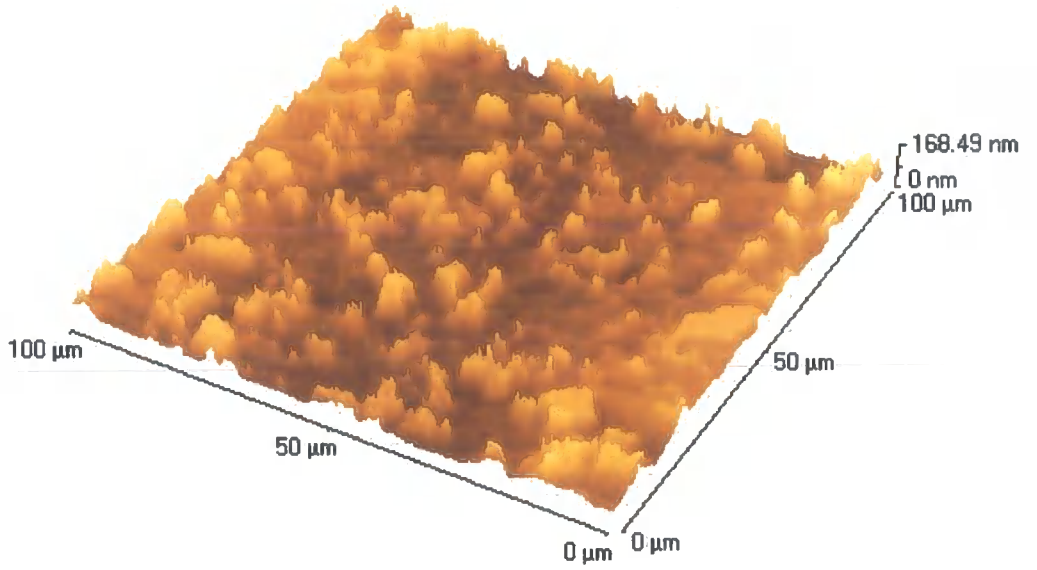

Figure 5.33. 1 x 10^{21} N^+ ions/cm^2 implanted Ti6Al4V topography (AFM) post *in vitro* wear testing (region of pin contact on plate)

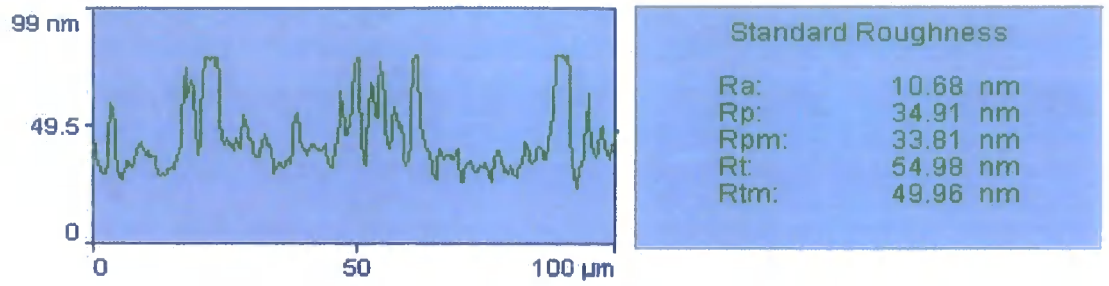

(a) 2 x 10^{17} N^+ ions/cm^2 implanted

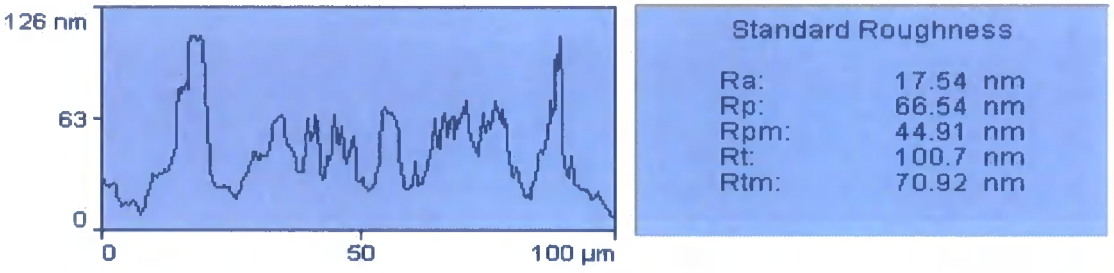

(b) 1 x 10^{18} N^+ ions/cm^2 implanted

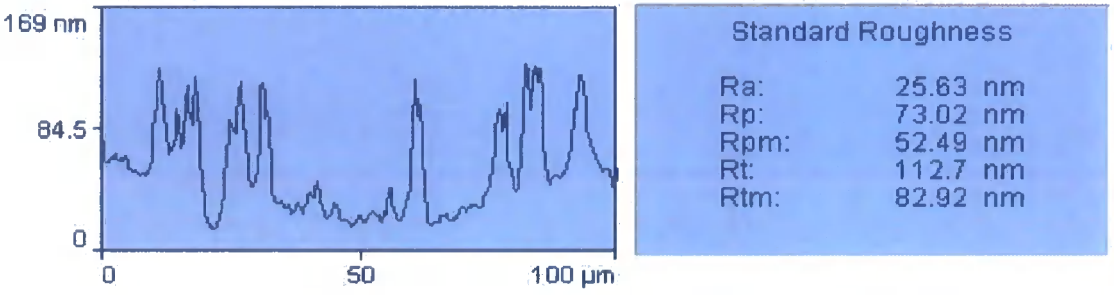

(c) 1 x10^{21} N^+ ions/cm^2 implanted

Figure 5.34. AFM line analysis profiles and topographic data taken from the AFM images (figs. 5.31 – 5.33)

It was seen by visual observation that the surface colour following ion implantation of the UHMWPE wear pins had changed from white to dark brown. Low magnification AFM examination of both modified and unmodified UHMWPE surfaces showed similar topographic features, characterised by machining and microtoming marks. Figure 5.35 is typical, showing top view 100 μm^2 AFM images of unmodified and 5 x 10^{15} N^+ ions/cm^2 implanted UHMWPE pre wear test. However, high magnification AFM examination of the modified UHMWPE surface (fig. 5.36) showed topographic modification (some form of surface degradation).

The surface topography of all the UHMWPE worn pins (modified or unmodified) post wear test against Ti6Al4V (modified or unmodified), showed similar surface morphology, which depended upon the surface area from which the analysis was carried out. AFM analysis from random surface areas on the worn UHMWPE surfaces revealed a distinctive surface morphology (fig. 5.37). The observed surface wear features post *in vitro* wear testing in this study (fig. 5.38 a) is typical of worn *ex vivo* UHMWPE components (fig. 5.38 b and c [133]).

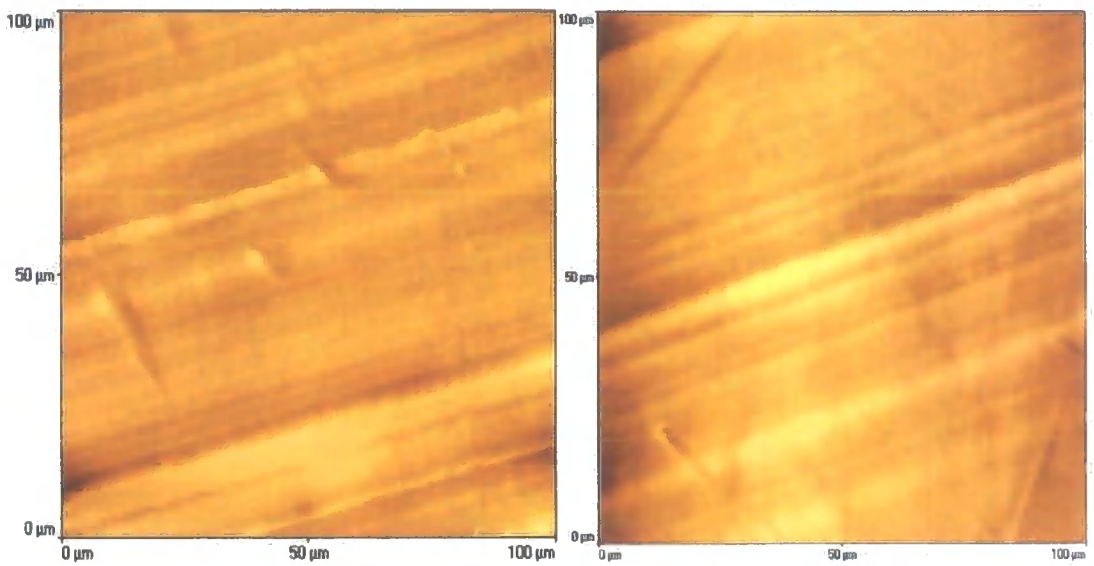

(a) unmodified *(b)* 5 x 10^{15} N^+ ions/cm^2 implanted

Figure 5.35. Top view AFM images of *(a)* unmodified UHMWPE and *(b)* 5 x 10^{15} N^+ ions/cm^2 implanted UHMWPE

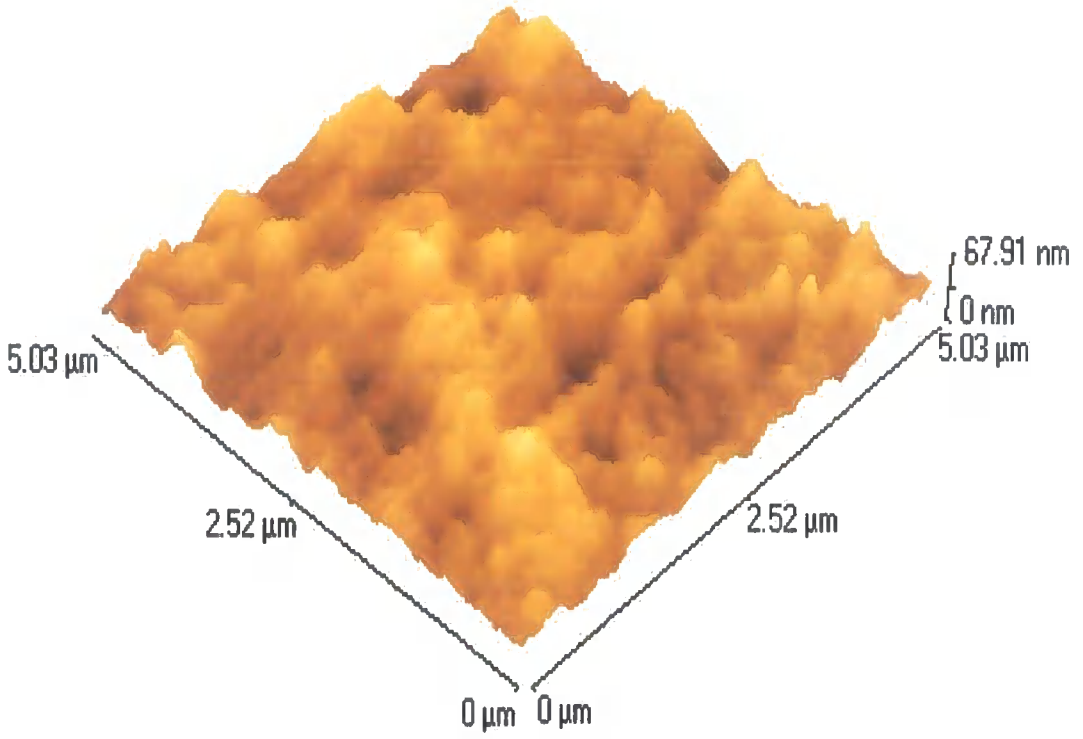

Figure 5.36. 3-D projection AFM image of 5 x 10^{15} N^+ ions/cm^2 implanted UHMWPE

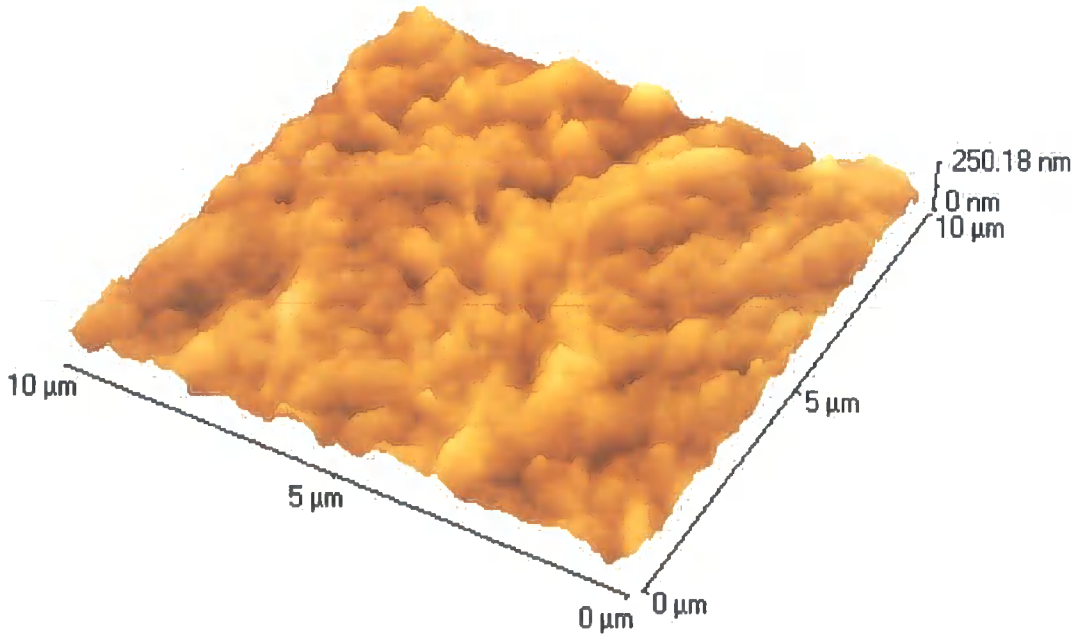

Figure 5.37. Wear induced topographic morphology of UHMWPE (AFM) following articulation against Ti6Al4V *in vitro*

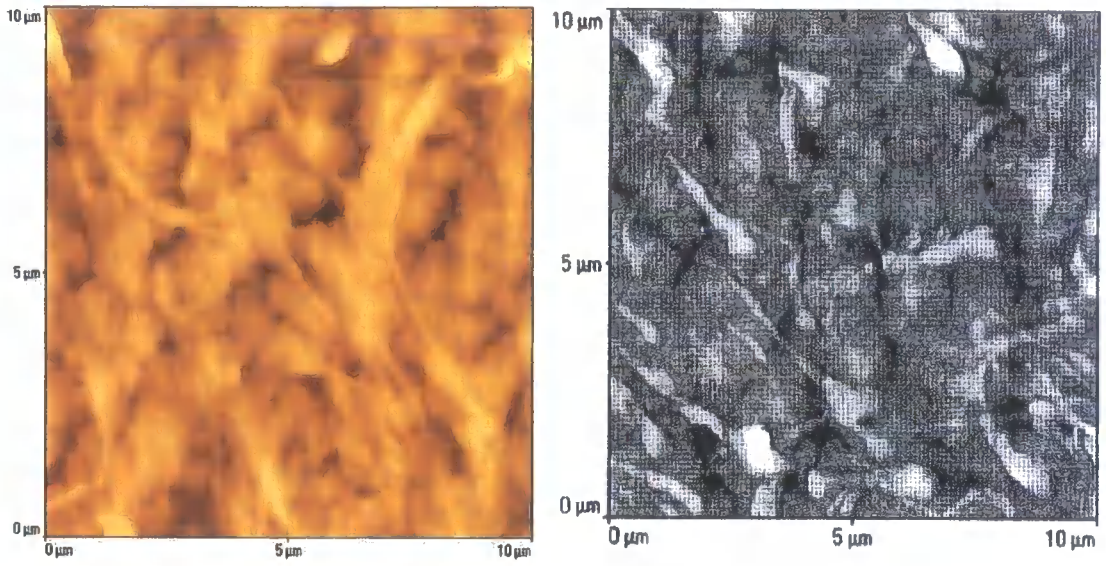

(a) *ex vitro* (b) *ex vivo*

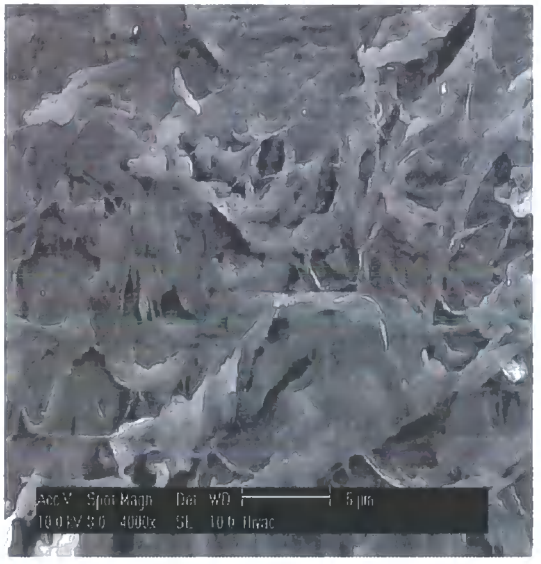

(c) *ex vivo*

Figure 5.38. Wear induced topographic morphologies of UHMWPE following articulation *in vitro* and *in vivo*: (a) AFM image of UHMWPE pin surface articulated against Ti6Al4V plate *in vitro* (b) AFM image of retrieved UHMWPE acetabular cup surface articulated against metallic femoral component *in vivo* [133] (c) SEM image of retrieved UHMWPE acetabular cup surface articulated against metallic femoral component *in vivo* [133]

5.1.6 Chemical Composition

5.1.6.0 Introduction

The chemical composition of the unmodified and N^+ ion implanted Ti6Al4V and UHMWPE materials pre and post ion implantation, and post wear testing were analysed using XPS, and the results are presented under the following sections (5.1.6.1-5.1.6.5). All XPS survey scan spectra were collected in the 0-1100 eV binding energy range using a pass energy of 50 eV. High resolution scans and areas of interest were made using 20 eV pass. Table 5.4 summarises the results of the quantification data (i.e., atomic % composition) of the species in the XPS spectra.

5.1.6.1 Polished Ti6Al4V alloy

Figure 5.39 shows the XPS survey spectrum of polished Ti6Al4V between binding energies of 0 and 1100 eV. The binding energy positions of Ti 2p, C 1s, O 1s, Ti Auger, C Auger and O Auger were apparent with minor peaks attributable to Al 2p and Al 2s. High resolution XPS collections of the Ti 2p, O 1s, and C 1s binding energy regions were made and the results are shown in figures 5.40 to 5.42.

The Ti 2p envelope (fig 5.40) was observed to exhibit two peaks known as a doublet, identified as Ti^{4+} 2p 3/2 at 458.7 eV and Ti^{4+} 2p ½ at 464.4 eV. This doublet was attributed entirely to TiO_2. The O 1s peak (fig. 5.41) showed O^{2-}, OH^- and chemisorbed H_2O peaks at 530.2, 531.6 and 533.03 eV respectively, with some of the O being present from C-O/C=O identified in the C 1s higher resolution spectrum. C-C/C-H at 285 eV, C-O at 286.3 eV and C=O at 288.8 eV were identified in the C 1s envelope shown in figure 5.43.

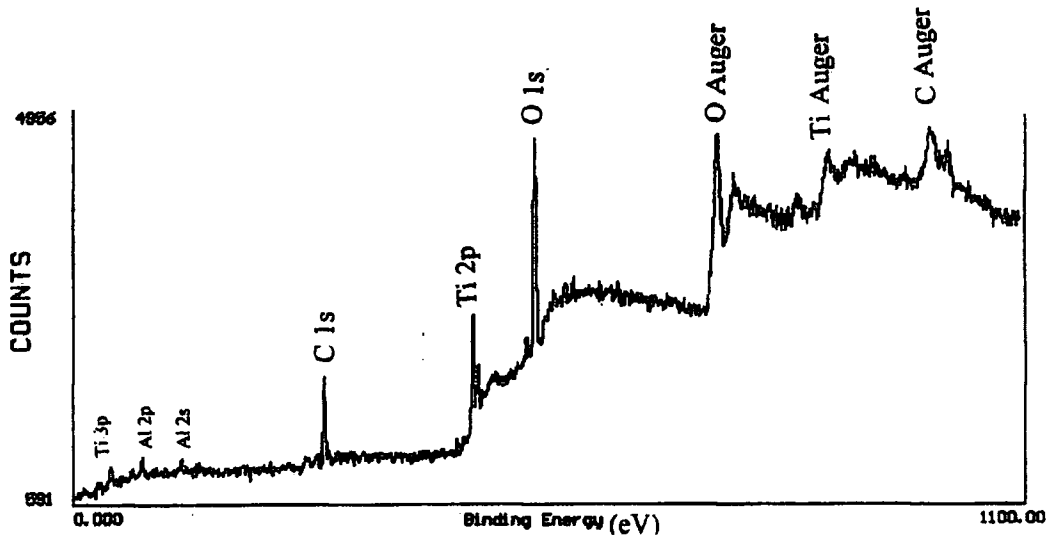

Figure 5.39. XPS energy spectrum of polished Ti6Al4V

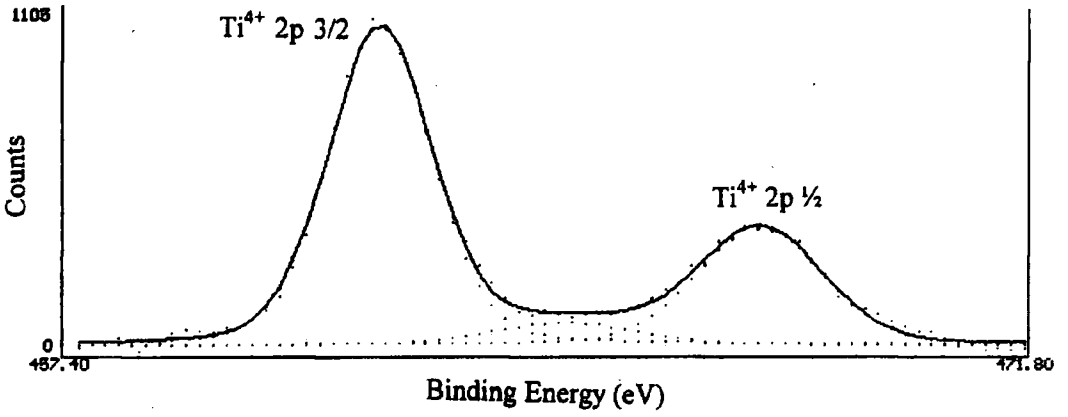

Figure 5.40. Ti 2p XPS energy spectrum of polished Ti6Al4V

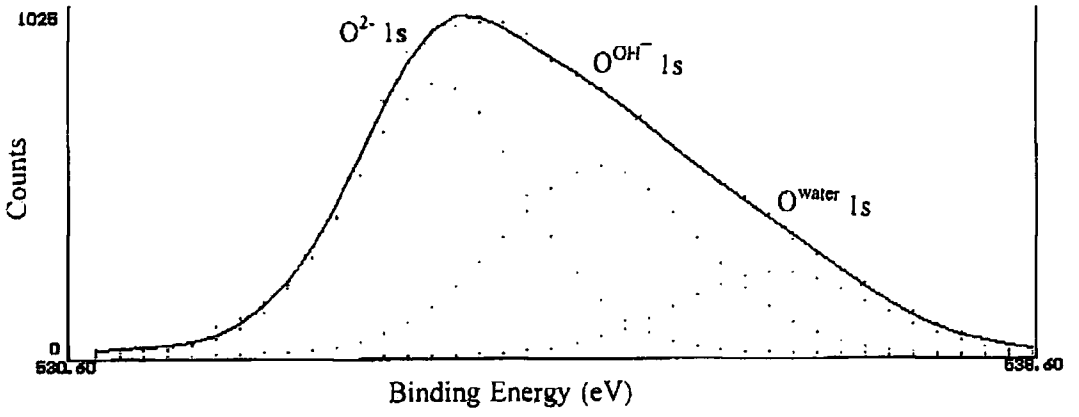

Figure 5.41. O 1s XPS energy spectrum of polished Ti6Al4V

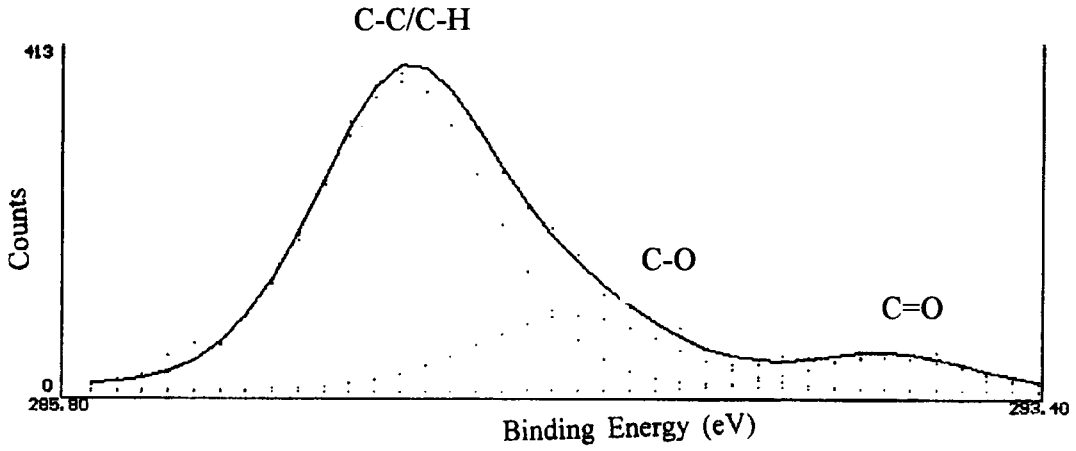

Figure 5.42. C 1s XPS energy spectrum of polished Ti6Al4V

5.1.6.2 2 x 10^{17} N^+ ions/cm^2 implanted Ti6Al4V

Figure 5.43 shows the XPS survey spectrum of 2 x 10^{17} N^+ ions/cm^2 implanted Ti6Al4V. The distinct binding energy position of N 1s was clearly discernable in the survey spectrum, an indication of the presence of N on the surface, which was not present on the surface of the unmodified material. The Ti 2p peak was observed to be more intense relative to the O 1s, when compared to that of the unmodified material (fig. 5.39). High resolution XPS collections of the Ti 2p and N 1s were made, the results of which are shown respectively in figures 5.45 and 5.48 respectively.

The Ti 2p peak was observed to exhibit a twin doublet comprising Ti^{4+} 2p 3/2 at 458.3 eV and Ti^{4+} 2p ½ at 464.3 eV (attributable to TiO_2, dominant peak); and Ti^+ 2p 3/2 at 455.62 eV and Ti^+ 2p ½ at 461.61 eV (attributable to TiN, lower energy), the positions of which are indicated on figure 5.45. The N 1s region scan showed a triple peak structure (fig. 5.48), the main one being a good match for TiN at 396.2 eV, and two smaller unidentified peaks of the form TiN_xO_y at 398.5 and 401.3 eV respectively. The O 1s sub-peaks were observed to be similar to those of the unmodified material (fig. 5.41) but with more O^{2-} relative to the OH^-/H_2O (table 5.4).

XPS energy spectrum of the wear track region of 2 x 10^{17} N^+ ions/cm^2 implanted Ti6Al4V post tribological wear test against 5 x 10^{15} N^+ ions/cm^2 implanted UHMWPE (fig. 5.44), was observed to have a similar spectra to that obtained from the pre wear test

2 x 10^{17} N^+ ions/cm^2 implanted material (fig. 5.43). The N 1s region scan showed a double peak structure (fig. 5.49), the main one being TiN at 396.3 eV, and an unidentified peak at 399.4 eV of the form TiN_xO_y. However, high resolution XPS analysis of the Ti 2p envelope (fig. 5.46) found the surface depleted in T^+ attributable to TiN relative to Ti^{4+} attributable to TiO_2, when compared to that of the pre worn material (table 4.4). The amount of N attributable to TiN within the N 1s envelope was reduced when compared to the analysis from the pre-tested material (table 5.4).

As with the worn 2 x 10^{17} N^+ ions/cm^2 implanted Ti6Al4V plate tested against modified UHMWPE, analysis from the wear track region of 2 x 10^{17} N^+ ions/cm^2 implanted Ti6Al4V tested against unmodified UHMWPE material was made, and was observed to have a similar spectra to that obtained from the 2 x 10^{17} N^+ ions/cm^2 implanted Ti6Al4V plate tested against modified UHMWPE (fig. 5.44). High resolution XPS analysis of the Ti 2p and N 1s envelopes are shown in figures 5.47 and 5.50 respectively. The analysis of the Ti 2p spectrum found the surface depleted in T^+ attributable to TiN relative to Ti^{4+} attributable to TiO_2, and the depletion was more than that of the same material tested against modified UHMWPE and the pre wear tested material (table 5.4).

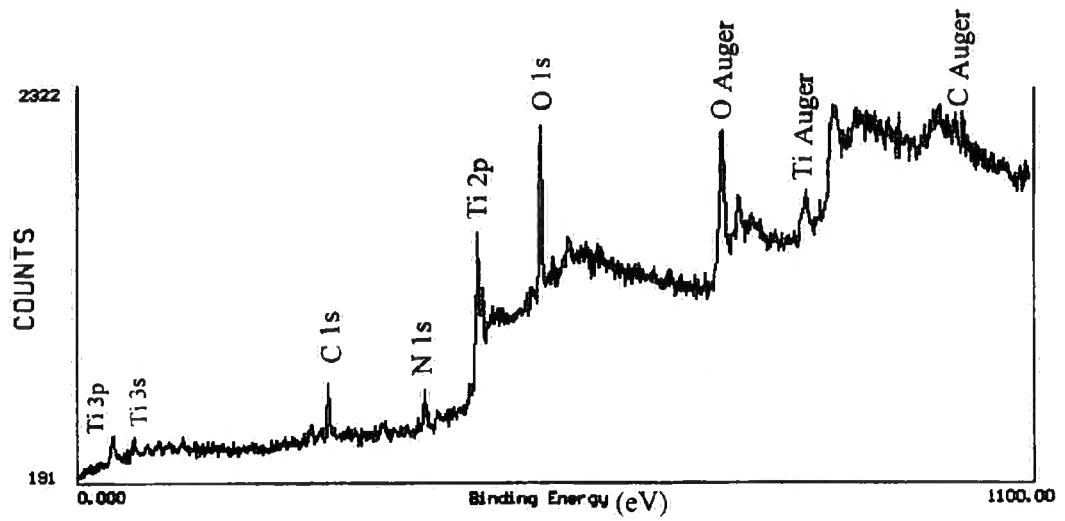

Figure 5.43. XPS energy spectrum of 2 x 10^{17} N^+ ions/cm^2 implanted Ti6Al4V plate

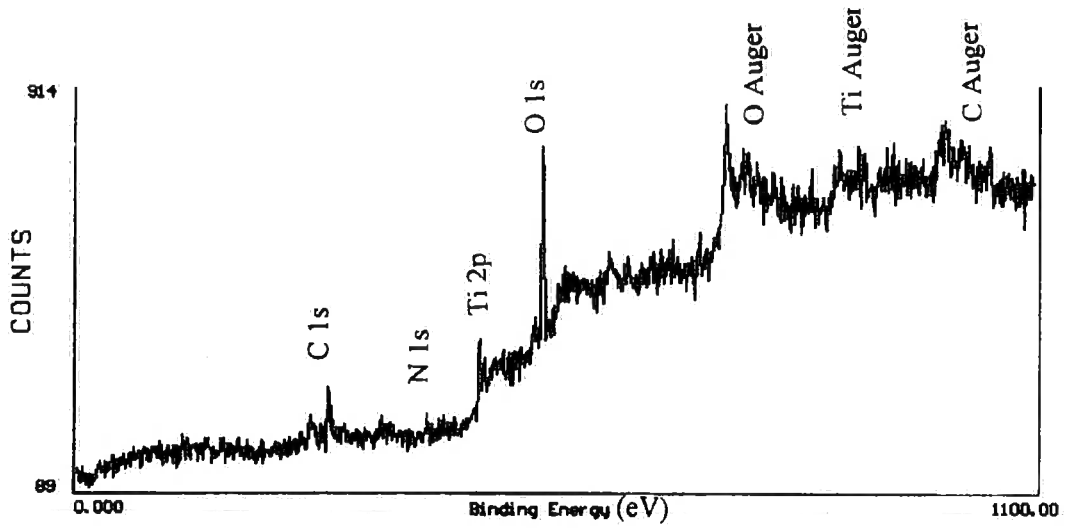

Figure 5.44. XPS energy spectrum of worn 2 x 10^{17} N^+ ions/cm^2 implanted Ti6Al4V plate tested against 5 x 10^{15} N^+ ions/cm^2 implanted UHMWPE

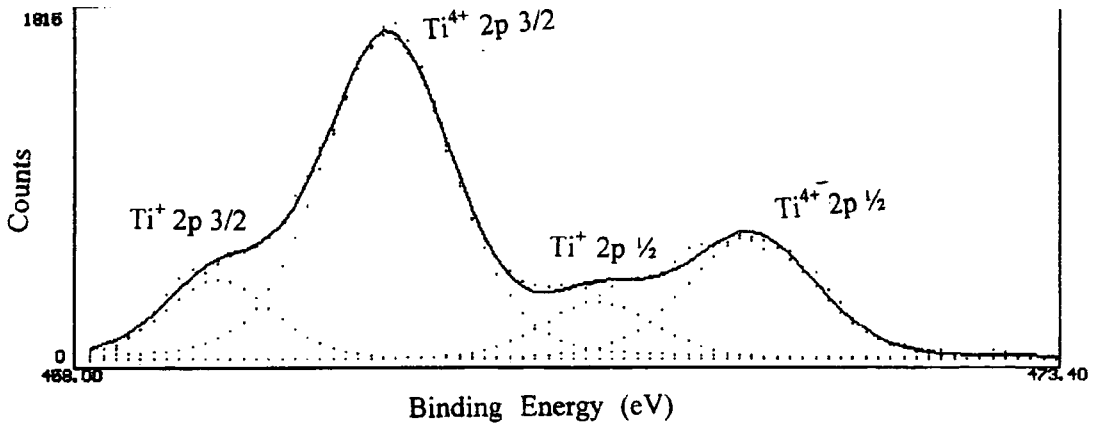

Figure 5.45. Ti 2p XPS energy spectrum of 2 x 10^{17} N^+ ions/cm^2 implanted Ti6Al4V

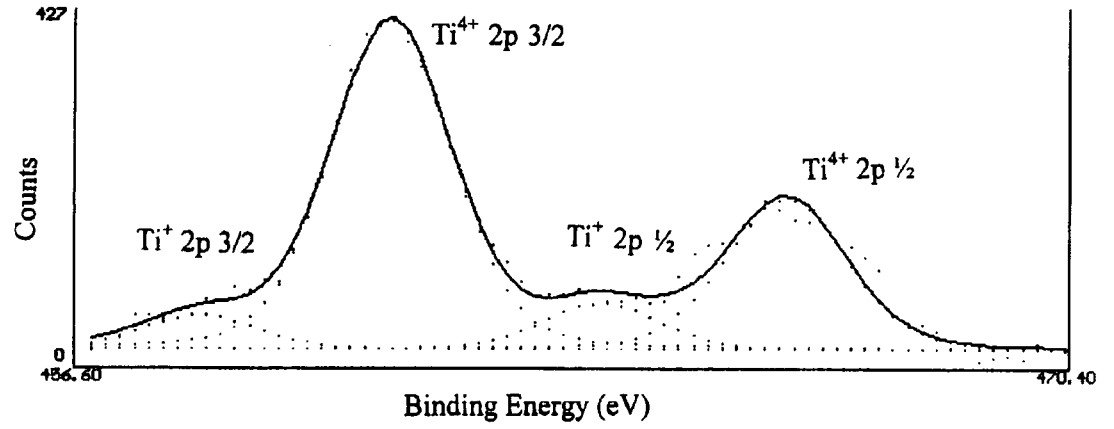

Figure 5.46. Ti 2p XPS energy spectrum of the worn region of 2 x 10^{17} N^+ ions/cm^2 implanted Ti6Al4V tested against 5 x 10^{15} N^+ ions/cm^2 implanted UHMWPE

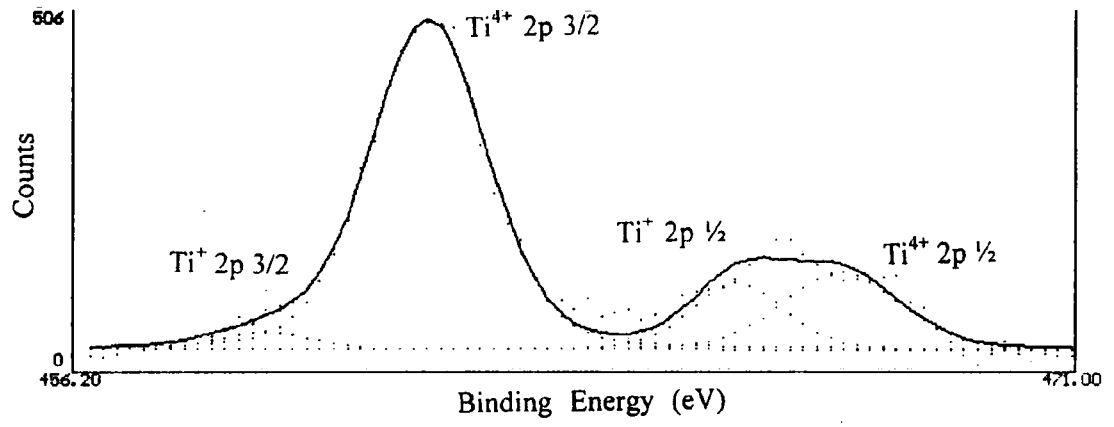

Figure 5.47. Ti 2p XPS energy spectrum of the worn region of 2 x 10^{17} N^+ ions/cm^2 implanted Ti6Al4V tested against unmodified UHMWPE

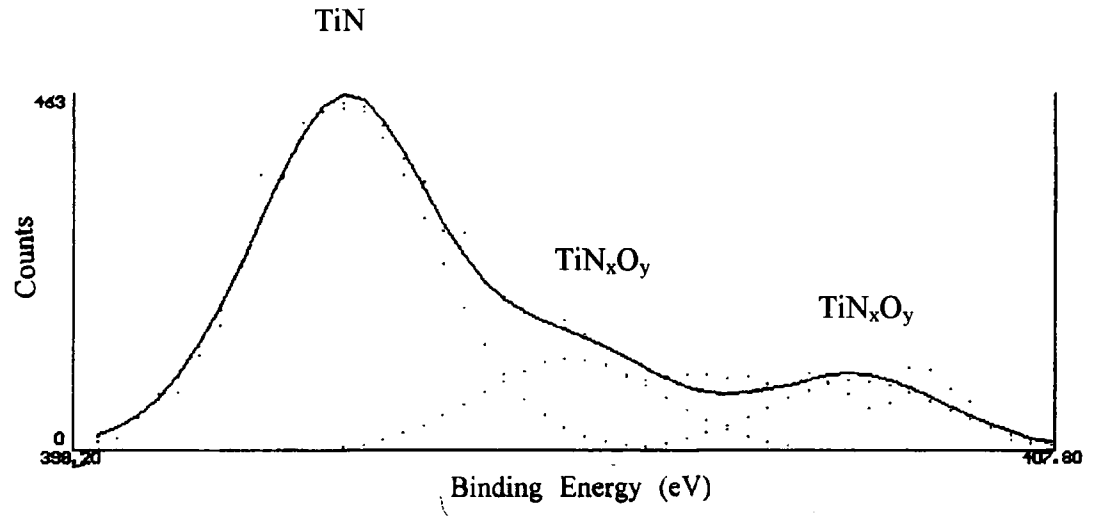

Figure 5.48. N 1s XPS energy spectrum of 2 x 10^{17} N^+ ions/cm^2 implanted Ti6Al4V

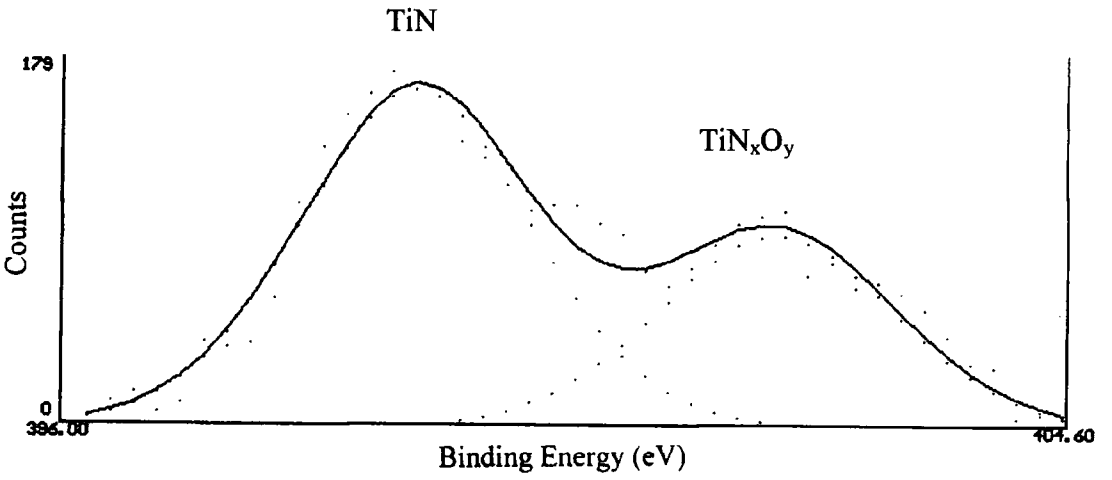

Figure 5.49. N 1s XPS energy spectrum of the worn region of 2 x 10^{17} N^+ ions/cm^2 Ti6Al4V tested against 5 x 10^{15} N^+ ions/cm^2 UHMWPE

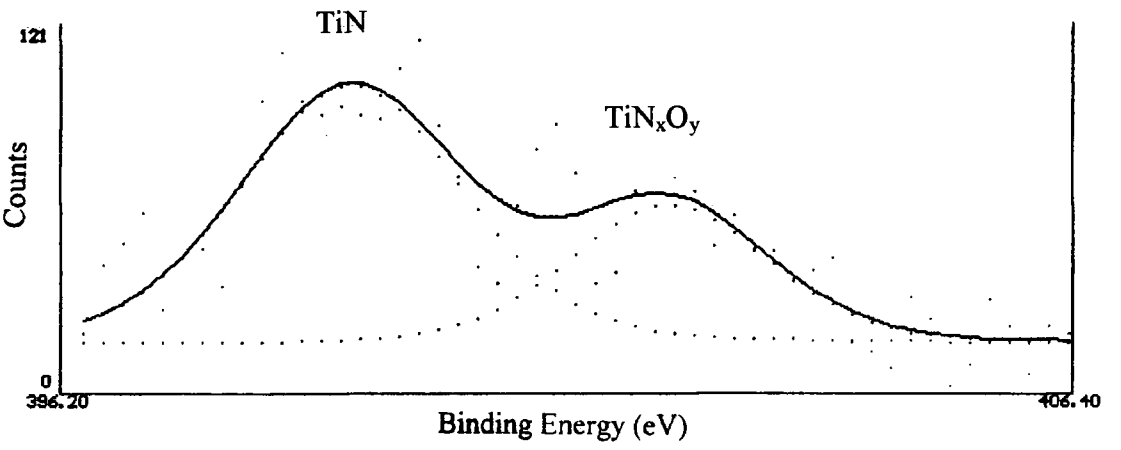

Figure 5.50. N 1s XPS energy spectrum of the worn region of 2 x 10^{17} N^+ ions/cm^2 Ti6Al4V tested against unmodified UHMWPE

5.1.6.3 1 x 10^{18} N^+ ions/cm^2 implanted Ti6Al4V

Figure 5.51 shows the XPS survey spectrum of 1 x 10^{18} N^+ ions/cm^2 implanted Ti6Al4V. The N 1s peak was detected in the survey spectrum, an indication of the presence of N on the surface of the material. High resolution XPS collections of the Ti 2p and N 1s were made and the results are shown in figures 5.52 and 5.53 respectively.

The Ti 2p twin doublet structure (fig. 5.52) showed a greater proportion of Ti^+ (attributable to TiN) relative to Ti^{4+} (attributable to TiO_2), when compared to that of the 2 x 10^{17} N^+ ion/cm^2 implanted material, although TiO_2 was still the dominant peak (table 5.4). The twin doublet comprised Ti^{4+} and Ti^+ attributable to TiO_2 and minor TiN respectively, the positions of which are indicated on the figure. The N 1s region scan (fig. 5.53) showed a double peak structure, the main one being attributed to TiN at 396.7 eV and an unidentified peak of the form TiN_xO_y at 398.8 eV. A greater proportion of the N 1s envelope was found to be due to TiN, when compared to the 2 x 10^{17} N^+ ion/cm^2 implanted material.

The analysis showed a larger amount of oxygenated carbon species compared to that of the 2 x 10^{17} N^+ ion/cm^2 implanted material, and more OH^-/H_2O relative to the O^{2-} reflecting the increase in oxidised carbon species (table 5.4).

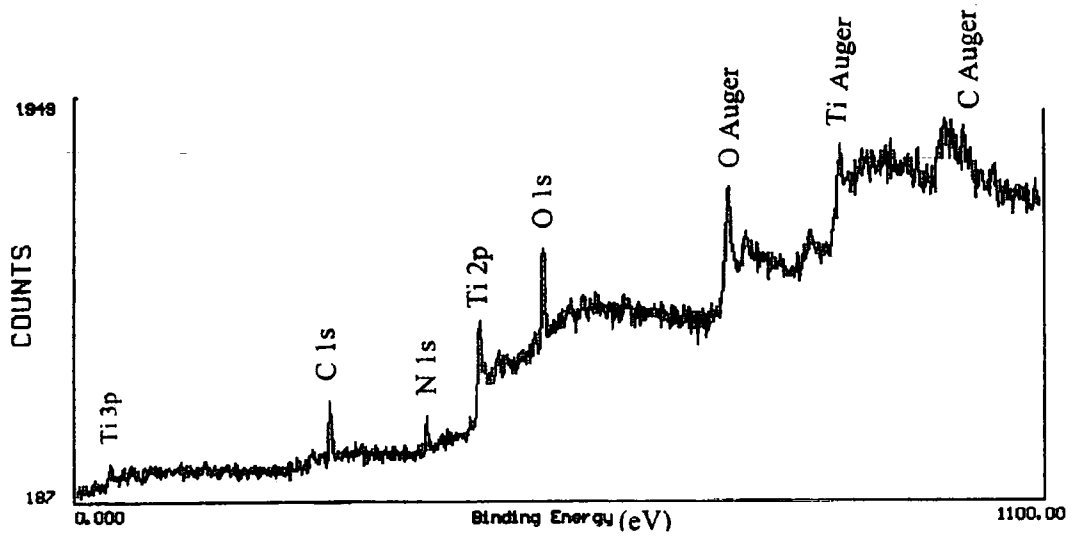

Figure 5.51. XPS energy spectrum of 1 x 10^{18} N^+ ions/cm^2 implanted Ti6Al4V

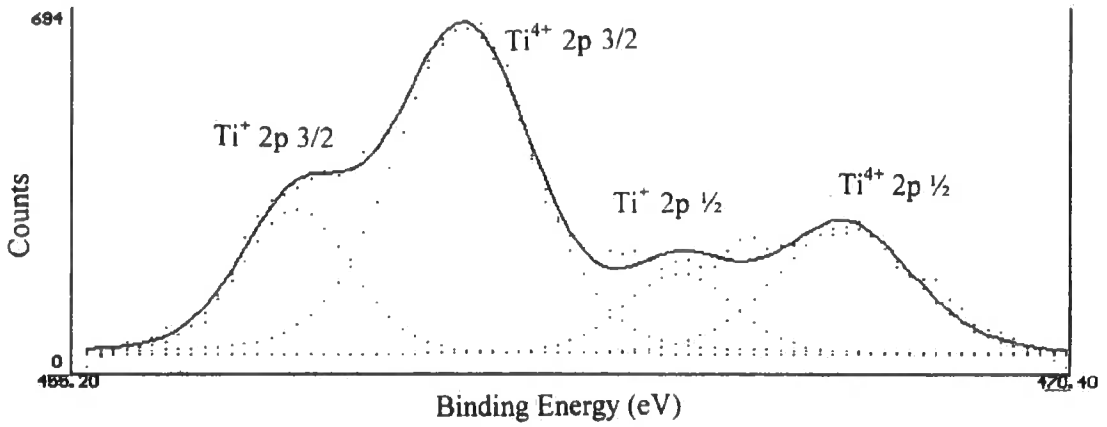

Figure 5.52. Ti 2p XPS energy spectrum of 1 x 10^{18} N^+ ions/cm^2 implanted Ti6Al4V

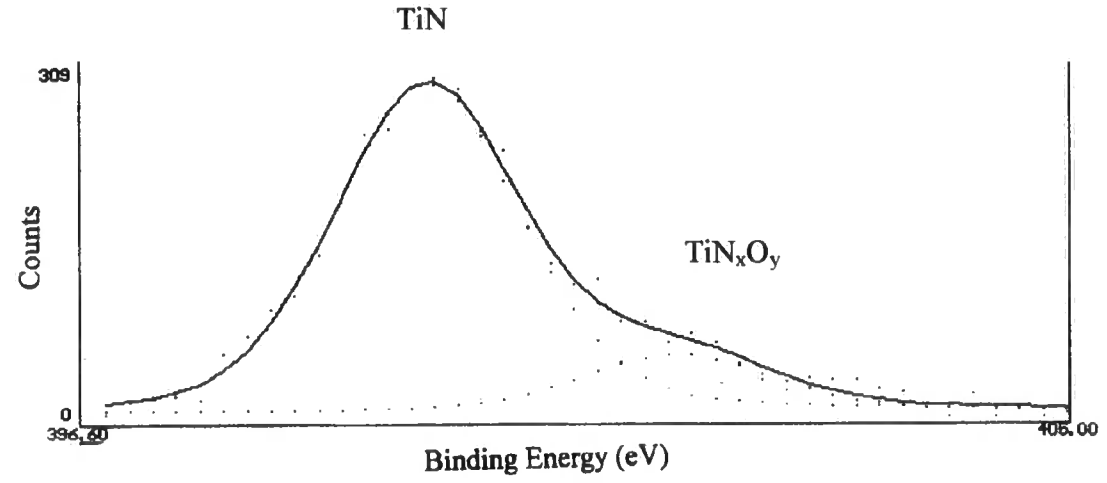

Figure 5.53. N 1s XPS energy spectrum of 1 x 10^{18} N^+ ions/cm^2 implanted Ti6Al4V

5.1.6.4 1 x 10^{21} N^+ ions/cm^2 implanted Ti6Al4V

Figure 5.54 shows the XPS survey spectrum of 1 x 10^{21} N^+ ions/cm^2 implanted Ti6Al4V. The C 1s and O 1s peaks were observed to dominate the sample. On a high resolution XPS collection, C-O peak was dominant in the C 1s spectrum reflecting the most intense O 1s peak at 533.1 eV. Only minor Ti and N peaks were present, because of the C/O over layer (table 5.4).

High resolution XPS collection of the Ti 2p and N 1s were made and the results are shown in figures 5.55 and 5.56 respectively. The N 1s peak (fig. 5.56) appeared to show

no TiN at all, with the two sub-peaks of the form TiN_xO_y (399.2 and 400.5 eV) at binding energies higher than that for TiN (397.3 eV [77]).

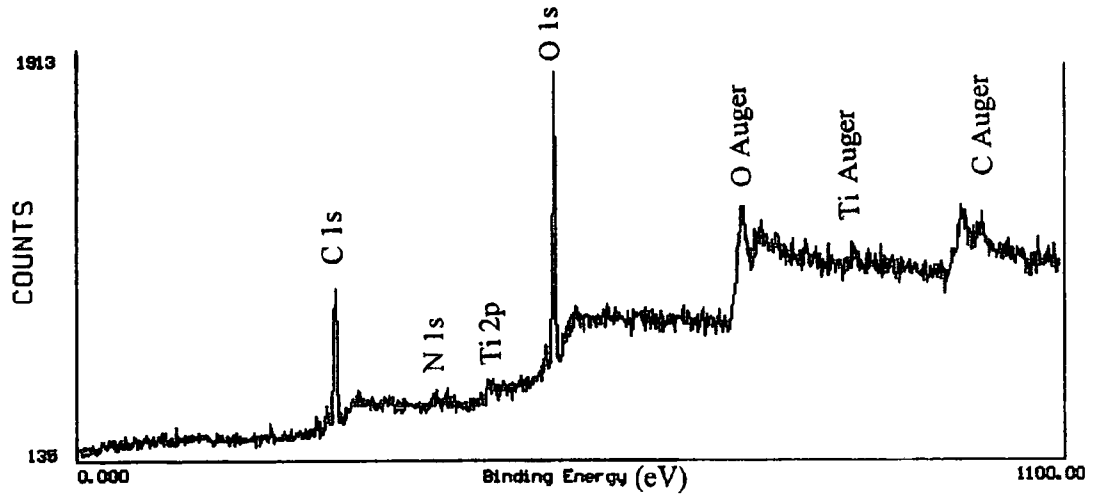

Figure 5.54. XPS energy spectrum of 1 x 10^{21} N^+ ions/cm^2 implanted Ti6Al4V

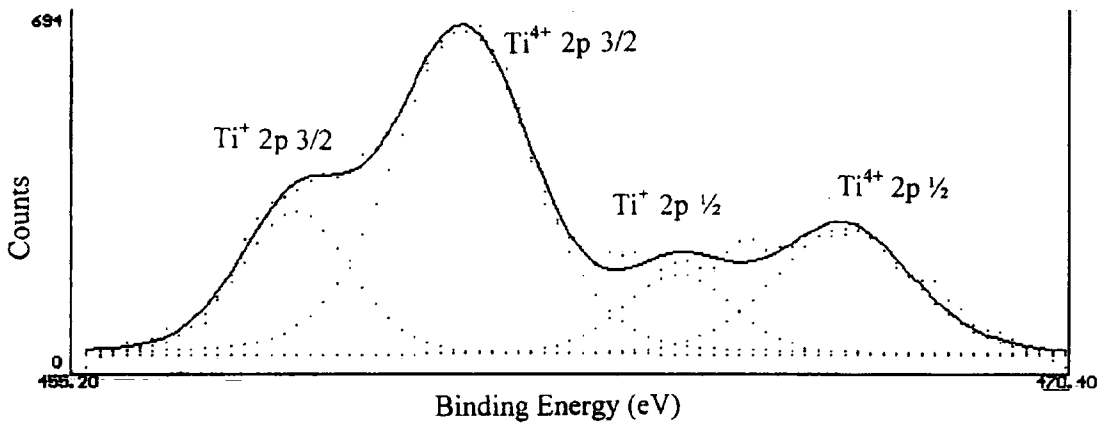

Figure 5.55. Ti 2p XPS energy spectrum of 1 x 10^{21} N^+ ions/cm^2 implanted Ti6Al4V

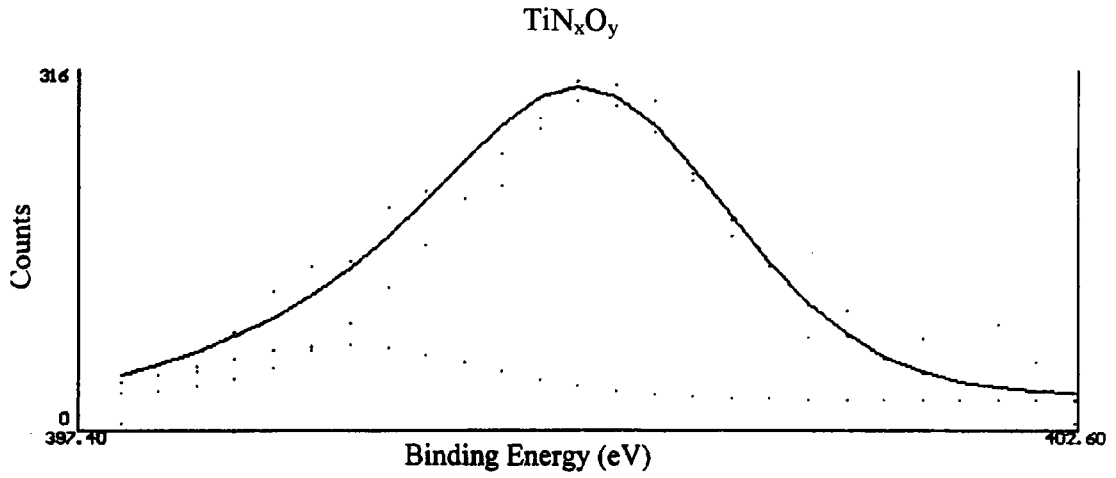

Figure 5.56. N 1s XPS energy spectrum of 1 x 10^{21} N^+ ions/cm^2 implanted Ti6Al4V

5.1.6.5 Unmodified and 5 x 10^{15} N^+ ions/cm^2 implanted UHMWPE

Figure 5.57 shows a typical spectrum for UHMWPE, with the main peak position of C 1s at 285 eV. The small amount of O reflects the oxidised carbon species that was seen in the high resolution XPS collection of the C 1s. Some OH-. C-C/C-H at 285 eV (main peak) and C-O at 286.6 eV binding energy positions, were detected in the C 1s spectrum.

Upon N^+ ion implantation, the samples showed a significant amount of O (fig. 5.58), which was reflected by the relatively large amount of oxidised carbon species observed in the C 1s spectrum. C-C/C-H at 285 eV (main peak), C-O at 286.8 eV, and C=C at 289.2 eV binding energy positions were observed on the C 1s spectrum of the implanted material. High resolution scans of the N 1s peak from the implanted sample showed a 2 sub-peak envelope with peaks at 398.4 and 400.1 eV respectively. Nearly 2 at % of N were found to be present in the implanted material (table 5.4).

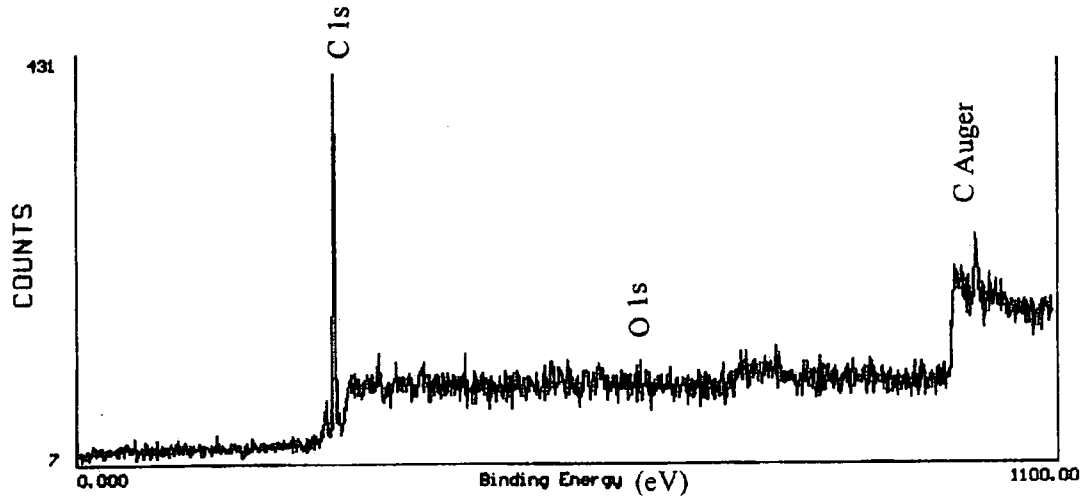

Figure 5.57. XPS energy spectrum unmodified UHMWPE

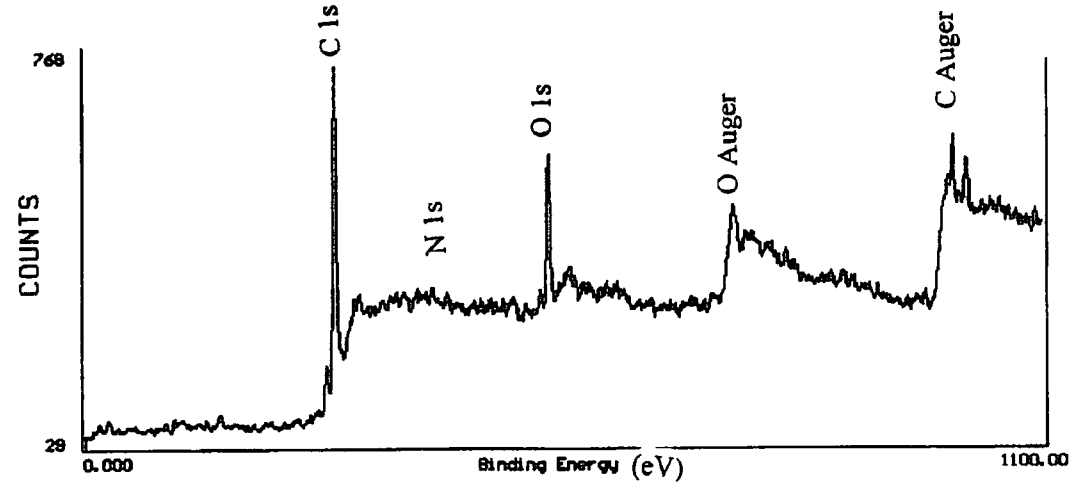

Figure 5.58. XPS energy spectrum of 5 x 10^{15} N^+ ions/cm^2 implanted UHMWPE

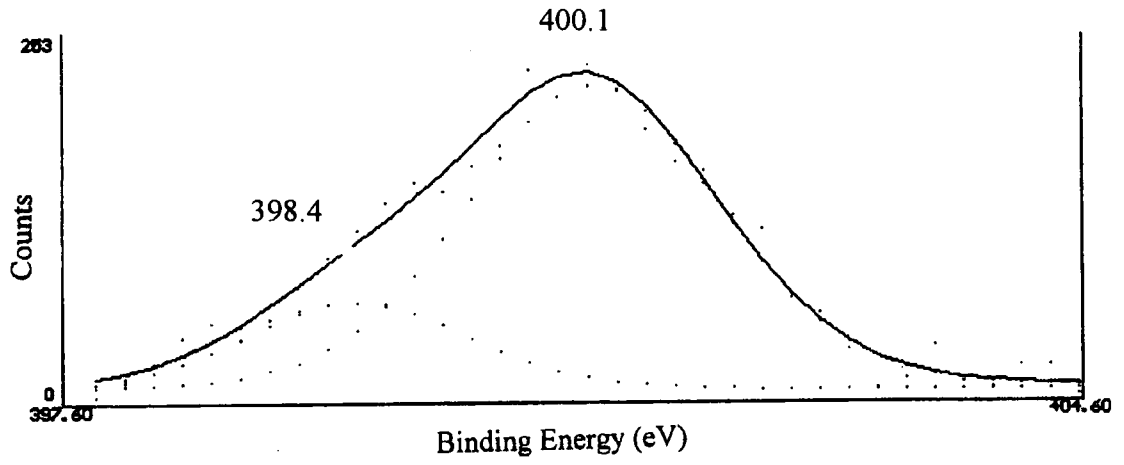

Figure 5.59. N 1s XPS energy spectrum of 5 x 10^{15} N^+ ions/cm^2 implanted UHMWPE

Table 5.4. XPS surface composition of modified and unmodified Ti6Al4V and UHMWPE

Species	Atomic % (± 5 %)							
	A	B	C	D	E	F	G[1]	H[1]
$C_{contam.}$	38	34	40	35	49	57.6	95	86.5
O^{2-}	25	18	20	26.3	9	1.4	0	0
O^{OH-/H_2O}	28	17	20	26	16	38	5	11.8
N^-	0	14	10	4	12	1	0	1.7
Ti^+	0	3	1	0.4	4	0.2	0	0
Ti^{4+}	9	14	9	8.3	10	1.8	0	0

[1]Polyethylene contains C, hence no C contamination

Where A is unmodified Ti6Al4V; B is 2 x 10^{17} N^+ ions/cm^2 implanted Ti6Al4V; C is 2 x 10^{17} N^+ ions/cm^2 implanted Ti6Al4V post wear (against modified UHMWPE); D is 2 x 10^{17} N^+ ions/cm^2 implanted Ti6Al4V post wear (against unmodified UHMWPE); E is 1 x 10^{18} N^+ ions/cm^2 implanted Ti6Al4V; F is 1 x 10^{21} N^+ ions/cm^2 implanted Ti6Al4V; G is UHMWPE; and H is 5 x 10^{15} N^+ ions/cm^2 implanted UHMWPE.

5.2 Stainless Steel and UHMWPE

5.2.0 Introduction

The metallographic results of the microstructure of the stainless steel alloy used in this study, N^+ ion implantation distribution in stainless steel, microhardness of the samples in both modified and unmodified forms, tribological wear test results of UHMWPE (modified and unmodified) articulating against stainless steel, topography and standard roughness of the as polished and modified samples are all presented under the following sections (5.2.1 to 5.2.5).

5.2.1 Metallography

An optical photomicrograph, SEM micrograph, and AFM image of the etched metallographic stainless steel samples are shown in figures 5.60, 5.61 and 5.62 respectively. As can be seen, the microstructures of the material have been clearly resolved.

Figure 5.60. Optical photomicrograph of etched unmodified stainless steel

Figure 5.61. SEM micrograph of etched unmodified stainless steel

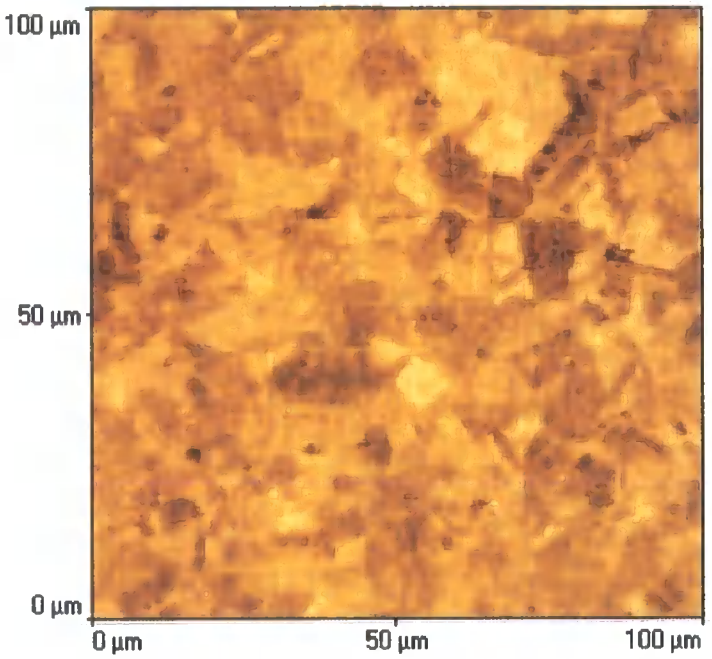

Figure 5.62. Top view AFM image of etched unmodified stainless steel

5.2.2 Projected N^+ ion Distribution

The results of the TRIM stopping range calculations for N^+ ions into stainless steel at an accelerating voltage of 90 keV are shown in figures 5.63 and 5.64. Target density of 7.8 g/cm^3 was used for the calculations.

Figure 5.63 shows the TRIM simulation of the range of N^+ ions into stainless steel target. Data from the results produced an estimated mean longitudinal range of N^+ ions at a depth of 0.1 μm with straggling of 0.04 μm as shown on the figure, and maximum estimated N^+ ion implantation depth of 0.21 μm within the sample surface was calculated. As shown on the figure, the overall distribution of the ions assumed approximately a Gaussian profile.

Figure 5.64 shows the calculation of the vacancy distribution produced by both N^+ ions and target atom recoil collisions. A total of 428 target vacancies produced by each incoming N^+ ion was calculated from the data.

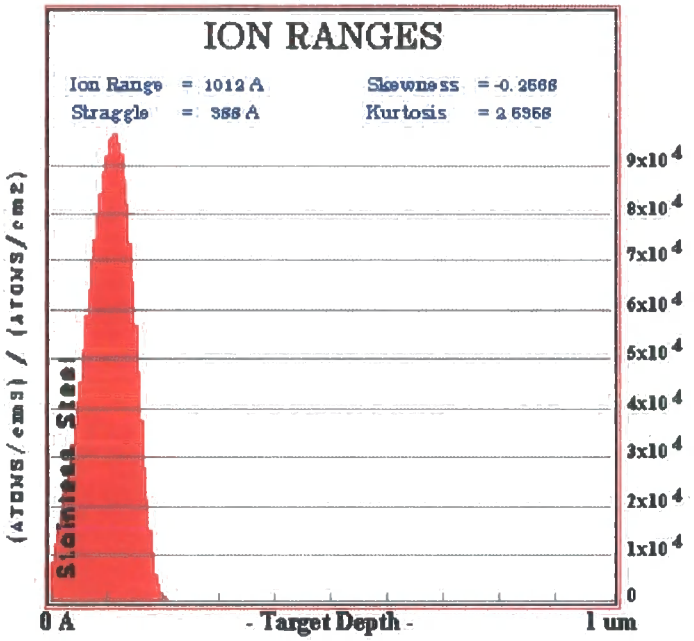

Figure 5.63. TRIM simulation of range of N^+ ions in stainless steel

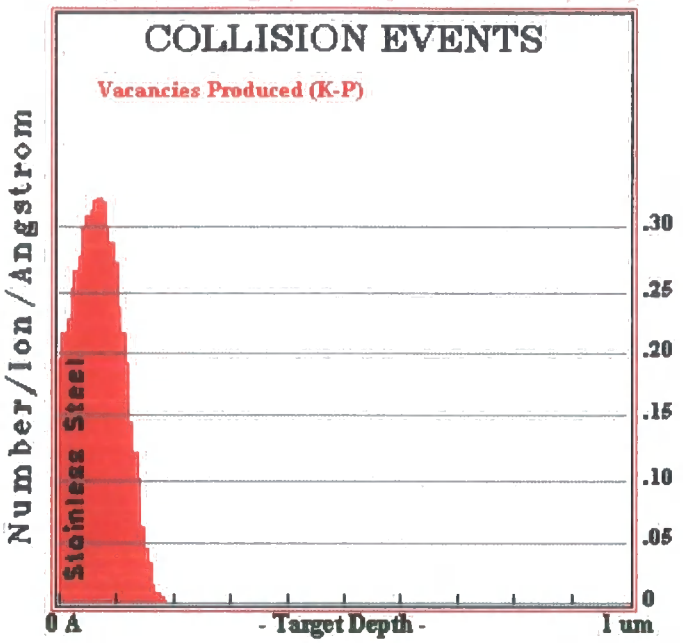

Figure 5.64. TRIM simulation of vacancy production within stainless steel target upon N^+ ion implantation

5.2.3 Knoop Microhardness Determination

The Knoop microhardness results of the unmodified and N^+ ion implanted stainless steel alloys are reproduced in figs 5.65. The microhardnesses of the modified samples was observed to increase with decreasing indentation load, with the highest values measured at an indentation load of 1 gf. The results indicated an increase in Knoop microhardness from 462 ± 47 KHN_{1gf} for the unmodified material, to 969 ± 110 KHN_{1gf} for the material implanted with 2 x 10^{17} N^+ ions/cm^2 (Appendix C2).

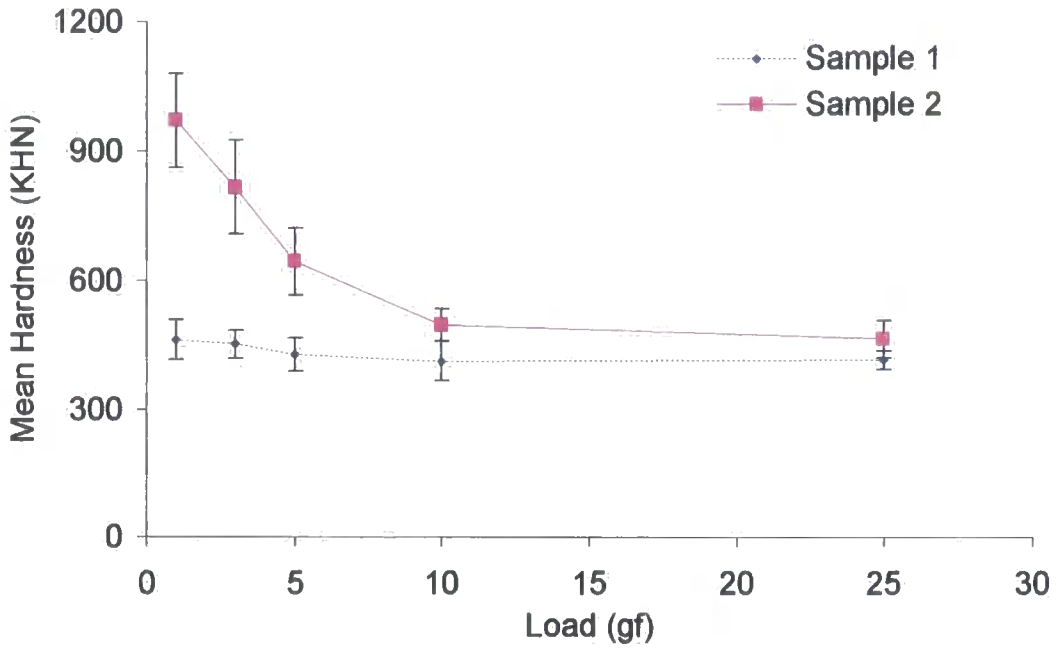

Figure 5.65. Knoop microhardness of unmodified and N^+ ions implanted stainless steel. Where sample 1 is unmodified stainless steel, and sample 2 is 2 x 10^{17} N^+ ions/cm^2 implanted stainless steel.

Inspection of figure 5.66 demonstrates the surface dependence and depth graded property modification induced upon ion implantation, where the mean hardness values at different loads have been plotted against the mean knoop indent penetration depth into the samples. The indentation depths were calculated from the indent width using the Knoop indenter geometry (Appendix C1) for loads of 1, 3, 5, 10 and 25 gf respectively. The reported values are an average of 10 measurements under each load (Appendix C1, table C1.4).

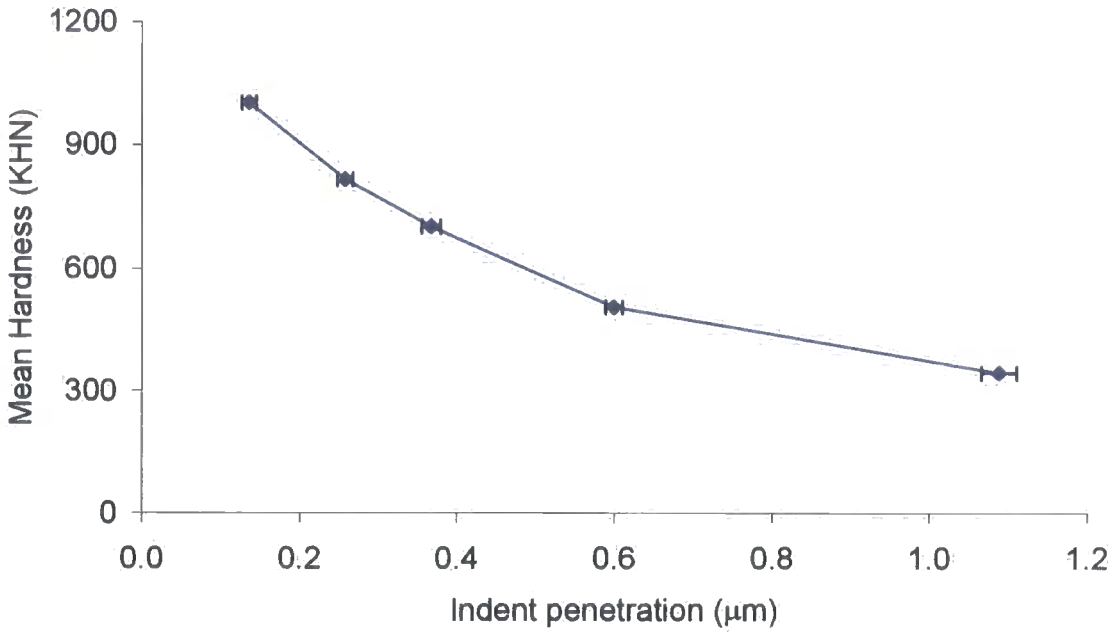

Figure 5.66. Depth dependence of Knoop microhardness for 2 x 10^{17} N^+ ion/cm^2 implanted stainless steel

5.2.4 Tribological Wear Test

5.2.4.0 Introduction

The tribological wear test results of UHMWPE (modified and unmodified) wear pins articulating against stainless steel plates (modified and unmodified) are reported under the following sections (5.2.4.1 to 5.2.4.3) (Appendix A6).

5.2.4.1 Unmodified UHMWPE against unmodified Stainless Steel

Tribological wear test results of unmodified UHMWPE against unmodified stainless steel sliding couple, expressed in volume loss (mm^3) of the UHMWPE wear pins against the sliding distance (km) over the test duration are shown in figure 5.67. There were no significant differences between the wear factors (k_o) of the polymer wear pins in the test, and a mean k_o of 1.59 ± 0.15 x 10^{-6} mm^3/Nm over a sliding distance of 208 km (> 5.5 million wear cycles) was calculated for the unmodified UHMWPE. An initial higher mean k_o of 1.99 ± 0.17 x 10^{-6} mm^3/Nm was calculated up to a sliding distance of

80 km, due to a wearing in type process. The steady-state mean wear factor of 1.02 ± 0.13 x 10^{-6} mm^3/Nm was calculated between 80-208 km sliding distance. Plate weight pre and post wear test (mean weight loss) are shown in table 5.5.

Distinctive wear tracks characterised by scratch marks and grooves were observed on the stainless steel plates following testing. There was no discolouration of the bovine serum lubricant following testing. Topographic examinations of the pin and plate surfaces post wear, using AFM and NCI respectively revealed the surface damage observed on the plates and wear features on the pins, and high R_a values on the plates and low R_a on the pins (table 5.6). Wear curves of the UHMWPE wear pins were linear, and no transfer films were observed on the stainless steel plates during and post wear.

Machining and microtoming marks on the surface of the UHMWPE wear pins wore away with test duration, and the surfaces became smooth, showing low R_a (table 5.6) post wear. Topographic examinations of the pin surfaces showed similar morphology with those of *ex vivo* UHMWPE components, as was observed on the worn unmodified UHMWPE surfaces tested against titanium.

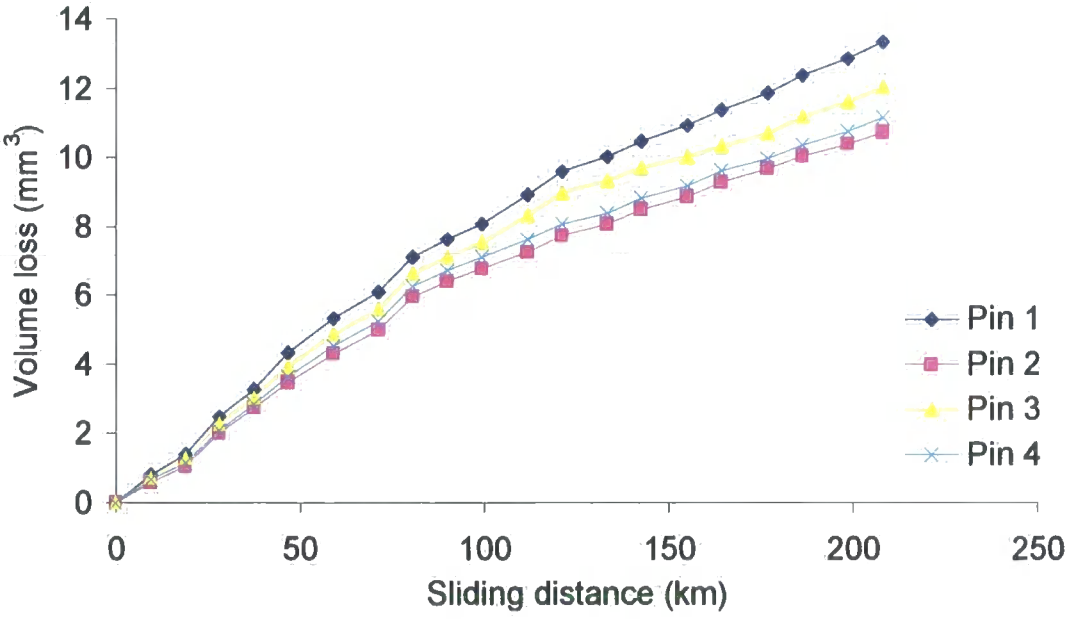

Figure 5.67. Wear of unmodified UHMWPE pins against unmodified stainless steel plates

5.2.4.2 Unmodified UHMWPE against N^+ ion implanted stainless steel

Wear results of unmodified UHMWPE wear pins sliding and rotating against 2 x 10^{17} N^+ ions/cm^2 implanted stainless steel plates are shown in figure 5.68. Linear wear curves with no significant differences between the wear volumes of the pins were measured, and a mean k_o of 0.98 ± 0.08 x 10^{-6} mm^3/Nm was calculated for the UHMWPE over a test duration of 210 km (> 5.5 million wear cycles). An initial slightly higher mean k_o of 1.14 ± 0.09 x 10^{-6} mm^3/Nm was measured up to a sliding distance of 65 km, due to a wearing in type process, and a steady-state mean wear factor of 0.82 ± 0.04 x 10^{-6} mm^3/Nm was measured between 65-210 km sliding distance. There was a reduction in polymer wear volume loss compared to the same UHMWPE material tested against unmodified stainless steel.

Compared with the unmodified UHMWPE against unmodified stainless steel test, less damage was observed in the wear tracks of the plates during and post wear test. Examination of the region of pin contact on the plates under AFM and NCI revealed no distinctive wear tracks and measured R_a values (table 5.6) were low. No transfer films were seen on the plates, and the wear curves wear linear. The UHMWPE worn surfaces showed similar surfaces morphology to those observed on the worn surfaces tested against unmodified stainless steel, and resembled *ex vivo* components.

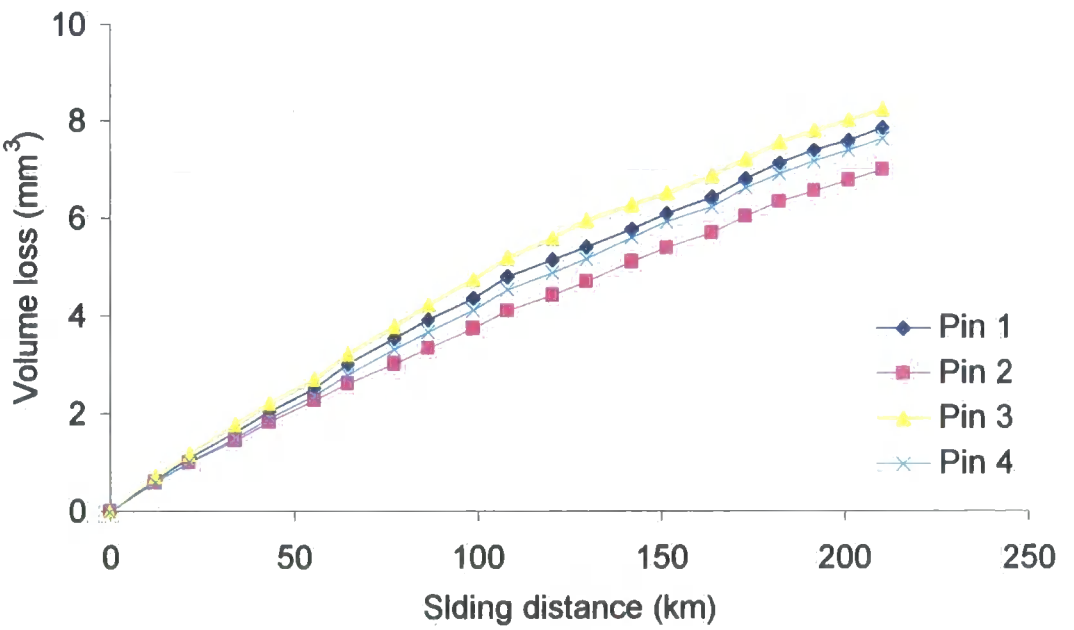

Figure 5.68. Wear of unmodified UHMWPE pins against 2 x 10^{17} N^+ ion/cm^2 implanted stainless steel plates

5.2.4.3 N^+ ion implanted UHMWPE against N^+ ion implanted stainless steel

Figure 5.69 shows the graph of 5 x 10^{15} N^+ ion/cm^2 implanted UHMWPE wear pins volume loss against sliding distance, when tested against 2 x 10^{17} N^+ ion/cm^2 implanted stainless steel. Linear wear curves were observed and a mean k_o of 0.82 ± 0.02 x 10^{-6} mm^3/Nm was calculated over a test duration of 205 km (> 5.5 million wear cycles). An initial slightly higher mean k_o of 0.98 ± 0.01 x 10^{-6} mm^3/Nm was measured up to a sliding distance of 74 km, due to a wearing in type process, and a steady-state mean wear factor of 0.59 ± 0.03 x 10^{-6} mm^3/Nm was measured between 74-205 km sliding distance.

AFM images and NCI analysis of the worn surfaces of the plates showed few scratches and measured low R_a values (table 5.6), compared to the surfaces of the unmodified stainless steel plates articulated against unmodified UHMWPE. There was no colouration of the bovine serum lubricant, and no transfer films were observed on the surface of the modified stainless steel plates, following testing.

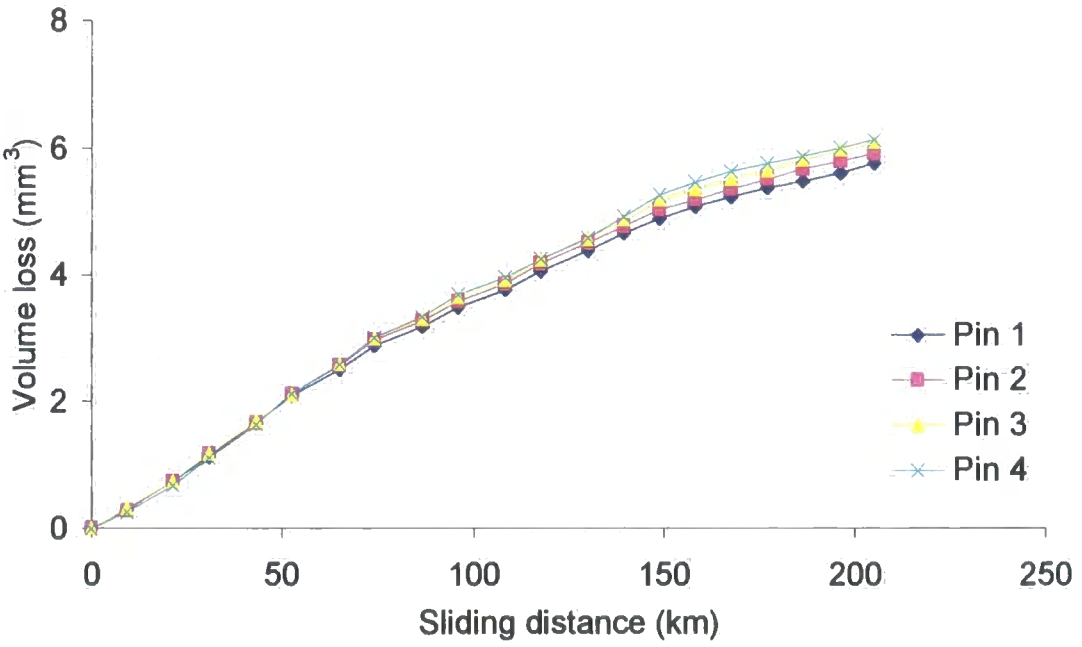

Figure 5.69. Wear of 5 x 10^{15} N^+ ion/cm^2 implanted UHMWPE pins against 2 x 10^{17} N^+ ion/cm^2 implanted stainless steel plates

5.2.4.4 Summary of Results

The tribological wear test results, and the mean R_a values of all the materials tested pre and post wear are summarised and presented respectively in tables 5.5 and 5.6. Table 5.7 summarises the measured changes in hardness for the stainless steel substrate.

Figure 5.70 summarises the results of the mean wear curves of UHMWPE pins (modified and unmodified) articulated against stainless steel plates (modified and unmodified).

Table 5.5. Summary of *in vitro* tribological performance of unmodified and N^+ ion implantation modified UHMWPE/stainless steel biomaterial couples after 5.5 million cycles of wear testing

Wear Couple[a]	Mean UHMWPE k_o (x 10^{-6} mm^3/Nm)	Mean Stainless Steel Plate Wt Loss (μg)[b]
Unmodified UHMWPE/unmodified stainless steel	1.59 ± 0.17	106 ± 0.19
Unmodified UHMWPE/2 x 10^{17} N^+ ions cm^{-2} implanted stainless steel	0.98 ± 0.08	60 ± 0.06
5 x 10^{15} N^+ ions cm^{-2} implanted UHMWPE/2 x 10^{17} N^+ ions cm^{-2} implanted stainless steel	0.82 ± 0.02	43 ± 0.06

[a]Samples implanted with N^+ ions at 90 keV (stainless steel) and 80 keV (UHMWPE)

[b]Plate measured before and at the end of test

Table 5.6. Mean arithmetic mean surface roughness (R_a) of stainless steel and UHMWPE samples

Sample Surface	Mean R_a (μm)	
	Pre wear	Post wear
Unmodified Stainless steel (articulated against unmodified UHMWPE)	0.006 ± 0.003	0.012 ± 0.002
2 x 10^{17} N^+ ions/cm^2 implanted stainless steel (articulated against modified and unmodified UHMWPE)	0.007 ± 0.002	0.009 ± 0.002
Unmodified UHMWPE (articulated against unmodified and modified stainless steel)	1.4 ± 0.13	0.05 ± 0.04
5 x 10^{15} N^+ ions/cm^2 implanted UHMWPE (articulated against unmodified and modified stainless steel)	1.3 ± 0.12	0.06 ± 0.02

Table 5.7. Summary of Knoop microhardness of unmodified and N^+ ion implantation modified stainless steel and UHMWPE substrates

Substrate[a]	Knoop Microhardness (KHN_{1gf})
Unmodified stainless steel	462 ± 47
2 x 10^{17} N^+ ions/cm^2 implanted stainless steel	969 ± 110
Unmodified UHMWPE	3.4 ± 0.5
5 x 10^{15} N^+ ions/cm^2 implanted UHMWPE	12.8 ± 1.6

[a]Substrates implanted with N^+ ions at 90 keV (Ti6Al4V), and 80 keV (UHMWPE)

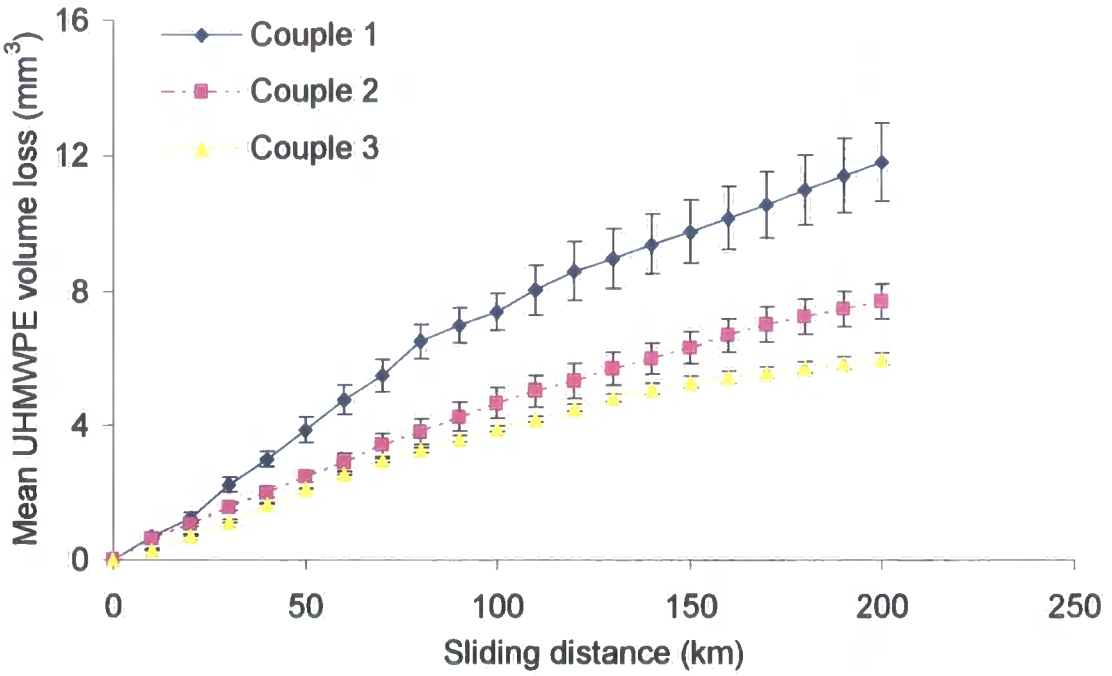

Figure 5.70. Mean wear behaviour of UHMWPE pins (modified and unmodified) against stainless steel plates (modified and unmodified). Where couple 1 is unmodified UHMWPE/unmodified stainless steel, couple 2 is Unmodified UHMWPE/2 x 10^{17} N^+ ions/cm^2 implanted stainless steel, and couple 3 is 5 x 10^{15} N^+ ions/cm^2 implanted UHMWPE/2 x 10^{17} N^+ ions/cm^2 implanted stainless steel (table 5.3).

5.2.5 Surface Topography

The surface topography of the modified and unmodified stainless steel plates pre and post wear test, and UHMWPE pin surfaces post wear were examined using AFM and NCI, and the results are shown in figures 5.71 to 5.75.

Figure 5.71 shows a top view 100 μm^2 AFM image of unmodified stainless steel, and surface analysis results of a line profile across the sample surface showing typical standard surface roughness data. The topography was typical of the surface achieved post polishing (characterised by scratch marks from polishing), and prior to surface modification and tribological testing.

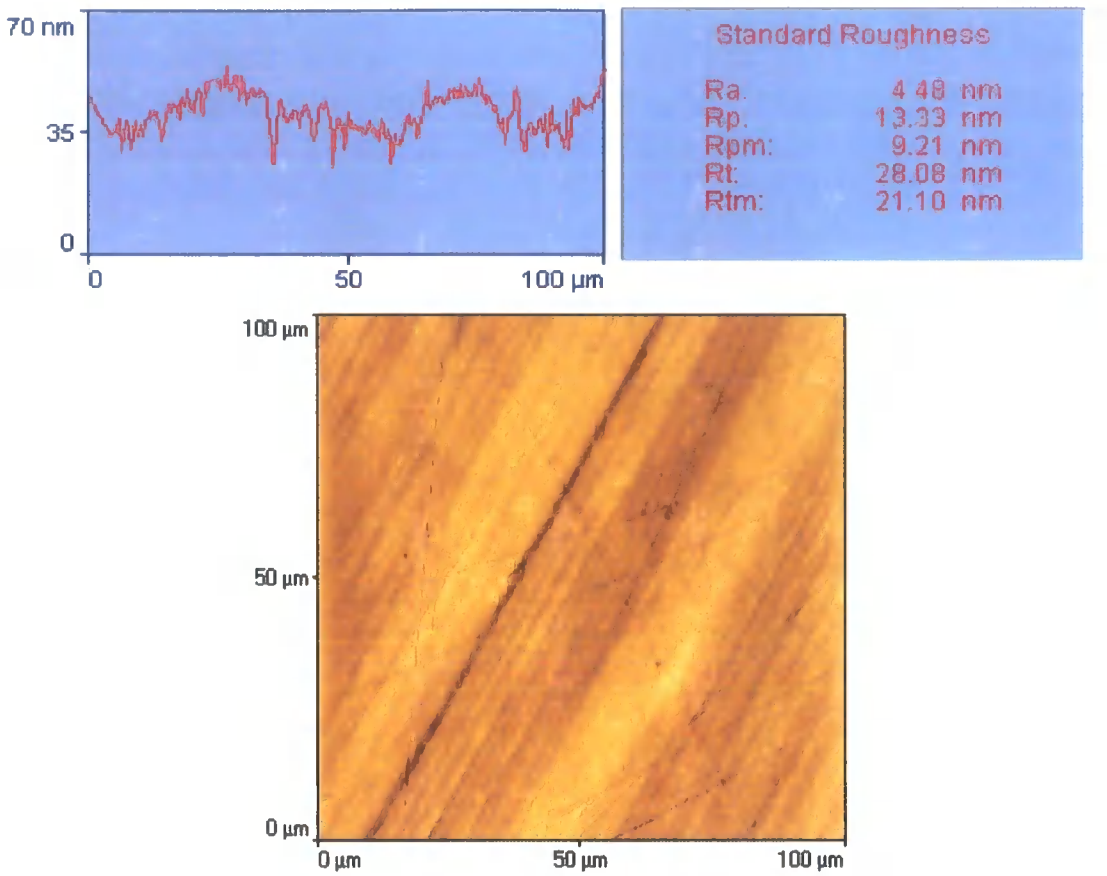

Figure 5.71. Top view AFM image and topographic data of unmodified stainless steel plate sample

100 μm^2 AFM image of 2 x 10^{17} N^+ ions/cm^2 implanted stainless steel samples showed no changes in the surface topography, and typical roughness values remained the same as the unmodified samples. However, high magnification examinations of the surfaces revealed some surface degradation patterns on the surface, as a result of N^+ ion implantation. Figure 5.72 shows a higher magnification AFM image of the unmodified and 2 x 10^{17} N^+ ions/cm^2 implanted stainless steel, illustrating the topographic modification post ion implantation.

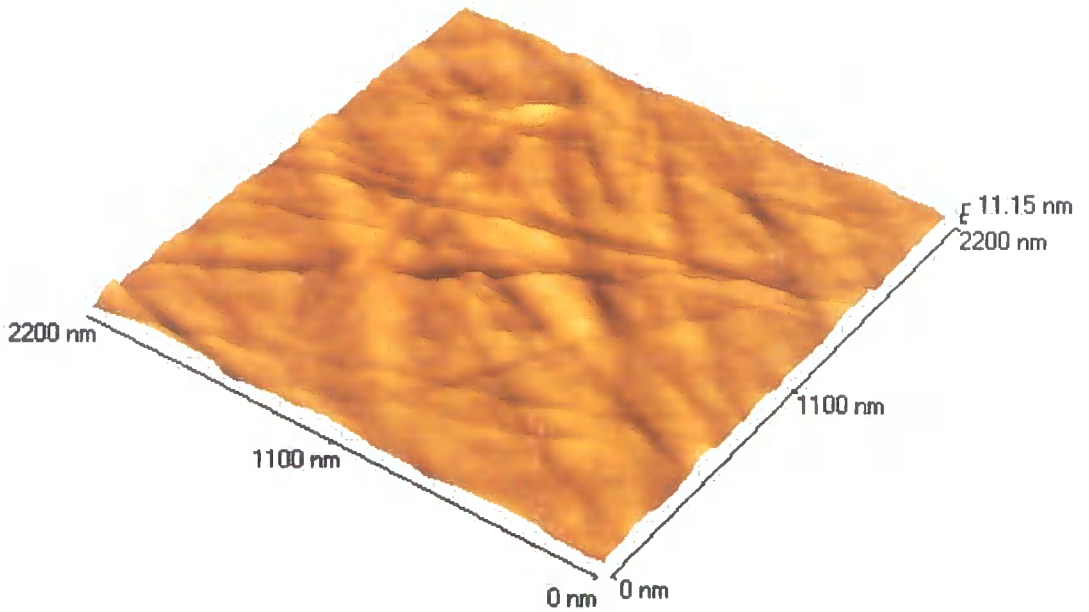

(a)

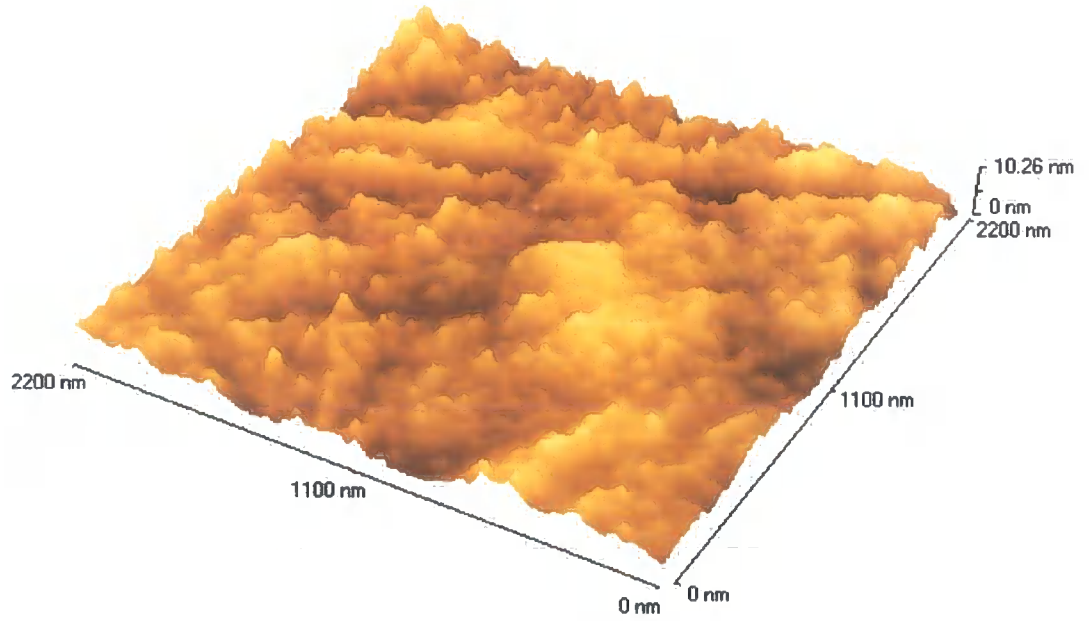

(b)

Figure 5.72. 3-D projection high magnification AFM image of (a) unmodified and (b) 2 x 10^{17} N^+ ions/cm^2 implanted stainless steel

Post wear testing, the surface topography of the unmodified stainless steel plates were characterised by random scratches and increased standard roughness values. In contrary, the topography of the ion implantation modified plates showed less post wear testing

damage and lower standard roughness values. Figures 5.73 and 5.74 shows 3-D projection 100 μm^2 AFM images and topographic data of the unmodified and 2 x 10^{17} N^+ ions/cm^2 implanted stainless steel plates articulated against unmodified and 5 x 10^{15} N^+ ions/cm^2 implanted UHMWPE respectively (post wear testing to 5.5 million wear cycles).

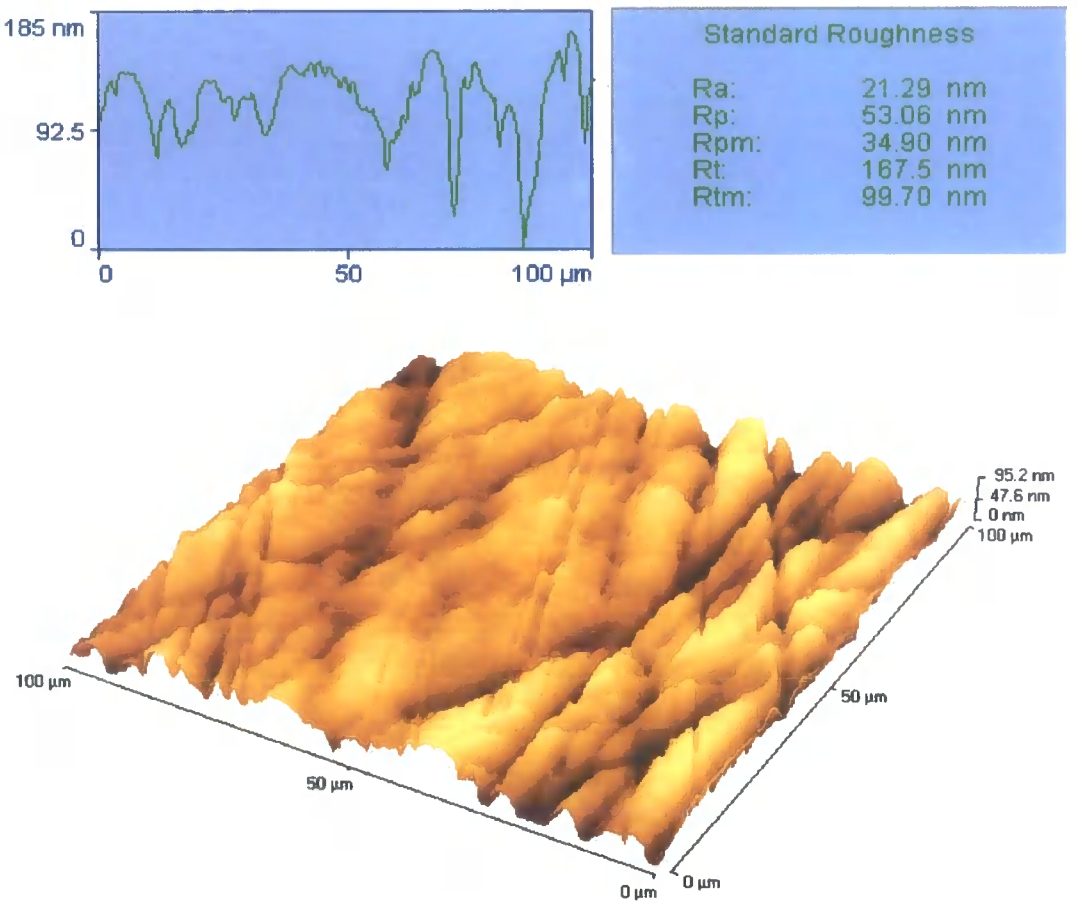

Figure 5.73. 3-D AFM projection and topographic data of unmodified stainless steel plate post wear against unmodified UHMWPE pin (wear track region)

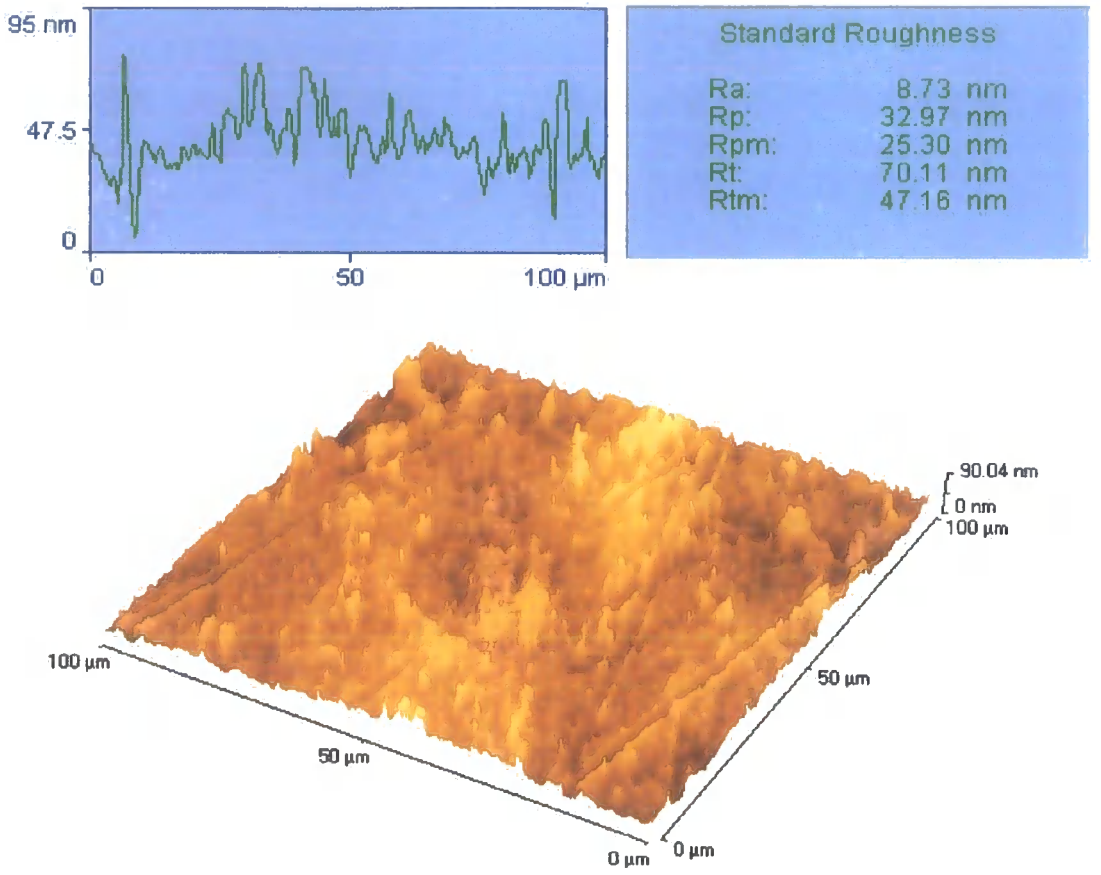

Figure 5.74. 3-D AFM projection and topographic data of 2 x 10^{17} N^+ ions/cm^2 implanted stainless steel plate post wear against modified UHMWPE pin

The surface topography of all UHMWPE wear pins (modified or unmodified) post wear test against stainless steel (modified or unmodified) (fig. 5.75), showed distinct surface morphologies characterised by wear features that resembled those observed on the samples tested against Ti6Al4V (modified and unmodified), and analysised *ex vivo* UHMWPE components (fig. 5.38 b).

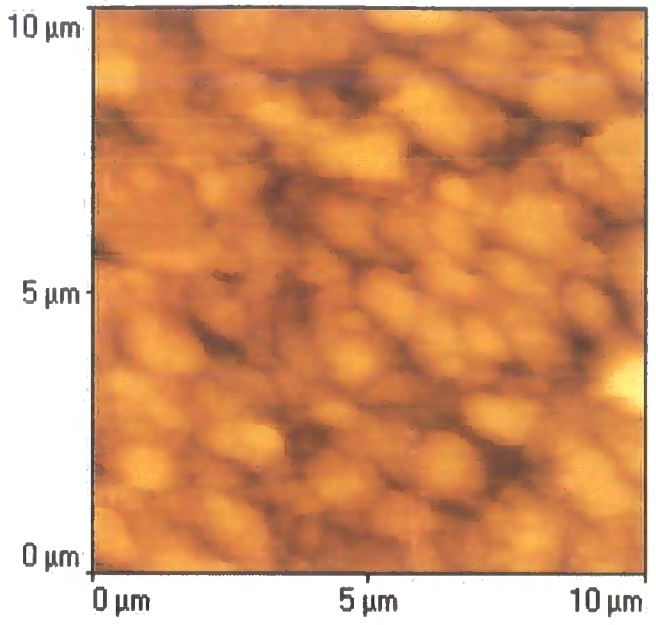

Figure 5.75. Wear induced topographic morphology of UHMWPE (AFM) following articulation against stainless steel *in vitro*

5.3 Co-Cr-Mo and UHMWPE

5.3.0 Introduction

The N^+ ion implantation distribution in Co-Cr-Mo, microhardness results of the samples in both modified and unmodified forms, tribological wear test results of UHMWPE (modified and unmodified) articulating against Co-Cr-Mo, topography and standard roughness of the as polished and modified Co-Cr-Mo are all presented under the following sections (5.3.1 to 5.3.4).

5.3.1 Projected N^+ Ion Distribution

The results of the TRIM stopping range calculations for N^+ ion implantation into Co-Cr-Mo target using density 8.4 g/cm2 with an accelerating energy of 90 keV are shown in figures 5.76 and 5.77.

Simulation of the range of N^+ ions into Co-Cr-Mo target is shown in figure 5.76. The estimated mean longitudinal range of N^+ ions in the target was calculated to be at a

depth of 0.1 μm with straggling of 0.04 μm. The overall distribution of the ions assumed approximately a classical Gaussian profile, as with the other materials (Ti6Al4V, stainless steel, and UHMWPE). The maximum N^+ ion penetration depth was approximately 0.2 μm into the Co-Cr-Mo surface.

Figure 5.77 shows the calculation of the vacancy distribution produced by both N^+ ion collisions and target atom recoil collisions, from which a total of 414 target vacancies per incoming N^+ ion was calculated.

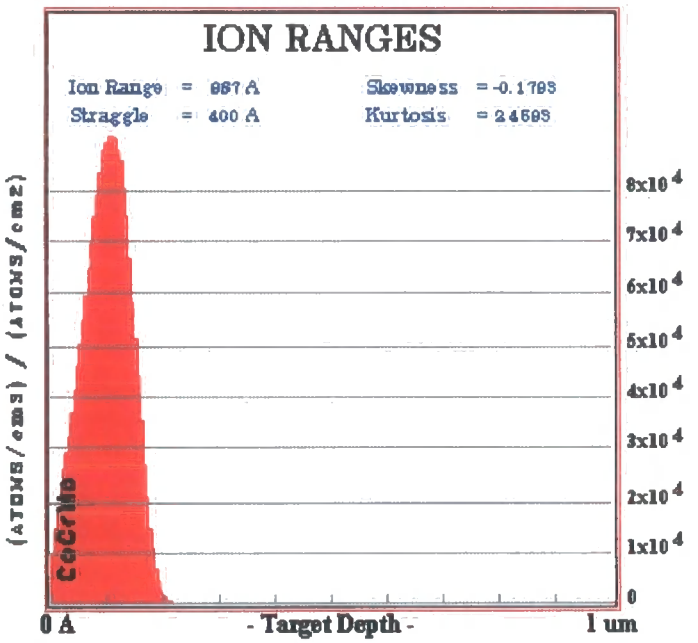

Figure 5.76. TRIM simulation of range of N^+ ions into Co-Cr-Mo

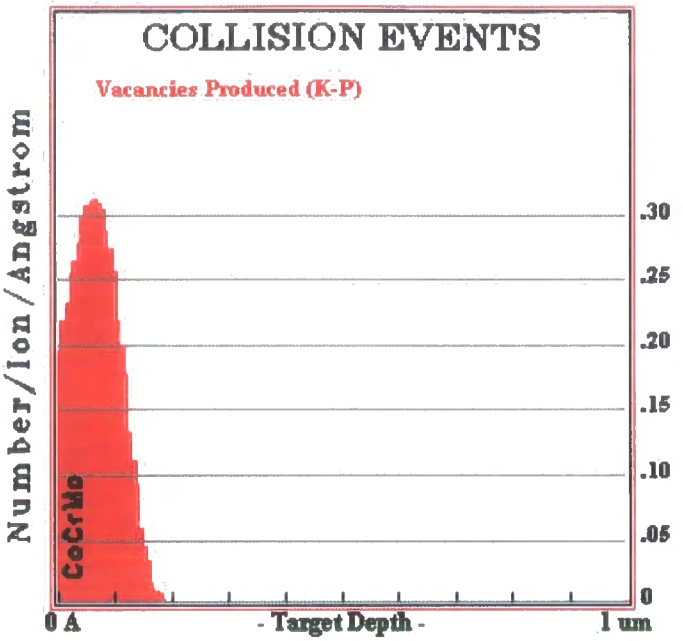

Figure 5.77. TRIM simulation of vacancy production within Co-Cr-Mo target upon ion implantation

5.3.2 Microhardness Determination

The Knoop microhardness results of the unmodified and N^+ ion implanted Co-Cr-Mo samples were reproduced and the results are shown in figure 5.78. The microhardnesses of the modified samples were observed to increase with decreasing indentation load, and the highest values were measured at an indentation load of 1 gf. The results indicated an increase in mean hardness from 570 ± 61 KHN_{1gf} for the unmodified material, to 1175 ± 101 KHN_{1gf} for the 2 x 10^{17} N^+ ions/cm^2 implanted material (Appendix C2).

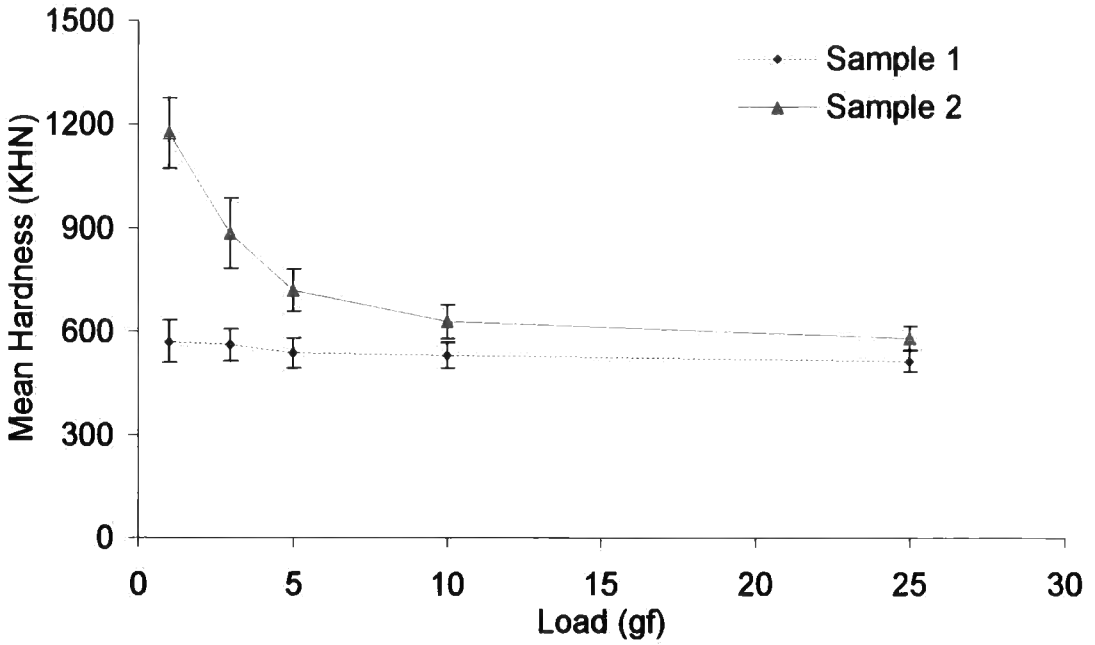

Figure 5.78. Knoop microhardness of unmodified and N^+ ions implanted Co-Cr-Mo. Where sample 1 is unmodified Co-Cr-Mo; and sample 2 is 2 x 10^{17} N^+ ions/cm^2 implanted Co-Cr-Mo.

Inspection of figure 5.79 demonstrates the surface dependence and depth graded property modification induced upon ion implantation, where the mean hardness values at different loads have been plotted against the mean knoop indent penetration depth into the samples. The indentation depths were calculated from the indent width using the Knoop indenter geometry (Appendix C1) for loads of 1, 3, 5, 10 and 25 gf respectively. The reported values are an average of 10 measurements under each load (Appendix C1, table C1.5).

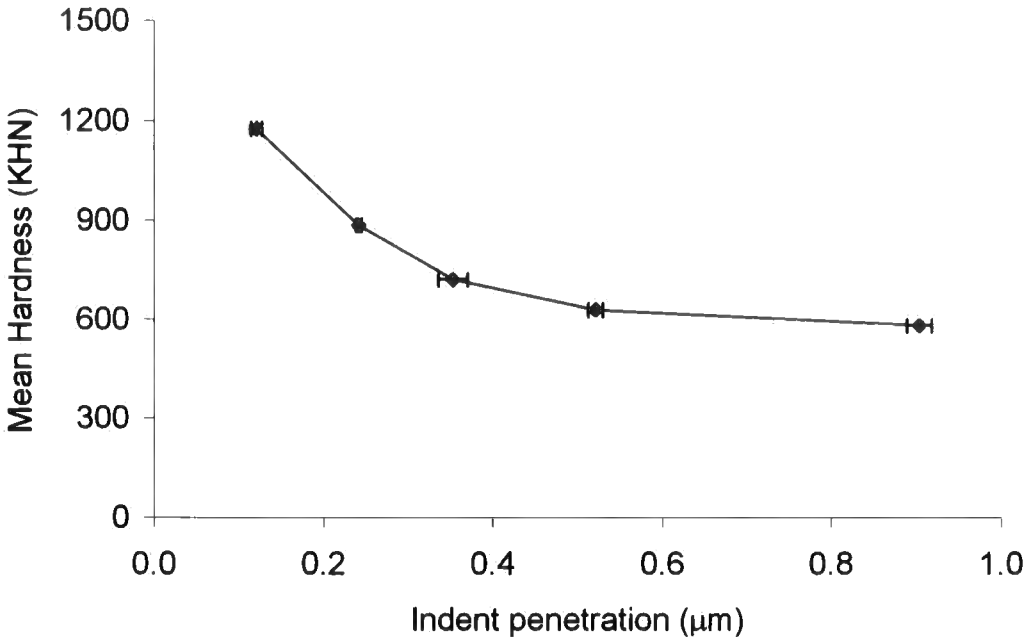

Figure 5.79. Depth dependence of Knoop microhardness for 2 x 10^{17} N^+ ion/cm^2 implanted Co-Cr-Mo

5.3.3 Tribological Wear Test

5.3.3.0 Introduction

The tribological wear test results of UHMWPE (modified and unmodified) wear pins against Ti6Al4V plates (modified and unmodified) are reported under the following sections (5.3.3.1 to 5.3.3.3) (Appendix A6).

5.3.3.1 Unmodified UHMWPE against unmodified Co-Cr-Mo

Tribological wear test results of unmodified UHMWPE against unmodified Co-Cr-Mo sliding couple, expressed in volume loss (mm^3) of the UHMWPE against sliding distance (km) are shown in figure 5.80. Two wear phases could clearly be distinguished on the wear curves. There were no significant differences between the wear factors of the UHMWPE wear pins, and a mean k_o of 1.29 ± 0.05 x 10^{-6} mm^3/Nm was calculated over a sliding distance of 206 km (> 5.5 million wear cycles). An initial mean k_o of 1.75 ± 0.08 x 10^{-6} mm^3/Nm was calculated up to a sliding distance of 54 km, and a steady-

state mean k_o of 0.96 ± 0.03 x 10^{-6} mm^3/Nm was calculated between 54 and 206 km sliding distance. The mean initial and final weight readings of the plates were recorded, and the mean weight loss results post wear reported in table 5.8.

Topographic examinations of the plate surfaces post wear test, using AFM and NCI (table 5.9) revealed wear tracks characterised by some scratches. Wear curves were linear, and no transfer films were observed on the plates during and post wear. There was no discolouration of the bovine serum lubricant following wear testing. Machining and microtoming marks on the surface of the UHMWPE wear pins wore away with test duration, and the surfaces became smooth. Topographic examinations of the worn UHMWPE pins showed similar surface morphology observed on the UHMWPE pins tested against Ti6Al4V and stainless steel, and resembled those of *ex vivo* UHMWPE components examined under AFM.

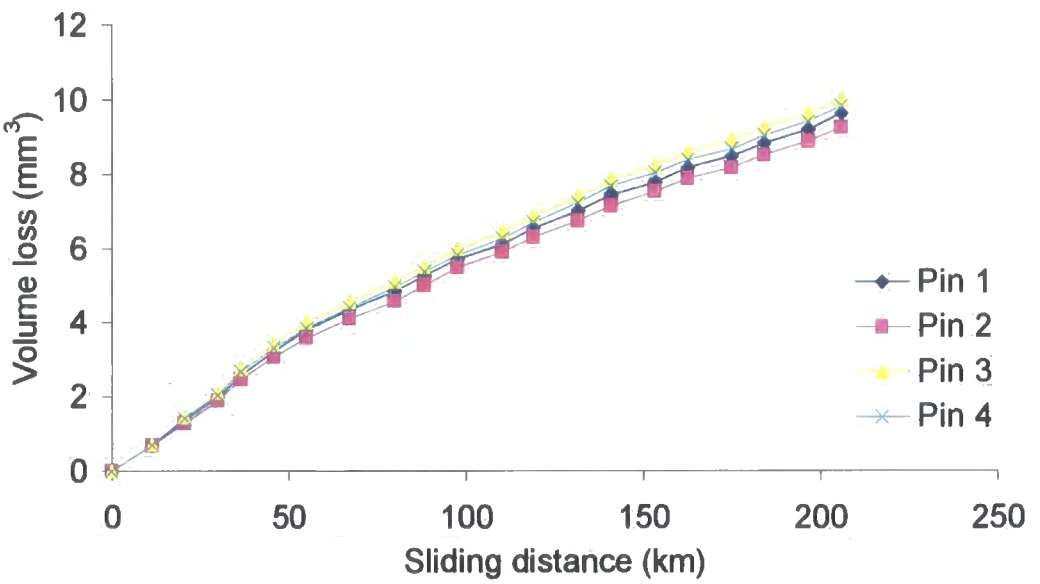

Figure 5.80. Wear of unmodified UHMWPE pins against unmodified Co-Cr-Mo plates

5.3.3.2 Unmodified UHMWPE against N^+ ion implanted Co-Cr-Mo

Figure 5.81 shows the wear volume loss against sliding distance graph of unmodified UHMWPE sliding and rotating against 2 x 10^{17} N^+ ion/cm^2 implanted Co-Cr-Mo. Linear wear curves with no significant differences between the wear volumes of the

pins were measured, and a mean k_o of 0.75 ± 0.03 x 10^{-6} mm^3/Nm was calculated over a sliding distance of 216 km (> 5.5 million wear cycles). An initial slightly higher mean k_o of 0.95 ± 0.06 x 10^{-6} mm^3/Nm was measured up to a sliding distance of 42 km, due to a wearing in type process, and a steady-state mean wear factor of 0.63 ± 0.005 x 10^{-6} mm^3/Nm was measured between 42-216 km sliding distance. There was a reduction in mean k_o of the UHMWPE compared with samples tested against unmodified Co-Cr-Mo.

No surface damage was observed in the region of pin contact on the plate during and post testing. AFM images and NCI analysis (table 5.9) revealed the undamaged surface topography and low R_a values of the surface respectively.

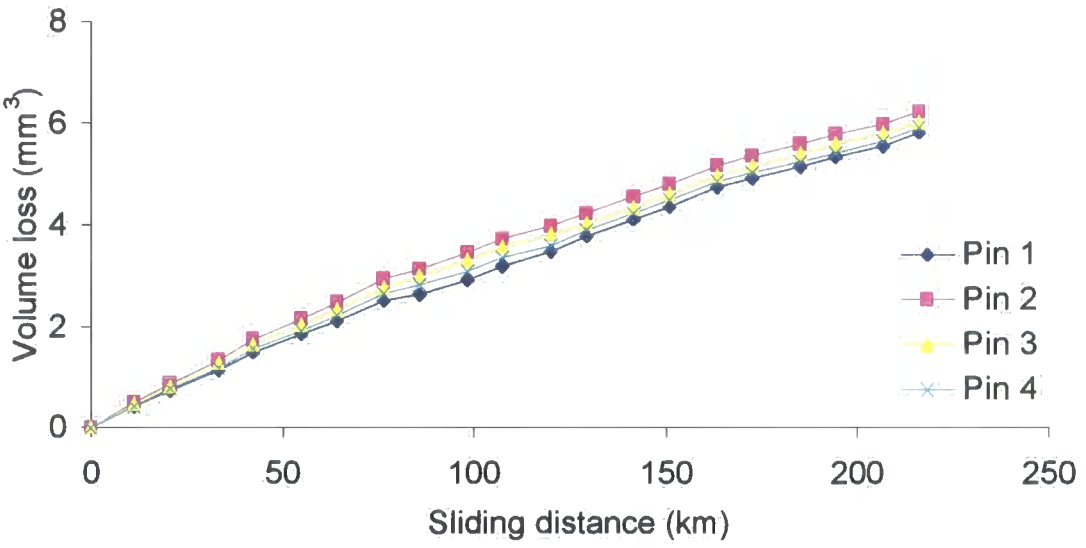

Figure 5.81. Wear of unmodified UHMWPE pins against 2 x 10^{17} N^+ ions/cm^2 implanted Co-Cr-Mo plates

5.3.3.3 N^+ ion implanted UHMWPE against N^+ ion implanted Co-Cr-Mo

Figure 5.82 shows the graph of 5 x 10^{15} N^+ ion/cm^2 implanted UHMWPE wear volume loss against sliding distance, when tested against 2 x 10^{17} N^+ ion/cm^2 implanted Co-Cr-Mo. Linear wear curves were observed and a mean k_o of 0.67 ± 0.03 x 10^{-6} mm^3/Nm was calculated over the test duration of 204 km (> 5.5 million wear cycles). An initial slightly higher mean k_o of 0.75 ± 0.05 x 10^{-6} mm^3/Nm was measured up to a sliding distance of 64 km, due to a wearing in type process, and a steady-state mean wear factor

of 0.58 ± 0.02 x 10^{-6} mm^3/Nm was measured between 64-204 km sliding distance. Compared with unmodified UHMWPE pins tested against unmodified Co-Cr-Mo plates, there was a reduction in the mean k_o of the modified UHMWPE pins.

AFM images of the wear surfaces of the plates showed no damage in the the region of pin contact on the plate and low R_a values (table 5.9), compared with unmodified Co-Cr-Mo plates tested against unmodified UHMWPE pins. AFM images of all the worn polymer surfaces showed similar wear features post wear, to those observed on UHMWPE samples articulated against Ti6Al4V and stainless steel plates, and resembled those seen on *ex vivo* UHMWPE components.

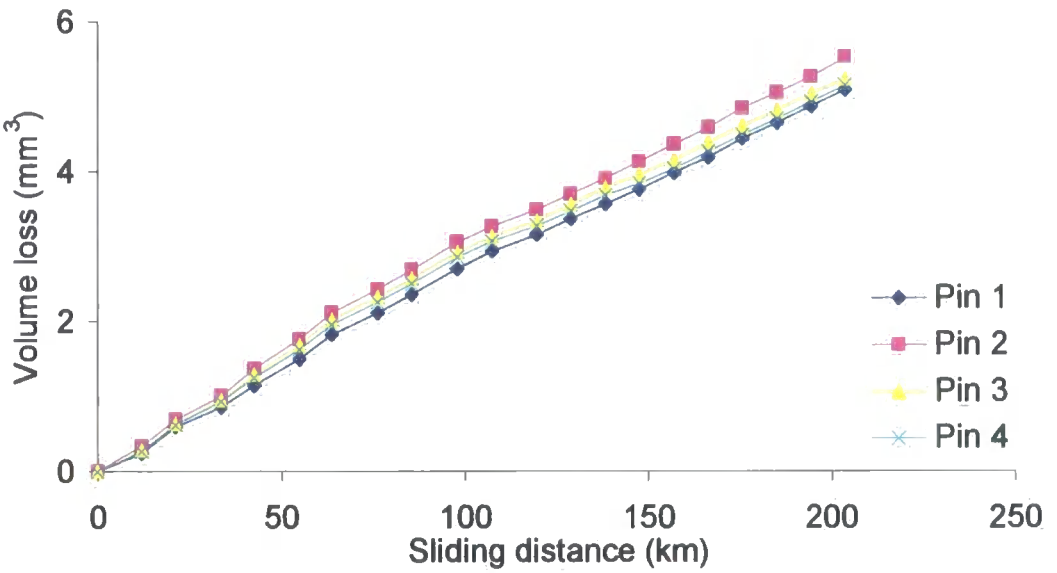

Figure 5.82. Wear of 5 x 10^{15} N^+ ion/cm^2 implanted UHMWPE pins against 2 x 10^{17} N^+ ion/cm^2 implanted Co-Cr-Mo plates

5.3.3.4 Summary of Results

The tribological wear test results, and the mean R_a values of all the materials tested pre and post wear are summarised and presented respectively in tables 5.8 and 5.9. Table 5.10 summarises the measured changes in hardness for the Co-Cr-Mo and UHMWPE substrates.

Figure 5.83 summarises the results of the mean wear curves of UHMWPE pins (modified and unmodified) articulated against Co-Cr-Mo plates (modified and unmodified).

Table 5.8. Summary of *in vitro* tribological performance of unmodified and N^+ ion implantation modified UHMWPE/Co-Cr-Mo biomaterial couples after 5.5 million cycles of testing

Wear Couple[a]	Mean UHMPWE k_o (x 10^{-6} mm^3/Nm)	Mean Co-Cr-Mo Wt Loss (μg)[b]
Unmodified UHMWPE/unmodified Co-Cr-Mo	1.39 ± 0.05	45 ± 0.05
Unmodified UHMWPE / 2 x 10^{17} N^+ ions cm^{-2} implanted Co-Cr-Mo	0.75 ± 0.03	27 ± 0.05
5 x 10^{15} N^+ ions cm^{-2} implanted UHMWPE/2 x 10^{17} N^+ ions cm^{-2} implanted Co-Cr-Mo	0.67 ± 0.03	10 ± 0.02

[a]Samples implanted with N^+ ions at 90 keV (Co-Cr-Mo) and 80 keV (UHMWPE)

[b]Plate measured before and at the end of test

Table 5.9. Mean arithmetic mean surface roughness (R_a) of Co-Cr-Mo and UHMWPE samples

Material Surface	Mean R_a (μm)	
	Pre wear	Post wear
Unmodified Co-Cr-Mo (articulated against unmodified UHMWPE)	0.005 ± 0.002	0.011 ± 0.004
2 x 10^{17} N^+ ions/cm^2 implanted Co-Cr-Mo (articulated against modified and unmodified UHMWPE)	0.005 ± 0.002	0.008 ± 0.002
Unmodified UHMWPE (articulated against unmodified and modified Co-Cr-Mo)	1.3 ± 0.14	0.06± 0.05
5 x 10^{15} N^+ ions/cm^2 implanted UHMWPE (articulated against unmodified and modified Co-Cr-Mo)	1.3 ± 0.11	0.05 ± 0.05

Table 5.10. Summary of Knoop microhardness of unmodified and N^+ ion implantation modified Co-Cr-Mo and UHMWPE substrates

Substrate[a]	Knoop Microhardness (KHN_{1gf})
Unmodified Co-Cr-Mo	570 ± 61
2 x 10^{17} N^+ ions/cm^2 implanted Co-Cr-Mo	1175 ± 101
Unmodified UHMWPE	3.4 ± 0.5
5 x 10^{15} N^+ ions/cm^2 implanted UHMWPE	12.8 ± 1.6

[a]Substrates implanted with N^+ ions at 90 keV (Co-Cr-Mo), and 80 keV (UHMWPE)

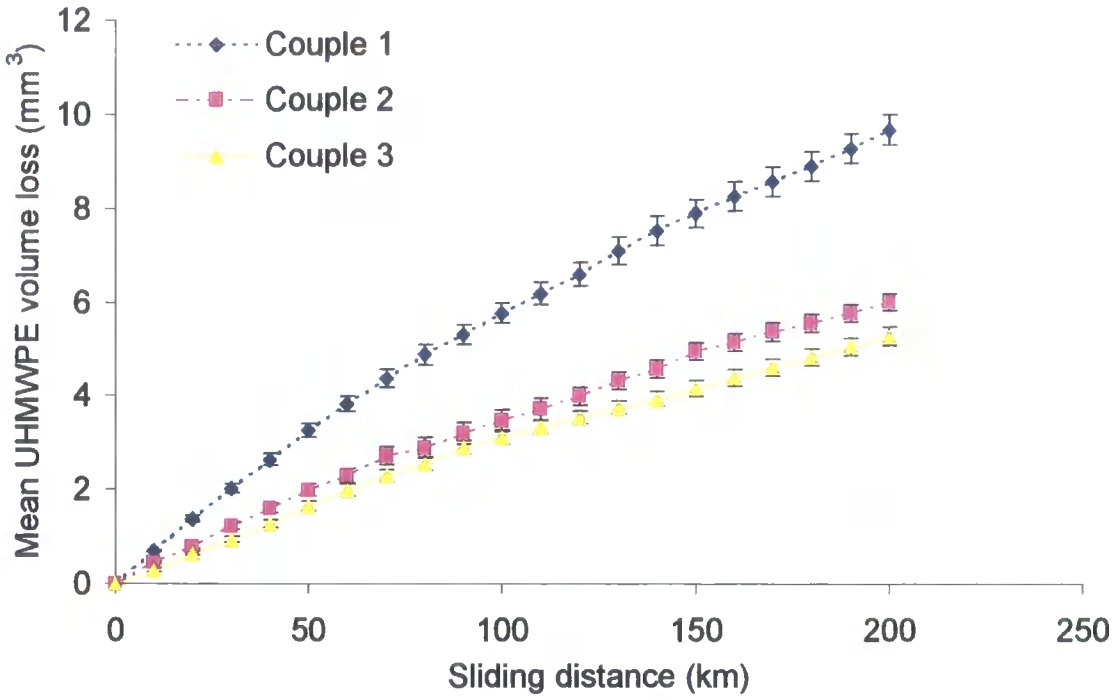

Figure 5.83. Mean wear behaviour of UHMWPE pins (modified and unmodified) against Co-Cr-Mo plates (modified and unmodified). Where couple 1 is unmodified UHMWPE/unmodified Co-Cr-Mo; couple 2 is Unmodified UHMWPE/2 x 10^{17} N^+ ions/cm^2 implanted Co-Cr-Mo; and couple 3 is 5 x 10^{15} N^+ ions/cm^2 implanted UHMWPE/2 x 10^{17} N^+ ions/cm^2 implanted Co-Cr-Mo (table 5.5).

5.3.4 Surface Topography

Topographic images of the modified and unmodified Co-Cr-Mo and UHMWPE surfaces pre and post wear test, are shown in figures 5.84 to 5.88.

Figure 5.84 shows a 100 μm^2 top view AFM image of unmodified Co-Cr-Mo and topographic data. The topography was typical of the surface achieved post polishing (characterised by scratch marks from polishing), and prior to surface modification and tribological testing.

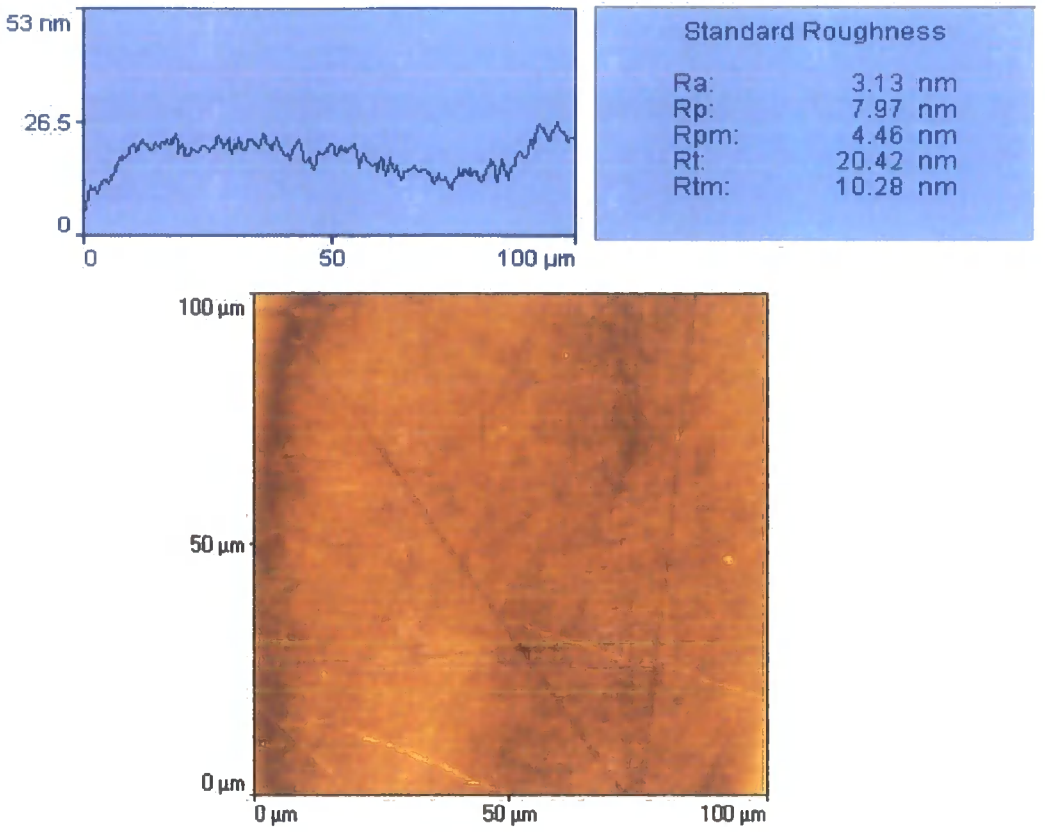

Figure 5.84. Top view AFM image and topographic data of unmodified Co-Cr-Mo

100 μm^2 AFM image of 2 x 10^{17} N^+ ions/cm^2 implanted Co-Cr-Mo samples showed no changes in the surface topography, and typical roughness values remained the same as the unmodified samples. However, high magnification examinations of the surfaces revealed some surface degradation patterns on the plates. Figure 5.85 shows a higher magnification image of the unmodified and 2 x 10^{17} N^+ ions/cm^2 implanted Co-Cr-Mo, illustrating the topographic modification post ion implantation.

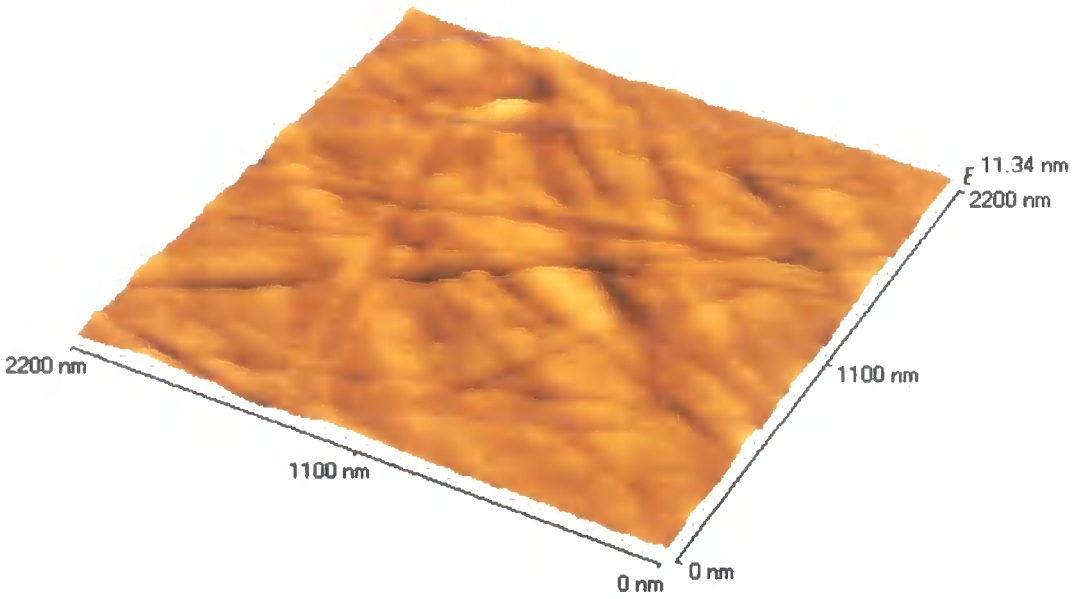

(a)

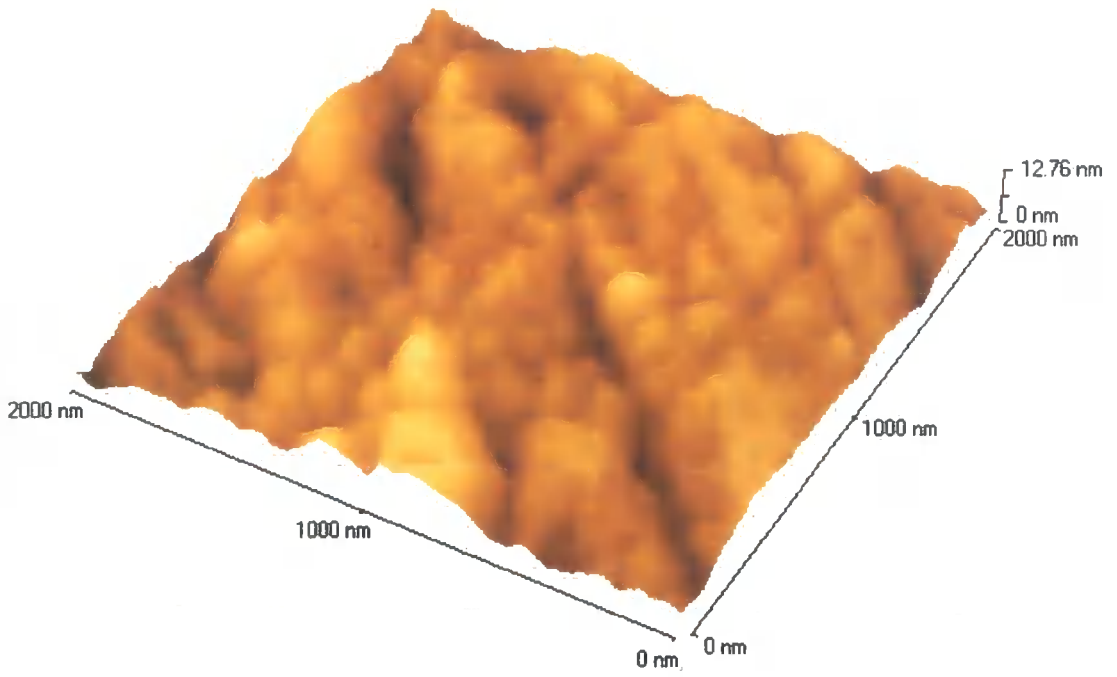

(b)

Figure 5.85. High magnification 3-D projection AFM image of (a) unmodified and (b) 2 x 10^{17} N^+ ions/cm^2 implanted Co-Cr-Mo

The surface topography of the unmodified Co-Cr-Mo plates post wear test were characterised by random scratches and higher standard roughness values. In contrast, the ion implantation modified plates showed less surface damage in the region of pin

contact on the plate. Figures 5.87 and 5.88 respectively shows the 3-D projection 100 μm^2 AFM images and topographic data of unmodified and 2 x 10^{17} N^+ ions/cm^2 implanted Co-Cr-Mo plates post wear.

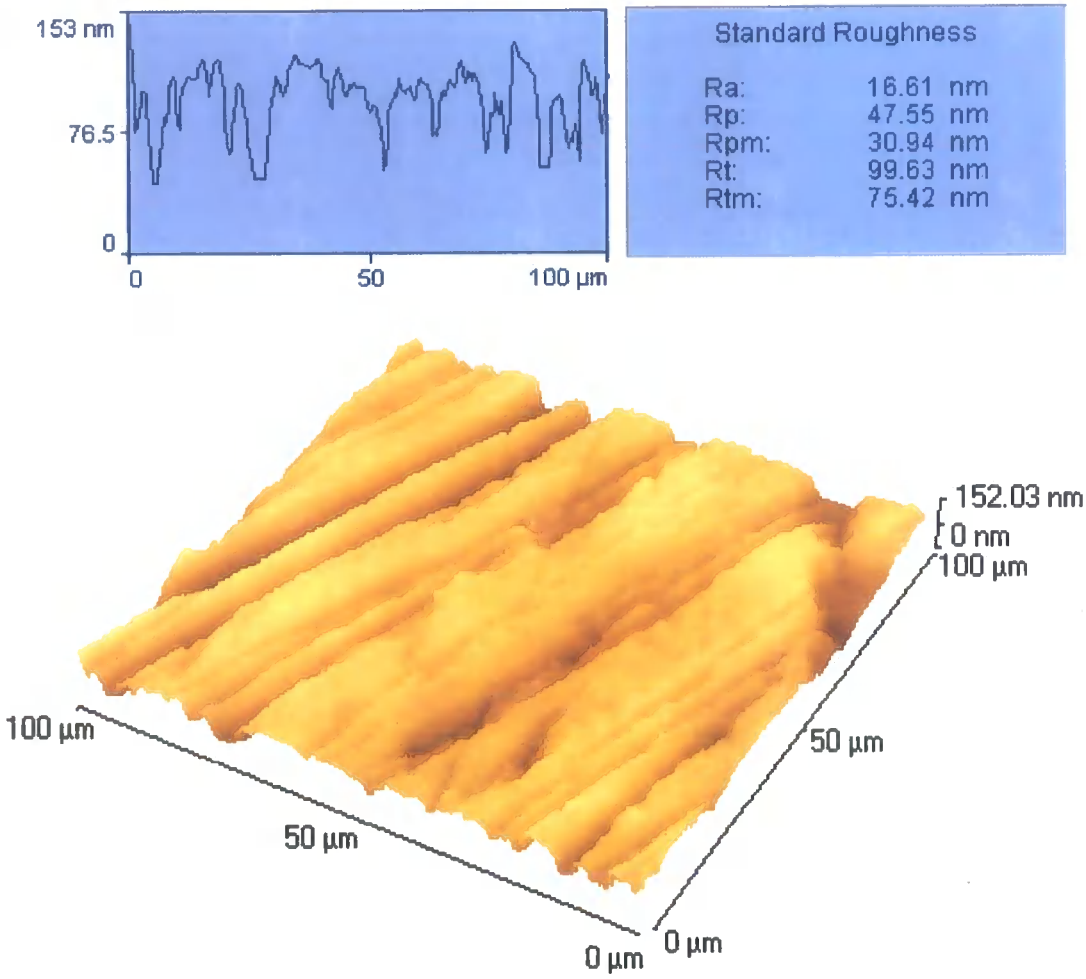

Figure 5.86. 3-D AFM projection and topographic data of unmodified Co-Cr-Mo post wear

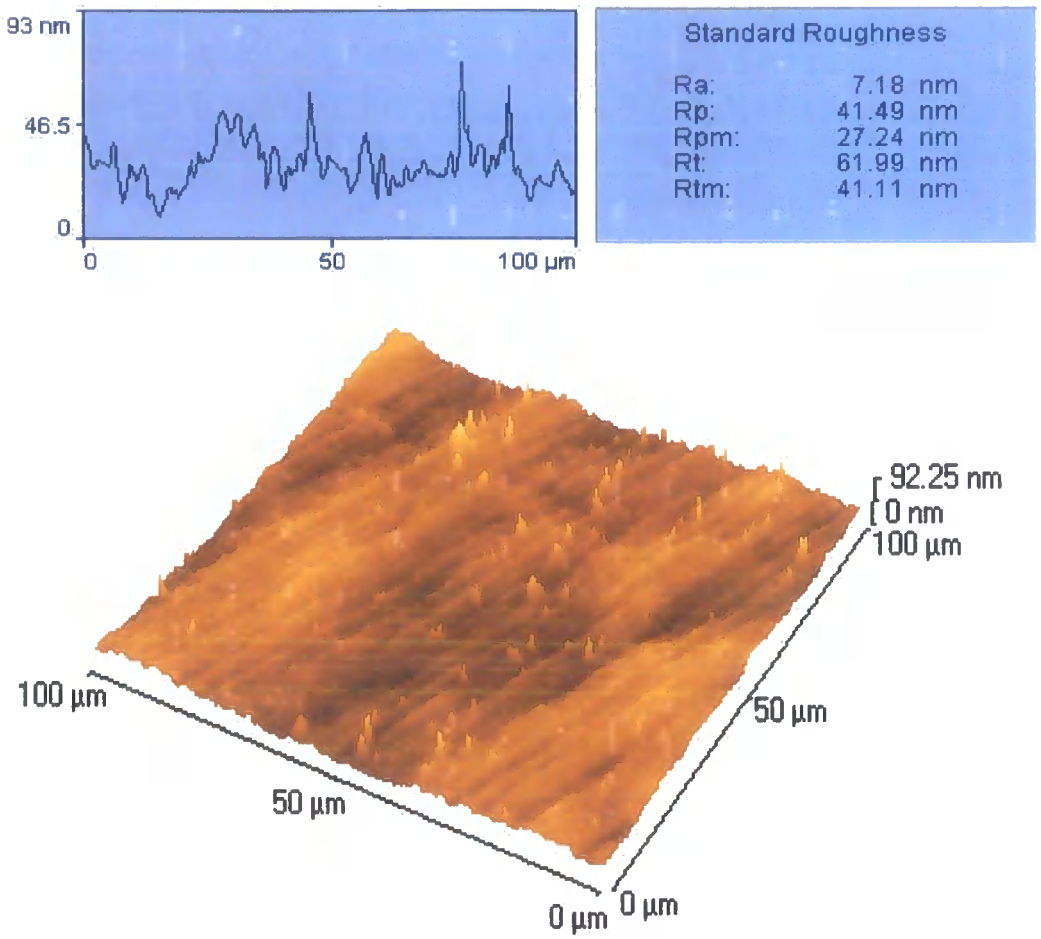

Figure 5.87. 3-D AFM projection and topographic data of 2 x 10^{17} N^+ ions/cm^2 implanted Co-Cr-Mo post wear

The surface topography of all UHMWPE pin samples (fig. 5.88) both modified and unmodified, showed similar surface morphology features post wear against Co-Cr-Mo (modified and unmodified), as was observed on the UHMWPE samples tested against Ti6Al4V and stainless steel.

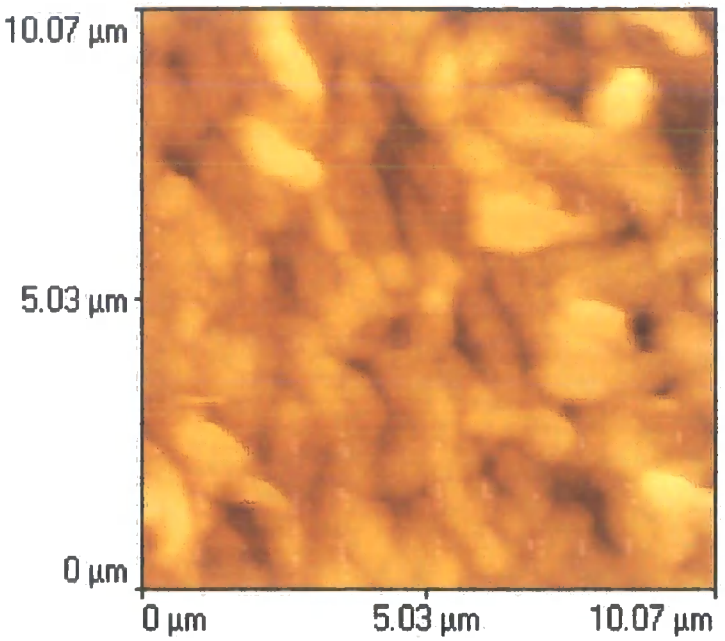

Figure 5.88. Wear induced topographic morphology of UHMWPE (AFM) following articulation against Co-Cr-Mo *in vitro*

CHAPTER SIX – DISCUSSION

6.0 Introduction

The following discussion will review the results of N^+ ion implantation on the biomaterials, in terms of the topographic, microhardness, chemical, and tribological properties of the materials selected and investigated in this study.

6.1 Effects Of N^+ Ion Implantation

6.1.0 Introduction

N^+ ion implantation into biomaterials is known to have numerous effects such as increase in hardness, wettability, wear and chemical resistance of the materials. The topographical, chemical, and microhardness effects of N^+ ion implantation are discussed under the following sections (6.2.1 to 6.2.3).

TRIM calculations were used to provide a theoretical profile of the depth and distribution of the N^+ ions within the biomaterials investigated in this work.

6.1.1 Effects of N^+ ion implantation on Ti6Al4V

6.1.1.0 Introduction

TRIM calculations estimated the mean projected N^+ ion depth and total ion range within which the volume of surface at. % N was dispersed within the Ti6Al4V material post N^+ ion implantation. From the calculations (section 5.1.2), a total of 358 target atom vacancies per incident N^+ ion were calculated. Such vacancies produced together with lattice defects as a result of the implantation process are known to lead to the tendency for swelling of the bombarded zone [74]. The maximum penetration depth of N^+ ion implantation into materials have been reported to vary between 0.1 to < 1 μm depending on the implantation energy, and is known to be typically within 0.2-0.5 μm in metals [26, 74, 134, 135]. A mean projected N^+ ion range of 0.15 μm and a corresponding maximum ion penetration depth of 0.25 μm into the target were calculated by TRIM simulations during the study.

The energy dissipation within the Ti6Al4V reached a maximum at the mean projected ion depth (a nuclear stopping phenomenon), as a result of the target atom recoils (fig. 5.6). It has been reported [74, 129] that, within such a mean depth, maximum concentrations of vacancies, dislocations and other lattice defects are found, producing a volume of severely disrupted lattice in the near-surface region. These observations were as a results of the physical changes induced by the ion implantation process due to atomic and nuclear collisions, and are known to increase the surface wear resistance (section 6.2.1.2) and chemical resistance of materials. Improvements in chemical resistance of the implanted Ti6Al4V samples were observed during the study, when the materials (both modified and unmodified) were etched with $HF/HNO_3/H_2O$ solution (section 4.3.1). The N^+ ion implanted Ti6Al4V alloys showed high resistance to the chemical attack and the microstructures were barely resolved, compared to the non-implanted material (figs. 5.3 (a) and (b)). This may be due to the N^+ ion implantation process stabilising a more chemical resistant structure on the surface of the alloy, such as α-titanium. Nitrogen is known to stabilise α-titanium (which has excellent corrosion resistance) on the surface of Ti6Al4V, and hence minimises the effects of chemical attack on the material surface post N^+ ion implantation [102]. In addition, N^+ ion implantation can significantly modify the near surface composition and hence reduce the chemical affinity of the surfaces in contact, and strengthen the metal oxide interface.

6.1.1.1 Topographical effects

The impact of energetic ions on material surfaces during the process of ion implantation is known to cause sputtering and blistering on the material surfaces, and has been found that blistering dominates if higher implantation doses ($> 10^{17}$ N^+ ions/cm^2) and energies (> 10 keV) are injected into metals [97, 136-138]. N^+ ions can combine together to form N_2 gas bubbles within the surfaces of the materials, during the process of N^+ ion implantation [97], so leading to the formation of the blisters.

Considering the implantation conditions used during the study (section 4.2.3, table 4.5) sputtering and surface blister formation would be expected to be the main topographic changes on the material surfaces. Such blister formations, were observed on the implanted Ti6Al4V surfaces under high magnification contact AFM imaging, compared with the unmodified material surfaces. As a result of the ion beam bombardment of the

energetic N^+ ions, surface blister formation as well as sputtering induced increased surface roughness of the Ti6Al4V surfaces increased with increasing implantation dose (figs. 5.25-5.29).

6.1.1.2 Chemical effects

The chemical effects of N^+ ion implantation on Ti6Al4V were investigated by XPS study in this work (section 5.1.6). XPS investigations confirmed the presence of N within all the implanted surfaces, by revealing the distinct N 1s binding energy peak in the survey spectrum (figs. 5.43, 5.51 and 5.54), compared with the unmodified material surface (fig. 5.39). High resolution XPS scans of the Ti 2p binding energy positions on both ion implanted and unmodified Ti6Al4V surfaces revealed twin Ti 2p XPS doublets (fig. 5.45) on the implanted surface, and a single Ti 2p XPS doublet (fig. 5.40) on the unimplanted sample.

The presence of the N 1s peak, and Ti 2p attributable to Ti^+ 2p 3/2 species on the surface of the implanted samples indicated the presence of TiN (455.6 eV), the binding energy position of which agrees with the published data for TiN (455.7 eV) [139]. The formation of TiN crystallites on N^+ ion implanted Ti6Al4V alloys has also been observed by several other workers [128, 129, 140-142]. Correspondingly identified were Ti^+ 2p ½ species attributed to the formation of TiN. The Ti species on both modified and unmodified material attributable to Ti^{4+} 2p 3/2 were identified to be entirely due to the presence of TiO_2 oxide layer on the material surfaces, and their binding energies (458.3 and 458.7 eV respectively for species on modified and unmodified Ti6Al4V) were in agreement with published data for pure TiO_2 [139]. Correspondingly, Ti species on both modified and unmodified material surface identified as Ti^{4+} 2p ½ were also attributed to the presence of TiO_2.

In addition, high resolution scan of the N 1s peak showed a triple peak structure (fig. 5.48) with a main peak at 396.2 eV, which corresponded to nitride formation and was in agreement with published work by Garcia *et al* [77]. The N 1s peak positions were approximately the same for the different implantation doses investigated in this work, indicative of the same type of nitride formation in the implanted materials. The two smaller unidentified peaks at approximately 398 eV and 400 eV binding energies were probably of the form TiN_xO_y, and have been identified by some investigators as

oxinitrides and a mixture of TiN-TiO [102, 135]. These compounds are known to produce a variety of colours from bright gold to dark purple on Ti6Al4V surfaces, which were observed on visual inspection during the study, when the implantation dose increased from 2 x 10^{17} to 1 x 10^{18} and 1 x 10^{21} N^+ ions/cm^2 respectively.

The presence of the protective oxide surface layer (TiO_2) is known to provide the Ti6Al4V alloy with high corrosion resistance under static conditions [18, 21, 35, 143], as well as contribute to its favourable biocompatibility. However, these layers are easily removed during articulation with other materials in artificial joints, and leads to severe abrasive wear of both articulating surfaces. The identification of the TiN formation on the alloy upon N^+ ion implantation is significant, as TiN is known to stabilise the outer protective oxide layer [89, 134], and hence reduce the rate of removal and severe wear of the surfaces during articulation with other materials.

6.1.1.3 Microhardness effects

The microhardnesses of the ion implanted Ti6Al4V samples were measured to be significantly higher than those of the unimplanted ones, and increased with increasing implantation dose (section 5.1.3, fig. 5.12). Increasing hardness with increasing implantation dose and ion energy is known to occur and be more favourable for the formation of hard phase TiN precipitates [134, 143-145]. TiN was observed on all the implanted samples during the study with XPS (sections 5.1.6.2 to 5.1.6.4), indicating that the minimum implantation dose of 2 x 10^{17} N^+ ions/cm^2 used during the study, was more than the minimum dose required for the formation of the hard phase TiN. The formation of TiN leads to high hardness, and at a load of 1 gf, significant hardness increases of $\approx$ 2.1, 3.1, and 4.1 times were calculated respectively for when the materials were ion implanted with 2 x 10^{17}, 1 x 10^{18}, and 1 x 10^{21} N^+ ions/cm^2, compared with the unmodified material (table 5.3).

The hardness increase upon N^+ ion implantation and with implantation dose in this study, have been similarly observed by several other workers [72, 100, 101, 140, 145-148]. Oliver *et al* [72] performed microhardness tests on 3.5 x 10^{17} N^+ ions/cm^2 implanted Ti6Al4V samples (at an energy of 90 keV), and observed an increase in hardness of $\approx$ 2 times at an indentation depth of 0.05 μm, compared to the unmodified material. Itoh *et al* [145] similarly observed an increase in Knoop hardness with

increasing implantation ion dose, and measured an increase in hardness of almost 1.6 times for Ti6Al4V samples implanted with a dose of 5 x 10^{17} N^+ ions/cm^2 compared to the unimplanted substrate (increasing from 347.5 KHN for unmodified to 556 KHN for modified material), using a Knoop microhardness tester. Using nano-indentation hardness technique, Williams *et al* [146] observed an increase in hardness of N^+ ion implanted Ti6Al4V alloys with increasing implantation dose, and measured an increase in hardness from 4 GPa for unmodified material to 12 GPa for 6 x 10^{17} ions/cm^2 implanted material.

Using an ultra-microhardness tester, Berberich *et al* [140] measured an increase in Vickers hardness of about 40 % (under a load of 5 mN) on plasma immersion N^+ ion implanted Ti6Al4V samples compared to the unmodified samples. Han *et al* [148] found that plasma source N^+ ion implanted Ti6Al4V samples showed higher hardnesses compared to the unmodified samples, especially at low loads using a microhardness tester (under loads of 10, 25, 50, 100, and 200 gf). Alonzo *et al* [147] carried out micro-indentation tests (with a load range of 0.4 - 10 mN) on N^+ ion implanted Ti6Al4V samples and observed a significant change in surface hardness of the implanted samples compared with the unimplanted material. An increase in hardness of more than 100 % was measured at low applied loads corresponding to indentation depths of about 0.05 μm.

The microhardness on all the implanted samples decreased towards that of the unmodified with increasing indentation load, an indication of ion implantation having a near surface hardening effect on the samples. Because the implantation layer is of the order of 0.15 μm (section 5.1.2), high indentation loads would be expected to penetrate the implanted layer and reflect the hardness of the bulk material as the indentation depth becomes much deeper than the thickness of the modified layer. Clearly on figure 5.12, the microhardness of the implanted materials decreased with increasing indentation loads. The hardness depth profiles (figs. 5.13-5.15) described the typical near surface hardening effect of ion implantation, and the lack of discrete interface between modified and unmodified material. The increase in the near surface microhardness of the implanted Ti6Al4V have been attributed to the combined action of the extreme hardness of TiN formed (2000 HV (Vickers Hardness) [149, 150]), dislocation rearrangement and associated reduction in dislocation mobility, as a result of N^+ ion implantation [151].

The Knoop microindenter used during the experimental work was calculated, from the indent geometry, to penetrate the implanted samples to a depth of ≈ 0.1, 0.2 and 0.3 μm respectively at loads of 1, 3 and 5 gf. Clearly at a load of 1 and 3 gf, the penetration depth was of the order of both the mean projected N^+ ion range and maximum ion penetration depth calculated using TRIM (0.15/0.25 μm). Therefore, the hardness occurring at a load of 1 and 3 gf are mainly influenced by the N^+ ion implanted region within the near-surface of the Ti6Al4V, while the indenter penetrates this region at higher loads of 5, 10 and 25 gf (section 5.1.3). Deeper indents beyond the implantation zone on the implanted samples using loads of 5, 10 and 25 gf, also showed increase in hardness over that of the unimplanted material, though not significantly. The results are likely to be attributable to the diffusion of N^+ ion species beyond the implantation zone (although not proven in this study), as observed in stainless steel [30].

6.1.2 Effects of N^+ ion implantation on stainless steel and Co-Cr-Mo

6.1.2.0 Introduction

The microstructure (figs. 5.61-5.63) and main elemental composition (table 4.1) of the stainless steel, and the main elemental composition of the Co-Cr-Mo (table 4.1) used in this study were investigated with optical microscopy, AFM and SEM, and the results are shown in the respective figures and tables given.

From TRIM calculations, a total of 428 (section 5.2.2), and 414 (section 5.3.1) target atom vacancies per incident N^+ ion were calculated respectively for the stainless steel and Co-Cr-Mo targets. The corresponding maximum ion penetration depth/mean projected N^+ ion range into the respective targets, were 0.21/0.10 μm and 0.20/0.096 μm. These observations are in agreement with published ion penetration depth distributions in metals (0.2-0.5 μm) [26, 135].

6.1.2.1 Topographical effects

On visual and low magnification AFM inspection of the N^+ ion implanted stainless steel and Co-Cr-Mo sample surfaces, ion implantation was observed not to affect the surface morphology of the materials. Further microscopic inspection of the implanted surfaces indicated that their roughness was not altered by the ion implantation treatment.

However, some surface deformation and blister formation on the surfaces of the implanted samples were observed under high magnification contact AFM (figs. 5.72 and 5.85 respectively). These observations were attributed to the formation of N_2 gas bubbles and blisters on the material surfaces during the ion implantation process.

High dose (> 10^{17} ions/cm^2) implantation of N^+ ions into austenitic stainless steels is known to cause gas bubble formation [71], and the process could have similarly occurred in the stainless steel and Co-Cr-Mo materials used in this study.

6.1.2.2 Microhardness effects

The microhardnesses of all the implanted stainless steel and Co-Cr-Mo samples were significantly higher than those of their respective unimplanted samples, and again the surface hardness decreased towards that of the unmodified with increasing indentation load as the indenter penetrated the bulk material (fig. 5.65 and 5.78 respectively). This near surface hardness effect of N^+ ion implantation on materials and lack of the discrete interface between modified and unmodified volume, were described by the stainless steel and Co-Cr-Mo hardness depth profiles (figs. 5.66 and 5.79 respectively).

At an indentation load of 1 gf, a significant microhardness increase of $\approx$ 2.1 times, was measured for both ion implanted stainless steel and cobalt chrome samples (compared to their respective unmodified samples). The measurements were calculated to be within a depth of 0.1 μm on both material surfaces using the Knoop indent geometry, and were in agreement with both the mean projected N^+ ion range and maximum depth calculated using TRIM (sections 5.2.2 and 5.3.1 respectively). The reported increase in hardness values are therefore as a result of the near surface N^+ ion implantation modification. Clearly the hardness occurring at a load of 1 gf is mainly influenced by the N^+ ion implanted region within the near-surface region of the stainless steel and Co-Cr-Mo samples, while the indenter penetrates this region at higher loads of 3, 5, 10 and 25 gf (sections 5.2.3 and 5.3.2). However, the deeper indents beyond the implantation zone on the implanted samples using loads of 3, 5, 10 and 25 gf, showed increase in hardnessess over that of the unmodified samples, though not significantly. The results are likely to be attributable to the diffusion of N^+ ion species beyond the implantation zone, as observed in stainless steels [30].

Several other investigators have similarly observed significant increases in hardness of ion implanted stainless steel and Co-Cr-Mo samples [72, 152-154]. Studies [153, 154] have suggested that N hardens the surface layer of implanted stainless steels, by interstitial solid-solution effects or by the formation of nitride phases. Such hardening processes would be expected on the N^+ ion implanted stainless steel and Co-Cr-Mo samples used in this study. Oliver *et al* [72] performed microhardness tests on 3.5 x 10^{17} N^+ ions/cm^2 implanted stainless steel and hard Cr plate samples (at an energy of 90 keV), and observed an increase in hardness of $\approx$ 1.3 times on both materials at an indentation depth of 0.05 μm, compared to the respective unmodified materials.

6.1.2.3 Chemical effects

N^+ ion implanted microstructures in stainless steel and cobalt chrome alloys are known to be much more complex, because of the large number of N compounds that Fe, Cr and Ni can form [102], and investigation and identification of these were not carried out in this work. Using high resolution TEM, Baron *et al* [155] observed the precipitation of CrN in both 304 and 316 stainless steels implanted with high dose N^+ ions (> 10^{17} ions/cm^2). Considering the ion implantation conditions used in this study (section 4.2.3, table 4.5), such nitrides (CrN) would be expected to form on the surfaces of both the stainless steel and Co-Cr-Mo samples.

Chemical effects of N^+ ion implantation such as nitride formation would result in surface hardening. The hardness increase observed in both implanted stainless steel and Co-Cr-Mo samples used in this study, are likely to be attributable to the formation of hard phase nitride precipitates (CrN), precipitation hardening and increased resistance to dislocation motion upon N^+ ion implantation.

6.1.3 Effects of N^+ ion implantation on UHMWPE

6.1.3.0 Introduction

A total of 368 (section 5.1.2) target atom vacancies per incident N^+ ion were calculated for UHMWPE from TRIM calculations. The corresponding maximum ion penetration depth/mean projected N^+ ion ranges into the target was 0.35/0.26 μm. Because of the lower density of the C based UHMWPE compared to the metallic biomaterials, the

penetration depth of the N^+ ions calculated was higher, despite using lower ion doses and energy. The energy dissipation within the polyethylene was observed to reach a maximum at the projected ion depth (fig. 5.10) as a result of the target atom recoils (a nuclear stopping effect), and the ionisation energy loss was observed to be highest closest to the sample surface (fig. 5.11), ionisation being an electronic effect.

During ion implantation in polymers, the constituent atoms can be ionised (by electronic mechanisms) and / or displaced from their original sites (by nuclear mechanisms), depending on the local environment and energy densities (section 3.2.1.1). However, ionisation is known to dominate at high energy (> 10 keV) [9, 79, 81] to induce atomic and molecular ionisation phenomena, and hence the formation of excited states and radicals. These changes lead to cross-linking, and hence increase in molecular weight of the polymer. According to the implantation conditions used in this study (table 4.3), it is expected that the UHMWPE surface is modified dominantly through the formation of cross-linked molecular microstructure induced by electronic stopping primarily undertaken by the incident N^+ ions during the process. Hence weak secondary bonds between long molecular chains in the unmodified material are replaced by much stronger covalent bonds at the cross linked points. This effect significantly decreases the flexibility of the molecular chain due to the increased rigidity of the back-bone structure by anchoring molecular chains. This was strongly supported during the microhardness investigations, where the modified UHMWPE samples exhibited higher surface hardness ($\approx$ 4 times higher) compared with the unmodified material (section 5.1.3).

6.1.3.1 Topographic effects

The surface colour of the N^+ ion implanted UHMWPE wear pins post implantation changed from white to dark brown, probably caused by processes involving thermal effects and dehydrogenation [9, 156]. During the process of the ion implantation, highly energetic N^+ ions pass through the UHMWPE surface, and some of their energy is dissipated onto the treated surface as heat. Chen *et al* [156] showed using elastic recoil detection (ERD) that a hydrogen deficient surface layer is formed after N^+ ion implantation into UHMWPE. The removal of H from the surfaces of UHMWPE is known to facilitate the formation of a series of conjugated double bonds, to which the surface colour is sensitive.

Following low magnification AFM inspection of the N^+ ion implanted UHMWPE samples, the surfaces appeared to have a very similar appearance to the unmodified samples. However, some deformation on the surfaces of the implanted samples in the form of regular patterns (blistering), were observed under high magnification contact AFM (figs. 5.36). This was attributed to the ion beam bombardment of the energetic ions or so-called ion etching effects which has been observed by other workers [9, 78].

6.1.3.2 Chemical effects

The XPS findings of the N^+ ion implanted and unmodified UHMWPE (section 5.1.6.5) were in agreement with published data [156]. Nearly 2 at. % of N (table 5.4) were found to be present on the implanted samples, with the N 1s envelope showing a 2 sub-peak envelope at 398.4 and 400.1 eV (fig. 5.59). The N 1s binding energy positions seen in this study, are consistent with the published data [156] for N- sp3 C (at 398.4 eV) and N- sp2 C (at 400.25 eV). Also, it was reported that [156], the N 1s peaks position for -C≡N (nitrile) is at 399.4 eV, and that for -N≡C (isonitrile) would be expected at a lower value. Hence the peaks at 398.4 and 400.1 eV observed in this study, may correspond to the -N≡C (isonitrile) and -C≡N (nitrile) respectively.

XPS studies have shown that, when N^+ ions are implanted into polymers, the implanted N^+ ions form chemical bonds with the polymer chains instead of forming precipitates by self-clustering [156].

6.1.3.3 Microhardness effects

N^+ ion implantation had a pronounced hardening effect on the UHMWPE samples (and the XLPE samples tested for comparison), with the degree of hardening observed to increase with increasing implantation ion dose in the UHMWPE material. At a load of 1 gf, increases in hardness of $\approx$ 2.5 and 3.8 times respectively were measured for UHMWPE implanted with doses of 1×10^{15} and 5×10^{15} N^+ ions/ cm^2 compared with the unmodified material (table 5.3), and complements hardness studies by other investigators [156]. Chen *et al* [156] measured an increase in hardness of $\approx$ 4 times for modified UHMWPE compared with the unmodified material using a nanoindenter (increasing from 0.11 GPa for unmodified to 0.4 GPa for 5×10^{15} N^+ ions/cm^2 implanted UHMWPE at 40 keV). The hardness increased with increased implantation

dose, and was probably due to the fact that the degree of cross-linking increased with increasing ion dose. An increase in hardness of ≈ 2.4 times was also calculated for XLPE samples implanted with 5 x 10^{15} N^+ ions/ cm^2, compared with the untreated material. The degree of cross-linking can therefore be increased probably up to the formation of a full three dimensionally networked cross-linked molecular chain structure.

The improvement of surface hardness can be entirely attributed to the ionisation phenomena induced in the near surface region (leading to the formation of a three-dimensional network linking the chains with strong covalent bonds). N^+ ions are known to have elevated ionisation power [81] and hence are more effective in causing ionisation during N^+ ion implantation.

6.2. Tribological Wear Behaviour of N^+ ion Implanted Biomaterials

6.2.0 Introduction

Biomaterials used in the fabrication of implants for artificial joints are subjected to surface wear during articulation, and wear has been shown to be detrimental to their long-term success. Ultra high molecular weight polyethylene wear debris has been shown by several investigators to trigger an osteolytic reaction, which leads to the loosening of the implant (chapter one). N^+ ion implantation has been a most widely accepted surface treatment, and shows promise in improving the wear resistance of commercially used biomaterials in total joint replacements.

The results of the tribological behaviour of the used biomaterials (in both modified and unmodified forms) evaluated on a multidirectional pin-on-plate wear apparatus during the study, are discussed under the following sections (6.2.1 to 6.2.4). Four sets of specimens for each material both in the form of modified or unmodified were used in the tests as an indication of the repeatability and reproducibility of the results, and no significant differences between the wear pins in the results of a particular test were measured. Due to the different operating conditions used by several other workers, such as force, lubrication, temperature, sliding distance and type of wear apparatus, and the presentation of wear results, difficulties arise in the comparison of tribological wear results. As a result of such difficulties, wear tests with different material couple

combinations (both in modified or unmodified forms) were performed in this study to directly compare the wear of unmodified biomaterial couples with those of modified biomaterial couple combinations, when tested under the same operating conditions and on the same wear apparatus. Comparisons with previous studies have been made where appropriate, subject to variations in the tribological conditions and operating apparatus used.

Most previous tribological wear studies have used simple reciprocating motion pin-on-plate machines, and distilled water or saline solution as the lubricant, which generally produce wear factors (for UHMWPE articulated against metallic counterfaces) one or two orders of magnitude less than those found using multidirectional motion pin-on-plate machines, and *in vivo* (section 4.1). The reason for this discrepancy is that the UHMWPE turns to be strain hardened in the direction of the motion during reciprocating wear tests [157, 158], and hence becomes stronger in the sliding direction, leading to reduced wear. Also distilled water used as a lubricant in tribological studies has been shown to alter the tribological properties of the bearing system significantly [159]. The use of distilled water lubrication during wear tests, has been reported to lead to the formation of heavy transfer films of polyethylene on the counterface metallic material (section 4.1.1.1), and no such films have been observed when the tests are carried out under bovine serum lubrication.

6.2.1 Tribological wear behaviour of Ti6Al4V/UHMWPE couples

6.2.1.1 Unmodified Ti6Al4V/UHMWPE sliding couples

Tests with unmodified UHMWPE pins articulating against unmodified Ti6Al4V plates (section 5.1.4.1) showed the most severe surface wear of the Ti6Al4V plates and the highest wear factors (k_o) of the UHMWPE pins, compared with other materials investigated in this work.

A mean k_o of $2.77 \pm 0.16 \times 10^{-6}$ mm^3/Nm and mean weight loss of 214 ± 0.08 μg were calculated respectively for the UHMWPE pins and Ti6Al4V plates, up to a sliding distance of 207 km (table 5.1). This high wear of the UHMWPE was attributable to the poor surface wear properties of the counterface Ti6Al4V plates. Previous *in vitro* wear tests by several other investigators [42, 111] have similarly found high wear

factors/wear rates for unmodified UHMWPE articulating against unmodified Ti6Al4V compared with UHMWPE articulating against other metallic counterfaces (such as stainless steel or Co-Cr-Mo), under different tribological conditions.

Poor surface wear of unmodified Ti6Al4V was seen on all the plates after the wear testing, and was observed on the AFM image of figure 5.30. The surfaces of the plates were observed (visually and microscopically) to be severely damaged, and characterised by numerous random scratches and grooves, due to the continuous rubbing action of the UHMWPE, and the surface observations were in reasonable agreement with those observed by various other workers in both *in vitro* and *in vivo* wear studies [13, 36, 37, 111, 160, 161]. Due to such poor surface wear of unmodified Ti6Al4V, continued articulation against the UHMWPE pins caused severe scratches on the metal surface. Two-body abrasive wear occurred resulting in a quick deterioration of both Ti6Al4V and the UHMWPE surfaces. The machining and microtoming marks on the surface of the UHMWPE pins present prior to testing, wore off after the test, indicating the surface deterioration caused by abrasion. Mean UHMWPE pin volume loss of 21.6 mm^3 was measured when articulating against unmodified Ti6Al4V, compared to 12.6 mm^3 when articulating against modified Ti6Al4V plates.

Dark colouration and debris seen in the bovine serum lubricant and on the surfaces of worn UHMWPE pins post testing, have also been observed by several other authors in both *in vitro* wear tests and *in vivo* [37, 48, 96, 111], and the debris have been identified as titanium oxide (TiO_2) particles. These observations have been attributed to the easy removal of the relatively hard TiO_2 layer from the Ti6Al4V surfaces during articulation against the UHMWPE. The hard debris then remain between the pin and plate and in the lubricant during testing, and promote a severe three-body abrasive wear process, resulting in further deterioration of both Ti6Al4V and UHMWPE surfaces. The oxide layer re-forms readily after removal from the surface due to the high affinity for O of Ti and Al [96], and hence the abrasion wear mechanism is further accelerated [21, 147]. Further more, UHMWPE has a strong adhesion to the titanium oxide film, and this further promotes the three-body abrasive wear mechanism [134, 145, 147]. This is an oxidative wear process (section 3.1.1.1.2), which gradually increases the Ti6Al4V surface roughness with articulation and hence the associated UHMWPE wear.

Using a flat-on-flat wear apparatus and bovine calf serum lubrication, McKellop *et al* [111] found Ti6Al4V samples to be susceptible to abrasive wear by particles of acrylic cement, compared to stainless steel and Co-Cr-Mo samples when articulating against UHMWPE. Clark *et al* [161] found on a pin-on-disc test that, the entrapment of acrylic cement particles between UHMWPE and Ti6Al4V resulted in severe wear of the titanium alloy counterface, with the production of large amounts of black metallic wear debris. A similar form of wear was observed on seven revised titanium alloy total hip prostheses by Agins *et al* [37] *in vivo*, with a severe inflammatory response in the surrounding tissues due to large amounts of Ti6Al4V and UHMWPE debris.

6.2.1.2 Modified Ti6Al4V/UHMWPE sliding couples

In contrast to unmodified wear couples, N^+ ion implantation significantly improved the surface wear resistance of the Ti6Al4V samples, and no dark colouration was observed in the bovine serum lubricant in any of the tests carried out (during articulation against modified or unmodified UHMWPE) in this study. The absence of darkening of the lubricant with test duration is an indication of the fact that N^+ ion implantation stabilised the surface oxide layer of the Ti6Al4V during articulation with the UHMWPE, and hence reduced its removal to prevent severe abrasive wear.

When Ti6Al4V plates were implanted with 2 x 10^{17} N^+ ions/cm^2 (section 5.1.4.4), minor surface damage (mild wear effect) was observed by AFM on the plate surfaces even after more than 5 million wear cycles against 5 x 10^{15} N^+ ions/cm^2 implanted UHMWPE pins (fig. 5.31), and no appreciable colour change was observed in the bovine serum lubricant used. AFM further resolved the surface features of both modified and unmodified plates post wear, giving both height data and material information. As can be seen in figures 5.30 and 5.31 (section 5.1.5), there was a significant reduction in the surface topography depth of the region of pin contact on Ti6Al4V plates, when the plates were implanted with 2 x 10^{17} N^+ ions/cm^2, reducing from $\approx$ 436 nm (unmodified plate) to $\approx$ 99 nm (modified plate), and hence a reduction in the mean surface roughness (table 5.2) compared with the unimplanted samples post wear.

The distinctive wear tracks seen on the unmodified plates were clearly not visible on any of the implanted plates post wear (figs. 5.31-5.33). Further more, compared to the

results from the unmodified wear couples (section 5.1.4.1), significant reductions of ≈ 41 % and ≈ 62 % respectively in the mean wear factors of the mating UHMWPE pins (from 2.77 x 10^{-6} ± 0.16 to 1.65 x 10^{-6} ± 0.05 mm^3 /Nm), and mean weight loss of the Ti6Al4V plates (from 214 ± 0.08 to 81 ± 0.06 μg), were calculated after testing (table 5.1). The surfaces of the ion implanted Ti6Al4V plates with higher ion doses (1 x 10^{18} and 1 x 10^{21} N^+ ions/cm^2 implanted plates) also showed significant improvement in surface wear resistance and reduction in the mean wear factors of the mating UHMWPE pins, compared with those of unmodified and modified UHMWPE pins articulating against unmodified Ti6Al4V plates.

The results add to existing tribological studies by several other authors using different tribological conditions [36, 101, 134, 142, 147, 150, 162-164] (section 3.2.1.3.1), who have similarly observed improvements in the wear resistance of ion implanted Ti6Al4V when articulated against UHMWPE, compared with unmodified wear couples. Mckellop *et al* [36] found that N^+ ion implantation with 3 x 10^{17} N^+ ions/cm^2 implanted Ti6Al4V samples (at an ion energy of 80 KeV and a temperature of 100 °C), resulted in good protection of the metal surface against third body wear by PMMA, when articulating against UHMWPE on a ten-station computer controlled joint simulator. Using bovine serum lubricated pin-on-disc wear tests, Alonzo *et al* [147] showed a marked decrease in wear of both Ti6Al4V and UHMWPE samples when the alloy was implanted with 4 x 10^{17} N^+ ions/cm^2 at 180 keV (resulting in Ti6Al4V wear tracks with roughness values less than 0.05 μm R_a), compared with the unimplanted sliding couples (Ti6Al4V wear tracks showed deep grooves 50 μm with traces of transferred UHMWPE material). Using a ball-on-disc wear testing device, Lifang *et al* [150] showed improved tribological properties of Ti6Al4V samples plasma-based ion implanted with N^+ (then acetylene) compared with unmodified samples.

The wear studies conducted on Ti6Al4V samples with different ion implantation doses articulating against unmodified UHMWPE samples, showed that 2 x 10^{17} N^+ ions/cm^2 implanted Ti6Al4V plates exhibited the lowest surface wear, and when tested against 5 x 10^{15} N^+ ions/cm^2 UHMWPE pins, a significant reduction in the mean wear factor of the modified UHMWPE from ≈ 2.77 x 10^{-6} ± 0.16 mm^3/Nm (unmodified material) to ≈ 1.25 ± 0.05 x 10^{-6} mm^3/Nm (modified material) was calculated, representing an improvement in UHMWPE wear of ≈ 55 %. An improvement in mean weight loss of

the modified Ti6Al4V plate of ≈ 63 % was also calculated (table 5.1). N^+ ion implantation was found to improve the surface hardness of both Ti6Al4V and UHMWPE articulating surfaces, and hence contributed to the reduced deterioration of the material surfaces. Increase in hardness would imply strengthening of the substrates and an improved wear resistance, as observed by other workers [147]. Moreover, ion implantation can stabilise the Ti6Al4V protective passive oxide layer (section 3.1.1.1.2), avoiding the detachment of abrasive oxide particles and resulting in a very mild wear mechanism on both articulating surfaces.

XPS energy spectrum (section 5.1.6.2) of the region of pin contact on the implanted Ti6Al4V plates post wear against unmodified UHMWPE and implanted UHMWPE (fig. 5.44), were both observed to show the distinct binding energy peak due to the N 1s, which was present on the pre wear tested material (fig. 5.43). This was an indication of the fact that N was still present on the surfaces of the implanted materials even after more than 5 million wear cycles. However, high resolution XPS analysis of the Ti 2p (figs. 5.46, and 5.47) envelopes of the regions were found to be clearly depleted in TiN relative to TiO_2. More depletion of the Ti^+ species attributable to TiN was observed in the region of pin contact on the modified Ti6Al4V plates following testing with unmodified UHMWPE pins than with modified UHMWPE pins (table 4.4), compared to that from the pre wear tested Ti6Al4V plates. In addition, the amount of TiN within the N 1s envelope was also reduced post wear, when compared to the analysis from the pre-tested modified Ti6Al4V samples, and again more reduction in plates articulating against unmodified UHMWPE samples was observed than in plates articulating against modified UHMWPE samples (table 4.4). This is an indication of the reduction in the amount of N on the modified Ti6Al4V surfaces due to articulation with the UHMWPE pins. The XPS results suggests that, N^+ ion implantation of Ti6Al4V alloys creates TiN on the material surfaces, the hardness of which can enhance the surface wear resistance of the alloy by effectively protecting the articulating surfaces over 5 million wear cycles (*in vitro*), until the TiN is depleted and the protective passive oxide layer wears away. When the Ti6Al4V surface is exposed, the unmodified Ti6Al4V/UHMWPE sliding couple wears rapidly by a three-body abrasion mechanism [147] (section 6.2.1.1).

The surface roughness of the modified Ti6Al4V plates increased with the implantation dose (table 5.2), and this was observed to increase the mean wear factors of the mating unmodified UHMWPE pins, though not significantly, such that wear factors were still

lower than those found for the unmodified UHMWPE pins articulated against unmodified Ti6Al4V plates. Increases in the UHMWPE mean wear factors of ≈ 8 % and ≈ 26 % respectively were calculated when the implantation dose increased from 2 x 10^{17} N^+ ions/cm^2 to 1 x 10^{18} and 1 x 10^{21} N^+ ions/cm^2 (compared with the mean wear factor against 2 x 10^{17} N^+ ions/cm^2 Ti6Al4V). This was attributed to the increase in surface roughness caused by the increased implantation dose (table 5.2) as a result of physical and chemical changes induced by the implantation process. The surface topography of the 1 x 10^{18} and 1 x 10^{21} N^+ ions/cm^2 implanted Ti6Al4V surfaces post wear, are shown in figures 5.32 and 5.33 respectively, where the R_a determined by AFM (fig. 5.34) was found to be ≈ 17.5 nm and ≈ 25.6 nm respectively for 1 x 10^{18} and 1 x 10^{21} N^+ ions/cm^2 implanted plates, higher than that of the tested 2 x 10^{17} N^+ ions/cm^2 implanted plate (≈ 10.7 nm).

Despite the increase in hardness observed with the increase in implantation ion dose (section 5.1.3), the wear of the mating UHMWPE increased, though not significantly, with the increasing ion dose (section 5.1.4.3). These wear results show that a weak correlation exists between the hardness and wear behaviour of the ion implanted Ti6Al4V surfaces when articulating against UHMWPE. However, a good correlation between hardness and wear would be expected to exist up to an optimum implantation ion dose on the Ti6Al4V surface (2 x 10^{17} N^+ ions/cm^2 in this study). Beyond 2 x 10^{17} N^+ ions/cm^2 implantation dose, the surface hardness of the Ti6Al4V increases with dose, but the wear resistance of the alloy and the mating UHMWPE decreases following articulation compared to 2 x 10^{17} N^+ ions/cm^2 implanted Ti6Al4V/unmodified UHMWPE wear couple. This may be due to the sputtering and blistering induced significant increase in mean arithmetic surface roughness observed on increasing the implantation dose from 2 x 10^{17} N^+ ions/cm^2 (12 nm R_a) to 1 x 10^{18} N^+ ions/cm^2 (32 nm R_a) and 1 x 10^{21} N^+ ions/cm^2 (49 nm R_a). Alternatively, the increase in wear of the mating UHMWPE with increasing implantation dose on Ti6Al4V could be attributed to the surface structure formed upon N^+ ion implantation with higher ion doses. Increasing the implantation dose could increase the size of the TiN precipitates formed (though this was not ascertained in this work), and this could have reduced the adherence of the surface oxide layer and hence promoted its removal during articulation. The removal of the large sized TiN precipitates and surface TiO_2 layer could act as three-body abrasive wear particles in the lubricant during articulation to promote wear of the softer UHMWPE. Also the surface chemistry of Ti6Al4V is changed upon ion implantation as

a result of chemical reactions between the implanted species and the surface atoms, and this could be significant during articulation in bovine serum, which contains physiological concentrations of proteins. The proteins could have different interactions with the modified surfaces depending on the implantation dose, and hence influence the lubrication and wear of the articulating surfaces. The effect of protein interactions with N^+ ion implanted surfaces could be investigated further.

6.2.1.3 Summary

Due to their lower modulus, superior biocompatibility and excellent corrosion resistance when compared to stainless steels and cobalt chrome alloys, Ti6Al4V alloys have been increasingly used as biomaterials. However, the poor shear strength of the TiO_2 surface layer and the wear resistance of the alloys are known to limit their biomedical use.

The wear studies in this work have shown that the wear of unmodified Ti6Al4V/UHMWPE sliding couples results from a two/three-body abrasion mechanism. As the UHMWPE rubs against the Ti6Al4V, debris particles are formed and pulled out of the Ti6Al4V surface. These hard particles then become abrasive particles between the pin and plate or embedded in the polymer, causing a severe abrasive wear. In artificial joints, such poor tribological properties of the unmodified Ti6Al4V femoral components articulating against unmodified UHMWPE acetabular cups would be detrimental and are known to lead to failure of the joints [18, 37, 40]. The removed surface oxide layer during articulation not only promotes third-body abrasion, but also exposes the metal surface and hence can lead to soluble metal ions such as V (which has been reported to be toxic and show adverse tissue effects) to be released locally into the surrounding tissue. In fact, it has been well documented that Ti6Al4V without a surface treatment is not recommended for *in vivo* bearing applications due to the poor surface wear resistance [13, 18].

N^+ ion implantation on Ti6Al4V is known to be able to retard the start of severe abrasive wear on the alloys [72, 89, 134, 147], and hence reduce the friction and wear between the alloy and mating UHMWPE sliding couples. However the precise mechanism that delays the onset of the abrasive wear is not yet clear. During the wear studies undertaken in this work, N^+ ion implantation was seen to affect the wear of Ti6Al4V/UHMWPE sliding couples significantly, due to modification induced changes

such as increase in microhardness of the Ti6Al4V (section 3.1.1.3), strengthening the alloy samples and hence improving the wear of both Ti6Al4V and UHMWPE during articulation. In addition, the harder and wear resistant TiN precipitate that forms below the protective oxide layer (section 5.1.1.2) stabilises the outer oxide layer as well as reduces its thickness, leading to reduction in abrasive oxide particles removed from the surface, and hence resulting in a very mild wear mechanism.

Unfortunately, there is as yet no evidence that ion implantation changes the wear behaviour of Ti6Al4V alloys beyond the implantation zone (due to poor wear when the implanted layer is worn through), and that if the implanted layer were to be completely worn away, the wear properties would revert to those of the unmodified alloy bearing against UHMWPE. AFM (figs. 5.34 *a*) measured the depths of the region of pin contact on the 2 x 10^{17} N^+ ion/cm^2 implanted Ti6Al4V samples (< 0.1 μm) to be within the mean ion implantation depth (0.15 μm), and XPS analysis confirmed the presence of N on the surface after more than 5 million wear cycles against 5 x 10^{15} N^+ ion/cm^2 implanted UHMWPE pins. The results suggest that, after 10 million wear cycles against implanted UHMWPE pins, the depth of the region of pin contact on the implanted Ti6Al4V samples could be about < 0.2 μm (still within the maximum ion penetration depth, 0.25 μm), and hence the wear resistance of the alloy could still be enhanced until after this number of wear cycles.

In addition, radiation-enhanced diffusion of ions in implanted materials is known to occur and has been observed in metals [165], although the phenomenon is said to be complex and not fully understood. Such radiation damage is expected to induce diffusion of the implanted species and result in a final profile that extends several factors deeper than that expected from a simple ion range calculation. The excess vacancies produced as a result of ion implantation (section 5.1.2) are also known to enhance the rate of diffusion at relatively low temperatures. The diffusion processes of N^+ ions beyond the implantation zone in stainless steels have been reported [30], and could have similarly have occurred in the implanted Ti6Al4V samples used in this study. The observed increase in hardnesses of the implanted Ti6Al4V samples beyond the implantation zone compared to that of the unimplanted samples at the same loads (5, 10, and 25 gf) during the study (section 5.1.3, fig. 5.12) suggests that such diffusion process may have occurred. If present, such diffusion processes could further enhance the wear resistance of the modified alloy over several millions of wear cycles (> 10

million) when articulating against modified UHMWPE (*in vitro*). However further diffusion of N^+ ions in Ti6Al4V alloys beyond the implantation zone needs to be studied to verify the occurrence of such processes.

About one million cycles in a wear apparatus corresponds to one year of active use of a hip joint prosthesis (a cycle on the pin-on-plate rig is obtained by two passes, whereas a complete walking cycle is represented by two steps), hence if the modified Ti6Al4V surface wear measured qualitatively (using AFM and XPS) and quantitatively *in vitro*, were applied to clinical use, the wear resistance of the modified alloy would be expected to probably last for more than 10 years of use, until the protective passive oxide layer wears away.

6.2.2 Tribological wear behaviour of stainless steel/UHMWPE couples

6.2.2.1 Unmodified stainless steel/UHMWPE sliding couples

Compared with the surfaces of Ti6Al4V plates, the tribological surface wear properties of the stainless steel used during this study were found to be better, and in turn, lower wear factors of the mating UHMWPE pins were recorded, even when the materials were unmodified.

Unmodified UHMWPE mean k_o of $1.59 \pm 0.15 \times 10^{-6}$ mm^3/Nm was calculated after more than 5.5 million sliding wear cycles against unmodified stainless steel (section 5.2.4.1). Via AFM, some scratches and grooves were observed on the stainless steel plates in the region of pin contact post wear (fig. 5.73), as a result of the articulating action of the mating UHMWPE pins. Studies on retrieved stainless steel femoral heads from THRs have indicated that the scratches formed on the heads are multidirectional [166, 167], reflecting the multidirectional motion found *in vivo*. The scratches observed on the test plates in this study were similar in appearance to the multidirectional scratches seen on the retrieved femoral heads, and scratches observed on test plates in previous *in vitro* studies [116]. The bovine serum lubricant showed no colour change and contained no dark particulate debris, suggesting the passive oxide layer (Cr_2O_3) on the surface of the stainless steel plates to be more adherent than that of TiO_2 on Ti6Al4V. The results suggest that, the main wear mechanism that occurred during testing was probably two-body rather than three-body abrasive wear, owing to the

adherence of the surface oxide layer. This abrasive wear mechanism was mild compared to the three-body mechanism found for Ti6Al4V samples.

The wear results in this study, support and add to existing tribological studies by other workers using different conditions [110, 111, 114, 116, 119, 168] and were similar to those found in clinical observations [169-171]. Kumar *et al* [110] calculated a mean k_o of 1.81 ± 0.07 x 10^{-7} mm^3/Nm for UHMWPE articulating against stainless steel (under bovine serum lubrication *in vitro*), a value that is an order of magnitude lower than the mean calculated in this study. Using a twelve-station circularly translating pin-on-disc (CTPOD) device, Saikko *et al* [114] found mean k_o of 0.8 x 10^{-6} mm^3/Nm for UHMWPE articulating against stainless steel plates. The mean k_o was of the same order of magnitude to that reported in this study (though lower). Joyce *et al* [116], reported a mean k_o of 1.10 x 10^{-6} ± 0.45 mm^3/Nm for UHMWPE articulating against stainless steel in bovine serum, on a multidirectional pin-on-plate machine. This value compares very well with the mean k_o reported in the present study. Saikko *et al* [168] performed long-term simulator tests of Charnley prostheses under water lubrication (unmodified UHMWPE/stainless steel wear couples), and calculated an UHMWPE mean k_o of 1.46 x 10^{-6} mm^3/Nm. The k_o was similar to that recorded in the present study. The differences in the *in vitro* mean wear factors of UHMWPE in this study and that obtained by the other authors, may be due to the different tribological conditions used (section 6.2.0).

The internal volume changes of 25 acetabular cups of UHMWPE/stainless steel Charnley prostheses removed after 2 to 16 years, were studied by Atkinson *et al* [169] who found the mean clinical k_o to be 2.9 x 10^{-6} mm^3/Nm (ranging from 0.09 x 10^{-6} to 7.2 x 10^{-6} mm^3/Nm) for the mating UHMWPE. Clearly, the mean k_o obtained in the present study falls within the range found in the clinical observations and was of the same order of magnitude as the mean value, though slightly lower. Hall *et al* [170] investigated 129 Charnley acetabular components acquired at the time of revision surgery, and calculated a mean clinical k_o of 2.1 x 10^{-6} ± 0.2 mm^3/Nm for the mating UHMWPE, a value which was slightly higher but of the same order of magnitude as that recorded in this study. Wroblewski *et al* [171] calculated a mean clinical UHMWPE k_o of 3.9 x 10^{-6} ± 1.4 mm^3/Nm, which is considerably higher than that found in this study (though of the same order of magnitude). The high clinical mean wear factors compared to the mean k_o calculated in this study, may be attributable to the

numerous scratches found on the femoral heads (caused by bone cement particles *in vivo*), or the dynamic loading undergone by the UHMWPE components in a normal gait.

6.2.2.2 Modified stainless steel/UHMWPE sliding couples

N^+ ion implantation was found to further improve the surface wear resistance of the stainless steel, when the materials were implanted with 2 x 10^{17} N^+ ions/cm^2 and tested against unmodified UHMWPE (section 5.2.4.2).

The effect of wear on the implanted plate samples post wear was very mild (fig. 5.74), maintaining the low surface roughness of the samples pre wear. Roughness measurements showed deep scratches and hence higher roughness values on the unimplanted stainless steel plates post wear, compared with those on the implanted samples (table 5.5). Mean UHMWPE k_o of 0.98 ± 0.08 x 10^{-6} mm^3/Nm was calculated after more than 5.5 million wear cycles against the modified stainless steel. Compared with the UHMWPE mean k_o calculated when articulating against unmodified stainless steel, N^+ ion implantation on stainless steel improved the wear of the mating UHMWPE by ≈ 38 %.

Further improvement in the wear of the mating UHMWPE was observed when both stainless steel and UHMWPE articulating surfaces were N^+ ion implanted (section 5.2.4.3). 5 x 10^{15} N^+ ions/cm^2 implanted UHMWPE mean k_o of 0.82 ± 0.02 x 10^{-6} mm^3/Nm was calculated following testing against the 2 x 10^{17} N^+ ions/cm^2 implanted stainless steel plates, an improvement in wear of the modified UHMWPE by ≈ 48 % and 16 % respectively, compared with that of the unmodified UHMWPE articulated against unmodified stainless steel (section 5.2.4.1) and unmodified UHMWPE articulated against modified stainless steel (section 5.2.4.2). Goode *et al* [172] suggested that N stabilises the passive oxide layer on the surface of N^+ ion implanted pure iron and thus indirectly reduces the surface wear of the material during articulation. Such surface passive oxide layer stabilisation by N^+ ion implantation may have similarly have occurred on the implanted stainless steel plates, to enhance the surface wear resistance observed in this study.

The work extends upon results from previous tribological wear studies by several other workers, investigating the effect of N^+ ion implantation on the wear properties of stainless steel, using different conditions [91, 99, 102, 107, 153, 154] (section 3.2.1.3.2).

6.2.2.3 Summary

Stainless steel alloys have acceptable friction and wear properties in joint implants, and are well known to be less sensitive than titanium alloys to wear damaging, but crevice corrosion may occur in some cases during use as a biomaterial in TJR. N^+ ion implantation of stainless steel has been studied to further produce significant improvement in the wear resistance of the alloy used in this study, and in turn, significantly reduced the wear experienced by the mating UHMWPE.

Worn tracks of the unimplanted stainless steel showed groves and scratches caused by two-body abrasion due to the rubbing action of the UHMWPE, whereas the effect of wear on the implanted samples was very mild. AFM (figs. 5.74) measured the depths of the region of pin contact on the 2 x 10^{17} N^+ ion/cm^2 implanted steel samples (< 0.09 μm) to be within the mean ion implantation and maximum penetration depths (0.1 and 0.21 μm respectively), after more than 5 million wear cycles against 5 x 10^{15} N^+ ion/cm^2 implanted UHMWPE pins, suggesting that, the wear resistance enhancement of the alloy by N^+ ion implantation could exist for several millions of wear cycles against modified UHMWPE *in vitro* (at least 10 million wear cycles until the maximum ion penetration depth is reached).

In addition, it has also been demonstrated that the improvement in wear resistance achieved by N^+ ion implantation into several types of stainless steels persists to a depth of wear as much as 10 times the penetration depth of the N^+ ions, as a result of diffusion of the ions beyond the implantation dose [30, 106, 173-177]. Some studies [173, 175, 176] indicated that the N migrates to such depths during the tribological wear tests. Hale *et al* [177] suggested that the implanted N initiates the formation of a wear resistant layer that was able to propagate at or ahead of the wear front. Such diffusion processes (if present), and the fact that the N^+ ion implanted stainless steel surfaces were significantly less damaged post wear testing in the study, suggest that the improved hardening and surface wear properties by N^+ ion implantation would be expected to be beneficial in artificial joints.

6.2.3 Tribological behaviour of Co-Cr-Mo/UHMWPE couples

6.2.3.1 Unmodified Co-Cr-Mo/UHMWPE sliding couples

The tribological wear studies have shown that unmodified Co-Cr-Mo plates have excellent surface wear properties compared with unmodified stainless steel and Ti6Al4V plates, when articulating against unmodified UHMWPE pins. The mean surface roughness of the plates pre and post wear of all the metallic materials can be seen in tables 5.2 (Ti6Al4V, section 5.1.4.7), 5.6 (stainless steel, section 5.2.4.4) and 5.9 (Co-Cr-Mo, section 5.3.3.4) for comparison.

Co-Cr-Mo worn plates showed few scratches and grooves (fig. 5.86), even after more than 5.5 million cycles of wear against UHMWPE. The excellent surface wear of Co-Cr-Mo was due to the high hardness of the material compared with that of the stainless steel and Ti6Al4V samples, which in turn, improved the wear of the mating UHMWPE (by experiencing less severe wear conditions). Mean UHMWPE k_o of $1.29 \pm 0.05 \times 10^{-6}$ mm^3/Nm was calculated when articulating against the unmodified Co-Cr-Mo (section 5.3.3.1).

The lack of discolouration of the bovine serum test lubricant during and following wear testing suggested the oxide layer on the surface of the Co-Cr-Mo plates (Cr_2O_3) to be more adherent than that of TiO_2 on Ti6Al4V. The results suggested that, the main wear mechanism that occurred during testing was probably mild two-body rather than the severe three-body abrasive wear, owing to the adherence of the surface oxide layer.

The results add to existing tribological studies by several other workers using different conditions [24, 111, 178]. The differences in the mean wear factors of UHMWPE in this study and that obtained by other investigators may be due to the different tribological conditions used (section 6.2.0). Wright *et al* [178] tested Co-Cr-Mo pins against UHMWPE samples in a pin-on-disc machine (such that the UHMWPE samples were cyclically loaded and unloaded), and observed a mean k_o of the order of 1.0×10^{-6} mm^3/Nm for the mating UHMWPE. The results was similar to that recorded in this study. The mean k_o obtained for UHMWPE (1.0×10^{-7} mm^3/Nm) articulated against Co-Cr-Mo on a three-station reciprocating pin-on-plate apparatus (distilled water lubrication) by Saikko *et al* [24], was an order of magnitude lower than that in the

present study. Mckellop *et al* [111] obtained mean k_o of two orders of magnitude lower than that in this study for UHMWPE, using a twelve-station reciprocating motion pin-on-plate apparatus (under serum lubrication).

6.2.3.2 Modified Co-Cr-Mo/UHMWPE sliding couples

N^+ ion implantation further improved the microhardness (section 6.1.2.2), and hence the surface wear resistance of the Co-Cr-Mo samples, and in turn, reduced the wear of the mating unmodified UHMWPE samples even further (section 5.3.3.2).

The modified and worn plates showed few scratches and grooves, and these were most probably a consequence of polishing (fig. 5.87), and maintained the low roughness appearance of the plate prior to wear testing even after more than 5.5 million cycles of wear against the unmodified UHMWPE pins. A mean UHMWPE k_o of $0.75 \pm 0.03 \times 10^{-6}$ mm^3/Nm was calculated, an improvement in wear of $\approx$ 42 %, compared with that calculated for unmodified UHMWPE samples articulated against unmodified Co-Cr-Mo samples (section 5.3.3.1).

Implantation of the mating UHMWPE pins articulating against modified Co-Cr-Mo plates (section 5.3.3.3), further improved the wear of the modified UHMWPE by $\approx$ 48 % and 11 % respectively, compared with that of the unmodified UHMWPE samples articulated against unmodified Co-Cr-Mo (section 5.3.3.1) and modified Co-Cr-Mo (section 5.3.3.2) samples. A mean modified UHMWPE k_o of $0.67 \pm 0.03 \times 10^{-6}$ mm^3/Nm was calculated following testing against modified Co-Cr-Mo samples.

6.2.3.3 Summary

Cobalt chrome alloys used as biomaterials, are known to be durable and have excellent wear resistance. This was observed in this study, where wear tests with Co-Cr-Mo plates produced the lowest surface damage of the plates and wear of the mating UHMWPE pins. However in TJR consisting of Co-Cr-Mo articulating against UHMWPE components, the UHMWPE wears down over time, and the wear particles activate a biological response that leads to bone resorption and to implant loosening and failure.

N^+ ion implantation of Co-Cr-Mo and UHMWPE articulating surfaces was found to further reduce the wear of the mating UHMWPE after more than 5 million wear cycles during the study, and would be beneficial in reducing the UHMWPE wear debris induced osteolysis in TJR, by reducing the wear debris generated.

The tribological results of modified and unmodified Co-Cr-Mo/UHMWPE wear couples in this study complements previous studies by several other workers using different conditions [17, 24, 26, 27, 98] (section 3.2.1.3.3).

6.2.4 Wear behaviour of UHMWPE

6.2.4.1 Wear factors

The mean wear factors of UHMWPE (both in modified or unmodified forms) in all the tests carried out in this study have been summarised in tables 5.1, 5.5 and 5.8.

In all the wear tests carried out this study, 5 x 10^{15} N^+ ions/cm^2 implanted UHMWPE samples exhibited the lowest wear rates when articulated against 2 x 10^{17} N^+ ions/cm^2 implanted metallic plates, followed by unmodified UHMWPE samples against modified 2 x 10^{17} N^+ ions/cm^2 implanted metallic samples, compared with unmodified UHMWPE/metallic wear couples. N^+ ion implantation improves the properties of UHMWPE by cross-linking the linear structure of the material. Cross-linking strengthens UHMWPE and therefore the material can resist any wear processes, including molecular orientation during sliding (section 6.2.4.2). The observed significant improvements in wear resistance may be, in part, attributed to the ion implantation induced cross-linking, which in turn, increased hardness of the UHMWPE samples significantly (table 5.3).

Even though the implanted layer on the UHMWPE wear pins wore off after a few number of wear cycles, the material still resisted the high wear rates exhibited by the unmodified UHMWPE samples articulated against unmodified metallic samples (Ti6Al4V in particular). This was probably due to a diffusion process of the N^+ ions within the material, strengthening the UHMWPE beyond the implanted region. Modification of the counterface metallic plates further enhanced the surface hardnesses,

and deterioration of the modified UHMWPE samples were decreased as a result of experiencing less severe wear conditions.

6.2.4.2 Wear mechanisms

Adhesive, abrasive and fatigue wear have all been found in previous wear tests of UHMWPE against metallic biomaterials [24, 111, 119, 179-181], and in the wear of UHMWPE in total joint replacements (section 3.1.1.1.1).

The UHMWPE wear faces became smooth and polished following articulation against the metallic counterfaces *in vitro*, as is the case with the worn region of retrieved UHMWPE acetabular cups [93, 182]. The main wear mechanism of UHMWPE found in this study was abrasive wear. This was indicated by wear features observed on worn UHMWPE surfaces (fig. 5.37), and random grooves and scratches in the direction of sliding on the metallic counterface surfaces, following wear testing. Abrasive wear is associated with the removal of material from the softer UHMWPE surface by a cutting or shearing action of asperities from the harder metallic counterface (asperity height of the order of 3 x R_a) or by the presence of hard particles either between the articulating surfaces or embedded in one of them [183]. The cutting action of asperities from the harder counterface corresponds to two-body abrasion and was found in all the wear tests carried out, although was milder in tests with N^+ ion implanted material combinations. The cutting action by the presence of hard particles between the articulating surfaces were seen, only when unmodified and modified UHMWPE pins were articulated against unmodified Ti6Al4V plates. This was attributed to TiO_2 particulate debris known to be introduced into the sliding system during articulation as the product of two-body abrasion wear from the unmodified Ti6Al4V surfaces, which in turn increased the wear of the mating UHMWPE significantly. N^+ ion implantation of the Ti6Al4V surface stabilised the TiO_2, and hence reduced its removal from the surface and wear of the UHMWPE, reverting the wear mechanism back to the milder two-body abrasion.

Adhesive wear is associated with intermolecular forces, and known to occur significantly when UHMWPE articulates against clean, hard and smooth metallic counterfaces under unlubricated, starved lubrication and non biological lubrication conditions. The interfacial shear strength of the adhesive junction has been observed to

be greater than that of the polymer during articulation, and the contact ruptures within the polymer as sliding continues, owing to low yield strength. The polymer is then transferred to the harder counterface and subsequently removed as wear debris. Due to the effects of the proteins in the bovine serum lubricant (section 4.1.1.1), no transfer films were observed on any of the counterface metallic plates in any of the tests carried out during the study. SEM investigations in particular of the metallic plates post wear, showed no charging (i.e., non-conducting) deposits to indicate polymer transfer onto the plates. Bovine serum used as a lubricant in wear studies is known to suppress polyethylene transfer. The absence of any transfer films was indicative of the absence of adhesive wear in this study and a consequence of the use of bovine serum lubricant.

Fatigue wear is known to be observed only after a substantial period of articulation, and hence may not be detected in short-term tests. Fatigue wear debris results from the formation of small cracks on the surfaces of the UHMWPE associated with elastic deformation over a number of contact cycles, and particles of wear debris become removed by the growth and intersection of the cracks. Upon visual and microscopic inspection of the worn UHMWPE pins from all the tests carried out during the study, no evidence of such cracks were seen on any of the pins, indicating the absence of fatigue wear. Also the linear wear curves of the UHMWPE pins obtained, further suggested that fatigue wear mechanisms were not present during the testing.

N^+ ion implantation of the UHMWPE further strengthened the surfaces of the UHMWPE pins and hence discouraged the formation of transfer films on the counterface plates, and resisted crack formation during the wear testing.

6.2.4.3 Surface morphology

The worn surfaces of all the UHMWPE samples (modified or unmodified) tested in this study, had a very similar appearance. On visual inspection, the contact surfaces were smooth and glossy, and microscopic inspection revealed characteristic wear features in the form of surface ripples and fibre-like texture orientation on the worn surfaces. AFM of the worn UHMWPE surfaces (figs. 5.37, 5.75 and 5.88), revealed a characteristic appearance of the surface morphology, which were observed to resemble those of worn *ex vivo* polyethylene cups (fig 5.38 b and c) examined by Elfick *et al* [133] at Durham University. The surface morphology was mostly in the form of fibril formation

(fibrillation), which has been observed and described be several other investigators [6, 11, 36, 49, 157], irrespective of the UHMWPE mating metallic counterface *in vitro* or *in vivo*. This characteristic surface wear feature has been attributed to crystalline anisotropy induced by molecular orientation of the UHMWPE at the sliding surface, during multidirectional articulation [11, 157].

The wear surface of UHMWPE is known to undergo a molecular reorganisation process, driven by plastic strain accumulation at the surface by repeated cyclic asperity contact, and leads to strain softening and weakening of the wear surface, during multidirectional sliding [11]. The direct evidence of this molecular orientation was identified by Wang *et al* [11], who revealed a preferential orientation of UHMWPE crystalline lamellae in the direction of the principal motion (i.e., the direction of flexion/extension) on worn UHMWPE surfaces (components tested on hip and knee simulators). Other investigators also observed the appearance of surface stretching in the form of fibril formation on worn UHMWPE components as forms of evidence of molecular orientation [49]. Such fibrillar appearance on the worn surfaces are known to reflect the occurrence of molecular orientation as a result of either adhesive, micro-adhesive or abrasive wear [157], and were observed in this study. The oriented fibrillar structures can also be readily formed on UHMWPE surfaces by surface traction forces during sliding (even in the absence of three-body abrasion) [49, 157], and are stronger in the orientation direction but weaker in the transverse direction, which is perpendicular to the orientation direction. Wear particles are therefore produced when weak fibrillar features are separated from their neighbours by tearing rupture in the transverse direction, during multidirectional motion.

N^+ ion implantation improved the wear resistance of the UHMWPE compared with the unmodified samples during the wear testing in this study, and the results could be attributed to the effects of cross-linking (which makes UHMWPE more isotropic). Cross-linking retards chain mobility and hence can directly reduce the degree of molecular orientation during sliding. In addition, the increased density of C-C chemical bonds between adjacent molecular chains by cross-linking, further makes it more difficult to split one molecule from another. Under the conditions of multidirectional motion, the orientation-softening phenomenon is known to be predominantly responsible for the detachment of fibrous wear debris from UHMWPE worn surfaces [157], and from AFM and SEM examination of the worn UHMWPE surfaces in this

study, the results would indicate that the orientation softening phenomenon was probably the main mechanism for the detachment of fibrous wear debris from the UHMWPE surfaces during testing.

The resemblance of the worn UHMWPE surfaces in this study with those of *ex vivo* components is indicative of similar or near similar wear mechanisms occurring during the wear studies and *in vivo*, and provides confirmation that the multidirectional pin-on-plate wear machine used in the study to be an appropriate experimental device for the assessment of *in vitro* wear performance.

6.3 Summary of Discussion

Summarised wear results of all the couple combinations tested in this study are presented in tables 5.1, 5.5, and 5.8, from which it can be seen that N^+ ion implantation of either polymer or metal substrate effected a reduction in the wear of the couple when compared to unmodified couple. Further, this improvement in the wear resistance was maintained over the duration of the test with no degradation observed over the period. The most significant reductions in wear volumes of the polymer were attained when both articulating components were ion implanted. Of particular significance is the tribological improvement observed for the surface modified Ti6Al4V/UHMWPE wear couples, for which the application of N^+ ion implantation surface modification brought the polymeric wear factor down to levels approaching those of unmodified stainless steel and Co-Cr-Mo/UHMWPE wear couples.

AFM examination of the topographic effects of both the ion implantation process and the tribological testing, provided validatory evidence for the appropriateness of the *in vitro* multidirectional pin-on-plate test rig used during this study. Similarities in post wear topographies, indicating common wear mechanisms, were revealed on the surfaces of the examined wear couples and those from *ex vivo* retrieved total joint hip prostheses, as illustrated in figure 5.38 (UHMWPE post wear). The topographical changes upon N^+ ion implantation were evident for all the biomaterial samples, being most marked for the lowest density Ti6Al4V alloy, with increasing ion dose causing an increase in surface roughness due to raised sputter yield and subsurface N_2 gas bubbles blister formation (figs. 5.26-5.29). Post wear testing, the ion implantation induced increased resistance to surface damage was apparent on all the alloy samples, but again was most

marked for Ti6Al4V, which unmodified was characterised by extensive scratching (fig. 5.30) whereas following ion implantation, wear induced damage was significantly reduced (fig. 5.31). This was quantified via surface roughness measurements, which indicated that unmodified Ti6Al4V that was polished to a typical R_a of 0.01 μm prior to testing against unmodified UHMWPE suffered third body abrasive surface damage from the poorly adherent TiO_2 oxide increasing the R_a to 0.08 μm following 5 million cycles of multidirectional *in vitro* wear testing. This compares poorly with the post testing R_a of 0.02 μm exhibited by the same alloy implanted N^+ ions to a dose of 2 x 10^{17} at 90 keV. Similar improvements in surface roughness of N^+ ion implanted samples compared to unmodified samples post wear testing were observed for the stainless steel (table 5.6) and Co-Cr-Mo (table 5.9) samples.

Surface sensitive Knoop microhardness measurements used to quantify N^+ ion implantation induced surface hardening on the selected biomaterials in this study, correlated well with the computer-based TRIM Monte Carlo predictions for the sub-micron mean N^+ ion depth travelled within the substrates. Figures 5.9, 5.10, 5.11 illustrates the depth dependence for Ti6Al4V substrates implanted with 2 x 10^{17} N^+ ions/cm^2, 1 x 10^{18} N^+ ions/cm^2, and 1 x 10^{21} N^+ ions/cm^2 respectively, and figures 5.57 and 5.69 illustrates that for stainless steel and Co-Cr-Mo substrates respectively. For all the substrates, significant increases in surface hardness were recorded (tables 5.3, 5.7. 5.10), which were consistent with the observed improvement in multidirectional *in vitro* wear resistance.

Despite the fact that surface modification by N^+ ion implantation is confined to a very thin layer beneath the surface, significantly improved surface properties such as surface hardness and wear, have been well identified in this study, and were attributed to the change in structure conferred by N^+ ion implantation induced interaction between the energetic N^+ ions and the biomaterial surfaces. Such near surface improvements in the properties of biomaterials would be beneficial in total joint replacement applications. During the process of N^+ ion implantation in metallic biomaterials, atomic and nuclear collisions lead to the formation of highly disordered and amorphous structures in the near-surface region, and the formation of new chemical bonds between substrate atoms and the implanted ions lead to the formation of hard-phase nitride precipitates (high dose implantation, > 10^{17} N^+ ions/cm^2). These changes typically combine to create surfaces that are harder and more resistant to wear and chemical attack (section 3.2.1).

In polymeric biomaterials, ionisation interactions of implantation ions with substrate atoms (dominant at the high energies), lead to cross-linking in adjacent polymer chains, creating a three-dimensionally cross-linked surface layer with much higher hardness and much improved wear resistance (section 3.2.1.1). The ion implantation conditions used in this study (section 4.2.3, table 4.3), promoted ionisation (high ion energy > 10 keV), and reduced oxidation effects (carried out in a high vacuum environment).

CHAPTER SEVEN – CONCLUSIONS

This study has investigated the effects of N^+ ion implantation of metallic and UHMWPE biomaterials, and has added to the understanding of the tribological behaviour of N^+ ion implanted biomaterial sliding combinations. In particular the effects of N^+ ion implantation on the tribological performance of Ti6Al4V/UHMWPE sliding couples are noteworthy. The following conclusions can be drawn from the review of the results:

1 Reciprocation and rotation pin-on-plate machine

1.1 The multidirectional motion pin-on-plate machine used in this study produced results similar to clinical wear factors, and the wear features observed on the UHMWPE samples following articulation against metallic counterfaces during the study, were similar to those observed on *ex vivo* UHMWPE acetabular cup components. The tribological results suggest that the machine is a useful device for evaluating bearing materials for use in TJRs. The reciprocation and rotation pin-on-plate machine is considered to be a cheap, simple, and more accurate method (than the simple reciprocation pin-on-plate or the pin-on-disc machine) of comparing the wear of different biomaterial combinations prior to simulator testing and clinical trials.

1.2 N^+ ion implantation significantly increased the surface wear resistance of the investigated biomaterials (Ti6Al4V, stainless steel, Co-Cr-Mo and UHMWPE) in *in vitro* testing using multidirectional pin-on-plate testing.

2 Modified and unmodified Ti6Al4V/UHMWPE wear couple

2.1 Severe three body abrasive wear mechanism was found to dominate unmodified Ti6Al4V/UHMWPE wear couples under multidirectional motion and bovine serum lubrication, leading to extensive surface damage of the alloy and severe wear of the mating UHMWPE. No adhesive or fatigue wear mechanisms were found.

2.2 N^+ ion implantation at 90 keV with 2 x 10^{17} ions/cm^2 improved the surface hardness of Ti6Al4V by a factor of 2.1, and enhanced chemical resistance and surface wear resistance of the alloy. The mating UHMWPE in turn, experienced less severe wear conditions, and the wear resistance was improved by ≈ 41 %, compared to the wear of untreated UHMWPE against unmodified Ti6Al4V.

2.3 N^+ ion implantation at 90 keV with 1 x 10^{18} ions/cm^2 improved the surface hardness of Ti6Al4V by a factor of 3.1, and enhanced the chemical resistance and surface wear resistance of the alloy. The mating UHMWPE in turn, experienced less severe wear conditions, and the wear resistance was improved by ≈ 35 %, compared to the wear of untreated UHMWPE against unmodified Ti6Al4V.

2.4 N^+ ion implantation at 90 keV with 1 x 10^{21} ions/cm^2 improved the surface hardness of Ti6Al4V by a factor of 4.1, and enhanced the chemical resistance and surface wear resistance of the alloy. The mating UHMWPE in turn, experienced less severe wear conditions, and the wear resistance was improved by ≈ 25 %, compared to the wear of untreated UHMWPE against unmodified Ti6Al4V.

2.5 N^+ ion implantation increased the surface roughness of Ti6Al4V when the implantation ion dose increased from 2 x 10^{17} to 1 x 10^{18} and 1 x 10^{21} ions/cm^2 respectively. The respective increase in surface roughness on the alloy surfaces, in turn, reduced the percentage improvement in the wear resistance of the mating UHMWPE though not significantly (≈ 5 % and 15 % respectively), compared to the wear improvement of unmodified UHMWPE against 2 x 10^{17} ions/cm^2 implanted Ti6Al4V.

2.6 XPS analysis indicated the presence of Ti^+ and N^- species attributable to TiN on the surfaces of the N^+ ion implanted Ti6Al4V, which was predominantly responsible for the hardening effect of the implanted surface.

2.7 N^+ ion implantation at 80 keV with 1 x 10^{15} and 5 x 10^{15} ions/cm^2 increased the surface hardness of UHMWPE by a factor of 2.5 and 3.8 respectively. An increase in hardness of XLPE material by a factor of 2.4 was calculated.

2.8 N^+ ion implantation at 90 keV with 2 x 10^{17} ions/cm^2 on Ti6Al4V, and 80 KeV with 5 x 10^{15} ions/cm^2 on UHMWPE wear couples, improved the surface hardness and wear of the articulating surfaces significantly. A significant improvement in the wear factor of the modified UHMWPE of ≈ 55 % was calculated following *in vitro* wear testing, compared to the unmodified UHMWPE articulated against unmodified Ti6Al4V.

2.9 N^+ ion implantation enhanced the tribological performance of the Ti6Al4V/UHMWPE sliding couple by impeding third body formation through stabilisation of the weak surface oxide layer on the Ti6Al4V counterface, and hence reduced the effects of severe three-body abrasive wear of the articulating surfaces.

2.10 XPS studies confirmed that surface species present on Ti6Al4V upon ion implantation were retained following *in vitro* multidirectional wear testing, indicating that the surface integrity of the ion implantation treatment was retained for the test duration. This was confirmatory to the wear test data that demonstrated no diminution in the favourable wear resistance for the ion implanted surfaces over the duration of the testing. XPS analysis made on ion implanted Ti6Al4V substrates post wear testing indicated the presence of TiN within the surface of the wear couple contact zone.

3 Modified and unmodified stainless steel/UHMWPE wear couple

3.1 Two body abrasive wear mechanism was found to dominate unmodified stainless steel/UHMWPE wear couples under multidirectional motion and bovine serum lubrication, leading to mild surface damage of the alloy and wear of the mating UHMWPE (compared to the unmodified Ti6Al4V/UHMWPE wear couples). No adhesive or fatigue wear mechanisms were found.

3.2 N^+ ion implantation at 90 keV with 2 x 10^{17} ions/cm^2 improved the surface hardness of stainless steel by a factor of 2.1 and enhanced the surface wear resistance of the alloy. The mating UHMWPE in turn, experienced less severe wear conditions, and the wear resistance was improved by ≈ 38 %, compared to the wear of untreated UHMWPE against unmodified stainless steel.

3.3 N^+ ion implantation at 90 keV with 2 x 10^{17} ions/cm^2 on stainless steel, and 80 KeV with 5 x 10^{15} ions/cm^2 on UHMWPE wear couples, improved the surface hardness and wear of both articulating surfaces significantly. A significant improvement in the wear resistance of the modified UHMWPE of ≈ 48 % was calculated following *in vitro* wear testing, compared to the unmodified UHMWPE articulated against unmodified stainless steel.

4.0 **Modified and unmodified Co-Cr-Mo/UHMWPE wear couple**

4.1 Two body abrasive wear was found to dominate unmodified Co-Cr-Mo/UHMWPE wear couples under multidirectional motion and bovine serum lubrication, leading to mild surface damage of the alloy and wear of the mating UHMWPE (compared to the unmodified Ti6Al4V/UHMWPE wear couples). No adhesive or fatigue wear mechanisms were found.

4.2 N^+ ion implantation at 90 keV with 2 x 10^{17} ions/cm^2 increased the surface hardness of Co-Cr-Mo by a factor of 2.1 and enhanced the surface wear resistance of the alloy. The mating UHMWPE in turn, experienced less severe wear conditions, and the wear resistance was improved by ≈ 42 %, compared to the wear of untreated UHMWPE against unmodified Co-Cr-Mo.

4.3 N^+ ion implantation at 90 keV with 2 x 10^{17} ions/cm^2 on Co-Cr-Mo, and 80 KeV with 5 x 10^{15} ions/cm^2 on UHMWPE wear couples, improved the surface hardness and wear of both articulating surfaces. A significant improvement in the wear resistance of the modified UHMWPE of ≈ 48 % was calculated following *in vitro* wear testing, compared to that of the unmodified UHMWPE articulated against unmodified Co-Cr-Mo.

In summary, it can be concluded from the results of the research project that N^+ ion implantation of the selected biomaterials offers significant potential for improvement in tribological performance under *in vitro* conditions, and likely improvements under *in vivo* conditions. The modified surfaces investigated showed significant improvements in wear volumes generated over the duration of 5 million wear cycles of testing when compared to unmodified surfaces, and for Ti6Al4V articulating against UHMWPE, wear volumes of modified surfaces were reduced to levels associated with the clinically

used, but high elastic modulus alloys (316L stainless steel and Co-Cr-Mo). The improvements in wear resistance can be attributed to increase in surface hardness and changes in surface chemistry induced by N^+ ion implantation, and these beneficial effects were retained for the duration of the investigated tribological evaluations. No evidence of wear induced penetration through the ion implanted surface modified zone to the unmodified bulk substrate was observed following detailed topographic examinations and chemical analysis via XPS.

The tribological assessment of the modified biomaterials showed that, 2 x 10^{17} N^+ ions/cm^2 implanted metallic samples at 90 keV and 5 x 10^{15} N^+ ions/cm^2 implanted UHMWPE samples at 80 keV wear couples, produced the optimum tribological performance of the investigated biomaterial couple combinations *in vitro*.

This study contributes to understanding of the *in vitro* tribological performance of the selected N^+ ion implanted biomaterials. It extends upon and differs from previous work because of the combination of experimental and analytical methodologies adopted to investigate the effects of N^+ ion implantation upon the selected biomaterials. Specifically, extensive multidirectional *in vitro* wear testing to over 5.5 million wear cycles was performed on the selected modified and unmodified biomaterial wear couples. This work is novel because it incorporated an *in vitro* methodology that utilised a bovine serum lubricated multidirectional wear path with load, frequency of cycle, and stoke length modelled on the human walking gait cycle. It is the appropriateness of the *in vitro* methodology and the duration of the testing that underpin this work and set it apart from other published work (typically run to 1-3 million wear cycles).

In addition to the evaluation of the wear behaviour of the modified and unmodified materials, N^+ ion implantation was performed on samples of the selected biomaterials and study of the induced surface hardening was investigated to provide complementary evidence in order to understand the effect of the surface modification on the tribological performance of these biomaterials. Similarly, chemical changes and topographical changes upon N^+ ion implantation of the selected biomaterials were investigated in order to provide complementary evidence to explain the effects on tribological performance of the surface modification treatment. Further, topographical analysis of the modified and unmodified substrates as tribological testing progressed was also carried out which together provide a comprehensive study of the tribological

performance of the materials over the duration of the *in vitro* testing. It is this combination of experimental and analytical approaches that sets this work apart from previous, often piecemeal and short-duration studies of the wear of ion implanted biomaterials.

CHAPTER EIGHT - FUTURE WORK

Further long term joint simulator wear studies of all the selected unmodified and N^+ ion implantation modified metallic/polymer biomaterial wear couples would provide additional information as to the durability of such a narrow surface modified layer.

Chemical analysis of saved bovine serum lubricant from N^+ ion implantation modified Ti6Al4V/UHMWPE wear couples to confirm the absence of TiO_2 particles following *in vitro* wear testing.

Further microscopic investigations of the UHMWPE and metallic samples should be performed following *in vitro* wear testing, to detect the presence of crack formation on the UHMWPE samples (fatigue wear) or the presence of transfer films on the metallic samples (adhesive wear).

Ion beam milling or depth profile XPS analysis through the surface of the of the ion implanted samples would provide confirmatory or additional information to support the observed hardness increase in the 1×10^{21} N^+ ions/cm^2 samples.

Cross-sectional TEM investigations of the nano-structural effects of N^+ ion implantation on the selected biomaterials would provide additional information as to the physical effects of ion implantation on microstructure.

DSC and Raman Spectroscopy characterisation of N^+ ion implanted and unmodified UHMWPE would offer improved understanding of the microstructural and chemical changes upon ion implantation.

Given the similar nature of energetic ion species of ion implantation to irradiation methods of sterilisation, long term stability in particular, and mechanical properties should be investigated.

CHAPTER NINE – REFERENCES

1. http://www.boneandjointdecade.org.

2. Long, M. and H.J. Rack, Titanium alloys in total joint replacement - a materials science perspective. Biomaterials, 1998. **19**: p. 1621-1639.

3. Lausmaa, J., T. Rostlund, and H. McKellop, A Surface Spectroscopic Study of Nitrogen Ion-implanted Ti and Ti-6AL-4V Wear Against UHMWPE. Surf. Inter. Anal., 1990. **15**: p. 328-336.

4. Ash, H., Development of Surface Replacement Prostheses for the Proximal Interphalangeal and Metacarpo-phalangeal Joints, in Centre of Biomedical Engineering. 1997, University of Durham: Durham. p. 1-357.

5. Volz, R.G. and J.B. Benjamin, The Current Status of Total Joint Replacement. Invest. Radiol., 1990. **25**: p. 86-92.

6. Rostlund, T., et al., Wear of ion-implanted pure titanium against UHMWPE. Biomaterials, 1989. **10**: p. 176-181.

7. Schmalzried, T.P. and J.J. Callaghan., Current Concepts Review: Wear in Total Hip and Knee Replacements. J. Bone Joint Surg., 1999. **81-A**: p. 115-136.

8. Kurtz, S.M., et al., Advances in the processing, sterilisation, and crosslinking of UHMWPE for total joint arthroplasty. Biomaterials, 1999. **20**: p. 1659-1688.

9. Shi, W., X.Y. Li, and H. Dong, Improved wear resistance of ultra-high molecular weight polyethylene by plasma immersion ion implantation. Wear, 2001. **250**(1-12): p. 544-552.

10. Wang, A., A unified theory of wear for ultra-high molecular weight polyethylene in multi-direction sliding. Wear, 2001. **248**: p. 38-47.

11. Wang, A., et al., Orientation softening in the deformation and wear of ultra-high molecular weight polyethylene. Wear, 1997. **203-204**: p. 230-241.

12. Dearnley, P.S., A review of metallic, ceramic and surface-treated metals used for bearing surfaces in human joint replacements. Proc. I Mech. Part H; J. Eng. in Med, 1999. **213**: p. 107-135.

13. Campbell, P. and H.C. Amstutz. The Need for Improved Orthopaedic Bearing Surfaces: A Clinical Perspective. in Proceedings of the Fifth International Conference on Surface Modification Technology V. 1992. Birmingham, UK: The Institute of Materials.

14. Sudarshan, T.S. and J.F. Braza. Surface Modification Technology V. in Proceedings of the Fifth International Conference. 1991. Birmingham, UK: The Institute of Materials.

15. Bartel, D.L., et al. Generation of Debris in Total Hip Replacements Due to Damage of the Articulating Surfaces. in Proceedings of the Fifth International Conference on Surface Modification Technology V. 1992. Birmingham, UK: The Institute of Materials.

16. Davidson, J.A. and A.K. Mishra. Surface modification issues for orthopaedic implant bearing surfaces. in Proc. Fifth International Conf. on Surface Modification Technology. 1991. Birmingham, UK: The Institute of Materials.

17. Onate, J.I., et al., Wear reduction effect on ultra-high-molecular-weight polyethylene by application of hard coatings and ion implantation on cobalt chromium alloy, as measured in a knee wear simulation machine. Surface and Coatings Technology, 2001. **142-144**: p. 1056-1062.

18. Lombardi, A.V., et al., Aseptic Loosening in Total Hip Arthroplasty Secondary to Osteolysis Induced by Wear Debris from Titanium-Alloy Modular Femoral Heads. J. Bone Joint Surg., 1989. **71-A**(9): p. 1337-1342.

19. Schmalzried, T.P., M. Jasty, and W.H. Harris, Periprosthetic Bone Loss in Total Hip Arthroplasty: polyethylene wear debris and the concept of the effective joint space. J. Bone Joint Surg., 1992. **74-A**: p. 849-863.

20. Barbour, P.S.M., M.H. Stone, and J. Fisher, A study of the wear resistance of three types of clinically applied UHMWPE for total replacement hip prostheses. Biomaterials, 1999. **20**: p. 2101-2106.

21. Davidson, J.A., Characteristics of Metal and Ceramic Total Hip Bearing Surfaces and Their Effect on Long-Term UHMWPE Wear. Clin. Orth. Rel. Res., 1993. **294**: p. 360-376.

22. Goodman, S.B. The Role of Polymer Particles in the Process of Aseptic Loosening of Joint Arthroplasties. in Proceedings of the Fifth International Conference on Surface Modification Technology V. 1992. Birmingham, UK: The Institute of Mterials.

23. Schmalzried, T.P., et al., The mechanism of loosening of cemented acetabular components in total hip arthroplasty. Clin. Orth. Rel. Res., 1992. **274**: p. 60-78.

24. Saikko, V., Wear and friction properties of prosthetic joint materials evaluated on a reciprocating pin-on-flat apparatus. Wear, 1993. **166**: p. 169-178.

25. Barbour, P.S.M., D.C. Barton, and J. Fisher, The influence of contact stress on the wear of UHMWPE for total hip prostheses. Wear, 1995. **181-183**: p. 250-257.

26. Cui, F.Z. and Z.S. Luo, Biomaterials modification by ion-implantation processing. Surf. Coat. Tech, 1999. **112**: p. 278-285.

27. Sioshansi, P. and E.J. Tobin, Surface treatment of biomaterials by ion beam processes. Surf. Coat. Technol., 1996. **83**: p. 175-182.

28. Park, J.B. and R.S. Lakes, Biomaterials: An Introduction. Second ed. 1992, New York; London: Plenum Press.

29. Reitz, W., The Critical Role of Surface Modification in Biomaterials. JOM., 1997: p. 44.

30. Dearnaley, G., Ion implantation and ion assisted coatings for wear resistance in metals. Surf. Eng., 1986. **2**(3): p. 213-221.

31. Bosetti, M., et al., In vivo evaluation of bone tissue behaviour on ion implanted surfaces. J. Mater. Sci-Mater. Med., 2001. **12**(5): p. 431-435.

32. Ratner, B.D., et al., eds. Biomaterials Science: An Introduction to Materials in Medicine. 1996, Sandiego; London: Academic Press.

33. Baker, D.A., Macro-and Microscopic Evaluation of Fatigue in Medical Grade Ultrahigh Molecular Weight Polyethylene. PhD Theses. May 2001, University of California: Berkeley. P. 1-223.

34. Dearnley, P.A., A review of metallic, ceramic and surface-treated metals used for bearing surfaces in human joint replacements. Proc. I Mech. Part H; J. Eng. in Med, 1999. **213**: p. 107-135.

35. Mcgovern, T.E., et al., In vivo wear of Ti6Al4V femoral heads: A retrieval study. J. Biomed. Mater. Res., 1996. **32**: p. 447-457.

36. McKellop, H.A. and T.V. Rostlund, The wear behaviour of ion-implanted Ti6Al4V against UHMW polyethylene. J. Biomed. Mater. Res., 1990. **24**: p. 1413-1425.

37. Agins, H.J., et al., Metallic Wear in Failed Titanium-Alloy Total Hip Replacements. J. Bone Joint Surg., 1988. **70-A**(3): p. 347-356.

38. Albrektsson, T., et al., Osseointegrated titanium implants - Requirements for ensuring a long-lasting, direct bone-to-bone implant anchorage in man. Acta Orthop. Scand., 1981. **52**: p. 155-170.

39. Khan, M.A., R.L. Williams, and D.F. Williams, Conjoint corrosion and wear in titanium alloys. Biomaterials, 1999. **20**(8): p. 765-772.

40. Black, J., et al., Metallosi Associated with a Stable Titanium-Alloy Femoral Component in Total Hip Replacement. J. Bone Joint Surg., 1990. **72-A**(1): p. 126-130.

41. Black, J., Orthopaedic Biomaterials In Research And Practice. 1988, New York: Churchill Livingstone.

42. Black, J. and G. Hastings, eds. Handbook of Biomaterial Properties. First ed. 1998, London: Chapman & Hall.

43. Sundararajan, T., et al., Effect of nitrogen ion implantaion on the localised corrosion behaviour of titanium modified type 316L stainless steel in simulated body fluid. J. Mater. Eng. Perform., 1999. **8**: p. 252-260.

44. Leitao, E., R.A. Silva, and M.A. Barbosa, Electrochemical and surface modifications on N+-ion-implanted 316L stainless steel. J. Mater. Sci. Mater. Med., 1997. **8**: p. 365-368.

45. Streicher, M., Ionizing irradiation for sterilisation and modification of high molecular weight polyethylenes. Plastics and Rubber Processing and Applications, 1988. **10**: p. 221-229.

46. Farrar, D.F. and A.A. Brain, The microstructure of ultra-high molecular weight polyethylene used in total joint replacements. Biomaterials, 1997. **18**: p. 1677-1685.

47. Olley, R.H., et al., On morphology of consolidated UHMWPE resin in hip cups. Biomaterials, 1999. **20**(21): p. 2037-2046.

48. Semlitsch, M. and H.G. Willert, Clinical wear behaviour of ultra-high molecular weight polyethylene cups paired with metal and ceramic ball heads in comparison to metal-on-metal pairings of hip joint replacements. Proc. Instn. Mech. Engrs. Part H, 1997. **211**: p. 73-88.

49. Wang, A., et al., Lubrication and wear of ultra-high molecular weight polyethylene in total joint replacements. Tribol. Int., 1998. **31**(1-3): p. 17-33.

50. Joyce, T.J., H.E. Ash, and A. Unsworth, The wear of cross-linked polyethylene against itself. Proc. I Mech. Part H; J. Eng. in Med, 1996. **210**: p. 11-16.

51. Williams, D.F., Biocompatibility of orthopaedic implants. Vol. 1. 1982, CRC Press.

52. Atkinson, J.R. and R.Z. Cicek, Silane cross-linked polyethylene for prosthetic applications Part I. Certain physical and mechanical properties related to the nature of the material. Biomaterials, 1983. **4**: p. 267-275.

53. Dowson, D. and V. Wright, eds. An Introduction to the Bio-mechanics of Joints and Joint Replacement. 1981, London: Mechanical Engineering publications. p. 1-248.

54. Hutchings, I.M., TRIBOLOGY. 1992, London: Arnold.

55. Belak, J.F., Nanotribology. Mrs Bulletin, 1993: p. 15-16.

56. ASTM Designation: G40-93, Standard Terminology Relating to Wear and Erosion. 1993.

57. Dong, H. and T. Bell, State-of-the-art overview: ion beam modification of polymers towards improving tribological properties. Surf.Coat.Tech, 1999. **111**: p. 29-40.

58. Dowson, D., A comparative study of the performance of metallic and ceramic femoral head components in total replacement hip joints. Wear, 1995. **190**: p. 171-183.

59. Atkinson, J.R., J.M. Dowling, and R.Z. Cicek, Materials for internal prostheses: the present position and possible future developments. Biomaterials, 1980. **1**(2): p. 89-96.

60. Sutula, L.C., et al., Impact of gamma-sterilisation on clinical performance of polyethylene in the hip. Clin. Orthop Rel. Res., 1995. **319**: p. 28-40.

61. Sychterz, C.J., et al., Wear of polyethylene cups in total hip arthroplasty. J. Bone Joint Surg., 1996. **78-A**(8): p. 1193-1200.

62. Haynes, D.R., T.N. Crotti, and M.R. Haywood, Corrosion of and changes in biological effects of cobalt chrome alloy nd 316L stainless steel prosthetic particles with age. J. Biomed. Mater. Res., 2000. **49**: p. 167-175.

63. Wang, A., et al., Effect of Femoral Head Surface Roughness on the Wear of Ultrahigh Molecular Weight Polyethylene Acetabular Cups. The Journal of Arthroplasty, 1998. **13**(6): p. 615-620.

64. Dowson, D., et al. Proc. Int. Symp. on Polymer Wear and Its Control. 1984. St. Louis, MO: American Chemical Society, New York.

65. Lancaster, J.G., et al., The wear of ultra-high molecular weight polyethylene sliding on metallic and ceramic counterfaces representative of current femoral surfaces in joint replacement. Proc. I Mech. Part H; J. Eng. in Med, 1997. **211**(1): p. 17-24.

66. Dowson, D., J.R. Atkinson, and K.J. Brown, Advances in polymer friction and wear. Polymer Science and Technology Symposia Series, ed. L.-H. Lee. Vol. 5B. 1974, New York: Plenum Press. P. 1-533.

67. Dowson, D. and N.C. Wallbridge, Laboratory wear tests and clinical observations of the penetration of femoral heads into acetabular cups in total replacement hip joints I: Charnley prostheses with polytetrafluoroethylene acetabular cups. Wear, 1985. **104**: p. 203-215.

68. Bragdon, C.R., et al., The influence of multidirectional motion on the wear of polyethylene. Proc. I Mech. Part H; J. Eng. in Med, 1996. **210**: p. 157-165.

69. Dowson, D., Friction and wear of medical implants and prosthetic devices. ASM Handbook, 1992. **18**: p. 656-664.

70. Unsworth, A., D. Dowson, and V. Wright, The frictional behaviour of human synovial joints - Part 1: Natural joints. Trans. ASME, J. Lub. Techn., 1975. **97**: p. 369-376.

71. McHargue, C.J., Ion implantation into metals and ceramics. International Metals Reviews, 1986. **31**: p. 49-76.

72. Oliver, W.C., R. Hutching, and J.B. Pethica, The wear behaviour of nitrogen-implanted metals. Metallurgical Transactions, 1984. **A 15A**: p. 2221-2229.

73. Poate, J.M., G. Foti, and D.C. Jacobson, Surface Modification And Alloying, by Laser, Ion, and Electron Beams, by Laser, Ion, and Electron Beams. 1993, New York: Plenum Press.

74. Dearnaley, G. and N.E. Hartley, Ion Implantation into Metals and Carbides. Thin Solid Films, 1978. **54**: p. 215-232.

75. Dong, H., W. Shi, and T. Bell, Potential of improving tribological performance of UHMWPE by engineering the Ti6AL4V counterfaces. Wear, 1999. **225-229**: p. 146-153.

76. Jones, A.M. and S.J. Bull, Changing the tribological performance of steels using low energy, high temperature nitrogen ion implantation. Surf. Coat. Technol., 1996. **83**: p. 269-274.

77. Garcia, J.A., et al., Nitrogen ion implantation on group IVb metals: chemical, mechanical and tribological study. Vacuum, 2002. **64**(3-4): p. 343-351.

78. Venkatesan, T., High Energy Ion Beam Modification Of Polymers Films. Nucl. Instr. Meth. Phys. Res., 1985. **B7/8**: p. 461-467.

79. Guzman, L., et al., Hard coating adhesion on ion implanted polymer surfaces. Thin Solid Films, 2000. **377-378**: p. 760-765.

80. Dong, H. and T. Bell, Plasma ion implantation of UHMWPE. J. Mater. Sci. Lett., 2000. **19**: p. 11471149.

81. Guzman, L., et al., Polymer surface modification by ion implantation and reactive deposition of transparent films. Surf.Coat.Tech., 1998. **103-104**: p. 375-379.

82. Popok, V.N., et al., High fluence ion beam modification of polymer surfaces: EPR and XPS studies. Nuclear Instruments and Methods in Physics Research Section B: Beam Interactions with Materials and Atoms, 2001. **178**(1-4): p. 305-310.

83. Picq, V., J.M. Ramillon, and E. Balanzat, Swift heavy ions on polymers: Hydrocarbon gas release. Nuclear Instruments and Methods in Physics Research Section B: Beam Interactions with Materials and Atoms, 1998. **146**(1-4): p. 496-503.

84. Kondyurin, A., V. Karmanov, and R. Guenzel, Plasma immersion ion implantation of polyethylene. Vacuum, 2001. **64**(2): p. 105-111.

85. McKellop, H., F.-W. Shen, and R. Salovey. Extremely low wear rate of gamma-crosslinked/remelted UHMW polyethylene acetabular cups. in 44th Annual Meeting of the Orthopaedic Research Society. 1998. New Orleans, Lousiana.

86. Shen, F.-W., H. McKellop, and R. Salovey. Improving the resistance of wear and oxidation of acetabular cups of UHMWPE by gamma radiation crosslinking and remelting. in 24th Annual Meeting of the Society for Biomaterials. 1998. San Diego, California.

87. Bragdon, C.R., et al. A new polyethylene with undetectable weat at 12 million cycles. in 24th Annual Meeting of the Society for Biomaterials. 1998. San Diego, California.

88. Chiesa, R., et al., Enhanced wear performance of highly crosslinked UHMWPE for artificial joints. J. Biomed. Mater. Res., 2000. **50**(3): p. 381-387.

89. Schmidt, H., A. Achminke, and D.M. Ruck, Tribological behaviour of ion-implanted Ti6AL4V sliding against polymers. Wear, 1997. **209**: p. 49-56.

90. Dearnaley, G., Application of ion implantation in metals. Thin Solid Films, 1983. **107**: p. 315-326.

91. Rieu, J., et al., Deterioration mechanisms of joint prosthesis materials. Several solutions by ion implantion surface treatments. Biomaterials, 1990. **11**: p. 51-54.

92. Mjoberg, B., Theories of wear and loosening in hip prostheses. Wear-induced loosening vs loosening-induced wear - a review. Acta. Orthop. Scand, 1994. **65 (3)**: p. 361-371.

93. Elfick, A.P.D., et al., Wear in Retrieved Acetabular Components. J. Athrop., 1998. **13**(3): p. 291-295.

94. Hanawa, T., In vivo metallic biomaterials and surface modification. Mater. Sci. Eng, 1999. **A 267**: p. 260-266.

95. Miyagawa, Y., et al., Retention of nitrogen implanted into metals. Nuclear Instruments and Methods in Physics Research Section B: Beam Interactions with Materials and Atoms, 1995. **106**(1-4): p. 170-173.

96. Allen, C., A. Bloyce, and T. Bell, Sliding wear behaviour of ion implanted UHMWPE against a surface modified titanium alloy Ti-6AL-4V. Tribol. Int., 1996. **29**: p. 527-534.

97. Schmidt, H. and H.E. Exner, Wear, Corrosion and Fatigue Properties of Ion Implanted Titanium Alloy Ti6AL4V. Z. Metallkd, 1999. **90**: p. 594-601.

98. Taylor, S.K., P. Serekian, and M. Manley. UHMWPE debris generation from acetabular cup inserts articulating against untreated CoCr, ion implanted CoCr, and Zro2 bearings under hip joint simulation. in 39th Annual Meeting, Orthopaedic Research Society. 1993. San Francisco, California.

99. Rieu, J., et al., Ion implantation effects on friction and wear of joint prosthesis materials. Biomaterials, 1991. **12**: p. 139-143.

100. Li, H.T., et al., Some experimental studies on metal implantation. Nucl. Instr. Meth. Phys. Res., 1981. **182-183**: p. 915-917.

101. Schmidt, H., et al., Compound formation and abrasion resistance of ion-implanted Ti6Al4V. Act Mater., 2001. **49**: p. 487-495.

102. Rieu, J., et al., Structural modifications induced by ion implantation in metals and polymers used for orthopaedic prostheses. Mater. Sci. Technol., 1992. **8**: p. 589-592.

103. Yoshinari, M., et al., Influence of surface modifications to titanium on antibacterial activity in vitro. Biomaterials, 2001. **22**(14): p. 2043-2048.

104. Yoshinari, M., et al., Influence of surface modification to titanium on oral bacterial adhesion in vitro. J. Biomed. Mater. Res., 2000. **52**(2): p. 388-394.

105. Bordji, K., et al., Evaluation of the effect of three surface treatments on the biocompatibility of 316 stainless steel using human differentiated cells. Biomaterials, 1996. **17**: p. 491-500.

106. Cordier-Robert, C., et al., Optimisation of nitrogen implantation of austenitic 316L steel by microstructural analysis. Materials Letters, 1994. **20**: p. 113-118.

107. Richter, E., et al., Nitriding of stainless steel and aluminium alloys by plasma immersion ion implantation. Surf. Coat. Technol., 2000. **128-129**: p. 21-27.

108. Chen, J.S., et al., Structural and mechanical properties of nitrogen ion implanted ultra high molecular weight polyethylene. Surface and Coatings Technology, 2001. **138**(1): p. 33-38.

109. Onate, J.I., J.K. Dennis, and S. Hamilton, The effect of nitrogen ion implantation on the properties of coatings. Trans. IMF, 1987. **65**: p. 99-104.

110. Kumar, P., et al., Low wear rate of UHMWPE agaisnt zirconia ceramic (Y-PSZ) in comparison to alumina ceramic and SUS 316L alloy. J. Biomed. Mater. Res., 1991. **25**: p. 813-828.

111. McKellop, H., et al., Friction and wear properties of polymer, metal, and ceramic prosthetic joint materials evaluated on a multichannel screening device. J. Biomed. Mater. Res., 1981. **15**: p. 619-653.

112. ASTM Designation: F732-82, Standard practice for reciprocating pin-on-flat evaluation of friction and wear properties of polymeric materials for use in total joint prostheses. 1982.

113. ASTM Designation: F732-00, Standard Test Method for Wear Testing of Polymeric Materials Used in Total Joint Prostheses. 2000.

114. Saikko, V., A multidirectional motion pin-on-disc wear test method for prosthetic joint materials. J. Biomed. Mater. Res., 1998. **41**: p. 58-64.

115. Mathews, J.B., et al., Evaluation of the response to promary human peripheral blood mono-nuclear phagocytes to challenge with in vitro generated clinically relevant UHMWPE particles of known size and dose. J. Biomed. Mater. Res., 2000. **52**(2): p. 296-307.

116. Joyce, T.J., et al., A multi-directional wear screening device and preliminary results of UHMWPE articulating against stainless steel. Bio-Med. Mater. Eng., 2000. **10**: p. 241-249.

117. Cartwright, T., The effect of rotation on the wear of cross-linked polyehtylene (XLPE). 1998, University of Durham: Durham. p. 1-80.

118. Scholes, S.C., The Tribology of Hard Bearing Surfaces for Use in Hip Prostheses, in Centre for Biomedical Engineering. 1999, University of Durham: Durham. p. 1-212.

119. McKellop, H., Wear of artificial joint materials II. Twelve-chanenel wear-screening device: correlation of experimental and clinical results. Engineering in Medicine, 1981. **10**(3): p. 123-136.

120. Ahlroos, T. and V. Saikko, Wear of prosthetic joint materials in various lubricants. Wear, 1997. **211**: p. 113-119.

121. McKellop, H., et al., Wear characteristics of UHMW polyethylene: A method for accurately measuring extremely low wear rates. J. Biomed. Mater. Res., 1978. **12**: p. 895-927.

122. Wang, A., et al., Comparison of the size and morphology of UHMWPE wear debris produced by a hip joint simulator under serum and water lubricated conditions. Biomaterials, 1995. **17**: p. 865-871.

123. Ziegler, J.F. and J.P. Biersack, The Stopping and Range of Ions in Matter (SRIM Software) http://www.srim.org. 2002.

124. TopoMetrix Explorer Technical Briefs. 1996.

125. Zygo New View 100 Operation Manual. 1995.

126. Dieter, G.E., Mechanical Metallurgy. SI Metric ed. 1988, New York; London: McGraw-Hill. p. 751.

127. Callister, W.D., Mechanical Properties of Metals, in Materials Science And Engineering: An Introduction. 1994, John Wiley & Sons, Inc.: New York. p. 106.

128. Torregrosa, F., L. Barrallier, and L. Roux, Phase analysis, microhardness and tribological behaviour of Ti-6AL-4V after ion implantation of nitrogen in connection with its application for hip-joint prosthesis. Thin Solid Films, 1995. **266**: p. 245-253.

129. Green, S.M., The Surface Performance of Ni-Ti Shape Memory Alloys, in Department of Materials Engineering and Materials Design. 1995, University of Nottingham: Nottingham. p. 1-206.

130. Goodhew, P.J., J. Humphreys, and R. Beanland, Electron Microscopy and Analysis. Third ed. 2001: Taylor & Francis.

131. Axiotech Reflected Light Microscope Operational Manual. 1994.

132. Bowen, D.K. and C.R. Hall, Microscopy of Materials. 1975: Macmillan Press Ltd. P. 1-304.

133. Elfick, A.P.D., et al., A re-appraisal of wear features of acetabular sockets using atomic force microscopy. Wear, 2002. **253**: p. 839-847.

134. Ji, H., et al., Tribological performance of Ti-6Al-4V plasma-based ion implanted with nitrogen. Wear, 2000. **246**: p. 40-45.

135. Pichat, A., et al., Effect of ion implantation on titanium alloy/polyethylene and 316L stainless steel/polyethylene friction couples running in joint prostheses. Surf. Coat. Technol., 1991. **45**: p. 15-22.

136. Herman, H. Modification of the surface mechanical properties of ferrous alloys by nitrogen ion implantation. in Proceedings of the 3rd International Conference on Modification of Surface Properties of Metals by Ion implantation. 1981. UMIST, Manchester, UK: Pergamon Press.

137. Roth, J., R. Behrisch, and B.M.U. Scherzer, Blistering of nobium due to 0.5 to 9 keV helium and hydrogen bombardment. J. Nucl. Mater., 1974. **53**: p. 147-153.

138. Martel, J.G., et al., Preliminary observations of blistering of nobium by 1 - 15 keV helium ions. J. Nucl. Mater., 1974. **53**: p. 142-146.

139. Briggs, D. and M.P. Seah, eds. Practical Surface Analysis by Auger and X-ray Photoelectron Spectroscopy. 1983, John Wiley & Sons, Ltd.

140. Berberich, F., et al., Structural characterisation of hardening of Ti-Al-V alloys after nitridation by plasma immersion ion implantation. Applied Surface Science, 2001. **179**(1-4): p. 13-19.

141. Green, S.M., D.M. Grant, and J.V. Wood, XPS characterisation of surface modified Ni-Ti shape memory alloy. Mater. Sci. Eng., 1997. **A 224**: p. 21-26.

142. Lausmaa, J., T. Rostlund, and H. McKellop. Wear of Ion-implanted Pure Titanium and Ti-6Al-4V Alloy Against UHMWPE. in Proceedings of the Fifth International Conference on Surface Modification Technology V. 1992. Birmingham, UK.

143. Vollmer, D.P., et al., Electrochemical passivity of titanium implanted with 1 MeV gold ions. Corrosion Science, 1998. **40**(2-3): p. 297-306.

144. Mucha, A. and M. Braun, Requisite parameters for optimal wear performance of nitrogen-implanted titanium and Ti-6Al-4V. Surf Coat Technol., 1992. **50**: p. 139.

145. Itoh, Y., et al., Improving the tribological properties of Ti-6Al-4V alloy by nitrogen-ion implantation. Surf. Coat. Technol., 1999. **111**: p. 172-176.

146. Williams, J.M., et al., Properties of nitrogen-implanted alloys and comparison materials. Surf Coat Technol., 1996. **88**: p. 132-138.

147. Alonzo, F., et al., Mechanical properties and structure of Ti-6Al-4V alloy implanted with different light ions. Surf. Coat. Technol., 1995. **74-75**: p. 986-992.

148. Han, J., et al., Plasma source ion implantation of nitrogen, carbon and oxygen into Ti-6Al-4V alloy. Surface and Coatings Technology, 1996. **82**(3): p. 270-276.

149. Streicher, R.M., et al., Wear behaviour of different surfaces in comparison to TiN and ODH-treated Ti-6Al-7Nb alloy. Ceramics in Substitutive and Reconstructive Surgery, 1991: p. 781-788.

150. Lifang, X., et al., Structure and frictional characteristics of Ti-6Al-4V plasma-based ion implanted with nitrogen then acetylene. Wear, 1999. **225-229**(2): p. 835-842.

151. Ashworth, V., W.A. Grant, and R.P.M. Procter. Ion Implantation Into Metals. in Proceedings of the 3rd International Conference on Modification of Surface Properties of Metals by Ion Implantation. 1981. UMIST, Manchester, UK: Pergamon Press.

152. Kehler, B.A., et al., Tribological behavior of high-density polyethylene in dry sliding contact with ion-implanted CoCrMo. Surface & Coatings Technology, 1999. **114**(1): p. 19-28.

153. Yost, F.G., et al., The effects of N ion implantation on the wear and friction of type 304 and 15-5 PH stainless steels. Thin Solid Films, 1983. **107**: p. 287-295.

154. Hirvonen, J.K., Ion implantation in tribology and corrosion science. J. Vac. Sci. Technol., 1978. **15**: p. 1662-1668.

155. Baron, M., et al., Nitrogen distribution and nitride precipitation in 14N ion implanted 304 and 316 steels. Nucl. Instr. Meth. Phys. Res., 1981. **182-183**: p. 531-538.

156. Chen, J.S., et al., Structural and mechanical properties of nitrogen ion implanted ultra high molecular weight polyethylen. Surf. Coat. Technol., 2001. **138**: p. 33-38.

157. Wang, A., C. Stark, and J.H. Dumbleton, Mechanistic and morphological origins of ultr-high molecular weight polyethylene wear debris in total joint replacement prostheses. Proc. I Mech. Part H; J. Eng. in Med, 1996. **210**(Part H3): p. 141-155.

158. Wang, A., et al., Wear mechanisms of UHMWPE in total joint replacements. Wear, 1995. **181-183**: p. 241-249.

159. Fisher, J., Wear of Ultra High Molecular Weight Polyethylene in Total Artificial Joints. Current orthopaedic - Biomechanics masterclass. **3**: p. 164-169.

160. Dong, H. and T. Bell, Enhanced wear resistance of titanium surfaces by a new thermal oxidation treatment. Wear, 2000. **238**: p. 131-137.

161. Clarke, I.C., et al. Wear of Ti-6Al-4V implanted alloy and ultrahigh molecular weight polyethylene combinations. in Titanium Alloys in Surgical Implants, ASTM STP 796. 1983. Philadelphia.

162. Leng, Y.X., et al., Properties of titanium oxide biomaterials synthesized by titanium plasma immersion ion implantation and reactive ion oxidation. Thin Solid Films, 2000. **377-378**: p. 573-577.

163. Najjar, D., et al., Influence of a foreign body on the wear of metallic femoral heads and polyethylene acetabular cups of total hip prostheses. J. Mater. Sci. Mater Med., 2000. **35**: p. 4583-4588.

164. Alonzo, F., et al., Effects of ion implantation on Ti-6Al-4V on its frictional behaviour against UHMWP. Surf. Coat. Technol., 1996. **83**: p. 301-306.

165. Picraux, S.T., E.P. EerNisse, and F.L. Vook. Applications of ion beams to metals. in International Conference on Applications of Ion Beams to Metals. 1973. Albuquerque, New Mexico: Plenum Press.

166. Hall, R.M., et al., The surface topography of retrieved femoral heads. J. Mater. Sci.: Mater Med, 1996. **8**: p. 739-744.

167. Isaac, G.H., et al., The role of cement in the long term performance and premature failure of Charnley low friction arthroplasties. Engineering in Medicine, 1986. **15**: p. 19-22.

168. Saikko, V.O., P.O. Paavolainen, and P. Slatis, Wear of the polyethylene acetabular cup. Acta Orthop. Scand., 1993. **64**: p. 391-402.

169. Atkinson, J.R., et al., Laboratory wear tests and clinical observations of the penetration of femoral heads into acetabular cups in total replacement hip joints III: The measurement of internal volume changes in explanted Charnley sockets after 2-16 years in vivo and the determination of wear factors. Wear, 1985. **104**: p. 225-244.

170. Hall, R.M. and A. Unsworth, Wear in retrieved Charnley acetabular sockets. Proc. I Mech. Part H; J. Eng. in Med, 1996. **210**: p. 197-207.

171. Wroblewski, B.M., Direction and rate of socket wear in Charnley low-friction arthroplasty. J. Bone Joint Surg., 1985. **67B**: p. 757-761.

172. Goode, P.D., A.T. Peacock, and J. Asher, A study of the wear behaviour of ion implanted pure iron. Nucl. Instr. Meth. Phys. Res., 1983. **209-210**: p. 925-931.

173. Cui, F.-Z., H.-D. Li, and X.-Z. Zhang, Modification of tribological characteristics of metals after nitrogen implantation. Nucl. Instr. Meth. Phys. Res., 1983. **209-210**: p. 881-887.

174. Sommerer, T.J. and E.B. Hale, Characterisation of wear modes in ion-implanted steel from auger measurements. Mater. Sci. Eng, 1985. **69**: p. 149-154.

175. Feller, H.G., R. Klinger, and W. Benecke, Tribo-enhanced diffusion of nitrogen implanted into steel. Mater. Sci. Eng, 1985. **69**: p. 173-180.

176. Dimigen, H. and K. Kobs, Wear resistance of nitrogen-implanted steels. Mater. Sci. Eng, 1985. **69**: p. 181-190.

177. Hale, E.B., et al. Surface modification of materials by ion beams. in Proceedings Conference. 1984. Heidelberg.

178. Wright, K.W.J., H.S. Dobbs, and J.T. Scales, Wear studies on prosthetic materials using the pin-on-disc machine. Biomaterials, 1982. **3**: p. 41-48.

179. Poggie, R.A., A.K.Mishra, and J.A. Davidson, Three-body abrasive wear behaviour of orthopaedic implants bearing surfaces from titanium debris. J. Mater. Sci. Mater. Med., 1994. **5**: p. 387-392.

180. Poggie, R.A., et al., Friction and wear characterization of UHMWPE in reciprocating sliding contact with Co-Cr, Ti-6Al-4V, and Zirconia implant bearing surfaces. in wear and friction of elastomers. ASTM STP 1145, 1992: p. 65-81.

181. Tateishi, T., A. Terui, and H. Yunoki, Friction and wear properties for biomaterials for artificial joint. Bioceramics, 1990. **2**: p. 145-151.

182. Elfick, A.P.D., et al., The influence of femoral head surface roughness on the wear of ultrahigh molecular weight polyethylene sockets in cementless total hip replacement. J. Biomed. Mater. Res., 1999. **48**: p. 712-718.

183. Lancaster, J.K., Abrasive wear of polymers. Wear, 1969. **14**: p. 223-239.

184. Jahan, M.S. and K.S. McKinny, Radiation -sterisation and subsequent oxidation of medical grade polyethylene: an ESR study. Nucl. Instr. Meth. Phys. Res., 1999. **B 151**: p. 207-212.

APPENDICES

APPENDIX A

Calibration of the Pin-On-Plate Wear Apparatus, Articulation Distance Calculation (in THR), Polymer Pin and Metallic Plate Cleaning and Weighing Protocols, Experimental Errors, and Pin-On-Plate Wear and Standard Deviation Measurements

A1: Calibration of the Pin-On-Plate Wear Apparatus (Pin Force)

The components used to apply the required force of 40N on the pins during the pin-on-plate testing include the aluminium lever arm (159 g), a screw and nut (9 g) to adjust the lever arm, a peg (14 g) to locate the additional weights on the lever arm, pin holder (74 g), and additional weights (?). The additional weights required to exert a force of 40 N on the pins was calculated by taking moments about the pivot of the lever arm.

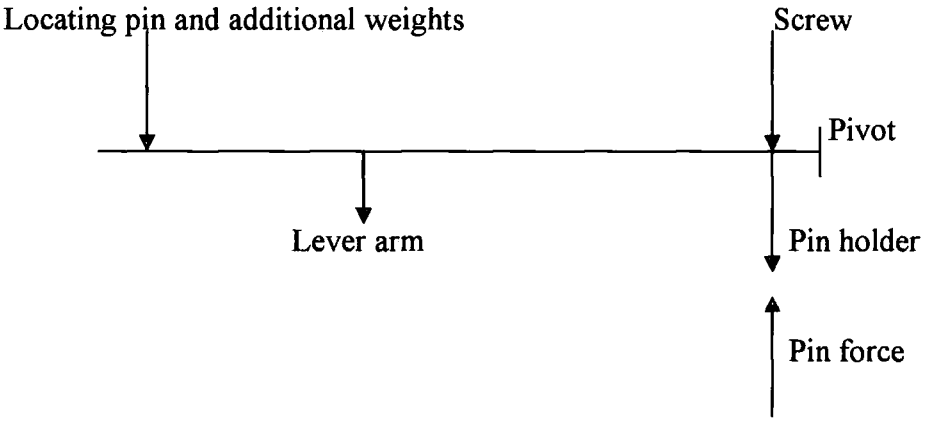

Figure A1.1. Force diagram of the lever arm

To calculate the weight (F1) applied to the lever arm at a distance (d1) from the pivot to exert a force of 40 N on the pins, the following equation can be used:

$$(F1 \times d1) + (F2 \times d2) + (F3 \times d3) = F \times d3 \qquad \text{equation A1.1.}$$

Where F1 is the additional weights and d1 (138 mm) is the distance between the pivot point and the locating pin point; F2 is the lever arm weight (including the screw and nut

to adjust the lever arm, and the peg to locate the additional weights on the lever arm), and d2 (91 mm) is the distance between the pivot point and the centre of gravity of the lever arm; F3 is the pin holder force and d3 (30 mm) is the distance between the holder and the pivot; F is the pin force and d3 (30 mm) is the distance between the pin and the pivot point. An additional weight of ≈ 733 g was calculated and used.

A2. Calculation of Articulation Distance in THR Joints

The diameter of surgically used femoral head components in THR with metal-polyethylene pairings can range between 22-32 mm (or > 32 mm) depending on the design. The Charnley hip endoprosthesis design has a femoral head diameter of 22 mm, whereas the Muller design has a head diameter of 32 mm. During a walking cycle, the hip joint has an angle of ≈ 70° swing (flexion/extension) at 1 Hz.

$S = r\theta$ equation A2.1.

Where S is the sliding distance, r is the radius of joint, and θ is the angle of swing in radians.

2π radians = 360° equation A2.2.

π radians = 180° equation A2.3.

From equation A2.3,

70° = 1.22 rads equation A2.3.

For a Charnley hip endoprosthesis of head diameter 22 mm, r is 11 mm, which implies:

S = 11 x 1.22 = 13.44 mm

A complete walking cycle is represented by 2 steps, therefore, for a walking cycle the sliding distance is ≈ 27 mm.

For a Muller hip endoprosthesis of head diameter 32 mm, r is 16 mm, which implies:

$S = 16 \times 1.22 = 19.52$ mm

A complete walking cycle is represented by 2 steps, therefore, for a walking cycle the sliding distance is ≈ 39 mm.

For such designs, an articulating distance in the range 27-39 mm / walking cycle would be expected. Therefore, to simulate *in vivo* conditions of a hip joint replacement of such designs, an *in vitro* sliding distance in the range 27-39 mm/cycle is required.

A3: Pin and Plate Cleaning and Weighing Protocol

The cleaning protocols for both pin and plate are detailed below, with that of the pins closely following the ASTM standard F732-00 (part 6) recommendations.

1. Turn off motor(s) to stop motion
2. Turn off the controller
3. Remove loads from cantilever loading arms
4. Unscrew and remove pin arms from main rig and remove pins from holders
5. Unscrew and remove the electronic lubricant level and temperature sensors
6. Unscrew and remove plastic frame plate holder from lubricant bath
7. Remove plates from plastic frame holder
8. Rinse plates with tap water to remove contaminants
9. Clean plates with a solution of detergent and then acetone
10. Dry plates with lint-free tissue and air-dry in a dust-free environment
11. Remove control and test pins from holders
12. Rinse pins with tap water to remove contaminants
13. Wash pins in an ultrasonic cleaner in a solution of 1 % detergent for 15 min
14. Rinse pins in a stream of distilled water
15. Rinse pins in an ultrasonic bath cleaner in distilled water for 5 min
16. Rinse pins in a stream of distilled water
17. Dry pins with lint free tissue
18. Immerse pins in acetone for 3 min
19. Dry pins with lint free tissue

20. Air-dry pin(s) in a dust-free environment at room temperature for 30 min
21. Weigh pins four times and take an average
22. Clean lubricant bath, pin and plate holders and the wear machine
23. Reassemble wear machine and add new lubricant
24. Turn the controller on
25. Turn motor(s) on to start motion, once the lubricant temperature equilibrates at 37 ± 1 °C

A4: Experimental Errors

Even if we have a highly controlled test procedure and a most precise measuring apparatus, there will always be some scatter in the collected data from test samples of the same material, and therefore appropriate measures are necessary to minimise the possibility of measurement error. The factors that lead to uncertainty in measured data include the test method, variation in sample fabrication procedure, operator basis, inhomogeneity in the same material, and apparatus calibration.

Despite the variation that may exist in the experimental measurements during this work, typical values were reported by taking an average of all the data measured. The average $\bar{x}$ of some parameter x is given by:

$$\bar{x} = \frac{\sum_{i=1}^{n} x_i}{n} \qquad \text{Equation A4.1.}$$

Where n is the number of measurements and x_i is the value of discrete measurement.

The degree of scatter of the measured data was also quantified using standard deviation where applicable, during the experimental measurements. Standard deviation s is determined using the following expression:

$$s = \left[\frac{\sum_{i=1}^{n} \left(x_i - \bar{x}\right)^2}{n-1} \right]^{\frac{1}{2}}$$ Equation A4.2.

Where x_i, $\bar{x}$, and n are defined above. A high value of the standard deviation corresponds to a high degree of scatter or variability in the data collected from samples of the same material.

A5: Pin-on-plate wear volume loss measurement values for UHMWPE/Ti6Al4V couples

The tabulated pin wear volumes were calculated using an average of 4 weight loss measurements and the deviations from the mean of the weight loss measurements were less than 10 % in all cases.

Table A5.1. Unmodified UHMWPE pin wear volume (mm^3) measurements (articulated against unmodified Ti6Al4V, fig. 5.16)

Sliding distance (km)	Pin 1	Pin 2	Pin 3	Pin 4
0	0	0	0	0
12.59	1.65	1.61	1.35	1.65
22.36	2.95	2.67	2.74	2.72
35.15	4.69	3.89	4.33	4.03
44.67	5.84	4.78	5.59	5.03
57.61	7.42	6.62	7.22	6.92
67.04	8.56	7.75	8.40	8.07
79.46	9.87	8.93	9.69	9.25
88.92	11.05	10.19	10.89	10.54
101.34	12.69	11.63	12.43	12.01
110.72	13.68	12.45	13.44	12.94
123.13	14.86	13.58	14.43	14.04
132.54	15.76	14.51	15.49	15.04
145.01	17.02	15.51	16.83	16.09
154.37	17.89	16.21	17.74	16.85
166.84	19.34	17.42	19.02	18.08
176.17	20.12	18.18	19.68	18.82
188.55	21.41	19.37	20.86	20.02
197.80	21.95	19.94	21.44	20.65

207.16	22.54	20.50	21.98	21.25

TableA5.2. Modified UHMWPE pin wear volume (mm^3) measurements (articulated against unmodified Ti6Al4V, fig. 5.17)

Sliding distance (km)	5 x 10^{15} N^+/cm^2 implanted pin 1	5 x 10^{15} N^+/cm^2 implanted pin 2	1 x 10^{15} N^+/cm^2 implanted pin 3	1 x 10^{15} N^+/cm^2 implanted pin 4
0	0	0	0	0
9.59	1.00	1.13	1.38	1.36
22.30	2.09	2.18	2.67	2.56
31.65	3.07	3.18	3.85	3.67
44.46	4.33	4.39	5.07	5.02
53.35	5.43	5.50	6.34	6.17
64.69	6.53	6.66	7.29	7.09
73.50	7.54	7.65	8.40	8.20
85.67	8.69	8.76	9.69	9.49
94.61	9.69	9.83	10.55	10.30
106.14	10.58	10.70	11.42	11.20
117.81	11.53	11.66	12.40	12.12
126.90	12.47	12.62	13.34	13.02
139.55	13.37	13.55	14.24	13.93
148.44	14.27	14.41	15.12	14.82
161.08	15.39	15.49	16.19	15.90
170.26	16.40	16.57	17.24	16.92
182.61	17.46	17.60	18.25	17.88
191.81	18.40	18.63	19.27	18.86
203.84	19.30	19.50	20.23	19.79

Table A5.3. 5 x 10^{15} N^+/cm^2 implanted UHMWPE pin wear volume (mm^3) measurements (articulated against unmodified Ti6Al4V, fig. 5.18)

Sliding distance (km)	Pin 1	Pin 2	Pin 3	Pin 4
0	0	0	0	0
9.52	1.15	1.24	1.27	1.25
21.97	2.30	2.51	2.57	2.46
31.47	3.39	3.57	3.65	3.51
44.46	4.44	4.72	4.80	4.61
53.35	5.43	5.77	5.93	5.64
65.73	6.68	7.00	7.22	6.80

74.94	7.65	8.00	8.29	7.70
87.47	8.67	9.18	9.42	8.87
96.77	9.56	10.09	10.35	9.74
109.09	10.47	11.02	11.29	10.66
121.41	11.44	11.92	12.19	11.62
130.77	12.31	12.87	13.05	12.48
143.15	13.31	14.04	14.09	13.48
152.51	14.29	15.03	15.20	14.47
164.89	15.41	16.15	16.36	15.56
174.24	16.40	17.19	17.35	16.58
186.58	17.39	18.20	18.43	17.56
196.15	18.07	18.90	19.20	18.21
205.28	18.72	19.54	19.85	18.85

Table A5.4. Unmodified UHMWPE pin wear volume (mm^3) measurements (articulated against 2 x 10^{17} N^+/cm^2 implanted Ti6Al4V, fig. 5.19)

Sliding distance (km)	Pin 1	Pin 2	Pin 3	Pin 4
0	0	0	0	0
2.19	0.30	0.30	0.26	0.27
14.04	1.33	1.38	1.30	1.32
22.99	1.98	2.03	1.90	1.88
32.16	2.51	2.72	2.38	2.70
42.41	3.31	3.37	3.13	3.26
58.33	4.07	4.20	3.86	4.11
63.14	4.63	4.87	4.35	4.75
79.66	5.32	5.62	5.01	5.52
86.32	5.88	6.22	5.49	6.11
95.91	6.47	6.87	6.09	6.78
105.38	7.18	7.59	6.83	7.39
115.53	7.76	8.11	7.40	7.98
125.34	8.35	8.68	7.96	8.53
135.83	8.91	9.25	8.68	9.10
146.43	9.46	9.92	9.37	9.67
160.93	10.29	10.72	10.22	10.47
171.76	11.06	11.45	10.92	11.17
186.22	11.82	12.20	11.62	11.98
197.17	12.48	12.95	12.29	12.72

Table A5.5. Unmodified UHMWPE pin wear volume (mm^3) measurements (articulated against 1 x 10^{21} N^+/cm^2 (pins 1 and 2) and 1 x 10^{18} N^+/cm^2 (pins 3 and 4) implanted Ti6Al4V, fig. 5.20)

Sliding distance (km)	Pin 1	Pin 2	Pin 3	Pin 4
0	0	0	0	0
9.92	0.97	1.07	1.00	1.08
19.80	2.10	2.18	2.12	2.22
30.58	3.19	3.33	3.21	3.40
37.33	3.80	3.95	3.82	4.03
47.09	4.52	4.67	4.54	4.81
57.55	5.28	5.39	5.34	5.20
67.26	5.90	6.05	5.98	5.73
75.73	6.47	6.61	6.33	6.12
85.50	7.22	7.39	6.87	6.68
94.79	7.97	8.12	7.40	7.22
103.99	8.72	8.92	8.03	7.85
114.28	9.55	9.75	8.65	8.47
123.74	10.32	10.54	9.18	9.03
134.32	11.09	11.29	9.65	9.47
143.98	11.84	12.04	10.20	9.96
153.42	12.50	12.68	10.70	10.43
162.78	13.15	13.35	11.15	10.87
172.09	13.80	13.99	11.60	11.32
181.45	14.44	14.57	12.01	11.69

Table A5.6. 5 x 10^{15} N^+/cm^2 implanted UHMWPE pin wear volume (mm^3) measurements (articulated against 2 x 10^{17} N^+/cm^2 implanted Ti6Al4V, fig. 5.21)

Sliding distance (km)	Pin 1	Pin 2	Pin 3	Pin 4
0	0	0	0	0
9.21	0.56	0.64	0.62	0.53
18.54	1.21	1.29	1.27	1.15
27.39	1.81	1.84	1.82	1.70
37.37	2.37	2.36	2.33	2.32
47.00	2.73	2.72	2.74	2.75
56.24	3.27	3.22	3.25	3.21
65.74	3.72	3.66	3.68	3.69
74.03	4.15	4.07	4.06	4.12
86.85	4.80	4.57	4.62	4.76

96.53	5.18	4.94	5.00	5.12
106.82	5.74	5.36	5.44	5.62
119.75	6.33	5.96	6.01	6.21
128.87	6.79	6.32	6.43	6.64
138.57	7.38	6.76	6.97	7.23
147.83	7.84	7.16	7.37	7.63
157.66	8.18	7.47	7.68	7.94
170.70	8.91	8.02	8.40	8.67
180.43	9.39	8.34	8.85	9.14
193.03	9.87	8.73	9.24	9.58

Table A5.7. Unmodified XLPE pin wear volume (mm^3) measurements (articulated against unmodified Ti6Al4V)

Sliding distance (km)	Pin 1	Pin 2	Pin 3	Pin 4
0	0	0	0	0
12.81	1.99	2.47	2.21	1.60
22.40	3.77	4.68	4.21	3.61
35.01	6.39	7.47	6.81	6.28
44.52	8.54	9.65	8.96	8.30
57.61	10.45	11.53	10.85	10.21

Table A5.8. 5 x 10^{15} N^+/cm^2 implanted XLPE (pin 1 and 2) and unmodified (pins 3 and 4) wear volume (mm^3) measurements (articulated against 2 x 10^{17} N^+/cm^2 implanted Ti6Al4V, fig. 5.22)

Sliding distance (km)	Modified pin 1	Modified pin 2	Pin 3	Pin 4
0	0	0	0	0
10.72	0.53	0.52	0.65	0.65
20.80	1.01	0.98	1.29	1.28
31.14	1.50	1.46	1.85	1.88
40.80	1.90	1.81	2.41	2.40
50.86	2.47	2.30	3.03	3.08
59.70	2.95	2.73	3.57	3.59
69.56	3.40	3.17	4.08	4.03
79.19	3.90	3.69	4.68	4.63
88.41	4.28	4.13	5.23	5.13
98.16	4.73	4.58	5.72	5.60
107.90	5.08	4.96	6.09	5.98

118.22	5.39	5.32	6.43	6.32
128.29	5.67	5.59	6.74	6.59
138.15	5.94	5.82	7.03	6.86
147.92	6.18	6.09	7.31	7.14
157.68	6.45	6.31	7.48	7.30
167.53	6.69	6.53	7.74	7.55
177.32	6.89	6.74	7.95	7.73
187.04	7.08	6.93	8.16	7.95

Table A5.9. Table of values for mean UHMWPE volume loss graph (fig. 5.23)

Sliding distance (km)	Couple 1	Couple 2	Couple 3	Couple 4	Couple 5
0	0	0	0	0	0.0
10.00	1.57	0.28	1.02	1.04	0.59
20.00	2.77	1.33	2.14	2.17	1.23
30.00	4.23	1.94	3.26	3.30	1.79
40.00	5.31	2.58	3.87	3.93	2.35
50.00	7.05	3.27	4.60	4.68	2.74
60.00	8.20	4.06	5.34	5.27	3.24
70.00	9.44	4.65	5.98	5.86	3.69
80.00	10.67	5.37	6.54	6.23	4.10
90.00	12.19	5.93	7.30	6.77	4.69
100.00	13.13	6.55	8.04	7.31	5.06
110.00	14.23	7.25	8.82	7.94	5.54
120.00	15.20	7.81	9.65	8.56	6.13
130.00	16.36	8.38	10.43	9.10	6.55
140.00	17.17	8.98	11.19	9.56	7.08
150.00	18.46	9.60	11.94	10.08	7.50
160.00	19.20	10.43	12.59	10.57	7.82
170.00	20.41	11.15	13.25	11.01	8.50
180.00	21.00	11.91	13.90	11.46	8.93
190.00	21.57	12.61	14.50	11.85	9.36

Table A5.10. Standard deviations of the mean UHMWPE volume loss values in table A5.9 (fig. 5.23)

Couple 1 (±)	Couple 2 (±)	Couple 3 (±)	Couple 4 (±)	Couple 5 (±)
0	0	0	0	0
0.14	0.02	0.07	0.06	0.05
0.13	0.04	0.05	0.07	0.06
0.35	0.07	0.10	0.14	0.06
0.49	0.16	0.11	0.15	0.02
0.35	0.10	0.10	0.19	0.01
0.36	0.14	0.08	0.09	0.03
0.43	0.22	0.11	0.17	0.02
0.38	0.27	0.10	0.15	0.04
0.47	0.32	0.12	0.14	0.11
0.54	0.35	0.11	0.13	0.11
0.54	0.32	0.14	0.13	0.17
0.55	0.31	0.14	0.13	0.17
0.70	0.31	0.15	0.11	0.21
0.79	0.25	0.14	0.13	0.28
0.88	0.24	0.14	0.17	0.30
0.87	0.22	0.12	0.18	0.31
0.90	0.23	0.14	0.20	0.39
0.88	0.24	0.14	0.20	0.45
0.89	0.29	0.09	0.23	0.49

Table A5.11. Mean bedding in and steady state wear factors of UHMWPE/Ti6Al4V wear couples

Wear test	Mean bedding in k_o (x 10^{-6} mm^3/Nm)	Sliding distance (km)	Mean steady state k_o (x 10^{-6} mm^3/Nm)	Sliding distance (km)
Test 1	3.04 ± 0.17	0-67	2.41 ± 0.11	67-207
Test 2 (a)	2.56 ± 0.01	0-95	2.26 ± 0.01	95-204
Test 2 (b)	2.82 ± 0.05	0-95	2.23 ± 0.03	95-204
Test 3	1.86 ± 0.08	0-63	1.50 ± 0.02	63-197
Test 4 (a)	2.47 ± 0.04	0-58	1.35 ± 0.01	58-181
Test 4 (b)	2.46 ± 0.06	0-58	1.90 ± 0.01	58-181
Test 5	1.46 ± 0.01	0-66	1.13 ± 0.09	66-193

Where Test 1 is Unmodified UHMWPE/unmodified Ti6Al4V; Test 2 (a) is 5 x 10^{15} N^+ ions/cm^2 implanted UHMWPE/Unmodified Ti6Al4V; Test 2 (b) is 1 x 10^{15} N^+ ions/cm^2 implanted UHMWPE/Unmodified Ti6Al4V; Test 3 is Unmodified UHMWPE/2 x 10^{17} ions/cm^2 implanted Ti6Al4V; Test 4 (a) is Unmodified UHMWPE/1 x 10^{18} N^+ ions cm^{-2} implanted Ti6Al4V; Test 4 (b) is Unmodified UHMWPE/1 x 10^{21} N^+ ions/cm^2 implanted Ti6Al4V; Test 5 is 5 x 10^{15} N^+ ions/cm^2 implanted UHMWPE/2 x 10^{17} N^+ ions/cm^2 implanted Ti6Al4V wear couples.

A6: Pin-on-plate wear volume loss measurement values for UHMWPE/stainless steel couples

Table A6.1.Unmodified UHMWPE pin wear volume (mm^3) measurements (articulated against unmodified stainless steel, fig. 5.67)

Sliding distance (km)	Pin 1	Pin 2	Pin 3	Pin 4
0	0	0	0	0
9.43	0.81	0.59	0.74	0.67
18.80	1.42	1.07	1.29	1.16
28.13	2.49	2.01	2.29	2.11
37.47	3.30	2.74	3.06	2.87
46.80	4.34	3.49	3.94	3.67
59.04	5.32	4.31	4.87	4.55
71.28	6.09	4.98	5.60	5.25
80.64	7.13	5.96	6.62	6.27
90.00	7.63	6.40	7.11	6.72
99.37	8.07	6.77	7.55	7.12
111.78	8.93	7.25	8.34	7.62
121.14	9.62	7.73	8.99	8.06
133.41	10.04	8.08	9.34	8.40
142.74	10.48	8.50	9.72	8.85
155.16	10.95	8.88	10.03	9.17
164.49	11.40	9.29	10.35	9.62
176.90	11.88	9.69	10.71	9.97
186.23	12.37	10.05	11.19	10.38
198.61	12.87	10.40	11.61	10.76
207.97	13.34	10.74	12.05	11.16

Table A6.2. Unmodified UHMWPE pin wear volume (mm^3) measurements (articulated against 2 x 10^{17} N^+/cm^2 implanted stainless steel, fig.5.68)

Sliding distance (km)	Pin 1	Pin 2	Pin 3	Pin 4
0	0	0	0	0
12.39	0.65	0.61	0.71	0.61
21.65	1.10	1.01	1.16	1.02
34.04	1.62	1.44	1.76	1.50
43.33	2.06	1.83	2.22	1.91
55.72	2.52	2.28	2.69	2.38
65.05	3.01	2.62	3.22	2.79

77.44	3.55	3.02	3.79	3.32
86.70	3.93	3.33	4.22	3.68
99.02	4.37	3.75	4.74	4.13
108.24	4.80	4.11	5.18	4.54
120.62	5.15	4.43	5.59	4.89
129.88	5.41	4.70	5.95	5.17
142.30	5.77	5.11	6.28	5.61
151.57	6.10	5.39	6.52	5.94
163.98	6.44	5.70	6.87	6.24
173.27	6.82	6.04	7.23	6.63
182.56	7.13	6.34	7.57	6.93
191.88	7.40	6.56	7.81	7.19
201.17	7.61	6.77	8.03	7.40
210.48	7.86	7.00	8.26	7.65

Table A6.3. 5 x 10^{15} N^+/cm^2 implanted UHMWPE pin wear volume (mm^3) measurements (articulated against 2 x 10^{17} N^+/cm^2 implanted stainless steel, fig. 5.69)

Sliding distance (km)	Pin 1	Pin 2	Pin 3	Pin 4
0	0	0	0	0
9.30	0.30	0.28	0.33	0.26
21.57	0.75	0.74	0.74	0.67
30.89	1.12	1.17	1.18	1.11
43.31	1.65	1.65	1.68	1.64
52.66	2.09	2.12	2.10	2.11
64.89	2.50	2.56	2.60	2.58
74.19	2.87	2.96	2.99	3.00
86.65	3.18	3.27	3.30	3.33
95.99	3.49	3.59	3.64	3.68
108.39	3.77	3.86	3.92	3.97
117.74	4.06	4.18	4.24	4.26
130.20	4.38	4.51	4.56	4.59
139.56	4.66	4.78	4.88	4.93
148.98	4.89	5.03	5.19	5.26
158.40	5.09	5.19	5.36	5.47
167.76	5.23	5.35	5.51	5.63
177.12	5.38	5.51	5.65	5.76
186.55	5.49	5.67	5.82	5.87
196.29	5.61	5.79	5.98	6.01

205.31	5.76	5.92	6.10	6.14

Table A6.4. Table of values for mean UHMWPE volume loss graphs (figure 5.70)

Sliding distance (km)	Couple 1	Couple 2	Couple 3
0.00	0	0	0
10.00	0.70	0.64	0.29
20.00	1.24	1.07	0.73
30.00	2.22	1.58	1.14
40.00	2.99	2.00	1.66
50.00	3.86	2.47	2.11
60.00	4.76	2.91	2.56
70.00	5.48	3.42	2.96
80.00	6.49	3.79	3.27
90.00	6.97	4.25	3.60
100.00	7.38	4.66	3.88
110.00	8.03	5.01	4.19
120.00	8.60	5.31	4.51
130.00	8.96	5.69	4.81
140.00	9.39	5.99	5.09
150.00	9.76	6.31	5.28
160.00	10.17	6.68	5.43
170.00	10.56	6.99	5.58
180.00	11.00	7.24	5.71
190.00	11.41	7.45	5.85
200.00	11.82	7.69	5.98

Table A6.5. Standard deviations of the mean UHMWPE volume loss values in table A6.4 (fig. 5.70)

Couple 1 (±)	Couple 2 (±)	Couple 3 (±)
0	0	0
0.09	0.05	0.03
0.15	0.07	0.04
0.21	0.14	0.03
0.24	0.17	0.02
0.37	0.18	0.01
0.44	0.26	0.04
0.48	0.33	0.06

0.50	0.38	0.07
0.53	0.42	0.08
0.56	0.45	0.09
0.75	0.49	0.09
0.86	0.52	0.09
0.89	0.48	0.12
0.89	0.47	0.16
0.93	0.49	0.17
0.93	0.49	0.18
0.98	0.51	0.17
1.03	0.52	0.17
1.10	0.52	0.19
1.15	0.53	0.18

Table A6.6. Mean bedding in and steady state wear factors for UHMWPE/stainless steel wear couples

Wear test	Mean bedding in k_o (x 10^{-6} mm^3/Nm)	Sliding distance (km)	Mean steady state k_o (x 10^{-6} mm^3/Nm)	Sliding distance (km)
Test 1	1.99 ± 0.17	0-80	1.02 ± 0.13	80-208
Test 2	1.14 ± 0.09	0-65	0.82 ± 0.04	65-210
Test 3	0.98 ± 0.01	0-74	0.59 ± 0.03	74-205

Where Test 1 is Unmodified UHMWPE/unmodified stainless steel; Test 2 is Unmodified UHMWPE/2 x 10^{17} ions/cm^2 implanted stainless steel; and Test 3 is 5 x 10^{15} ions/cm^2 implanted UHMWPE/2 x 10^{17} ions/cm^2 implanted stainless steel wear couples.

A7: Pin-on-plate wear volume loss measurement values for UHMWPE/Co-Cr-Mo couples

Table A7.1. Unmodified UHMWPE pin wear volume (mm^3) measurements (articulated against unmodified Co-Cr-Mo, fig. 5.80)

Sliding distance (km)	Pin 1	Pin 2	Pin 3	Pin 4
0	0	0	0	0
11.48	0.69	0.69	0.71	0.71
20.76	1.37	1.30	1.45	1.42
30.13	1.99	1.91	2.12	2.07
36.32	2.59	2.47	2.78	2.70
45.64	3.23	3.08	3.42	3.32
54.93	3.81	3.59	4.00	3.86
67.34	4.35	4.12	4.57	4.40
79.96	4.85	4.58	5.11	4.96
88.61	5.28	5.02	5.52	5.38
97.92	5.73	5.48	6.00	5.83
110.36	6.11	5.90	6.45	6.28
119.19	6.53	6.29	6.88	6.70
131.62	7.01	6.75	7.42	7.22
140.93	7.44	7.15	7.87	7.67
153.35	7.79	7.54	8.22	8.05
162.65	8.17	7.87	8.61	8.38
175.07	8.49	8.19	8.94	8.69
184.38	8.85	8.51	9.26	9.05
196.81	9.20	8.90	9.63	9.41
206.13	9.65	9.25	10.01	9.83

Table A7.2. Unmodified UHMWPE pin wear volume (mm^3) measurements (articulated against 2×10^{17} N^+/cm^2 implanted Co-Cr-Mo, fig. 5.81)

Sliding distance (km)	Pin 1	Pin 2	Pin 3	Pin 4
0	0	0	0	0
11.38	0.43	0.50	0.46	0.43
20.69	0.74	0.87	0.81	0.77
33.12	1.14	1.33	1.27	1.19
42.43	1.49	1.75	1.64	1.56
54.86	1.85	2.14	2.03	1.90
64.18	2.11	2.47	2.34	2.22

76.58	2.50	2.94	2.77	2.64
85.90	2.62	3.13	2.99	2.82
98.33	2.92	3.46	3.30	3.09
107.62	3.20	3.73	3.57	3.36
120.04	3.47	3.99	3.83	3.59
129.37	3.78	4.22	4.03	3.90
141.80	4.11	4.55	4.35	4.24
151.10	4.36	4.80	4.62	4.50
163.53	4.75	5.18	4.99	4.87
172.83	4.93	5.38	5.18	5.05
185.26	5.15	5.60	5.42	5.26
194.57	5.36	5.80	5.61	5.44
207.00	5.57	5.99	5.82	5.67
216.23	5.83	6.24	6.04	5.92

Table A7.3. 5 x 10^{15} N^+/cm^2 implanted UHMWPE pin wear volume (mm^3) measurements (articulated against 2 x 10^{17} N^+/cm^2 implanted Co-Cr-Mo, fig. 5.82)

Sliding distance (km)	Pin 1	Pin 2	Pin 3	Pin 4
0	0	0	0	0
12.01	0.25	0.34	0.29	0.28
21.31	0.60	0.69	0.64	0.63
33.74	0.87	1.01	0.95	0.94
42.58	1.16	1.38	1.29	1.26
55.02	1.51	1.77	1.68	1.64
63.84	1.83	2.13	2.02	1.97
76.30	2.12	2.43	2.33	2.26
85.63	2.37	2.70	2.59	2.51
98.02	2.72	3.07	2.93	2.87
107.33	2.94	3.28	3.14	3.08
119.78	3.17	3.50	3.36	3.29
129.07	3.38	3.70	3.57	3.49
138.42	3.58	3.91	3.79	3.70
147.86	3.77	4.14	3.96	3.85
157.21	3.99	4.37	4.17	4.05
166.52	4.21	4.60	4.40	4.28
175.85	4.45	4.85	4.63	4.51
185.14	4.67	5.06	4.83	4.71
194.49	4.89	5.28	5.05	4.95
203.80	5.11	5.54	5.25	5.17

Table A7.4. Table of values for mean UHMWPE volume loss graph (fig. 5.83)

Sliding distance (km)	Couple 1	Couple 2	Couple 3
0.00	0.00	0.00	0.00
10.00	0.70	0.46	0.29
20.00	1.38	0.80	0.64
30.00	2.02	1.23	0.94
40.00	2.63	1.61	1.27
50.00	3.26	1.98	1.65
60.00	3.81	2.29	1.99
70.00	4.36	2.71	2.29
80.00	4.87	2.89	2.54
90.00	5.30	3.19	2.90
100.00	5.76	3.47	3.11
110.00	6.19	3.72	3.33
120.00	6.60	3.98	3.54
130.00	7.10	4.31	3.75
140.00	7.53	4.57	3.93
150.00	7.90	4.95	4.15
160.00	8.26	5.13	4.37
170.00	8.58	5.36	4.61
180.00	8.92	5.55	4.82
190.00	9.28	5.76	5.04
200.00	9.69	6.01	5.27

Table A7.5. Standard deviations of the mean UHMWPE volume loss values in table A7.4 (fig. 5.83)

Couple 1 (±)	Couple 2 (±)	Couple 3 (±)
0.00	0.00	0.00
0.01	0.03	0.04
0.07	0.06	0.04
0.09	0.09	0.06
0.13	0.11	0.09
0.15	0.13	0.11
0.17	0.16	0.12
0.18	0.19	0.13
0.22	0.22	0.14
0.21	0.23	0.15
0.22	0.23	0.14
0.24	0.23	0.14

0.25	0.19	0.14
0.29	0.19	0.14
0.31	0.19	0.16
0.30	0.18	0.17
0.31	0.19	0.17
0.32	0.19	0.18
0.32	0.19	0.18
0.31	0.18	0.17
0.33	0.17	0.19

Table A6.6. Mean bedding in and steady state wear factors for UHMWPE/Co-Cr-Mo wear couples

Wear test	Mean bedding in k_o (x 10^{-6} mm^3/Nm)	Sliding distance (km)	Mean steady state k_o (x 10^{-6} mm^3/Nm)	Sliding distance (km)
Test 1	1.75 ± 0.08	0-54	0.96 ± 0.03	54-206
Test 2	0.95 ± 0.06	0-42	0.63 ± 0.005	42-216
Test 3	0.75 ± 0.05	0-64	0.58 ± 0.02	64-204

Where Test 1 is Unmodified UHMWPE/unmodified Co-Cr-Mo; Test 2 is Unmodified UHMWPE/2 x 10^{17} ions/cm^2 implanted Co-Cr-Mo; and Test 3 is 5 x 10^{15} ions/cm^2 implanted UHMWPE/2 x 10^{17} ions/cm^2 implanted Co-Cr-Mo wear couples.

APPENDIX B

Material Data of the Selected Biomaterials Used in this Study

B1: Material data for Ti6Al4V

Table B1.1. Ti6Al4V data as supplied (Mill Annealed)

Material Designation (classification)	Ti6Al4V (alpha/beta)
ASTM Standard	ASTM F 1472
ISO Standard	ISO 5832-3
Density (g/cm^3)	4.4
Modulus of Elasticity (GPa)	114
Ultimate Tensile Strength (MPa)	860
Yield Tensile Strength (MPa)	790
Compressive Yield Strength (MPa)	860
Fatigue Strength (MPa)	300
Elongation to break (%)	15
Shear Modulus (GPa)	44
Shear Strength (MPa)	550

B2: Material data for Austenitic Stainless Steel (Rex 734/ORTRON 90)

Table B2.1. Rex 734 (ORTRON 90) data as supplied (Cold Worked)

Material Designation	Fe-21Cr-10Ni-3.5Mn-2.5Mo
ASTM Standard	ASTM F 1586
ISO Standard	ISO 5832-9
Density (g/cm^3)	7.9
Modulus of Elasticity (GPa)	193
Tensile Strength (MPa, min)	740
0.2 % Proof Stress (MPa, min)	430
Elongation to break (%, min)	35

B3: Material data for Co-Cr-Mo

Table B3.3. Co-Cr-Mo data as supplied (Wrought Alloy)

Material Designation	Co-28Cr-6Mo
ASTM Standard	ASTM F 1537
ISO Standard	ISO 5832-12
Density (g/cm^3)	8.3
Modulus of Elasticity (GPa)	210
Ultimate Tensile Strength (MPa)	1035
Yield Tensile Strength, 0.2 % Offset (MPa)	585
Elongation to break (%)	25
Reduction of Area (%)	23

B4: Material data for UHMWPE

Table B4.1. UHMWPE data as supplied (Ram Extruded)

Weight Average Molecular Weight (g/mol)[a]	3.1×10^6
Density (kg/m^3)	927
Yield Strength (MPa, min)	21
Tensile strength (MPa, min)	37
Elongation (%, min)	300
Tensile Modulus (MPa)	689 – 1033
Crystallinity (%)	50
Melting Temperature, T_m (° C)	126
Glass Transition Temperature, T_g (° C)[b]	-120

[a]Data from [8]; [b]data from [184].

APPENDIX C

Hardness Determination Measurements

C1: Determination of the Knoop Indent Penetration Depth

To evaluate the effects of N^+ ion implantation on microhardness, the Knoop indenter penetration depth into the modified samples were investigated. The Knoop diamond indenter penetration depth into the selected modified metallic biomaterials in this study, were calculated using the small indenter pyramidal geometry. The side and top view shape of the indentation are shown figure C1.1.

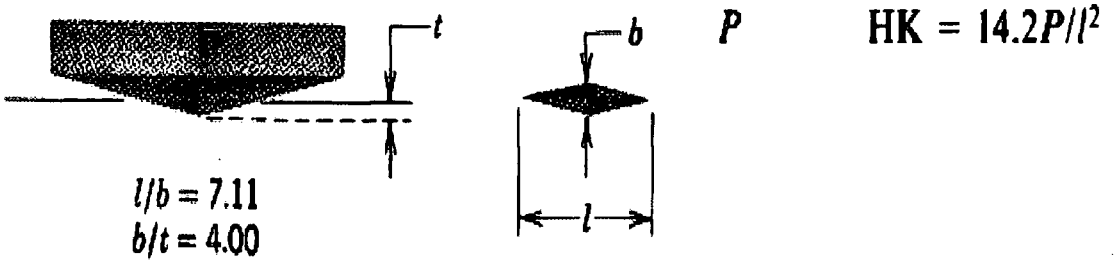

Figure C1.1. Shape of Knoop Indentation (side and top view respectively)

The angle of the diamond pyramid indenter (θ) is 172° indicated on figure C1.1.2 (a). From this angle the penetration depth of the indent (*d*) can be calculated using the indent geometry. Half the angle of the indenter (α) is 86° (fig. C1.2 (b)). During indentation measurements, the width of the indentation (*l*) is measured and the value (in μm) shown on the microhardness tester. From this value, half the width size (*l/2*) can be calculated. The penetration depth (*d*) was calculated using trigonometry. From figure C1.2 (a):

$\tan \alpha = (l/2) / d$ equation C1.1.

Which implies:

$d = (l/2) / \tan \alpha$ equation C1.2.

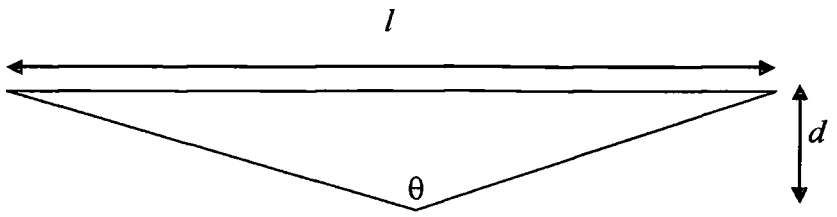

(a)

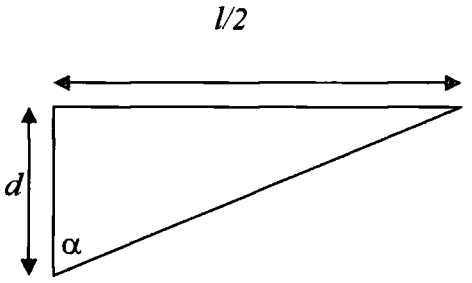

(b)

Figure C1.2 ((a) and (b)). Geometry of Knoop Indentation.Where θ is the angle of the indenter, α is half the angle, *l* is the indent width, *l/2* is half the indent width, and *d* is the indentation depth.

The calculated, *d* values on all the modified metallic samples tested are shown in tables C1.1-C1.5 respectively for 2 x 10^{17} N^+ ions/cm^2 implanted Ti6Al4V, 1 x 10^{18} N^+ ions/cm^2 implanted Ti6Al4V, 1 x 10^{21} N^+ ions/cm^2 implanted Ti6Al4V, 2 x 10^{17} N^+ ions/cm^2 implanted stainless steel, and 2 x 10^{17} N^+ ions/cm^2 Co-Cr-Mo.

Table C1.1. Knoop indent penetration depth measurement values for 2 x 10^{17} N^+ ions/cm^2 implanted Ti6Al4V (fig. 5.13)

Load (gf)	Mean hardness (KHN)	Mean indention width (μm)	Mean indentation depth (μm)
1	730	4.25	0.15 ± 0.007
3	646	8.06	0.28 ± 0.008
5	543	11.05	0.39 ± 0.010
10	428	17.78	0.62 ± 0.021
25	340	32.38	1.13 ± 0.015

Table C1.2. Knoop indent penetration depth measurement values for 1 x 10^{18} N^+ ions/cm^2 implanted Ti6Al4V (fig. 5.14)

Load (gf)	Mean hardness (KHN)	Mean indention width (μm)	Mean indentation depth (μm)
1	1064	3.72	0.13 ± 0.009
3	841	7.04	0.25 ± 0.006
5	633	10.77	0.38 ± 0.011
10	483	17.52	0.61 ± 0.016
25	396	30.19	1.06 ± 0.028

Table C1.3. Knoop indent penetration depth measurement values for 1 x 10^{21} N^+ ions/cm^2 implanted Ti6Al4V (fig. 5.15)

Load (gf)	Mean hardness (KHN)	Mean indention width (μm)	Mean indentation depth (μm)
1	1413	3.14	0.11 ± 0.007
3	1034	6.61	0.23 ± 0.012
5	791	9.54	0.33 ± 0.006
10	535	16.04	0.56 ± 0.020
25	430	28.55	1.00 ± 0.042

Table C1.4. Knoop indent penetration depth measurement values for 2 x 10^{17} N^+ ions/cm^2 implanted stainless steel (fig. 5.66)

Load (gf)	Mean hardness (KHN)	Mean indention width (μm)	Mean indentation depth (μm)
1	1003	3.90	0.14 ± 0.009
3	816	7.38	0.26 ± 0.010
5	701	10.51	0.37 ± 0.012
10	505	17.15	0.60 ± 0.010
25	343	31.16	1.09 ± 0.022

Table C1.5. Knoop indent penetration depth measurement values for 2 x 10^{17} N^+ ions/cm^2 implanted Co-Cr-Mo (figure 5.80)

Load (gf)	Mean hardness (KHN)	Mean indention width (μm)	Mean indentation depth (μm)
1	1175	3.47	0.12 ± 0.006
3	884	6.92	0.24 ± 0.003
5	719	10.09	0.35 ± 0.017
10	628	14.91	0.52 ± 0.009
25	581	25.85	0.90 ± 0.015

C2: Hardness Measurement Tables

C2.1. Hardness values for modified and unmodified Ti6Al4V (fig. 5.12)

Table C2.1.1. Microhardness measurements of unmodified Ti6Al4V

Load (gf)	1	3	5	10	25
Hardness (KHN)	343	327	353	301	308
	359	337	294	296	304
	338	345	301	293	305
	300	327	326	306	301
	354	312	338	324	315
	339	341	322	304	307
	348	348	350	302	300
	366	371	327	313	286
	350	322	322	326	299
	375	320	317	306	302
Mean hardness (KHN)	**347**	**335**	**325**	**307**	**302**
Standard deviation (±)	**20**	**17**	**19**	**11**	**8**

Table C2.1.2. Microhardness measurements of 2 x 10^{17} N^+ ions/cm^2.implanted Ti6Al4V

Load (gf)	1	3	5	10	25
Hardness (KHN)	715	622	505	373	347
	697	625	579	421	328
	717	680	512	445	343
	719	619	586	421	346
	721	647	597	409	341
	800	655	575	440	327
	721	662	529	465	345
	769	667	529	433	353
	736	663	507	409	347
	703	618	511	461	322
Mean hardness (KHN)	**730**	**646**	**543**	**428**	**340**
Standard deviation (±)	**32**	**23**	**37**	**27**	**10**

Table C2.1.3. Microhardness measurements of 1 x 10^{18} N^+ ions/cm^2.implanted Ti6Al4V

Load (gf)	1	3	5	10	25
Hardness (KHN)	1063	854	646	493	433
	1222	823	705	482	410
	1040	927	576	488	409
	1277	958	597	461	394
	1141	838	645	436	389
	966	876	632	524	373
	1027	800	579	501	380
	979	827	642	444	362
	887	755	737	494	401
	1043	749	567	502	408
Mean hardness (KHN)	**1064**	**841**	**633**	**483**	**396**
Standard deviation (±)	**119**	**67**	**56**	**27**	**21**

Table C2.1.4.Microhardness measurements of 1 x 10^{21} N^+ ions/cm^2.implanted Ti6Al4V

Load (gf)	1	3	5	10	25
Hardness (KHN)	1226	828	914	501	463
	1257	1122	822	562	412
	1561	1042	756	536	371
	1358	1001	753	573	478
	1209	1028	923	552	473
	1517	1122	730	612	397
	1670	1057	647	468	390
	1411	1040	824	565	452
	1677	987	742	512	454
	1243	1113	800	473	412
Mean hardness (KHN)	**1413**	**1034**	**791**	**535**	**430**
Standard deviation (±)	**183**	**87**	**84**	**46**	**38**

C2.2: Hardness values for modified and unmodified stainless steel (fig. 5.65)

Table C2.2.1. Microhardness measurements of unmodified stainless steel

Load (gf)	1	3	5	10	25
Hardness (KHN)	544	429	488	356	446
	406	443	467	423	441
	401	502	416	501	404
	448	449	400	467	399
	467	424	439	388	415
	439	440	423	380	436
	426	504	397	359	457
	469	481	366	430	409
	506	412	403	422	411
	510	423	468	390	388
Mean hardness (KHN)	**462**	**451**	**426**	**412**	**415**
Standard deviation (±)	**47**	**33**	**38**	**47**	**22**

Table C2.2.2. Microhardness measurements of 2 x 10^{17} N^+ ions/cm^2.implanted stainless steel

Load (gf)	1	3	5	10	25
Hardness (HKN)	1068	870	624	513	406
	966	751	704	537	440
	1061	1084	638	536	429
	800	773	667	463	516
	841	726	716	526	492
	1019	753	750	455	516
	831	881	690	483	426
	956	740	594	512	413
	1102	804	523	426	487
	1041	765	523	510	499
Mean hardness (HKN)	**969**	**815**	**643**	**496**	**462**
Standard deviation (±)	**109**	**108**	**78**	**38**	**44**

C2.3: Hardness values for modified and unmodified Co-Cr-Mo

Table C2.3.1. Microhardness measurements unmodified Co-Cr-Mo

Load (gf)	1	3	5	10	25
Hardness (HKN)	468	576	525	561	542
	602	639	604	522	502
	586	596	530	566	501
	522	501	532	525	499
	687	559,6	556	527	496
	580	556	523	481	519
	570	559	524	545	581
	599	486	599	464	491
	588	532	448	523	519
	503	588	533	579	501
Mean hardness (HKN)	**570**	**559**	**537**	**529**	**513**
Standard deviation (±)	**61**	**48**	**44**	**36**	**29**

Table C2.3.2. Microhardness measurements of 2 x 10^{17} N^+ ions/cm^2.implanted Co-Cr-Mo

Load (gf)	1	3	5	10	25
Hardness (KHN)	1078	993	759	537	594
	1117	759	599	673	632
	1057	1054	718	681	562
	1373	824	686	672	585
	1183	908	755	583	541
	1248	930	795	685	572
	1129	944	752	638	565
	1272	738	702	591	602
	1088	805	647	630	532
	1200	887	779	592	625
Mean hardness (KHN)	**1175**	**884**	**719**	**628**	**581**
Standard deviation (±)	**101**	**102**	**62**	**51**	**33**

APPENDIX D

Ion Implantation System Diagrams

D1: Ion implantation system diagrams

The model Z-100 zymeting™ system consists of the following six subsystems: beam generation, beam control, product handling, dose monitoring, vacuum system, and control system, which have been described in detail under section 4.2.3. Figure D1.1 shows the block diagram of the system, and the ion source system, scanning system, product handling, beamline and process chamber diagram, and the dose monitoring system are respectively shown in figures D1.2 – D1.6.

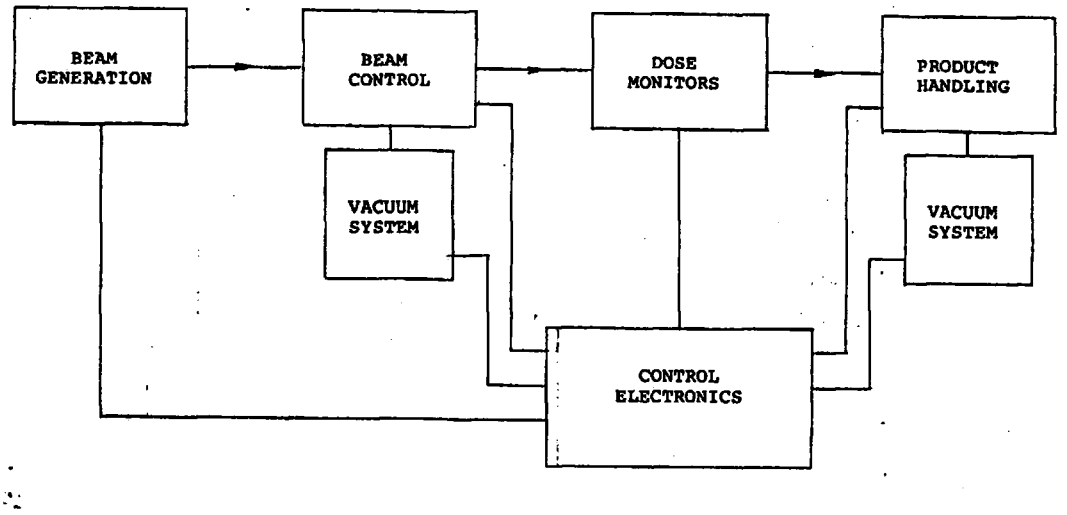

Figure D1.1. System Block Diagram

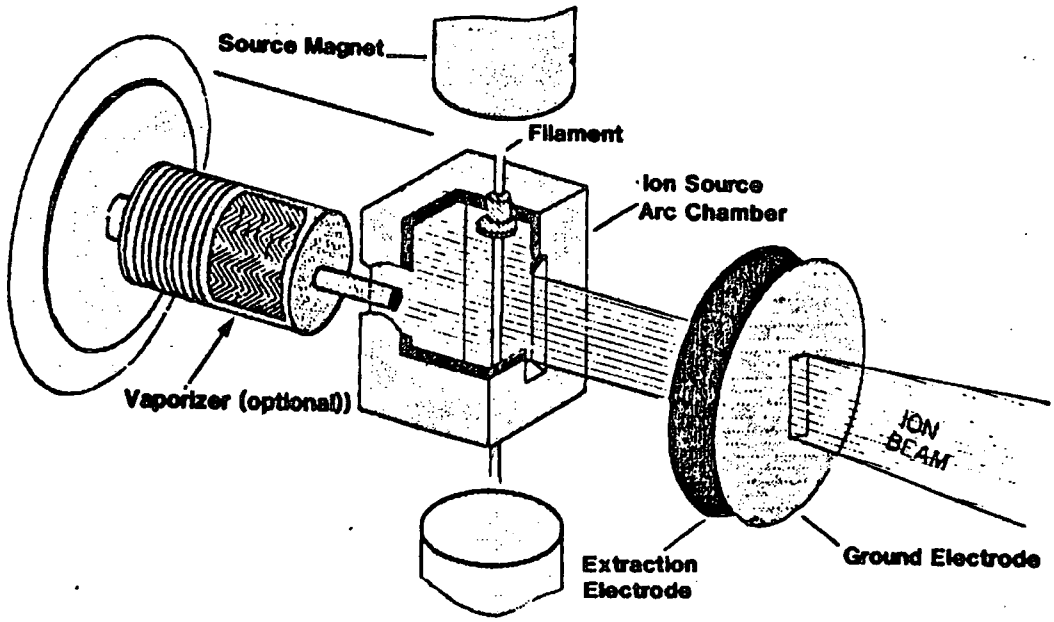

Figure D1.2. Ion Source System

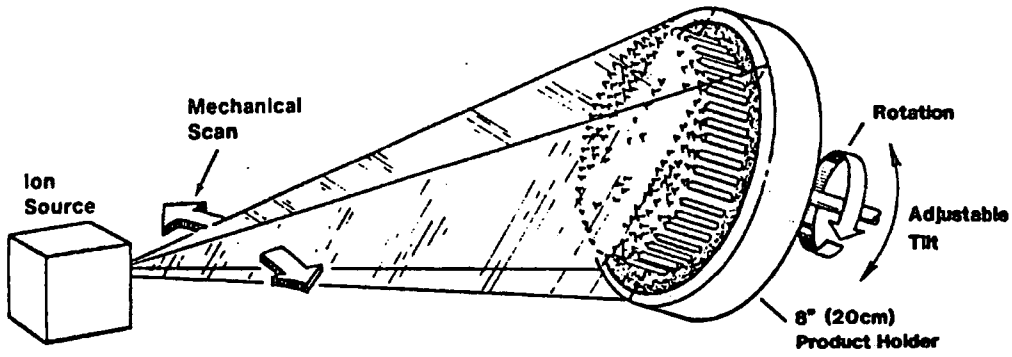

Figure D1.3. Z-100 Scanning System

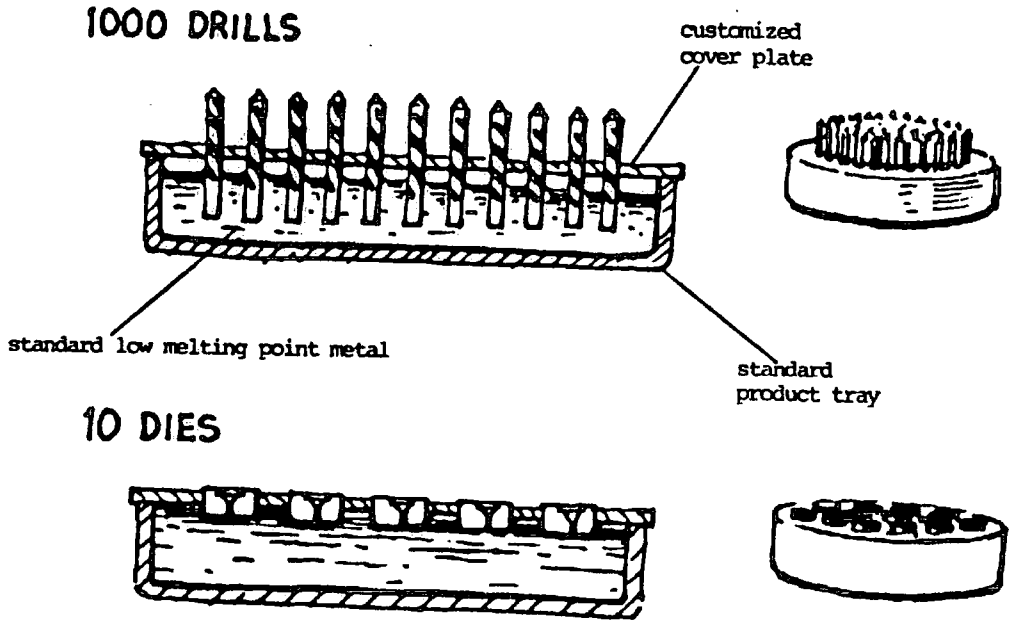

Figure D1.4. Product Handling, using low melting point metal

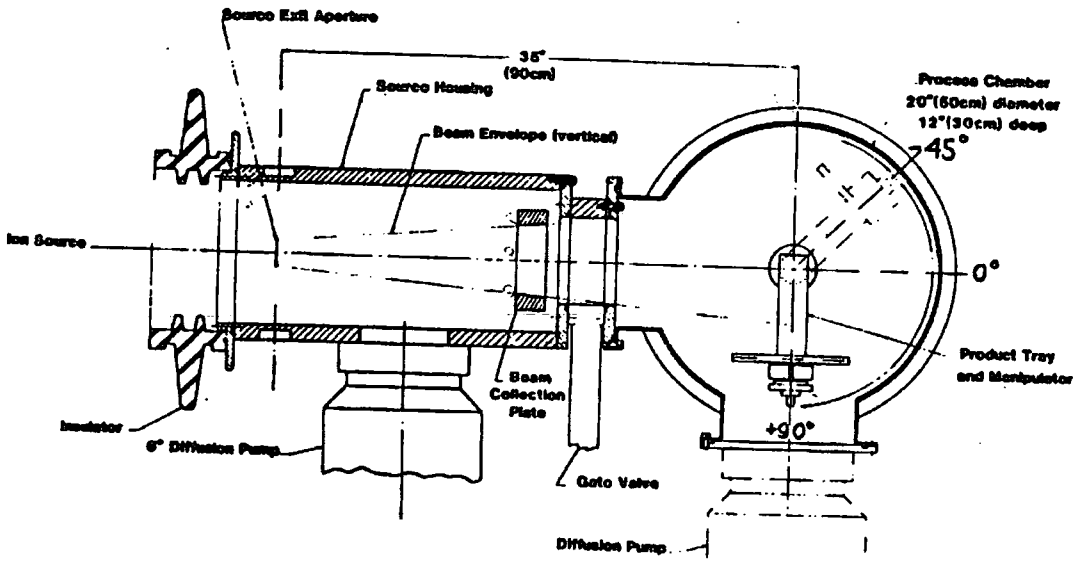

Figure D1.5. Beamline and Process Chamber Diagram

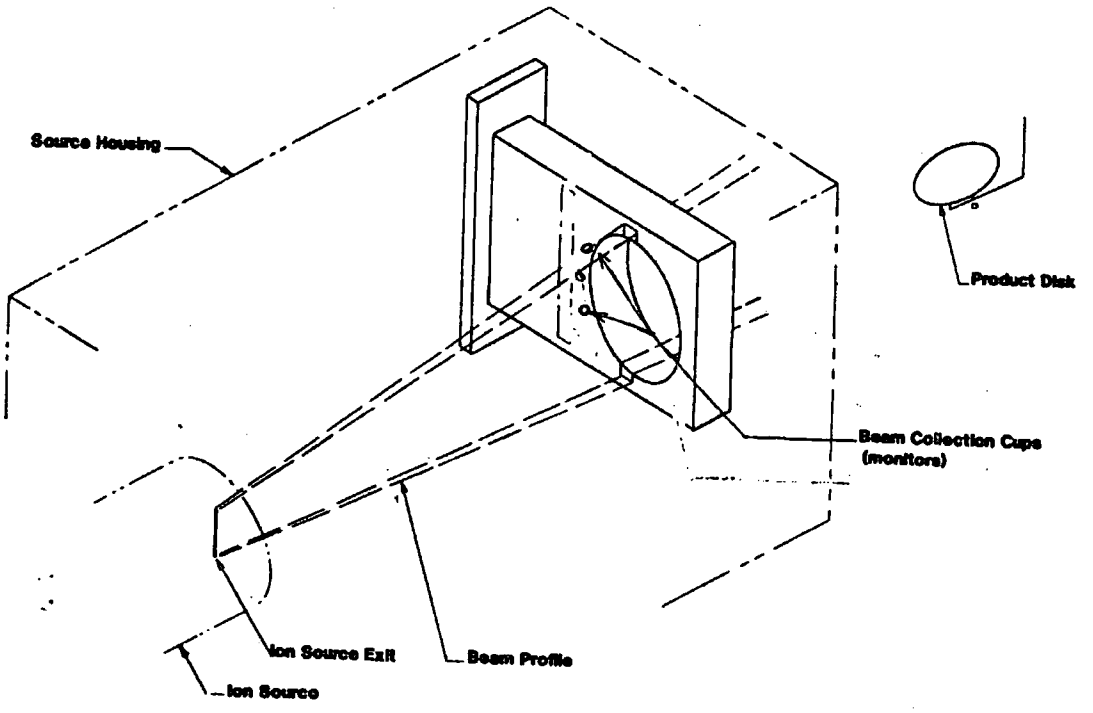

Figure D1.6. Dose Monitoring System

PUBLISHED WORK

1. DK Boampong, and SM Green, EFFECT OF N^+ ION IMPLANTATION ON THE TRIBOLOGICAL PERFORMANCE OF Ti6Al4V ALLOYS AND UHMWPE SLIDING COUPLES. Seminar, Modification of Materials for Biomedical Applications, 17th April 2002, Manchester Metropolitan University

2. D. Boampong, S. Scholes, A. Elfick, T. Joyce, K. Vassiliou, S. Green, and A. Unsworth, MEASUREMENT OF ARTIFICIAL JOINTS, EPSRC Sponsored Seminar, Metrology for Implants, Centre for Precision Technologies, University of Huddersfield, 4th July 2002, Huddersfield University

3. Derrick K. Boampong, Sarah. M. Green, and Anthony Unsworth, ION BEAM MODIFICATION OF Ti6Al4V ALLOY FOR TJR. Proceedings of the 17th European Society for Biomaterials Conference, Barcelona, Spain 11th to14th September 2002: p. L68

4. Derrick K. Boampong, Sarah. M. Green, and Anthony Unsworth, N^+ ION IMPLANTATION OF Ti6Al4V ALLOY AND UHMWPE FOR TOTAL JOINT REPLACEMENT APPLICATION. Accepted for publication in the Journal of Applied Biomaterials and Biomechanics, September 2003